

Syracuse University

**SURFACE**

---

Dissertations - ALL

SURFACE

---

8-2013

## Measurement of the CP Violating Asymmetry $a^s_{sl}$ using $B_s^0 \rightarrow (D_s \rightarrow \phi \pi) \mu \nu$

Alessandra Borgia

Follow this and additional works at: <https://surface.syr.edu/etd>



Part of the [Physics Commons](#)

---

### Recommended Citation

Borgia, Alessandra, "Measurement of the CP Violating Asymmetry  $a^s_{sl}$  using  $B_s^0 \rightarrow (D_s \rightarrow \phi \pi) \mu \nu$ " (2013). *Dissertations - ALL*. 1.  
<https://surface.syr.edu/etd/1>

This Dissertation is brought to you for free and open access by the SURFACE at SURFACE. It has been accepted for inclusion in Dissertations - ALL by an authorized administrator of SURFACE. For more information, please contact [surface@syr.edu](mailto:surface@syr.edu).

## Abstract

The time-integrated measurement of the semileptonic CP violating asymmetry,  $a_{\text{sl}}^s$ , with data acquired at the Large Hadron Collider with the LHCb experiment is presented. This measurement can help physicists understand some peculiarities in the Standard Model, which is the fundamental framework of knowledge of the universe. Should this asymmetry diverge from zero, new physics may be a main motivator. Using  $1 \text{ fb}^{-1}$  of collected data in 2011 with proton-proton collisions at a center-of-mass energy of 7 TeV, the measured value of  $a_{\text{sl}}^s$  presented is  $(-0.06 \pm 0.50 \pm 0.36)\%$ , where the first uncertainty is statistical and the second is systematic. This is in very good agreement with the Standard Model prediction of  $(0.0019 \pm 0.0003)\%$ , however divergent from the D0 collaboration measurement of  $(-1.12 \pm 0.74 \pm 0.17)\%$ .

# Measurement of the CP Violating

Asymmetry  $a_{sl}^s$  using

$$B_s^0 \rightarrow (D_s^{\mp} \rightarrow \phi \pi^{\mp}) \mu^{\pm} \nu_{\mu}$$

by

Alessandra Borgia

Bachelor of Science in Physics, State University of New York at Binghamton, 2007

DISSERTATION

Submitted in partial fulfillment of the requirements for the  
degree of Doctor of Philosophy in Physics  
in the Graduate School of Syracuse University

Syracuse University

August 2013

Copyright 2013 Alessandra Borgia

All Rights Reserved.

*This one is for me.*

*My next piece  
will be dedicated to others.*

*For now,  
this is all mine.*

# Acknowledgments

Through this long and arduous process that is graduate learning and research there have been many people who have made it seem as though it was not the end of the world, at times. First, this work would not have been possible without funding from the National Science Foundation as well as use of the facilities at CERN.

I would like to thank my thesis advisor *Marina Artuso* for her expertise and guidance. Her unending perseverance and exceptional knowledge in high energy physics has helped me grow as a physicist.

Thank you to my fantastic and loving partner, *Justin Garofoli*, for always being calm and cool no matter what challenges we face. Without his help and strength, I fear madness would have taken hold of me prior to graduation. Thank you for helping me grow into the person I am today, you are one of the most important people in my life. I look forward to spending days and nights relaxing with you...forever (!!).

Thank you to *Sheldon Stone*, *Tomasz Skwarnicki* and *Steve Blusk* for interesting and illuminating conversations over my six years at Syracuse University.

I give many thanks to *Ray Mountain* and *J.C. Wang* for all the helpful conversations and guidance. From hardware to software and anything in between, these two helped me with anything I threw at them.

A big thank you to *Zhou Xing*, my newest officemate and also  $a_{sl}^s$  colleague. I asked continual questions and he answered all of them with expertise I wish I had.

Thank you to *Penny Davis*, *Linda Pesce* and *Cindy Urtz* for the many times we had lunch on the bench and chats in the hallways. Each time I was reminded that lovely people can be found where you least expect them.

And a big thank you to all of those who have given me support during this trying time: especially my family and friends, who have dealt with my ups and downs. This stuff isn't easy...for anyone!

# Contents

<b>1</b>	<b>Theoretical Overview</b>	<b>1</b>
1.1	Overview of Elementary Particle Physics . . . . .	1
1.2	Symmetries . . . . .	4
1.3	Flavor Physics . . . . .	5
1.3.1	The Importance of Semileptonic Decays . . . . .	8
1.4	Neutral Meson Mixing and the Search for BSM Physics . . . . .	14
<b>2</b>	<b>The LHCb Experiment at CERN</b>	<b>26</b>
2.1	The Large Hadron Collider . . . . .	26
2.2	The LHCb Experiment and its Sub-Detectors . . . . .	28
2.2.1	Introduction . . . . .	28
2.2.2	Tracking: VELO, Magnet, ST and OT . . . . .	29
2.2.3	Identification: RICH1, RICH2, the Calorimeters and Muon System . . . . .	40
2.2.4	2011 Data Taking and Trigger . . . . .	53
<b>3</b>	<b>Measurement of <math>a_{\text{sl}}^s</math></b>	
	<b>with <math>B_s^0 \rightarrow (D_s^\mp \rightarrow \phi\pi^\mp)\mu^\pm\nu_\mu</math></b>	<b>57</b>
3.1	Stripping and Reconstruction . . . . .	58
3.2	Offline Selection . . . . .	62
3.3	Analysis Method . . . . .	64
3.4	Signal Extraction . . . . .	64

3.4.1	One Dimensional Fitting . . . . .	65
3.4.2	Two Dimensional Fitting . . . . .	71
3.5	Muon Detection Efficiency: ID and Trigger . . . . .	78
3.5.1	Criteria, Fitting and Results . . . . .	79
3.6	Final State Particle Tracking Corrections . . . . .	82
3.6.1	Criteria, Fitting and Results . . . . .	84
3.7	Background Studies . . . . .	90
3.7.1	Prompt and Fake Background Studies . . . . .	90
3.7.2	$b$ -Backgrounds . . . . .	94
3.8	Final Results . . . . .	98
<b>4</b>	<b>Conclusions</b>	<b>102</b>
 <b>Appendices</b>		
<b>1</b>	<b><math>q \times p_x</math> vs <math>p_y</math> Binned Signal Fits</b>	<b>103</b>
1.1	Magnet Down . . . . .	103
1.2	Magnet Up . . . . .	124
<b>2</b>	<b><math>q \times \varphi</math> vs <math>p_T</math> Binned Signal Fits</b>	<b>145</b>
2.1	Magnet Down . . . . .	145
2.2	Magnet Up . . . . .	166
<b>3</b>	<b>2D Binned Signal Fits</b>	<b>186</b>
3.1	Magnet Down . . . . .	187
3.2	Magnet Up . . . . .	190
<b>4</b>	<b>Muon Efficiency Studies</b>	<b>193</b>
4.1	L0 Trigger Muon Studies . . . . .	193
4.2	HLT2 Muon (and Other Hadron) Studies . . . . .	194



4.3 Muon Efficiencies . . . . .	194
<b>5 Pion Efficiency Studies</b>	<b>198</b>
<b>Bibliography</b>	<b>202</b>

# List of Figures

1.1	There are six CKM triangles. This is just one example, however the nicest to consider as it lies on the real axis, with one side having unit length. . . . .	8
1.2	Feynman spectator diagram representing the semileptonic decay, of $B_s \rightarrow D\ell\nu_\ell$ .	9
1.3	Feynman spectator diagram representing the semileptonic decay of $B_s^0 \rightarrow K\ell\nu_\ell$ .	13
1.4	A generic box Feynman diagram illustrating the neutral meson mixing. In this instance, the $K^0$ is mixing. . . . .	14
1.5	Leading order box Feynman diagrams involved in $B_s^0$ - $\bar{B}_s^0$ mixing. . . . .	16
1.6	Leading order box Feynman diagrams involved in $B_s^0$ - $\bar{B}_s^0$ mixing with the possibility of something new and exotic. . . . .	16
1.7	Acceptance function for $B_s^0$ signal in Monte Carlo simulation denoted by black dots with fit denoted by the red line. . . . .	24
2.1	A drawing of the complete injection chain of the LHC. . . . .	27
2.2	A three-dimensional plot illustrating the angles at which $b\bar{b}$ travel after proton-proton collisions. . . . .	28
2.3	An illustration of the LHCb Detector at the LHC. . . . .	30
2.4	A drawing of the VELO viewed from overhead. . . . .	31
2.5	A schematic diagram of one sensor and all the components necessary to read out data. . . . .	33

2.6	A plot of the VELO's $x$ and $y$ vertex resolutions. For a single primary vertex (PV) at the interaction point and for 25 tracks, the $x$ and $y$ vertex resolutions are $13.1\mu\text{m}$ and $12.5\mu\text{m}$ respectively. . . . .	33
2.7	Illustration of the magnet located in the LHCb experiment. The $+z$ -direction is coming out of the page at the reader. . . . .	35
2.8	A drawing of the first and third TT station planes, where the latter is set at an angle of $-5^\circ$ . The colored regions mark different readout sectors. . . . .	36
2.9	A schematic of the Inner Tracker. Each light-colored rectangle represents a sensor. The darker, smaller rectangles are readout hybrids. The central circle is the beam pipe. . . . .	37
2.10	A cut-away illustration of the Outer Tracker. The OT are in blue while the IT are the purple inner sections of the image. . . . .	38
2.11	A cross-sectional view of the Outer Tracker straw drift tubes in two layers that are slightly offset. Units are in millimeters. . . . .	39
2.12	A zoomed-in illustration of a particle passing through stacked drift tubes. . .	39
2.13	A schematic drawing of multiple types of tracks through the LHCb experiment and the magnetic field profile in the $y$ -direction (bending plane) along the experiment. . . . .	40
2.14	A schematic of RICH1 and RICH2. . . . .	41
2.15	A schematic of an HPD, a component of the RICH detectors. . . . .	42
2.16	Efficiencies of a pion (kaon) being misidentified as an electron, a muon or a pion. . . . .	44
2.17	A plot of the output of RICH1 with and without the $\vec{B}$ field, illustrating the incredible benefits of the calibration system. . . . .	45

2.18	An image of an HPD array of a RICH1 box. The HPDs are noted by grey circles and a MDCS light bar is in parked position at the right edge of the box. During calibration the bar moves to the left in steps and light spots from the LED are produced onto the HPDs to calibrate the hit positions. . . . .	46
2.19	Spatial residuals demonstrating the resolution with which the light spots of the test pattern in RICH1 are identified. The plots show the distance from the measured light spot center to the nearest test point. Residuals of the $x$ and $y$ direction of the RICH system before (dashed lines) and after (solid histogram) the application of the MDCS. The solid curved line is a Gaussian fit to the calibrated data. . . . .	47
2.20	An illustration of the Hadron Calorimeter structure. The layers of absorber (iron) and scintillating tiles are placed parallel to the beam axis as opposed to perpendicular as in the ECAL. Shown, is only one-quarter of the detector. .	47
2.21	The HCAL is subdivided into two regions, the inner region and the outer region.	48
2.22	A side view schematic of the muon system. . . . .	50
2.23	A diagram of a muon station with the four regions indicated. . . . .	51
2.24	An example of track finding in the muon stations. After $pp$ collision, two muons are produced and enter into the muon sub-detector where their hits are examined by an algorithm. The grey boxes represent the field of interest.	52
2.25	A schematic of the L0 Trigger and how all the components are connected. . .	54
2.26	A flow chart of the data through the trigger. . . . .	55
3.1	Two plots of the overall muon momentum from 6 – 100 GeV. (a) and (b) show the separate fit method results for $D_s^+$ and $D_s^-$ respectively. (c) and (d) show the simultaneous fitting between $D_s^+$ and $D_s^-$ . Results are shown for magnet down polarity only. The solid blue curve is the overall fit, the green and magenta dotted lines are the two Gaussians that share a mean and the black dashed line is the background. . . . .	66

3.2	Two-dimensional scatter plots of muons in the third Muon Station. The top plots are magnet up with $\mu^-$ and the bottom plots are magnet down with $\mu^-$ . The left plots are the first muon momentum bin (6 – 20 GeV) and the right plots are the last and highest muon momentum bin (50 – 100 GeV). . . . .	68
3.3	Two-dimensional scatter plots of muons in the third Muon Station. The top plots are magnet up with $\mu^+$ and the bottom plots are magnet down with $\mu^+$ . The left plots are the first muon momentum bin (6 – 20 GeV) and the right plots are the last and highest muon momentum bin (50 – 100 GeV). . . . .	69
3.4	The $q \times p_x$ vs $p_y$ binning chosen in which the mass of the $D_s$ is fitted. . . . .	70
3.5	From left to right starting from 1 ending with 10, these are the resulting fits for each bin in $q \times p_x$ vs $p_y$ . These fits are for the first muon momentum bin 6 – 20 GeV for magnet down only. The black points are data, the solid blue curve is the overall fit, the green and magenta dotted lines are the two Gaussians that share a mean and the black dashed line is the background. . . . .	71
3.6	Five muon momentum bin fits of the $D_s^+$ mass. Only magnet down polarity results are shown. The black points are data, the solid blue curve is the overall fit, the green and magenta dotted lines are the two Gaussians that share a mean and the black dashed line is the background. . . . .	73
3.7	A drawing to show the bins in the $\varphi$ variable chosen. . . . .	73
3.8	From left to right, starting from 1 and ending with 8, these are the resulting fits for each bin in $q \times \varphi$ vs $p_T$ . Shown is only fits for the lowest muon momentum bin, 6 – 20 GeV, for magnet down. The black points are data, the solid blue curve is the overall fit, the green and magenta dotted lines are the two Gaussians that share a mean and the black dashed line is the background. . . . .	74

3.9	Two-dimensional fit results for magnet down data in the muon momentum bin 6 – 20 GeV. The blue dotted line is $D_s$ signal (DfB), the red solid line is the prompt $D_s$ background, the black dashed line is false $D_s$ background (BKG). The top row represents fits for $D_s^+$ and the bottom for $D_s^-$ . . . . .	76
3.10	Two-dimensional fit results for wrong sign magnet down data in the muon momentum bin 6 – 20 GeV. The blue dotted line is $D_s$ signal (DfB), the red solid line is the prompt $D_s$ background, the black dashed line is false $D_s$ background (BKG). The top row represents fits for $D_s^+$ and the bottom for $D_s^-$ . 77	77
3.11	Muon momentum plots of the two muon specific samples illustrated in red and blue, and signal data in black. . . . .	80
3.12	Muon transverse momentum plots of the two muon specific samples illustrated in red and blue, and signal data in black. . . . .	80
3.13	The invariant mass of the $\mu^+ \mu^-$ pair for the KS sample of $J/\psi$ events. Probe muons are required to pass TIS, while tag muons are required to pass ID cuts. The red points represent the events rejected by the muon ID requirements and the black represent those accepted by this requirement. . . . .	82
3.14	Distributions of mass differences $m(\pi_s^+ K^- \pi^+ \pi^-) - m(K^- \pi^+ \pi^-)$ in partial reconstruction for (a) RS ( $D^{*+} \rightarrow D^0 \pi_s^+$ ) and (b) WS ( $D^{*+} \rightarrow D^0 \pi_s^-$ ) events. 85	85
3.15	Distributions of mass differences $m(\pi_s^- K^+ \pi^- \pi^+) - m(K^+ \pi^- \pi^+)$ in partial reconstruction for (a) RS ( $D^{*-} \rightarrow D^0 \pi_s^-$ ) and (b) WS ( $D^{*-} \rightarrow D^0 \pi_s^+$ ) events. 86	86
3.16	Distributions of mass differences $m(\pi_s^+ K^- \pi^+ \pi^- \pi^+) - m(K^- \pi^+ \pi^- \pi^+)$ in partial reconstruction for (a) RS ( $D^{*+} \rightarrow D^0 \pi_s^+$ ) and (b) WS ( $D^{*+} \rightarrow D^0 \pi_s^-$ ) events. . . . .	86
3.17	Distributions of mass differences $m(\pi_s^- K^+ \pi^- \pi^+ \pi^-) - m(K^+ \pi^- \pi^+ \pi^-)$ in partial reconstruction for (a) RS ( $D^{*-} \rightarrow D^0 \pi_s^-$ ) and (b) WS ( $D^{*-} \rightarrow D^0 \pi_s^+$ ) events. . . . .	87

3.18	The detection efficiency ratio of $\pi^+$ to $\pi^-$ as a function of the undetected pion momentum. The red points are the data sample with magnet polarity up and the blue points are the data sample with magnet polarity down. The errors on the points are statistical only. . . . .	88
3.19	The tracking efficiency ratio of $\pi^+$ to $\pi^-$ as a function of pion transverse momentum in three momentum bins. . . . .	89
3.20	Resulting plots of mass and lnIP from two-dimensional fits for magnet down in the first muon momentum bin 6 – 20 GeV. The top two plots, (a) and (b), refer to events occurring when the hadron accompanying the $D_s$ is a pion. Plots (c) and (d) refer to when the hadron is a kaon. The blue dotted line is DfB, the red solid line is Prompt, the black dashed line is BKG. . . . .	92
3.21	Mis-identification of kaons and pions as a muon. This is an important background to understand as it can create asymmetries in the signal. . . . .	95
3.22	This is a plot with $a_{\text{sl}}^d$ on $x$ -axis and $a_{\text{sl}}^s$ on $y$ -axis. The black dot represents the Standard Model prediction, the magenta backslash-band represents the LHCb measurement presented in this work, the blue forwardslash-bands and the green diamond-band represent the D0 results, and finally the red dotted-band represents a recent average result from $b$ -factories. The bands represent the sum in quadrature of the statistical and systematic errors on each central value result. . . . .	101
1.1	Signal data 1D fit results for magnet down, muon momentum bin 6 – 20 GeV, for $D_s^-$ . The blue dotted line is DfB and the black dashed line is BKG. The bins in each plot are the bins of $q \times p_x$ vs $p_y$ with respect to the muon. The upper left is bin 1, upper right is bin 2, middle left is bin 3, middle right is bin 4, and lowest plot is bin 5. . . . .	104

1.2	Signal data 1D fit results for magnet down, muon momentum bin 6 – 20 GeV for $D_s^-$ . The blue dotted line is DfB and the black dashed line is BKG. The bins in each plot are the bins of $q \times p_x$ vs $p_y$ with respect to the muon. The upper left is bin 6, upper right is bin 7, middle left is bin 8, middle right is bin 9, and lowest plot is bin 10. . . . .	105
1.3	Signal data 1D fit results for magnet down, muon momentum bin 20 – 30 GeV, for $D_s^-$ . The blue dotted line is DfB, the red solid line is PMT, the black dashed line is BKG. The bins in each plot are the bins of $q \times p_x$ vs $p_y$ with respect to the muon. The upper left is bin 1, upper right is bin 2, middle left is bin 3, middle right is bin 4, and lowest plot is bin 5. . . . .	106
1.4	Signal data 1D fit results for magnet down, muon momentum bin 20 – 30 GeV, for $D_s^-$ . The blue dotted line is DfB and the black dashed line is BKG. The bins in each plot are the bins of $q \times p_x$ vs $p_y$ with respect to the muon. The upper left is bin 6, upper right is bin 7, middle left is bin 8, middle right is bin 9, and lowest plot is bin 10. . . . .	107
1.5	Signal data 1D fit results for magnet down, muon momentum bin 30 – 40 GeV, for $D_s^-$ . The blue dotted line is DfB and the black dashed line is BKG. The bins in each plot are the bins of $q \times p_x$ vs $p_y$ with respect to the muon. The upper left is bin 1, upper right is bin 2, middle left is bin 3, middle right is bin 4, and lowest plot is bin 5. . . . .	108
1.6	Signal data 1D fit results for magnet down, muon momentum bin 30 – 40 GeV, for $D_s^-$ . The blue dotted line is DfB and the black dashed line is BKG. The bins in each plot are the bins of $q \times p_x$ vs $p_y$ with respect to the muon. The upper left is bin 6, upper right is bin 7, middle left is bin 8, middle right is bin 9, and lowest plot is bin 10. . . . .	109



1.7	Signal data 1D fit results for magnet down, muon momentum bin 40–50 GeV, for $D_s^-$ . The blue dotted line is DfB and the black dashed line is BKG. The bins in each plot are the bins of $q \times p_x$ vs $p_y$ with respect to the muon. The upper left is bin 1, upper right is bin 2, middle left is bin 3, middle right is bin 4, and lowest plot is bin 5. . . . .	110
1.8	Signal data 1D fit results for magnet down, muon momentum bin 40–50 GeV, for $D_s^-$ . The blue dotted line is DfB and the black dashed line is BKG. The bins in each plot are the bins of $q \times p_x$ vs $p_y$ with respect to the muon. The upper left is bin 6, upper right is bin 7, middle left is bin 8, middle right is bin 9, and lowest plot is bin 10. . . . .	111
1.9	Signal data 1D fit results for magnet down, muon momentum bin 50–100 GeV, for $D_s^-$ . The blue dotted line is DfB and the black dashed line is BKG. The bins in each plot are the bins of $q \times p_x$ vs $p_y$ with respect to the muon. The upper left is bin 1, upper right is bin 2, middle left is bin 3, middle right is bin 4, and lowest plot is bin 5. . . . .	112
1.10	Signal data 1D fit results for magnet down, muon momentum bin 50–100 GeV, for $D_s^-$ . The blue dotted line is DfB and the black dashed line is BKG. The bins in each plot are the bins of $q \times p_x$ vs $p_y$ with respect to the muon. The upper left is bin 6, upper right is bin 7, middle left is bin 8, middle right is bin 9, and lowest plot is bin 10. . . . .	113
1.11	Signal data 1D fit results for magnet down, muon momentum bin 6–20 GeV, for $D_s^+$ . The blue dotted line is DfB and the black dashed line is BKG. The bins in each plot are the bins of $q \times p_x$ vs $p_y$ with respect to the muon. The upper left is bin 1, upper right is bin 2, middle left is bin 3, middle right is bin 4, and lowest plot is bin 5. . . . .	114

1.12	Signal data 1D fit results for magnet down, muon momentum bin 6 – 20 GeV for $D_s^+$ . The blue dotted line is DfB and the black dashed line is BKG. The bins in each plot are the bins of $q \times p_x$ vs $p_y$ with respect to the muon. The upper left is bin 6, upper right is bin 7, middle left is bin 8, middle right is bin 9, and lowest plot is bin 10. . . . .	115
1.13	Signal data 1D fit results for magnet down, muon momentum bin 20 – 30 GeV, for $D_s^+$ . The blue dotted line is DfB, the red solid line is PMT, the black dashed line is BKG. The bins in each plot are the bins of $q \times p_x$ vs $p_y$ with respect to the muon. The upper left is bin 1, upper right is bin 2, middle left is bin 3, middle right is bin 4, and lowest plot is bin 5. . . . .	116
1.14	Signal data 1D fit results for magnet down, muon momentum bin 20 – 30 GeV, for $D_s^+$ . The blue dotted line is DfB and the black dashed line is BKG. The bins in each plot are the bins of $q \times p_x$ vs $p_y$ with respect to the muon. The upper left is bin 6, upper right is bin 7, middle left is bin 8, middle right is bin 9, and lowest plot is bin 10. . . . .	117
1.15	Signal data 1D fit results for magnet down, muon momentum bin 30 – 40 GeV, for $D_s^+$ . The blue dotted line is DfB and the black dashed line is BKG. The bins in each plot are the bins of $q \times p_x$ vs $p_y$ with respect to the muon. The upper left is bin 1, upper right is bin 2, middle left is bin 3, middle right is bin 4, and lowest plot is bin 5. . . . .	118
1.16	Signal data 1D fit results for magnet down, muon momentum bin 30 – 40 GeV, for $D_s^+$ . The blue dotted line is DfB and the black dashed line is BKG. The bins in each plot are the bins of $q \times p_x$ vs $p_y$ with respect to the muon. The upper left is bin 6, upper right is bin 7, middle left is bin 8, middle right is bin 9, and lowest plot is bin 10. . . . .	119

1.17	Signal data 1D fit results for magnet down, muon momentum bin 40–50 GeV, for $D_s^+$ . The blue dotted line is DfB and the black dashed line is BKG. The bins in each plot are the bins of $q \times p_x$ vs $p_y$ with respect to the muon. The upper left is bin 1, upper right is bin 2, middle left is bin 3, middle right is bin 4, and lowest plot is bin 5. . . . .	120
1.18	Signal data 1D fit results for magnet down, muon momentum bin 40–50 GeV, for $D_s^+$ . The blue dotted line is DfB and the black dashed line is BKG. The bins in each plot are the bins of $q \times p_x$ vs $p_y$ with respect to the muon. The upper left is bin 6, upper right is bin 7, middle left is bin 8, middle right is bin 9, and lowest plot is bin 10. . . . .	121
1.19	Signal data 1D fit results for magnet down, muon momentum bin 50–100 GeV, for $D_s^+$ . The blue dotted line is DfB and the black dashed line is BKG. The bins in each plot are the bins of $q \times p_x$ vs $p_y$ with respect to the muon. The upper left is bin 1, upper right is bin 2, middle left is bin 3, middle right is bin 4, and lowest plot is bin 5. . . . .	122
1.20	Signal data 1D fit results for magnet down, muon momentum bin 50–100 GeV, for $D_s^+$ . The blue dotted line is DfB and the black dashed line is BKG. The bins in each plot are the bins of $q \times p_x$ vs $p_y$ with respect to the muon. The upper left is bin 6, upper right is bin 7, middle left is bin 8, middle right is bin 9, and lowest plot is bin 10. . . . .	123
1.21	Signal data 1D fit results for magnet up, muon momentum bin 6 – 20 GeV, for $D_s^-$ . The blue dotted line is DfB and the black dashed line is BKG. The bins in each plot are the bins of $q \times p_x$ vs $p_y$ with respect to the muon. The upper left is bin 1, upper right is bin 2, middle left is bin 3, middle right is bin 4, and lowest plot is bin 5. . . . .	125

1.22	Signal data 1D fit results for magnet up, muon momentum bin 6 – 20 GeV for $D_s^-$ . The blue dotted line is DfB and the black dashed line is BKG. The bins in each plot are the bins of $q \times p_x$ vs $p_y$ with respect to the muon. The upper left is bin 6, upper right is bin 7, middle left is bin 8, middle right is bin 9, and lowest plot is bin 10. . . . .	126
1.23	Signal data 1D fit results for magnet up, muon momentum bin 20 – 30 GeV, for $D_s^-$ . The blue dotted line is DfB, the red solid line is PMT, the black dashed line is BKG. The bins in each plot are the bins of $q \times p_x$ vs $p_y$ with respect to the muon. The upper left is bin 1, upper right is bin 2, middle left is bin 3, middle right is bin 4, and lowest plot is bin 5. . . . .	127
1.24	Signal data 1D fit results for magnet up, muon momentum bin 20 – 30 GeV, for $D_s^-$ . The blue dotted line is DfB and the black dashed line is BKG. The bins in each plot are the bins of $q \times p_x$ vs $p_y$ with respect to the muon. The upper left is bin 6, upper right is bin 7, middle left is bin 8, middle right is bin 9, and lowest plot is bin 10. . . . .	128
1.25	Signal data 1D fit results for magnet up, muon momentum bin 30 – 40 GeV, for $D_s^-$ . The blue dotted line is DfB and the black dashed line is BKG. The bins in each plot are the bins of $q \times p_x$ vs $p_y$ with respect to the muon. The upper left is bin 1, upper right is bin 2, middle left is bin 3, middle right is bin 4, and lowest plot is bin 5. . . . .	129
1.26	Signal data 1D fit results for magnet up, muon momentum bin 30 – 40 GeV, for $D_s^-$ . The blue dotted line is DfB and the black dashed line is BKG. The bins in each plot are the bins of $q \times p_x$ vs $p_y$ with respect to the muon. The upper left is bin 6, upper right is bin 7, middle left is bin 8, middle right is bin 9, and lowest plot is bin 10. . . . .	130

1.27	Signal data 1D fit results for magnet up, muon momentum bin 40 – 50 GeV, for $D_s^-$ . The blue dotted line is DfB and the black dashed line is BKG. The bins in each plot are the bins of $q \times p_x$ vs $p_y$ with respect to the muon. The upper left is bin 1, upper right is bin 2, middle left is bin 3, middle right is bin 4, and lowest plot is bin 5. . . . .	131
1.28	Signal data 1D fit results for magnet up, muon momentum bin 40 – 50 GeV, for $D_s^-$ . The blue dotted line is DfB and the black dashed line is BKG. The bins in each plot are the bins of $q \times p_x$ vs $p_y$ with respect to the muon. The upper left is bin 6, upper right is bin 7, middle left is bin 8, middle right is bin 9, and lowest plot is bin 10. . . . .	132
1.29	Signal data 1D fit results for magnet up, muon momentum bin 50 – 100 GeV, for $D_s^-$ . The blue dotted line is DfB and the black dashed line is BKG. The bins in each plot are the bins of $q \times p_x$ vs $p_y$ with respect to the muon. The upper left is bin 1, upper right is bin 2, middle left is bin 3, middle right is bin 4, and lowest plot is bin 5. . . . .	133
1.30	Signal data 1D fit results for magnet up, muon momentum bin 50 – 100 GeV, for $D_s^-$ . The blue dotted line is DfB and the black dashed line is BKG. The bins in each plot are the bins of $q \times p_x$ vs $p_y$ with respect to the muon. The upper left is bin 6, upper right is bin 7, middle left is bin 8, middle right is bin 9, and lowest plot is bin 10. . . . .	134
1.31	Signal data 1D fit results for magnet up, muon momentum bin 6 – 20 GeV, for $D_s^+$ . The blue dotted line is DfB and the black dashed line is BKG. The bins in each plot are the bins of $q \times p_x$ vs $p_y$ with respect to the muon. The upper left is bin 1, upper right is bin 2, middle left is bin 3, middle right is bin 4, and lowest plot is bin 5. . . . .	135

1.32	Signal data 1D fit results for magnet up, muon momentum bin 6 – 20 GeV for $D_s^+$ . The blue dotted line is DfB and the black dashed line is BKG. The bins in each plot are the bins of $q \times p_x$ vs $p_y$ with respect to the muon. The upper left is bin 6, upper right is bin 7, middle left is bin 8, middle right is bin 9, and lowest plot is bin 10. . . . .	136
1.33	Signal data 1D fit results for magnet up, muon momentum bin 20 – 30 GeV, for $D_s^+$ . The blue dotted line is DfB, the red solid line is PMT, the black dashed line is BKG. The bins in each plot are the bins of $q \times p_x$ vs $p_y$ with respect to the muon. The upper left is bin 1, upper right is bin 2, middle left is bin 3, middle right is bin 4, and lowest plot is bin 5. . . . .	137
1.34	Signal data 1D fit results for magnet up, muon momentum bin 20 – 30 GeV, for $D_s^+$ . The blue dotted line is DfB and the black dashed line is BKG. The bins in each plot are the bins of $q \times p_x$ vs $p_y$ with respect to the muon. The upper left is bin 6, upper right is bin 7, middle left is bin 8, middle right is bin 9, and lowest plot is bin 10. . . . .	138
1.35	Signal data 1D fit results for magnet up, muon momentum bin 30 – 40 GeV, for $D_s^+$ . The blue dotted line is DfB and the black dashed line is BKG. The bins in each plot are the bins of $q \times p_x$ vs $p_y$ with respect to the muon. The upper left is bin 1, upper right is bin 2, middle left is bin 3, middle right is bin 4, and lowest plot is bin 5. . . . .	139
1.36	Signal data 1D fit results for magnet up, muon momentum bin 30 – 40 GeV, for $D_s^+$ . The blue dotted line is DfB and the black dashed line is BKG. The bins in each plot are the bins of $q \times p_x$ vs $p_y$ with respect to the muon. The upper left is bin 6, upper right is bin 7, middle left is bin 8, middle right is bin 9, and lowest plot is bin 10. . . . .	140

1.37	Signal data 1D fit results for magnet up, muon momentum bin 40 – 50 GeV, for $D_s^+$ . The blue dotted line is DfB and the black dashed line is BKG. The bins in each plot are the bins of $q \times p_x$ vs $p_y$ with respect to the muon. The upper left is bin 1, upper right is bin 2, middle left is bin 3, middle right is bin 4, and lowest plot is bin 5. . . . .	141
1.38	Signal data 1D fit results for magnet up, muon momentum bin 40 – 50 GeV, for $D_s^+$ . The blue dotted line is DfB and the black dashed line is BKG. The bins in each plot are the bins of $q \times p_x$ vs $p_y$ with respect to the muon. The upper left is bin 6, upper right is bin 7, middle left is bin 8, middle right is bin 9, and lowest plot is bin 10. . . . .	142
1.39	Signal data 1D fit results for magnet up, muon momentum bin 50 – 100 GeV, for $D_s^+$ . The blue dotted line is DfB and the black dashed line is BKG. The bins in each plot are the bins of $q \times p_x$ vs $p_y$ with respect to the muon. The upper left is bin 1, upper right is bin 2, middle left is bin 3, middle right is bin 4, and lowest plot is bin 5. . . . .	143
1.40	Signal data 1D fit results for magnet up, muon momentum bin 50 – 100 GeV, for $D_s^+$ . The blue dotted line is DfB and the black dashed line is BKG. The bins in each plot are the bins of $q \times p_x$ vs $p_y$ with respect to the muon. The upper left is bin 6, upper right is bin 7, middle left is bin 8, middle right is bin 9, and lowest plot is bin 10. . . . .	144
2.1	Signal data 1D fit results for magnet down, muon momentum bin 6 – 20 GeV, for $D_s^-$ . The blue dotted line is DfB and the black dashed line is BKG. The bins in each plot are the bins of $q \times \varphi$ vs $p_T$ with respect to the muon. The upper left is bin 1, upper right is bin 2, bottom left is bin 3 and bottom right is bin 4. . . . .	146

2.2	Signal data 1D fit results for magnet down, muon momentum bin 6 – 20 GeV for $D_s^-$ . The blue dotted line is DfB and the black dashed line is BKG. The bins in each plot are the bins of $q \times \varphi$ vs $p_T$ with respect to the muon. The upper left is bin 6, upper right is bin 7, bottom left is bin 8 and the bottom right is bin 9. . . . .	147
2.3	Signal data 1D fit results for magnet down, muon momentum bin 20 – 30 GeV, for $D_s^-$ . The blue dotted line is DfB and the black dashed line is BKG. The bins in each plot are the bins of $q \times \varphi$ vs $p_T$ with respect to the muon. The upper left is bin 1, upper right is bin 2, bottom left is bin 3, and the bottom right is bin 4. . . . .	148
2.4	Signal data 1D fit results for magnet down, muon momentum bin 20 – 30 GeV, for $D_s^-$ . The blue dotted line is DfB and the black dashed line is BKG. The bins in each plot are the bins of $q \times \varphi$ vs $p_T$ with respect to the muon. The upper left is bin 5, upper right is bin 6, bottom left is bin 7 and the bottom right is bin 8. . . . .	149
2.5	Signal data 1D fit results for magnet down, muon momentum bin 30 – 40 GeV, for $D_s^-$ . The blue dotted line is DfB and the black dashed line is BKG. The bins in each plot are the bins of $q \times \varphi$ vs $p_T$ with respect to the muon. The upper left is bin 1, upper right is bin 2, bottom left is bin 3 and bottom right is bin 4. . . . .	150
2.6	Signal data 1D fit results for magnet down, muon momentum bin 30 – 40 GeV, for $D_s^-$ . The blue dotted line is DfB and the black dashed line is BKG. The bins in each plot are the bins of $q \times \varphi$ vs $p_T$ with respect to the muon. The upper left is bin 5, upper right is bin 6, bottom left is bin 7 and the bottom right is bin 8. . . . .	151



2.7	Signal data 1D fit results for magnet down, muon momentum bin 40–50 GeV, for $D_s^-$ . The blue dotted line is DfB and the black dashed line is BKG. The bins in each plot are the bins of $q \times \varphi$ vs $p_T$ with respect to the muon. The upper left is bin 1, upper right is bin 2, bottom left is bin 3 and bottom right is bin 4. . . . .	152
2.8	Signal data 1D fit results for magnet down, muon momentum bin 40–50 GeV, for $D_s^-$ . The blue dotted line is DfB and the black dashed line is BKG. The bins in each plot are the bins of $q \times \varphi$ vs $p_T$ with respect to the muon. The upper left is bin 5, upper right is bin 6, bottom left is bin 7 and the bottom right is bin 8. . . . .	153
2.9	Signal data 1D fit results for magnet down, muon momentum bin 50–100 GeV, for $D_s^-$ . The blue dotted line is DfB and the black dashed line is BKG. The bins in each plot are the bins of $q \times \varphi$ vs $p_T$ with respect to the muon. The upper left is bin 1, upper right is bin 2, bottom left is bin 3 and bottom right is bin 4. . . . .	154
2.10	Signal data 1D fit results for magnet down, muon momentum bin 50–100 GeV, for $D_s^-$ . The blue dotted line is DfB and the black dashed line is BKG. The bins in each plot are the bins of $q \times \varphi$ vs $p_T$ with respect to the muon. The upper left is bin 5, upper right is bin 6, bottom left is bin 7 and the bottom right is bin 8. . . . .	155
2.11	Signal data 1D fit results for magnet down, muon momentum bin 6–20 GeV, for $D_s^+$ . The blue dotted line is DfB and the black dashed line is BKG. The bins in each plot are the bins of $q \times \varphi$ vs $p_T$ with respect to the muon. The upper left is bin 1, upper right is bin 2, bottom left is bin 3 and bottom right is bin 4. . . . .	156

2.12	Signal data 1D fit results for magnet down, muon momentum bin 6 – 20 GeV for $D_s^+$ . The blue dotted line is DfB and the black dashed line is BKG. The bins in each plot are the bins of $q \times \varphi$ vs $p_T$ with respect to the muon. The upper left is bin 5, upper right is bin 6, bottom left is bin 7 and the bottom right is bin 8. . . . .	157
2.13	Signal data 1D fit results for magnet down, muon momentum bin 20 – 30 GeV, for $D_s^+$ . The blue dotted line is DfB and the black dashed line is BKG. The bins in each plot are the bins of $q \times \varphi$ vs $p_T$ with respect to the muon. The upper left is bin 1, upper right is bin 2, bottom left is bin 3, and the bottom right is bin 4. . . . .	158
2.14	Signal data 1D fit results for magnet down, muon momentum bin 20 – 30 GeV, for $D_s^+$ . The blue dotted line is DfB and the black dashed line is BKG. The bins in each plot are the bins of $q \times \varphi$ vs $p_T$ with respect to the muon. The upper left is bin 5, upper right is bin 6, bottom left is bin 7 and the bottom right is bin 8. . . . .	159
2.15	Signal data 1D fit results for magnet down, muon momentum bin 30 – 40 GeV, for $D_s^+$ . The blue dotted line is DfB and the black dashed line is BKG. The bins in each plot are the bins of $q \times \varphi$ vs $p_T$ with respect to the muon. The upper left is bin 1, upper right is bin 2, bottom left is bin 3 and bottom right is bin 4. . . . .	160
2.16	Signal data 1D fit results for magnet down, muon momentum bin 30 – 40 GeV, for $D_s^+$ . The blue dotted line is DfB and the black dashed line is BKG. The bins in each plot are the bins of $q \times \varphi$ vs $p_T$ with respect to the muon. The upper left is bin 5, upper right is bin 6, bottom left is bin 7 and the bottom right is bin 8. . . . .	161

2.17	Signal data 1D fit results for magnet down, muon momentum bin 40–50 GeV, for $D_s^+$ . The blue dotted line is DfB and the black dashed line is BKG. The bins in each plot are the bins of $q \times \varphi$ vs $p_T$ with respect to the muon. The upper left is bin 1, upper right is bin 2, bottom left is bin 3 and bottom right is bin 4. . . . .	162
2.18	Signal data 1D fit results for magnet down, muon momentum bin 40–50 GeV, for $D_s^+$ . The blue dotted line is DfB and the black dashed line is BKG. The bins in each plot are the bins of $q \times \varphi$ vs $p_T$ with respect to the muon. The upper left is bin 5, upper right is bin 6, bottom left is bin 7 and the bottom right is bin 8. . . . .	163
2.19	Signal data 1D fit results for magnet down, muon momentum bin 50–100 GeV, for $D_s^+$ . The blue dotted line is DfB and the black dashed line is BKG. The bins in each plot are the bins of $q \times \varphi$ vs $p_T$ with respect to the muon. The upper left is bin 1, upper right is bin 2, bottom left is bin 3 and bottom right is bin 4. . . . .	164
2.20	Signal data 1D fit results for magnet down, muon momentum bin 50–100 GeV, for $D_s^+$ . The blue dotted line is DfB and the black dashed line is BKG. The bins in each plot are the bins of $q \times \varphi$ vs $p_T$ with respect to the muon. The upper left is bin 5, upper right is bin 6, bottom left is bin 7 and the bottom right is bin 8. . . . .	165
2.21	Signal data 1D fit results for magnet up, muon momentum bin 6 – 20 GeV, for $D_s^-$ . The blue dotted line is DfB and the black dashed line is BKG. The bins in each plot are the bins of $q \times \varphi$ vs $p_T$ with respect to the muon. The upper left is bin 1, upper right is bin 2, bottom left is bin 3 and bottom right is bin 4. . . . .	166

2.22	Signal data 1D fit results for magnet up, muon momentum bin 6 – 20 GeV for $D_s^-$ . The blue dotted line is DfB and the black dashed line is BKG. The bins in each plot are the bins of $q \times \varphi$ vs $p_T$ with respect to the muon. The upper left is bin 5, upper right is bin 6, bottom left is bin 7 and the bottom right is bin 8. . . . .	167
2.23	Signal data 1D fit results for magnet up, muon momentum bin 20 – 30 GeV, for $D_s^-$ . The blue dotted line is DfB and the black dashed line is BKG. The bins in each plot are the bins of $q \times \varphi$ vs $p_T$ with respect to the muon. The upper left is bin 1, upper right is bin 2, bottom left is bin 3, and the bottom right is bin 4. . . . .	168
2.24	Signal data 1D fit results for magnet up, muon momentum bin 20 – 30 GeV, for $D_s^-$ . The blue dotted line is DfB and the black dashed line is BKG. The bins in each plot are the bins of $q \times \varphi$ vs $p_T$ with respect to the muon. The upper left is bin 5, upper right is bin 6, bottom left is bin 7 and the bottom right is bin 8. . . . .	169
2.25	Signal data 1D fit results for magnet up, muon momentum bin 30 – 40 GeV, for $D_s^-$ . The blue dotted line is DfB and the black dashed line is BKG. The bins in each plot are the bins of $q \times \varphi$ vs $p_T$ with respect to the muon. The upper left is bin 1, upper right is bin 2, bottom left is bin 3 and bottom right is bin 4. . . . .	170
2.26	Signal data 1D fit results for magnet up, muon momentum bin 30 – 40 GeV, for $D_s^-$ . The blue dotted line is DfB and the black dashed line is BKG. The bins in each plot are the bins of $q \times \varphi$ vs $p_T$ with respect to the muon. The upper left is bin 5, upper right is bin 6, bottom left is bin 7 and the bottom right is bin 8. . . . .	171

2.27	Signal data 1D fit results for magnet up, muon momentum bin 40 – 50 GeV, for $D_s^-$ . The blue dotted line is DfB and the black dashed line is BKG. The bins in each plot are the bins of $q \times \varphi$ vs $p_T$ with respect to the muon. The upper left is bin 1, upper right is bin 2, bottom left is bin 3 and bottom right is bin 4. . . . .	172
2.28	Signal data 1D fit results for magnet up, muon momentum bin 40 – 50 GeV, for $D_s^-$ . The blue dotted line is DfB and the black dashed line is BKG. The bins in each plot are the bins of $q \times \varphi$ vs $p_T$ with respect to the muon. The upper left is bin 5, upper right is bin 6, bottom left is bin 7 and the bottom right is bin 8. . . . .	173
2.29	Signal data 1D fit results for magnet up, muon momentum bin 50 – 100 GeV, for $D_s^-$ . The blue dotted line is DfB and the black dashed line is BKG. The bins in each plot are the bins of $q \times \varphi$ vs $p_T$ with respect to the muon. The upper left is bin 1, upper right is bin 2, bottom left is bin 3 and bottom right is bin 4. . . . .	174
2.30	Signal data 1D fit results for magnet up, muon momentum bin 50 – 100 GeV, for $D_s^-$ . The blue dotted line is DfB and the black dashed line is BKG. The bins in each plot are the bins of $q \times \varphi$ vs $p_T$ with respect to the muon. The upper left is bin 5, upper right is bin 6, bottom left is bin 7 and the bottom right is bin 8. . . . .	175
2.31	Signal data 1D fit results for magnet up, muon momentum bin 6 – 20 GeV, for $D_s^+$ . The blue dotted line is DfB and the black dashed line is BKG. The bins in each plot are the bins of $q \times \varphi$ vs $p_T$ with respect to the muon. The upper left is bin 1, upper right is bin 2, bottom left is bin 3 and bottom right is bin 4. . . . .	176

2.32	Signal data 1D fit results for magnet up, muon momentum bin 6 – 20 GeV for $D_s^+$ . The blue dotted line is DfB and the black dashed line is BKG. The bins in each plot are the bins of $q \times \varphi$ vs $p_T$ with respect to the muon. The upper left is bin 5, upper right is bin 6, bottom left is bin 7 and the bottom right is bin 8. . . . .	177
2.33	Signal data 1D fit results for magnet up, muon momentum bin 20 – 30 GeV, for $D_s^+$ . The blue dotted line is DfB and the black dashed line is BKG. The bins in each plot are the bins of $q \times \varphi$ vs $p_T$ with respect to the muon. The upper left is bin 1, upper right is bin 2, bottom left is bin 3, and the bottom right is bin 4. . . . .	178
2.34	Signal data 1D fit results for magnet up, muon momentum bin 20 – 30 GeV, for $D_s^+$ . The blue dotted line is DfB and the black dashed line is BKG. The bins in each plot are the bins of $q \times \varphi$ vs $p_T$ with respect to the muon. The upper left is bin 5, upper right is bin 6, bottom left is bin 7 and the bottom right is bin 8. . . . .	179
2.35	Signal data 1D fit results for magnet up, muon momentum bin 30 – 40 GeV, for $D_s^+$ . The blue dotted line is DfB and the black dashed line is BKG. The bins in each plot are the bins of $q \times \varphi$ vs $p_T$ with respect to the muon. The upper left is bin 1, upper right is bin 2, bottom left is bin 3 and bottom right is bin 4. . . . .	180
2.36	Signal data 1D fit results for magnet up, muon momentum bin 30 – 40 GeV, for $D_s^+$ . The blue dotted line is DfB and the black dashed line is BKG. The bins in each plot are the bins of $q \times \varphi$ vs $p_T$ with respect to the muon. The upper left is bin 5, upper right is bin 6, bottom left is bin 7 and the bottom right is bin 8. . . . .	181

2.37	Signal data 1D fit results for magnet up, muon momentum bin 40 – 50 GeV, for $D_s^+$ . The blue dotted line is DfB and the black dashed line is BKG. The bins in each plot are the bins of $q \times \varphi$ vs $p_T$ with respect to the muon. The upper left is bin 1, upper right is bin 2, bottom left is bin 3 and bottom right is bin 4. . . . .	182
2.38	Signal data 1D fit results for magnet up, muon momentum bin 40 – 50 GeV, for $D_s^+$ . The blue dotted line is DfB and the black dashed line is BKG. The bins in each plot are the bins of $q \times \varphi$ vs $p_T$ with respect to the muon. The upper left is bin 5, upper right is bin 6, bottom left is bin 7 and the bottom right is bin 8. . . . .	183
2.39	Signal data 1D fit results for magnet up, muon momentum bin 50 – 100 GeV, for $D_s^+$ . The blue dotted line is DfB and the black dashed line is BKG. The bins in each plot are the bins of $q \times \varphi$ vs $p_T$ with respect to the muon. The upper left is bin 1, upper right is bin 2, bottom left is bin 3 and bottom right is bin 4. . . . .	184
2.40	Signal data 1D fit results for magnet up, muon momentum bin 50 – 100 GeV, for $D_s^+$ . The blue dotted line is DfB and the black dashed line is BKG. The bins in each plot are the bins of $q \times \varphi$ vs $p_T$ with respect to the muon. The upper left is bin 5, upper right is bin 6, bottom left is bin 7 and the bottom right is bin 8. . . . .	185
3.1	Two dimensional fits of magnet down data for muon momentum bin 6 – 20 GeV. Top plots are for $D_s^+$ and bottom plots are for $D_s^-$ . . . . .	187
3.2	Two dimensional fits of magnet down data for muon momentum bin 20 – 30 GeV. Top plots are for $D_s^+$ and bottom plots are for $D_s^-$ . . . . .	188
3.3	Two dimensional fits of magnet down data for muon momentum bin 30 – 40 GeV. Top plots are for $D_s^+$ and bottom plots are for $D_s^-$ . . . . .	188

3.4	Two dimensional fits of magnet down data for muon momentum bin 40 – 50 GeV. Top plots are for $D_s^+$ and bottom plots are for $D_s^-$ . . . . .	189
3.5	Two dimensional fits of magnet down data for muon momentum bin 50 – 100 GeV. Top plots are for $D_s^+$ and bottom plots are for $D_s^-$ . . . . .	189
3.6	Two dimensional fits of magnet up data for muon momentum bin 6 – 20 GeV. Top plots are for $D_s^+$ and bottom plots are for $D_s^-$ . . . . .	190
3.7	Two dimensional fits of magnet up data for muon momentum bin 20 – 30 GeV. Top plots are for $D_s^+$ and bottom plots are for $D_s^-$ . . . . .	191
3.8	Two dimensional fits. Two dimensional fits of magnet up data for muon momentum bin 30 – 40 GeV. Top plots are for $D_s^+$ and bottom plots are for $D_s^-$ . . . . .	191
3.9	Two dimensional fits of magnet up data for muon momentum bin 40 – 50 GeV. Top plots are for $D_s^+$ and bottom plots are for $D_s^-$ . . . . .	192
3.10	Two dimensional fits of magnet up data for muon momentum bin 50 – 100 GeV. Top plots are for $D_s^+$ and bottom plots are for $D_s^-$ . . . . .	192
4.1	The left plot illustrates the efficiency for the muon portion of the HLT2 topological lines, for magnet down. The right plot illustrates the efficiency ratio of the $\mu^+$ to $\mu^-$ for the same HLT2 lines for both magnet up (red) and down (blue). . . . .	195
5.1	Four plots show the distribution of $p$ versus $p_x$ of the additional pion in the fully reconstructed sample prior to the application of the two sets of fiducial cuts. For data taken with magnet polarity up: (a) when $ p_y/p_z  > 0.02$ , (b) when $ p_y/p_z  < 0.02$ and for data taken with magnet polarity down: (c) when $ p_y/p_z  > 0.02$ , (d) when $ p_y/p_z  < 0.02$ . The red and blue points correspond to $\pi^+$ and $\pi^-$ , respectively. . . . .	201



# List of Tables

1.1	The Standard Model list of quarks [1]. . . . .	2
1.2	The Standard Model list of leptons [1]. . . . .	3
1.3	The Standard Model list of bosons and corresponding characteristics of each [1] [2]. . . . .	3
1.4	Results from BaBar and Belle for exclusive and inclusive semileptonic branching fractions. . . . .	12
2.1	Number of muon stations required to pass the “IsMuon” boolean cut. This cut is dependent on the muon momentum. . . . .	53
3.1	List of 2011 data samples used in this analysis. . . . .	59
3.2	Stripping cuts on the $B_s^0$ signal. . . . .	60
3.3	Offline selections on the $B_s^0$ signal. . . . .	62
3.4	List of triggers used in this analysis. . . . .	64
3.5	A listing of the parameters for the one dimensional fits in overall muon momentum region for both magnet down and magnet up. . . . .	67
3.6	Signal yields for magnet down in the entire muon momentum region considered only (6 – 100 GeV) for one-dimensional fits (after $L0p_T > 1.640$ GeV). . . . .	67
3.7	Signal yields for magnet down in the lowest momentum (6 – 20 GeV) bin for the individual kinematic bins of $q \times p_x$ vs $p_y$ only. . . . .	72
3.8	List of kinematic binning for the fine $q \times \varphi$ vs $p_T$ bins. . . . .	72

3.9	Signal yields for magnet down in the lowest momentum (6 – 20 GeV) bin for the individual kinematic bins of $q \times \varphi$ vs $p_T$ . . . . .	75
3.10	Signal yields for overall fits for muon momentum range 6 – 100 GeV for 2D fits.	76
3.11	Percentages of prompt contamination in signal for magnet down. . . . .	77
3.12	Percentages of prompt contamination in signal for magnet up. . . . .	78
3.13	Raw asymmetries calculated from raw yields resulting from fits explained above for all fit methods. . . . .	78
3.14	Quality and background suppression cuts applied to the two $\mu$ candidate tracks to select a minimum bias $J/\psi$ , for the KS (a.k.a. MB) sample. . . . .	79
3.15	Signal yields for the KS sample, where muons are required to have a momentum between 6 – 100 GeV and transverse momentum of 1.5 – 10 GeV. . . . .	81
3.16	Overall muon efficiency table using KS sample after the operation $q \times p_x$ vs $p_y$ for muon momentum bin 6 – 20 GeV. . . . .	83
3.17	List of the asymmetries in the signal with muon identification and trigger, in the two fine kinematic binning methods used. Errors are only statistical. . .	83
3.18	A table of bins and the corresponding inferred and detected momentum ranges for the pion efficiencies. . . . .	87
3.19	A table summarizing the tracking efficiency percentages in the six momentum bins for each magnet polarity and track sign. Only diagonal elements of the covariance matrix are shown as the errors. . . . .	90
3.20	Fake yields presented for magnet down in all momentum bins for $D_s^+$ and $D_s^-$ , for kaons faking muons. . . . .	93
3.21	Fake yields presented for magnet up in all momentum bins for $D_s^+$ and $D_s^-$ , for kaons faking muons. . . . .	93
3.22	Fake yields presented for magnet down in all momentum bins for $D_s^+$ and $D_s^-$ , for pions faking muons. . . . .	94

3.23	Fake yields presented for magnet up in all momentum bins for $D_s^+$ and $D_s^-$ , for pions faking muons. . . . .	94
3.24	Results of the 2D fake fits. The yields are multiplied by the fake rates, then they are added together to get a final number for a total fake number of hadrons accompanying the $D_s$ . The results are show for all muon momen- tum bins, for magnet down only, for $D_s^+$ and $D_s^-$ respectively. Fake Rates is represented with FR. . . . .	95
3.25	Results of the 2D fake fits. The yields are multiplied by the fake rates, then they are added together to get a final number for a total fake number of hadrons accompanying the $D_s$ . The results are show for all muon momen- tum bins, for magnet up only, for $D_s^+$ and $D_s^-$ respectively. Fake Rates is represented with FR. . . . .	95
3.26	List of Monte Carlo samples used in the analysis. . . . .	96
3.27	MC reconstruction efficiencies for multiple types of backgrounds as well as the signal channel (last row). . . . .	97
3.28	MC reconstruction branching fractions, signal to background ratios and pro- duction asymmetries for multiple types of backgrounds. . . . .	98
3.29	Included in this table are the branching fractions of the signal channel for this analysis as well as the charm decays used. . . . .	98
3.30	A listing of systematic uncertainties on quantities that enter into $A_{meas}$ . . . . .	99
4.1	Overall muon efficiency table using KS sample after the operation $q \times p_x$ vs $p_y$ for muon momentum bin 6 – 20 GeV. . . . .	195
4.2	Overall muon efficiency table using KS sample after the operation $q \times p_x$ vs $p_y$ for muon momentum bin 20 – 30 GeV. . . . .	196
4.3	Overall muon efficiency table using KS sample after the operation $q \times p_x$ vs $p_y$ for muon momentum bin 30 – 40 GeV. . . . .	196

4.4	Overall muon efficiency table using KS sample after the operation $q \times p_x$ vs $p_y$ for muon momentum bin 40 – 50 GeV. . . . .	197
4.5	Overall muon efficiency table using KS sample after the operation $q \times p_x$ vs $p_y$ for muon momentum bin 50 – 100 GeV. . . . .	197
5.1	Stripping cuts on $D^{*+} \rightarrow D^0(\rightarrow K^- \pi^+ \pi^- \pi^+) \pi_s$ . . . . .	199
5.2	Offline selections on $D^{*+} \rightarrow D^0(\rightarrow K^- \pi^+ \pi^- \pi^+) \pi_s$ , for the additional $\pi$ . . . . .	200

# Chapter 1

## Theoretical Overview

### 1.1 Overview of Elementary Particle Physics

For over 100 years, physicists have been studying particles more deeply than ever with hopes to continue the quest in understanding the basics of nature that has plagued humankind for centuries. Most notably is the development of a theory, the Standard Model (SM) of particles and interactions. It was formulated in the 1970s, and is still consistent with data. In the Standard Model, matter is made up of only six *quarks* and six *leptons* with three forces and corresponding *bosons* governing their interactions<sup>1</sup>. These elementary particles, as they are known, are the fundamental building blocks of nature.

The quarks, listed in table 1.1, each have fractional electric charge of value and sign depending on their flavor quantum number, where flavor is the type of quark, whether it be strange, top or bottom. They are fermions with spin  $1/2$ . The leptons listed in table 1.2 are also fermions of spin  $1/2$ , however only three of six have electric charge. The neutrinos are interesting particles of no mass or charge<sup>2</sup>.

Not included in the tables but most certainly included in nature are the anti-particles of all quarks and leptons. In the late 1920s, Paul Dirac developed his famous equation to

---

<sup>1</sup>Gravity is not incorporated properly into the SM, so it is not included here.

<sup>2</sup>Technically, neutrinos do in fact have mass, albeit extremely small, but for now it will not be discussed.

explain and describe the dynamics of spin 1/2 particles. Entities of positive and negative energies were results of the Dirac equation. However, there was no experimental evidence for this negative energy, and was the first step to uncovering anti-matter as states. These anti-particles have exactly the same values of each quantity listed (and others not listed) but opposite in sign, except for mass.

Table 1.1: The Standard Model list of quarks [1].

Quark	Mass [MeV]	Electric Charge	Spin
Up, $u$	$2.3^{+0.7}_{-0.5}$	$+\frac{2}{3}$	$\frac{1}{2}$
Down, $d$	$4.8^{+0.7}_{-0.3}$	$-\frac{1}{3}$	$\frac{1}{2}$
Strange, $s$	$95 \pm 5$	$-\frac{1}{3}$	$\frac{1}{2}$
Charm, $c$	$1275 \pm 25$	$+\frac{2}{3}$	$\frac{1}{2}$
Bottom, $b$	$4180 \pm 30$	$-\frac{1}{3}$	$\frac{1}{2}$
Top, $t$	$173500^{+600}_{-800}$	$+\frac{2}{3}$	$\frac{1}{2}$

These fundamental fermions interact via the three interactions listed in table 1.3, the *strong*, *electromagnetic* and *weak* forces. These forces are modeled as particle exchanges, e.g. photons are emitted and absorbed by electrons. Each force is responsible for certain types of occurrences in nature, for example the strong force is responsible for binding quarks into aggregate particles such as the proton and even further, binding protons and neutrons into the nucleus of an atom [2]. In this case, the strong force overrules the familiar electromagnetic repulsion strength of the particles, because if it did not the protons would repel one another and blast out of the nucleus! Physicists have not been able to see quarks individually due to this extremely strong force. These bound pairs or triply bound items manifest as larger states or particle aggregates, called *mesons* and *baryons* respectively, which make up a larger subgroup called *hadrons*. The proton is a baryon, in that there are three quarks bound together to form this particle; two  $u$  quarks and a  $d$  quark. Quantum chromodynamics (QCD) is the theory that describes these strong interactions of the quarks.

Leptons, on the other hand, are found freely wandering the space around us. Anyone

Table 1.2: The Standard Model list of leptons [1].

Lepton	Mass [MeV]	Electric Charge	Spin
Electron, $e$	0.511	-1	$\frac{1}{2}$
Muon, $\mu$	105.65	-1	$\frac{1}{2}$
Tau, $\tau$	$1776.82 \pm 0.16$	-1	$\frac{1}{2}$
$e$ Neutrino, $\nu_e$	$< 2 \times 10^{-6}$ @ 95% CL	0	$\frac{1}{2}$
$\mu$ Neutrino, $\nu_\mu$	$< 0.19$ @ 90% CL	0	$\frac{1}{2}$
$\tau$ Neutrino, $\nu_\tau$	$< 18.2$ @ 95%CL	0	$\frac{1}{2}$

familiar with physics is aware of the electromagnetic force that occurs in nature. The repelling characteristic of like-sign electrons is possible because of the fundamental particles interacting with one another. The boson mediating the electromagnetic force is the photon, a massless particle and electrically charge-less. The theory upheld by many years of empirical data is quantum electrodynamics (QED).

The weak force is different compared to either the strong or the electromagnetic forces for a few interesting reasons. The timescales on these types of interactions, strong and electromagnetic, is on the order of  $10^{-16}s$  and  $10^{-23}s$ , respectively. However, for weak interactions this is on the order of  $10^{-12}s$ . In fact, the available phase space for a decay such as  $\Sigma \rightarrow n + \pi$  is 0.12 GeV, which is about the same for a decay such as  $\Delta \rightarrow n + \pi$ , and the energy available for both to occur is almost exactly the same, however the lifetimes are dramatically different, about 13 orders of magnitude different [3]. A new theory had

Table 1.3: The Standard Model list of bosons and corresponding characteristics of each [1] [2].

Mediator Boson	Force	Mass [MeV]	Electric Charge	Coupling	Lifetime (s)
Gluons, G	Strong	0	0	1	$10^{-23}$
Photons, $\gamma$	Electromagnetic	$< 1 \times 10^{-24}$	$< 1 \times 10^{-35}$	$10^{-2}$	$10^{-20} \rightarrow 10^{-16}$
$W^\pm$	Weak	$80385 \pm 15$	$\pm 1$	$10^{-6}$	$10^{-12}$
$Z^0$	Weak	$91187.6 \pm 2.1$	0	$10^{-6}$	$10^{-12}$

to be developed, however this time, with the interaction bosons given mass, in order to

account for the slowed rate of the process. This in turn also accounts for the short-range of the force. From this reasoning also, the boson interacts with quarks and leptons with equal strength. Another interesting difference is that during weak interactions, the *flavor* of quarks are changed (e.g. a  $u$  changes to a  $d$ ), and electrons and muons are changed into neutrinos. This is something very novel indeed and plays an important role in this work. Also important to note is in both QED and QCD the bosons are massless and charge-less, but in the weak interactions the bosons come in both electrically charged and charge-less form, and each boson carries mass.

In the summer of 2012, the Higgs boson was discovered, a long standing theoretical particle that is the last missing element of the SM. However, this is not the end at all for particle physics. There are still a multitude of mysteries in this field. Firstly, there is an issue brushed over gently earlier about gravity in this sector of physics. This is because the energy scale is completely different from the other three forces,  $\sim 10^{33}$  orders different with respect to the weak force. Another issue is the problem of baryogenesis, or that there is more matter than anti-matter in the current universe. This is very perplexing since it is assumed that at the beginning of the universe there was equal parts of both types. These problems of understanding the most basic parts nature may be solved with further investigation of particles and their interactions.

## 1.2 Symmetries

Symmetries give physicists insights into fundamental forces. Under P, parity, the handedness of space is reversed, or the particle is inverted in space, e.g.  $x \rightarrow -x$ . Under C, charge conjugation, particles turn into their antiparticles and vice versa, by conjugating all internal quantum numbers, such as electric charge,  $q \rightarrow -q$ . Under T, time reversal, time is reversed on an interaction. If C and P are imposed together, CP symmetry is obtained. Prior to the discovery of the weak interaction, it was thought that C and P were conserved. Then



in 1957, the first observation of P violation was observed in nature during the famous  $^{60}\text{Co}$  experiment [4], which was summed up in a theoretical paper by Lee and Yang a year prior [5]. It was then discovered that CP was not conserved with the observation of the decay  $K_L \rightarrow \pi\pi$  by Christenson, Cronin, Fitch and Turlay in 1964 [6]. This was a “problem” because the  $K_S$  was seen to go to two pions, which is a CP even final state and simultaneously  $K_L$  was seen to go to three pions, which is a CP odd state. So when the  $K_L$  was seen in 1964 decaying into two pions, a CP even state, physicists were flabbergasted. How can the  $K_L$  decay into both CP even *and* odd states? Clearly CP is violated.

This new found violation could not be incorporated into the Cabibbo matrix of a two-generation SM. The *Cabibbo-Kobayashi-Maskawa (CKM) matrix* into the SM took into account many items of interest. Specifically, the complex nature of the elements of the CKM matrix introduces phases, for which five of six are accounted. The last phase that comes out of the CKM matrix is a CP violating phase, allowed in the SM.

Since those times much effort has gone into studying the nature of CP violation. CP violation is a crucial feature of any theory that attempts to explain the observed asymmetry between matter and antimatter in the universe starting from initially symmetric conditions.

### 1.3 Flavor Physics

Due to the peculiar nature of the weak interactions, quarks are able to mix with one another. This means that a charged current couples the quark states,  $u$  &  $d'$ , and  $c$  &  $s'$  for example, defined by a single parameter.

Initially when it was thought that there were only two quarks ( $u, d$ ) the theory described their interaction via a universal coupling constant. In other words, that the  $u$  and  $d$  quarks interact with one another (e.g. in the form of pion), it is necessary that this be related by some number. However, when the next two quarks of a second generation were discovered (the  $c$  and  $s$ ), rather than including a new coupling constant, a new “rotation” was intro-

duced. This was done because it was found that the mixing of quarks in different generations was possible and this cannot be related with some constant number. Particularly, the manifestation of the  $u$  and the  $\bar{s}$  quark *is* possible, as the discovery of the K meson proved, which decays via the weak interaction into a  $\mu$  and a  $\nu_\mu$ . Thus, the mixing of the generation of quarks was indeed more complex than a simple number. An example of this is shown when beginning with two fermion pairs,

$$\begin{pmatrix} u \\ d' \end{pmatrix} \quad \begin{pmatrix} c \\ s' \end{pmatrix} \tag{1.1}$$

where the primed quarks are the rotated states defined as

$$d' = d \cos \theta + s \sin \theta, \tag{1.2}$$

$$s' = -d \sin \theta + s \cos \theta. \tag{1.3}$$

To get from the  $(d, s)$  pair to the  $(d', s')$  pair, the unprimed pair is rotated with the following matrix,

$$\begin{pmatrix} \cos \theta_C & \sin \theta_C \\ -\sin \theta_C & \cos \theta_C \end{pmatrix}, \tag{1.4}$$

where the angle  $\theta_C$  is called the Cabibbo angle [7]. Due to the fact that this matrix is unitary it has  $N^2 - (2N - 1)$  free parameters and  $\frac{1}{2}(N - 1)(N - 2)$  of them are phases. Since  $N = 2$ , there is only one free parameter, this angle  $\theta_C$  and zero phases.

This holds when there are only two generations of quarks. If a third generation set of quarks was to be discovered at that time, the theorists had it under control. Adding a third generation to the theory simply meant making a  $3 \times 3$  matrix and utilizing the same  $N$ -dependent number of free parameters and phases. This gives four free parameters, one of which is a phase, and the rest being angles. This  $3 \times 3$  matrix is the CKM matrix, developed by Kobayashi and Maskawa motivated by the possibility that there was a third

generation of quark doublets, and having incorporated Cabibbo's work [8]. The CKM matrix is represented below,

$$V_{CKM} = \begin{pmatrix} V_{ud} & V_{us} & V_{ub} \\ V_{cd} & V_{cs} & V_{cb} \\ V_{td} & V_{ts} & V_{tb} \end{pmatrix} \quad (1.5)$$

or in another parametrization

$$V_{CKM} = \begin{pmatrix} c_{12}c_{13} & s_{12}c_{13} & s_{13}e^{-i\delta_{13}} \\ -s_{12}c_{23} - c_{12}s_{23}s_{13}e^{i\delta_{13}} & -c_{12}c_{23} - s_{12}s_{23}s_{13}e^{i\delta_{13}} & s_{23}c_{13} \\ s_{12}s_{23} - c_{12}c_{23}s_{13}e^{i\delta_{13}} & -c_{12}s_{23} - s_{12}c_{23}s_{13}e^{i\delta_{13}} & c_{23}c_{13} \end{pmatrix} \quad (1.6)$$

where  $c_{ij} = \cos(\theta_{ij})$ ,  $s_{ij} = \sin(\theta_{ij})$  and the angles  $\theta_{ij}$  are real. It can also be written in terms of  $V_{us} \simeq -V_{cd} \simeq \sin\theta \equiv \lambda = 0.22 \pm 0.002$ , shown below,

$$V_{CKM} = \begin{pmatrix} 1 - \frac{\lambda^2}{2} & \lambda & A\lambda^3(\rho - i\eta) \\ -\lambda & 1 - \frac{\lambda^2}{2} & A\lambda^2 \\ A\lambda^3(1 - \rho - i\eta) & -A\lambda^2 & 1 \end{pmatrix} \quad (1.7)$$

where  $(\bar{\rho} + i\bar{\eta}) = -\frac{V_{ud}V_{ub}^*}{V_{cd}V_{cb}^*}$ . This is known as the Wolfenstein approximation [9]. In this approximation, only  $V_{ub}$  and  $V_{td}$  have a complex phase,  $\eta$ , and CP violation is characterized by  $\eta \neq 0$ .

Again due to the unitarity of the  $3 \times 3$  matrix, it must satisfy two conditions, namely

$$V_{1j}^*V_{1k} + V_{2j}^*V_{2k} + V_{3j}^*V_{3k} = \delta_{jk} \quad (1.8)$$

and

$$V_{j1}^*V_{k1} + V_{j2}^*V_{k2} + V_{j3}^*V_{k3} = \delta_{jk}. \quad (1.9)$$

If  $j \neq k$ , then both equations are equal to zero and allows these relations to be represented by triangles drawn in a complex plane, known as the *unitary triangles*, where each term is the length of a side. There are six in total, however an important triangle (and one of the more friendly) is where the baseline lies from  $0 \rightarrow 1$  on the real axis, shown in figure 1.1 [1], coming from the equation  $V_{ud}V_{ub} + V_{cd}V_{cb} + V_{td}V_{tb} = 0$ . The angles  $\alpha$ ,  $\beta$  and  $\gamma$  in the figure

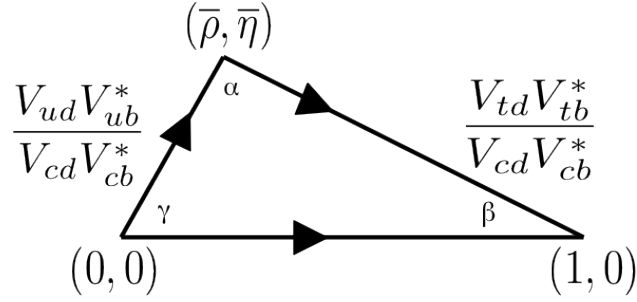


Figure 1.1: There are six CKM triangles. This is just one example, however the nicest to consider as it lies on the real axis, with one side having unit length.

are related to the CP violating quantities,  $V_{ub}$  and  $V_{td}$ , each represented as

$$\alpha = \arg \left[ - \frac{V_{td}V_{tb}^*}{V_{ud}V_{ub}^*} \right], \quad \beta = \arg \left[ - \frac{V_{cd}V_{cb}^*}{V_{td}V_{tb}^*} \right], \quad \text{and} \quad \gamma = \arg \left[ - \frac{V_{ud}V_{ub}^*}{V_{cd}V_{cb}^*} \right]. \quad (1.10)$$

Each element of the CKM matrix is important in uncovering the complexities and unknowns in the Standard Model. At present, some of them are not measured very precisely. Precision measurements, such as the study described in this work, are critical to improve knowledge.

### 1.3.1 The Importance of Semileptonic Decays

Semileptonic decays, those in which at least one of the final state particles is a lepton, are of particular interest because they allow a good handle on certain CKM matrix elements. Specifically,  $V_{ub}$  and  $V_{cb}$  are important as they are part of the main triangle mentioned earlier and can readily be examined via these type of decays. Two examples of  $B$  meson semileptonic decays are shown in the diagrams of figures 1.2 and 1.3. In each diagram there is a single

hadron current involving the spectator quark and the original  $b \rightarrow$  lightquark transition, and a leptonic current where the  $W$  boson interacts with the quarks and the leptons remain.

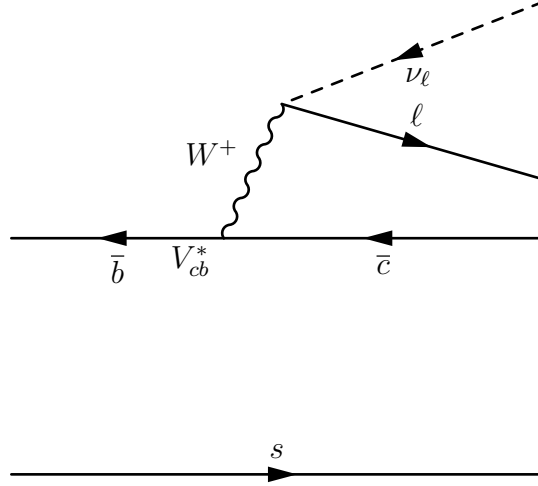


Figure 1.2: Feynman spectator diagram representing the semileptonic decay, of  $B_s \rightarrow D l \nu_\ell$ .

For  $V_{cb}$ , studies of the decay,  $B \rightarrow D^{(*)} l \nu_\ell$ , represented in the first diagram (figure 1.2), can be done, where  $l$  denotes a muon or an electron<sup>3</sup>. However, the measurement is limited by systematics with errors from theory being the dominant source [10]. The two methods of measuring this quantity, the so called *exclusive* and *inclusive* approaches, rely on different theoretical calculations and also make use of different experimental techniques. This allows a very nice test of physicists' understandings of these decays as well as a test for the Standard Model itself.

For the *exclusive* measurements, one studies a specific single hadron final state, such as the  $B \rightarrow D^{(*)} l \nu_\ell$ , as this restricts the dynamics of the process. Any remaining degrees of freedom can be expressed in terms of form factors, which depend on the invariant mass of the lepton-neutrino pair and  $q^2$ , the four-momentum transfer squared between  $B$  and  $D$ , or  $q^2 = p_B^\mu - p_D^\mu$  with  $p_B^\mu$  and  $p_D^\mu$  the  $B$  and  $D$  four-vectors, respectively. This can be done because of the nature of the theory applied, which is called the heavy quark effective theory (HQET). This theory essentially states that in heavy mesons composed of a heavy

<sup>3</sup>The  $\tau$  is not considered since the branching fraction of  $B \rightarrow D \tau \nu$  is highly suppressed.

quark and a light quark (for instance, the  $\bar{b}$  and  $s$ , which make up the  $B_s^0$  meson), when the limit of  $m_b \gg \Lambda_{QCD}$  is applied, some items are simplified and symmetries are induced [11]<sup>4</sup>. However, additional corrections must be made in order to account for the fact that the masses of heavy quarks are not infinite. Specifically, the heavy quark acts as a static color source with a fixed four-velocity,  $v^\mu$ , and the wave functions describing the interaction become insensitive to the spin and flavor of the heavy quark. This allows for easier calculation and measurement of quantities. For the  $b \rightarrow c$  transition, the only change occurring is the momentum transferred,  $\vec{p}_b \rightarrow \vec{p}_c$  and thus  $v_b \rightarrow v_c$  due to this symmetry from HQET. In 1989 Isgur and Wise formulated this theory [12].

In studying these semileptonic decays, it is more convenient to observe the four-velocity transfer,  $\omega \equiv v_b \cdot v_c$ , because at maximum four-velocity transfer,  $\omega = 1$ , the form factor  $\mathcal{F}$  is equal to 1. This means that physically the  $b$  quark transforms into the  $c$  quark without velocity change, also known as *zero recoil*. With this information and investigating the decay rate,  $|V_{cb}|$  can be studied. The decay rates are given by

$$\frac{d\Gamma(B \rightarrow D^* \ell \nu_\ell)}{d\omega} = \frac{G_F^2 |V_{cb}|^2}{48\pi^3} \mathcal{K}(\omega) \mathcal{F}(\omega)^2 \quad (1.11)$$

for the  $D^* \ell \nu$  final state and

$$\frac{d\Gamma(B \rightarrow D \ell \nu_\ell)}{d\omega} = \frac{G_F^2 |V_{cb}|^2}{48\pi^3} \mathcal{K}_D(\omega) \mathcal{G}(\omega)^2, \quad (1.12)$$

for the  $D \ell \nu$  final state, where  $G_F$  is the Fermi constant,  $\mathcal{K}(\omega)$  and  $\mathcal{K}_D(\omega)$  are known as phase space factors and  $\mathcal{F}(\omega)$  and  $\mathcal{G}(\omega)$  are the form factors for said final states, respectively. Both  $\mathcal{F}(\omega)$  and  $\mathcal{G}(\omega)$  are functions of other form factors; for the former, one vector,  $V(\omega)$ , and two axial,  $A_{1,2}(\omega)$ ; for the latter, just one vector [13]. The shapes of these form factors (and subsequently all form factors in semileptonic decays) are unknown but can be measured.

---

<sup>4</sup> $\Lambda_{QCD}$  is a constant and is the non-perturbative scale of QCD [1].

The form factors are written as

$$\mathcal{F}(\omega)^2 = \frac{|h_{A_1}(\omega)|^2}{(1-r)^2} \left[ (\omega-r)^2(1-R_2(\omega))^2 + 2(1-2\omega r-r^2) \left(1 - \frac{\omega-1}{\omega+1} R_2^2(\omega)\right) \right] \quad (1.13)$$

and

$$\mathcal{G}(\omega) = \mathcal{G}(1)[1 - 8\rho^2 z + (51\rho^2 - 10)z^2 - (252\rho^2 - 84)z^3], \quad (1.14)$$

with supplementary definitions of terms within equations 1.13 and 1.14 being

$$\begin{aligned} \frac{h_{A_1}(\omega)}{h_{A_1}(1)} &= 1 - 8\rho^2 z + (53\rho^2 - 15)z^2 - (231\rho^2 - 91)z^3, \\ R_1(\omega) &= R_1(1) - 0.12(\omega-1) + 0.05(\omega-1)^2 = V(\omega)/h_{A_1}(\omega), \\ R_2(\omega) &= R_2(1) - 0.11(\omega-1) + 0.06(\omega-1)^2 = A_2(\omega)/h_{A_1}(\omega), \end{aligned} \quad (1.15)$$

and

$$\begin{aligned} r &= \frac{m_{D^*}}{m_B}, \\ z &= \frac{\sqrt{\omega+1} - \sqrt{2}}{\sqrt{\omega+1} + \sqrt{2}}. \end{aligned} \quad (1.16)$$

The linear slope of the form-factor is given by the parameter  $\rho^2$ , and must be determined from the data. The term  $|\mathcal{F}(1) \cdot V_{cb}|^2$  can be determined by fitting the measured  $d\Gamma/d\omega$  distribution. In the infinite mass limit,  $\mathcal{F}(\omega=1) = h_{A_1}(\omega=1) = 1$  and for finite mass, the non-perturbative effects are expressed in powers of  $1/m_Q$ . This type of analysis can be done for the  $b \rightarrow c$  transitions with a  $u$  quark,  $d$  quark or a  $s$  quark as the spectator.

Determinations of  $V_{cb}$  using the *inclusive* approach are obtained using combined fits to inclusive B decay distributions and are based on calculations of the semileptonic decay rate via operator product expansion (OPE) [14], which provides the elements needed to relate the measured quantities to  $V_{cb}$ . The separation of perturbative and non-perturbative elements affects the accuracy with which the value of  $|V_{cb}|$  can be measured. In order to understand

semileptonic decays, it is important to measure the individual components of the semileptonic width.

Very good understanding of individual exclusive decays must be had in order to complete the inclusive measurement to a good degree of precision. In fact, when one sums the exclusive state branching fractions and compares this number to the inclusive semileptonic branching fraction, they should be equal. However, this is not the case. Table 1.4 [10] shows results from two experiments, BaBar and Belle, illustrating the strikingly different fractions.

Table 1.4: Results from BaBar and Belle for exclusive and inclusive semileptonic branching fractions.

$\mathcal{B}(\%)$	BaBar		Belle	
	$B^0$	$B^-$	$B^0$	$B^-$
Summed Exclusive	$7.63 \pm 0.25$	$8.68 \pm 0.25$	$7.51 \pm 0.73$	–
Inclusive	$10.15 \pm 0.43$	$10.90 \pm 0.47$	$10.46 \pm 0.38$	$11.17 \pm 0.38$

It is important to understand the composition of the inclusive  $B$  semileptonic decay rate in terms of the exclusive final states because there are many excited  $D$  and  $D_s$  states that the  $B$  mesons can decay into, with some better understood than others. For the  $D$  states, there are many  $D^{(*)}n\pi$  states that are resonant and non-resonant, and also  $D^{*,**}$  modes that are wide and narrow in width. In order to measure the semileptonic decay rate, the branching fractions must be measured well, and to do this, these many states must be understood well. Currently the measured values of  $|V_{cb}|$  [1] are

$$|V_{cb}|_{incl} = (41.9 \pm 0.7) \times 10^{-3}, \quad (1.17)$$

$$|V_{cb}|_{excl} = (39.6 \pm 0.9) \times 10^{-3},$$

which averages to

$$|V_{cb}| = (40.9 \pm 1.1) \times 10^{-3}. \quad (1.18)$$



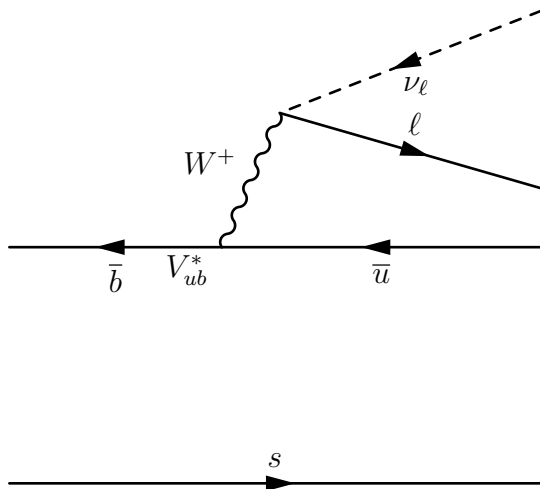


Figure 1.3: Feynman spectator diagram representing the semileptonic decay of  $B_s^0 \rightarrow K l \nu_\ell$ .

For  $V_{ub}$  determination, figure 1.2 shows the diagram of the included decay,  $B_s^0 \rightarrow K l \nu_\ell$  can be done. There are two methods to measure  $V_{ub}$ , once again the *exclusive* and *inclusive* methods. The first relies on the determination of branching fractions and form factors of exclusive charmless semileptonic decays. The *inclusive* method relies on measurements of inclusive charmless semileptonic decays as well as on heavy quark expansion [14]. These methods are completely analogous to the  $V_{cb}$  case. The big challenge experimentally for  $V_{ub}$  is that charmless semileptonic B decays are only 1% of all semileptonic decays, which means a very high level of background that must be suppressed. In fact, the dominant background is the  $b \rightarrow c l$ , which is the signal for the  $V_{cb}$  parameter. The differential rate of the  $B \rightarrow \pi l \nu$  decay is written as

$$\frac{d\Gamma(B \rightarrow \pi l \nu_\ell)}{d\omega} = \frac{G_F^2 |V_{ub}|^2}{192\pi^3 m_B^3} \lambda(q^2)^{3/2} |f_+(q^2)|^2 \quad (1.19)$$

where  $\lambda(q^2) = (q^2 + m_B^2 - m_\pi^2)^2 - 4m_B^2 m_\pi^2$  and  $f_+(q^2)$  is the form factor.

Currently the measured values of  $|V_{ub}|$  [1] are

$$\begin{aligned} |V_{ub}|_{incl} &= (4.41 \pm 0.15_{-0.17}^{+0.15}) \times 10^{-3}, \\ |V_{ub}|_{excl} &= (3.23 \pm 0.31) \times 10^{-3}, \end{aligned} \quad (1.20)$$

which averages to be

$$|V_{ub}| = (4.15 \pm 0.49) \times 10^{-3}. \quad (1.21)$$

This shows an intriguing tension between inclusive and exclusive determinations.

## 1.4 Neutral Meson Mixing and the Search for BSM Physics

Neutral mesons are a very interesting set of particles because they are the only ones that are able to oscillate between themselves and their antiparticles. This is true for  $K^0$ ,  $D^0$ ,  $B^0$  and  $B_s^0$  mesons as all are neutrally charged. Figure 1.4 illustrates the mixing as it is also called. Interestingly, there may be a connection between the CP violation discovered due to the  $K^0$  in 1964 and the fact that the  $K^0$  is one of the few particles to mix with its antiparticle.

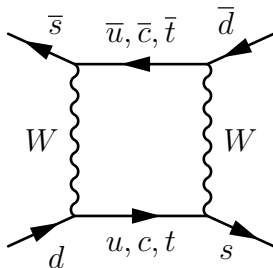


Figure 1.4: A generic box Feynman diagram illustrating the neutral meson mixing. In this instance, the  $K^0$  is mixing.

CP asymmetry in  $B_s^0 - \bar{B}_s^0$  mixing is an important item to study because it provides a good laboratory for testing the theory of QCD as well as possibly being a sector where new physics can reveal itself. Since the mediation is by a loop diagram, the system is sensitive to interference with new physics. The  $B_s^0$  and  $\bar{B}_s^0$  differ only in the sign of the beauty quantum number carried by the  $b$  quark. Since this is not a conserved quantity in weak decays, the eigenstates defined for the masses and lifetimes are not the  $b$  eigenstates created in the production reaction. A pure  $b$  eigenstate, which is a superposition of the two mass

eigenstates propagating with different frequencies, will then develop an oscillating mixture of the  $\bar{b}$  eigenstate [15].

In general, the CP operator acting on a meson state  $M$  is defined by the following equation, using Nierste's [16] notation,

$$\begin{aligned} CP|M(\vec{p}_M)\rangle &= -|\bar{M}(-\vec{p}_M)\rangle \\ CP|\bar{M}(\vec{p}_M)\rangle &= -|M(-\vec{p}_M)\rangle, \end{aligned} \tag{1.22}$$

where  $\bar{M}$  is the anti-meson state,  $\vec{p}_M$  is the momentum of the meson, and the operator  $CP$  is unitary, e.g.  $(CP)^{-1} = (CP)^\dagger$ . If the states  $|M\rangle$  and  $|\bar{M}\rangle$  do not mix, then the difference between  $|M\rangle \rightarrow f$  and  $|\bar{M}\rangle \rightarrow f$  can be measured. If this difference comes out to something other than zero, it is called *direct CP violation*. However, this asymmetry is very difficult to relate to fundamental CP phases. If  $B_s^0$  mesons mix, the superpositions of the two states  $|M\rangle$  and  $|\bar{M}\rangle$  can be studied. Since this is true, this can be studied.

The states  $|M\rangle$  and  $|\bar{M}\rangle$  are linear combinations of their mass eigenstates  $|M_L\rangle$  and  $|M_H\rangle$ , with ‘‘L’’ and ‘‘H’’ standing for low and high respectively, represented as,

$$\begin{aligned} |M_L\rangle &= p|M\rangle + q|\bar{M}\rangle \\ |M_H\rangle &= p|M\rangle - q|\bar{M}\rangle, \end{aligned} \tag{1.23}$$

with  $p$  and  $q$  originating from the box diagram of the possible B mixing, shown in figure 1.5, and  $p^2 + q^2 = 1$ .

The decay amplitudes of the meson states  $M$  and  $\bar{M}$  can be represented by

$$\begin{aligned} A_f &= A(M \rightarrow f) = \langle f|S|M\rangle \\ \bar{A}_f &= A(\bar{M} \rightarrow f) = \langle f|S|\bar{M}\rangle. \end{aligned} \tag{1.24}$$

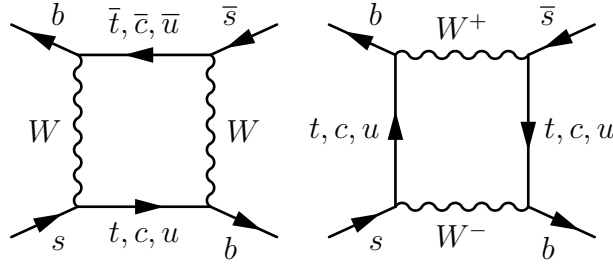


Figure 1.5: Leading order box Feynman diagrams involved in  $B_s^0-\bar{B}_s^0$  mixing.

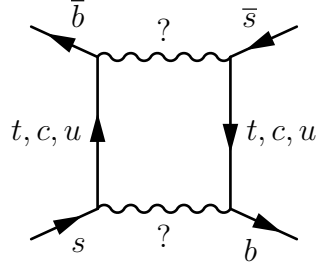


Figure 1.6: Leading order box Feynman diagrams involved in  $B_s^0-\bar{B}_s^0$  mixing with the possibility of something new and exotic.

The definition of a new variable  $\lambda$  presents a clear relation between  $A_f$  and  $\bar{A}_f$ ,

$$\lambda_f = \frac{q \bar{A}_f}{p A_f}, \quad (1.25)$$

where the ratio  $q/p$  is the phase between the two possible states. Here it is more evident that this is where the interesting physics lies. If  $q/p = 1$ , then  $CP$  is conserved. However as soon as  $q/p$  departs from 1,  $CP$  is violated. Consequently,  $\lambda_f$  is the quantity that holds the information of interference occurring when  $B_s^0$  and  $\bar{B}_s^0$  mix.

Further understanding of meson mixing is attained if the states are time-evolved. The two-state  $B_s^0-\bar{B}_s^0$  system oscillation is governed by the Schrödinger equation,

$$i \frac{d}{dt} \begin{pmatrix} |M(t)\rangle \\ |\bar{M}(t)\rangle \end{pmatrix} = \begin{pmatrix} M_s - \frac{i}{2}\Gamma_s \end{pmatrix} \begin{pmatrix} |M(t)\rangle \\ |\bar{M}(t)\rangle \end{pmatrix} \quad (1.26)$$

where  $M_s$  is the mass matrix and  $\Gamma_s$  is the decay matrix, the latter coming from the proba-

bility of finding an un-decayed meson at time  $t$ ,  $|\langle M|M(t)\rangle|^2 = e^{-\Gamma t}$ , and also  $M_s = M_s^\dagger$  and  $\Gamma_s = \Gamma_s^\dagger$ .

The Hamiltonian, the first term on the right-hand side of equation 1.26, is represented by

$$\begin{pmatrix} M_{11} - \frac{1}{2}\Gamma_{11} & M_{12} - \frac{1}{2}\Gamma_{12} \\ M_{12}^* - \frac{1}{2}\Gamma_{12}^* & M_{22} - \frac{1}{2}\Gamma_{22} \end{pmatrix}. \quad (1.27)$$

The diagonal elements of the matrix  $M_s$  are the masses of the  $M$  and  $\bar{M}$  states, which are generated from Lagrangian quark mass terms and the binding energy of the strong interaction [16], and describe the decay of the neutral  $B$  mesons. The off-diagonal elements of  $M_s$  and all elements of  $\Gamma_s$  come from the weak interaction and are responsible for the  $B$  meson mixing. CPT symmetry imposes  $M_{11} = M_{22}$  and  $\Gamma_{11} = \Gamma_{22}$ . This suggests that the physical quantities of interest are the off-diagonal terms  $M_{12}$  and  $\Gamma_{12}$ . These terms can be obtained via theory from the box diagrams.

Through the diagonalization of the Hamiltonian and transforming back to the flavor basis,

$$Q^{-1}HQ = \begin{pmatrix} M_L - i\Gamma_L/2 & 0 \\ 0 & M_H - i\Gamma_H/2 \end{pmatrix} \quad (1.28)$$

with

$$Q = \begin{pmatrix} p & p \\ q & -q \end{pmatrix} \quad (1.29)$$

and

$$Q^{-1} = \frac{1}{2pq} \begin{pmatrix} q & p \\ q & -p \end{pmatrix} \quad (1.30)$$

a new representation of the mass eigenstates is acquired. First, applying the above equations,

the column matrix of the two eigenstates is shown as,

$$\begin{pmatrix} |M(t)\rangle \\ |\bar{M}(t)\rangle \end{pmatrix} = Q \begin{pmatrix} e^{-iM_L t - i\Gamma_L t/2} & 0 \\ 0 & e^{-iM_H t - i\Gamma_H t/2} \end{pmatrix} Q^{-1} \begin{pmatrix} |M\rangle \\ |\bar{M}\rangle \end{pmatrix}. \quad (1.31)$$

Nierste utilizes a shorthand, writing the previous second term as

$$Q \begin{pmatrix} e^{-iM_L t - i\Gamma_L t/2} & 0 \\ 0 & e^{-iM_H t - i\Gamma_H t/2} \end{pmatrix} Q^{-1} = \begin{pmatrix} g_+(t) & \frac{p}{q}g_-(t) \\ \frac{q}{p}g_-(t) & g_+(t) \end{pmatrix} \quad (1.32)$$

where  $g_+(t)$  and  $g_-(t)$  defined as

$$\begin{aligned} g_+(t) &\equiv e^{-imt} e^{-\Gamma t/2} [\cosh \frac{\Delta\Gamma t}{4} \cos \frac{\Delta M t}{2} - i \sinh \frac{\Delta\Gamma t}{4} \sin \frac{\Delta M t}{2}] \\ g_-(t) &\equiv e^{-imt} e^{-\Gamma t/2} [-\sinh \frac{\Delta\Gamma t}{4} \cos \frac{\Delta M t}{2} + i \cosh \frac{\Delta\Gamma t}{4} \sin \frac{\Delta M t}{2}]. \end{aligned} \quad (1.33)$$

In equation 1.33, several new quantities appear, which are

$$\begin{aligned} m &= \frac{M_H + M_L}{2} \\ \Gamma &= \frac{\Gamma_H + \Gamma_L}{2} \\ \Delta M &= M_H - M_L, \\ \Delta\Gamma &= \Gamma_L - \Gamma_H. \end{aligned}$$

where,  $\Delta M > 0$ . Finally, the mass eigenstates can be written in a nice new form,

$$\begin{aligned} |M(t)\rangle &= g_+(t)|M\rangle + \frac{p}{q}g_-(t)|\bar{M}\rangle \\ |\bar{M}(t)\rangle &= \frac{q}{p}g_-(t)|M\rangle + g_+(t)|\bar{M}\rangle. \end{aligned} \quad (1.34)$$

From these many quantities that have been derived and defined, there are three main physical

quantities that are extremely important in  $B_s^0-\bar{B}_s^0$  mixing,

$$|M_{12}|, \quad |\Gamma_{12}|, \quad \text{and} \quad \phi_{12} \quad (1.35)$$

The last term,  $\phi_{12}$ , represented by

$$\phi_{12} = \arg\left(-\frac{M_{12}}{\Gamma_{12}}\right), \quad (1.36)$$

is the mixing phase for the  $B_s^0-\bar{B}_s^0$  mixing. This is not the same as the  $\phi_s$  measured in  $B \rightarrow J/\psi\phi$  analyses.  $\phi_{12}$  is very small,  $(0.22 \pm 0.06)^\circ$  [17], and is of interest because it may be where new physics can show itself. Specifically, if there is new physics, then the new phase becomes  $\phi_{12} = \phi_{12}^{SM} + \phi_{12}^\Delta$ , where the latter is the new physics part of the phase.

From a derivation in Nierste's paper, a relationship between  $q$ ,  $p$ , and the important physical quantities in equation 1.35 is obtained, shown as

$$\left(\frac{q}{p}\right)^2 = \frac{2M_{12}^* - i\Gamma_{12}^*}{2M_{12} - i\Gamma_{12}} = \frac{M_{12}^*(1 + i|\frac{\Gamma_{12}}{2M_{12}}|e^{i\phi_{12}})}{M_{12}(1 + i|\frac{\Gamma_{12}}{2M_{12}}|e^{-i\phi_{12}})}. \quad (1.37)$$

From this equation, if  $\phi_{12} \neq 0$  then  $|q/p| \neq 1$ , which is the definition of CP violation in mixing, confirming an earlier statement after equation 1.25. From experimental data it is known that the quantity  $\Delta M \gg \Delta\Gamma$ , and from theory it is known that  $|\Gamma_{12}| \ll \Delta M$ , since the possible impact of new physics on  $|\Gamma_{12}|$  is small. This then implies that equation 1.37 can be reduced to the form,

$$\left|\frac{q}{p}\right|^2 = 1 - a, \quad (1.38)$$

where  $a$  is small and can be represented as  $a = |\frac{\Gamma_{12}}{M_{12}}| \sin \phi_{12}$ .

In order to get a measurable quantity, a time-dependent decay rate of the meson state must be considered, written as

$$\Gamma(M(t) \rightarrow f) = \frac{1}{N_M} \frac{dN(M(t) \rightarrow f)}{dt}, \quad (1.39)$$

where  $dN(M(t) \rightarrow f)$  denotes the number of decays into the final state  $f$  occurring within time  $t$  and  $t + dt$  and  $N_M$  is the number of mesons produced at time  $t = 0$ . It can be re-written as the equation below, for meson  $M$  and the anti-meson  $\bar{M}$

$$\Gamma(M(t) \rightarrow f) = \mathcal{N}_f |\langle f|S|M(t)\rangle|^2, \quad \Gamma(\bar{M}(t) \rightarrow f) = \mathcal{N}_f |\langle f|S|\bar{M}(t)\rangle|^2, \quad (1.40)$$

with  $\mathcal{N}_f$ , a normalization factor. However, since  $B_s^0$  and  $\bar{B}_s^0$  particles are not produced equally due to initial conditions, the equations must reflect this. Thus  $\mathcal{N}_f$  is replaced with  $N$  initial particles for  $B_s^0$  and  $\bar{N}$  initial particles for  $\bar{B}_s^0$ . Writing the decay rates in terms of  $A_f$  and  $\bar{A}_f$  gives a more illustrative formula. Replacing the time-independent  $|M\rangle$  and  $|\bar{M}\rangle$  from  $A_f$  and  $\bar{A}_f$ , with the time-dependent states  $|M(t)\rangle$  and  $|\bar{M}(t)\rangle$  of equation 1.34, the decay rates become

$$\Gamma(M(t) \rightarrow f) = N |A_f|^2 e^{-\Gamma t} \left\{ \frac{1 + |\lambda_f|^2}{2} \cosh \frac{\Delta\Gamma t}{2} + \frac{1 - |\lambda_f|^2}{2} \cos(\Delta M t) - \text{Re}\lambda_f \sinh \frac{\Delta\Gamma t}{2} - \text{Im}\lambda_f \sin(\Delta M t) \right\}, \quad (1.41)$$

$$\Gamma(\bar{M}(t) \rightarrow f) = \bar{N} |A_f|^2 \frac{e^{-\Gamma t}}{1-a} \left\{ \frac{1 + |\lambda_f|^2}{2} \cosh \frac{\Delta\Gamma t}{2} - \frac{1 - |\lambda_f|^2}{2} \cos(\Delta M t) - \text{Re}\lambda_f \sinh \frac{\Delta\Gamma t}{2} + \text{Im}\lambda_f \sin(\Delta M t) \right\}. \quad (1.42)$$



Similarly these two equations can be written for the conjugate of the final state with  $\bar{A}_{\bar{f}}$

$$\Gamma(M(t) \rightarrow \bar{f}) = N |\bar{A}_{\bar{f}}|^2 e^{-\Gamma t} (1-a) \left\{ \frac{1 + |\lambda_{\bar{f}}|^{-2}}{2} \cosh \frac{\Delta\Gamma t}{2} - \frac{1 - |\lambda_{\bar{f}}|^{-2}}{2} \cos(\Delta M t) - \operatorname{Re} \frac{1}{\lambda_{\bar{f}}} \sinh \frac{\Delta\Gamma t}{2} + \operatorname{Im} \frac{1}{\lambda_{\bar{f}}} \sin(\Delta M t) \right\}, \quad (1.43)$$

$$\Gamma(\bar{M}(t) \rightarrow \bar{f}) = \bar{N} |\bar{A}_{\bar{f}}|^2 e^{-\Gamma t} \left\{ \frac{1 + |\lambda_{\bar{f}}|^{-2}}{2} \cosh \frac{\Delta\Gamma t}{2} + \frac{1 - |\lambda_{\bar{f}}|^{-2}}{2} \cos(\Delta M t) - \operatorname{Re} \frac{1}{\lambda_{\bar{f}}} \sinh \frac{\Delta\Gamma t}{2} - \operatorname{Im} \frac{1}{\lambda_{\bar{f}}} \sin(\Delta M t) \right\}. \quad (1.44)$$

Since the time dependence of a flavor-specific decay satisfies  $\bar{A}_f = A_{\bar{f}} = \lambda_f = 1/\lambda_{\bar{f}} = 0$ , equations 1.41 and 1.42 become

$$\Gamma(M(t) \rightarrow f) = N |A_f|^2 e^{-\Gamma t} \frac{1}{2} \left\{ \cosh \frac{\Delta\Gamma t}{2} + \cos(\Delta M t) \right\}, \quad (1.45)$$

$$\Gamma(\bar{M}(t) \rightarrow f) = \bar{N} |A_f|^2 \frac{e^{-\Gamma t}}{(1-a)} \frac{1}{2} \left\{ \cosh \frac{\Delta\Gamma t}{2} - \cos(\Delta M t) \right\}. \quad (1.46)$$

Again, using the satisfied quantity  $\bar{A}_{\bar{f}} = 1/\lambda_{\bar{f}} = 0$ , the conjugate equations 1.43 and 1.44 become

$$\Gamma(M(t) \rightarrow \bar{f}) = N |\bar{A}_{\bar{f}}|^2 e^{-\Gamma t} (1-a) \frac{1}{2} \left\{ \cosh \frac{\Delta\Gamma t}{2} - \cos(\Delta M t) \right\}, \quad (1.47)$$

$$\Gamma(\bar{M}(t) \rightarrow \bar{f}) = \bar{N} |\bar{A}_{\bar{f}}|^2 e^{-\Gamma t} \frac{1}{2} \left\{ \cosh \frac{\Delta\Gamma t}{2} + \cos(\Delta M t) \right\}. \quad (1.48)$$

Subtracting 1.47 from 1.48 and subtracting 1.45 from 1.46, then dividing the two quantities, a mixing asymmetry is defined as

$$a_{\text{sl}} = \frac{\Gamma(\bar{M} \rightarrow f) - \Gamma(M \rightarrow \bar{f})}{\Gamma(\bar{M} \rightarrow f) + \Gamma(M \rightarrow \bar{f})} = \frac{1 - (1-a)^2}{1 + (1-a)^2} = a + \mathcal{O}(a^2). \quad (1.49)$$

The measurement of such a quantity in equation 1.49 requires flavor-tagging and since un-

tagged decays are used in this work, the following equation defines the untagged decay rate:

$$\Gamma[f, t] = \Gamma(\overline{M}(t) \rightarrow f) + \Gamma(M(t) \rightarrow f). \quad (1.50)$$

This allows the determination of the final time-dependent flavor-specific  $a_{\text{sl}}(t)$  equation,

$$a_{\text{sl}}(t) = \frac{\Gamma[f, t] - \Gamma[\overline{f}, t]}{\Gamma[f, t] + \Gamma[\overline{f}, t]} = \frac{a_{\text{sl}}}{2} - \frac{a_{\text{sl}}}{2} \frac{\cos(\Delta M t)}{\cosh(\Delta \Gamma t/2)}. \quad (1.51)$$

However, flavor-specific means that if  $\overline{M} \rightarrow f$ , then  $M \rightarrow f$  and  $\overline{M} \rightarrow \overline{f}$  are forbidden. So it is easy to calculate the quantities of interest at this point. By inserting equations 1.45 and 1.46 into equation 1.50, the untagged decay rate is

$$\Gamma[f, t] = \frac{|A_f|^2 e^{-\Gamma t}}{2} \left\{ \cosh \frac{\Delta \Gamma t}{2} \left( N + \frac{\overline{N}}{1 - a_{\text{sl}}} \right) + \cos(\Delta M t) \left( N - \frac{\overline{N}}{1 - a_{\text{sl}}} \right) \right\}. \quad (1.52)$$

Repeating this exercise once more for the conjugate final state, defined as

$$\Gamma[\overline{f}, t] = \Gamma(M(t) \rightarrow \overline{f}) + \Gamma(\overline{M}(t) \rightarrow \overline{f}), \quad (1.53)$$

by inserting equations 1.47 and 1.48 into equation 1.53, the untagged conjugate decay rate is

$$\Gamma[\overline{f}, t] = \frac{|A_f|^2 e^{-\Gamma t}}{2} \left\{ \cosh \frac{\Delta \Gamma t}{2} (N(1 - a_{\text{sl}}) + \overline{N}) + \cos(\Delta M t) (-N(1 - a_{\text{sl}}) + \overline{N}) \right\}. \quad (1.54)$$

A production asymmetry of  $B_s^0$  and  $\bar{B}_s^0$  can be defined as

$$a_p \equiv \frac{N - \bar{N}}{N + \bar{N}}, \quad (1.55)$$

in order to take into account the initial conditions of unequal  $B_s^0$  and  $\bar{B}_s^0$  samples. Putting it all together,

$$a_{\text{sl}}(t) = \frac{\Gamma(\bar{M} \rightarrow f) - \Gamma(M \rightarrow \bar{f})}{\Gamma(\bar{M} \rightarrow f) + \Gamma(M \rightarrow \bar{f})} = \frac{a_{\text{sl}}}{2} + \left[ a_p - \frac{a_{\text{sl}}}{2} \right] \frac{e^{-\Gamma t} \cos(\Delta M t) \epsilon(t)}{e^{-\Gamma t} \cosh(\Delta \Gamma t / 2) \epsilon(t)}, \quad (1.56)$$

where  $e^{-\Gamma t}$  has been re-introduced and a new time-dependent acceptance function  $\epsilon(t)$  has been included. Since the measured values of  $\Delta M$  and  $\Delta \Gamma$  are not known with the precision necessary to this analysis,  $a_{\text{sl}}(t)$  is integrated over time, shown as

$$\begin{aligned} a_{\text{sl}}^s &= \frac{\Gamma(B_s^0 \rightarrow D_s^- \mu^+ \nu_\mu) - \Gamma(\bar{B}_s^0 \rightarrow D_s^+ \mu^- \bar{\nu}_\mu)}{\Gamma(B_s^0 \rightarrow D_s^- \mu^+ \nu_\mu) + \Gamma(\bar{B}_s^0 \rightarrow D_s^+ \mu^- \bar{\nu}_\mu)} \\ &= \frac{a_{\text{sl}}}{2} + \left[ a_p - \frac{a_{\text{sl}}}{2} \right] \frac{\int_{t=0}^{\infty} e^{-\Gamma t} \cos(\Delta M t) \epsilon(t) dt}{\int_{t=0}^{\infty} e^{-\Gamma t} \cosh(\frac{\Delta \Gamma t}{2}) \epsilon(t) dt}. \end{aligned} \quad (1.57)$$

The decay time acceptance function for  $B_s^0 \rightarrow D_s X \mu \nu$  is determined by Monte Carlo simulation. It is given by

$$\epsilon(t) = A \cdot \frac{[1 + \beta(t - t_0)][a(t - t_0)]^n}{1 + [a(t - t_0)]^n} \quad (1.58)$$

where  $a = 1.68$ ,  $n = 2.36$ ,  $t_0 = 0.0068$  and  $\beta = 0.0603$  and  $A = 6180$ . The integral in this equation represents the oscillating nature of the B meson and is also very small compared to the quantity being measured.

Including all parameters gives the final equation for  $a_{\text{sl}}$  of equation 1.57. The asymmetry is related to a measurable quantity in experimentation, which is defined as

$$2A_{\text{meas}} = a_{\text{sl}}^s \quad (1.59)$$

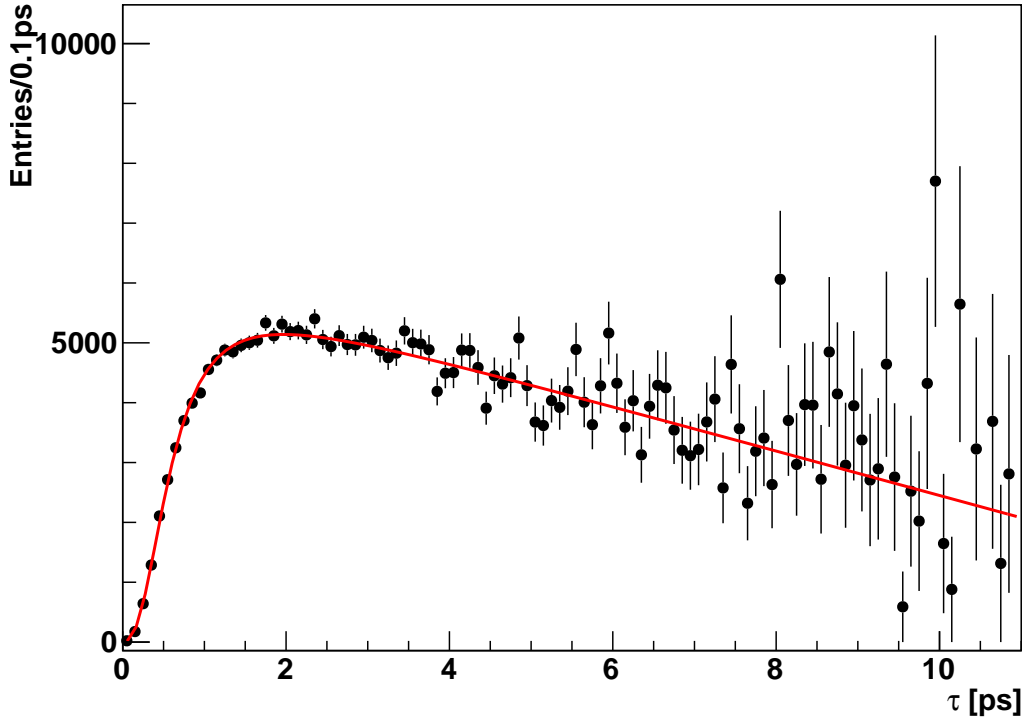


Figure 1.7: Acceptance function for  $B_s^0$  signal in Monte Carlo simulation denoted by black dots with fit denoted by the red line.

and

$$A_{meas} = \frac{\Gamma(D_s^- \mu^+) - \Gamma(D_s^+ \mu^-)}{\Gamma(D_s^- \mu^+) + \Gamma(D_s^+ \mu^-)}. \quad (1.60)$$

In this representation,  $A_{meas}$  is the measured quantity and the factor of 2 arises from the right-hand-side of equation 1.57. This measured quantity is broken down into three sub-components that are individual measurements of asymmetries and are discussed thoroughly in chapter 3. The quantity  $a_{sl}$  can be measured for the  $B_s^0$  meson as well as the  $B^0$  meson, making the term  $a_{sl}^d$  for the latter case. The Standard Model prediction for the asymmetries in  $B_s^0$  and  $B^0$  decays are  $a_{sl}^s = (0.0019 \pm 0.0003)\%$  and  $a_{sl}^d = (-0.041 \pm 0.006)\%$  [18], which both suggest that there is no asymmetry. However if the deviation from zero occurs this can show up in other ways as an enhancement, which can hint new physics. Currently, the D0 collaboration reported an anomalous asymmetry in same sign dileptons,

$A_{\text{sl}}^b = (-0.787 \pm 0.172 \pm 0.093)\%$ , which they relate to the asymmetries represented above by  $A_{\text{sl}}^b = (0.594 \pm 0.022)a_{\text{sl}}^d + (0.406 \pm 0.022)a_{\text{sl}}^s$ , based on the production and lifetime ratios [19]. Their most recent result of  $a_{\text{sl}}^s = (-1.12 \pm 0.74 \pm 0.17)\%$  and  $a_{\text{sl}}^d = (0.68 \pm 0.45 \pm 0.14)\%$  with a sample of  $D^\pm \mu^\mp$  events ([20], [21]) are consistent with their previous result and up to 1.5 sigma with the SM. Further precise asymmetry measurements of  $a_{\text{sl}}^s$  and  $a_{\text{sl}}^d$  can shed much light on the unknowns in the CKM matrix and in flavor physics in general.

# Chapter 2

## The LHCb Experiment at CERN

### 2.1 The Large Hadron Collider

The Large Hadron Collider (LHC) is a large particle accelerator machine in the old LEP (Large Electron-Positron Collider) tunnel located underneath both Switzerland and France. With a circumference of 27 km and energies reaching over 4 TeV, it is the largest and most powerful accelerator in the world. Along the LHC circle there are four major experiments (ALICE<sup>1</sup>, ATLAS<sup>2</sup>, CMS<sup>3</sup> and LHCb<sup>4</sup>), with each one receiving two beams of protons directed in opposite paths. These beams collide and produce very high energies, resulting in the form of particles that are known, and possibly unknown waiting to be found. The protons that eventually end up in each experiment first start mated with electrons in the form of hydrogen. Figure 2.1 shows the path the particles take as they begin in the Linac2, a thirty year old linear accelerator commissioned during the LEP times, in the 1980s. The LHC requires that the Linac2 have a beam of 180mA when the beam reaches the Proton Synchrotron Booster (PSB), upgraded since LEP. When the beam of protons enters the PSB, the pulse length is 100 $\mu$ s and the energy of the protons is 1.4 GeV. This energy is greater

---

<sup>1</sup>A Large Ion Collider Experiment

<sup>2</sup>A Toroidal LHC ApparatuS

<sup>3</sup>Compact Muon Solenoid

<sup>4</sup>LHC Beauty

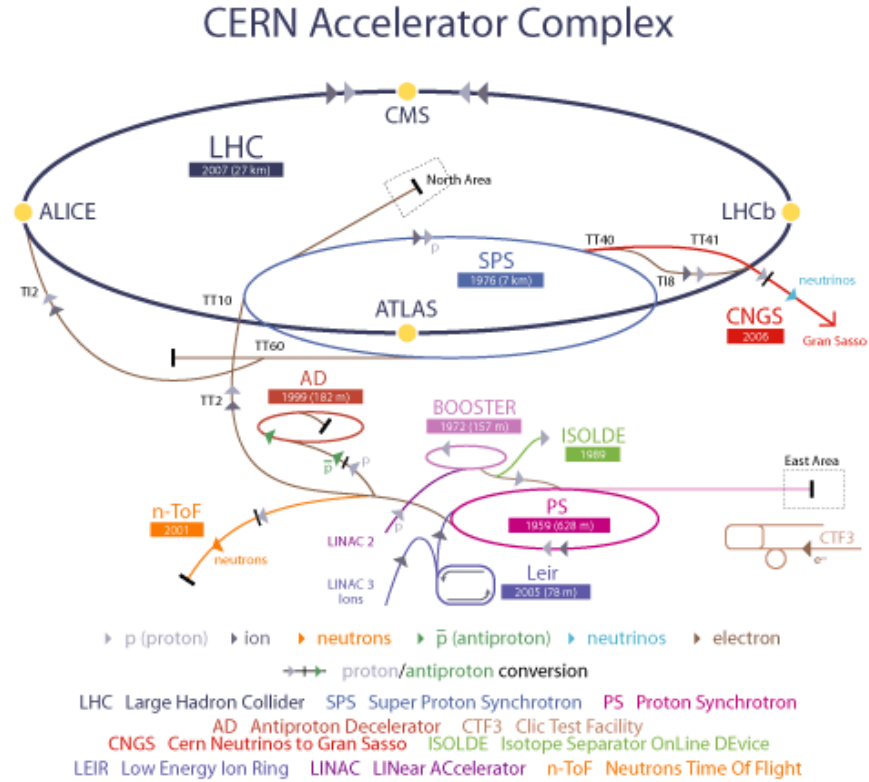


Figure 2.1: A drawing of the complete injection chain of the LHC.

than the energy at which it was originally designed to work, at 800 MeV. The beams are moved via kicker magnets from the four rings of the PSB and recombined into one string of bunches. These bunches are then sent into the Proton Synchrotron (PS).

In the PS, the protons are accelerated to an energy of 25 GeV, with a bunch spacing of 25 ns and 72 bunches per batch. Between two and four of the PS batches are injected to the Super Proton Synchrotron (SPS) every 3.6 seconds. The bunches, which contain  $1.2 \times 10^{11}$  protons each, are accelerated to an energy of 450 GeV. Once the beams reach this energy, they are *almost* ready to be sent to the LHC for collisions. Prior to LHC injection the current of all the systems, mainly magnets, must ramp up, the timing phase of the SPS must synchronize with that of the LHC to inject the bunches at the proper time, the bunch lengths are compressed, and the bunches are cleaned such that there are no errant tails of particles. Once all these tasks have been done, the beams can be injected into the LHC.

This is done at a rate of 40MHz, or 40 million times per second<sup>5</sup>.

The beams are injected via two transfer lines TI-2 towards ALICE and TI-8 towards LHCb, as seen in figure 2.1 They circulate in opposite directions, *beam 1* moving clockwise (having been injected towards ALICE) and *beam 2* moving counter clockwise (having been injected towards LHCb), as viewed from above. The collisions occur at four points on the ring, at each experiment, and data taking commences.

## 2.2 The LHCb Experiment and its Sub-Detectors

### 2.2.1 Introduction

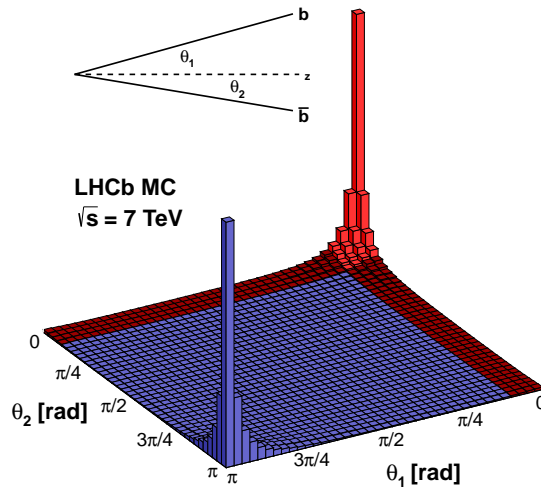


Figure 2.2: A three-dimensional plot illustrating the angles at which  $b\bar{b}$  travel after proton-proton collisions.

The LHCb experiment is a precision particle detector located in the LHC ring at CERN in Geneva, Switzerland. The LHCb experiment is primarily designed to study the effects of new particles, ones that have not yet been seen directly, on the decays of particles containing

<sup>5</sup>The process is obviously simplified here. Should the reader desire to know more, see reference [22].



either beauty quarks or charm quarks. The experiment presents a unique way to study new physics. It is very different from other LHC experiments in that it is not a barrel detector, where the two proton beams collide in the center of the experiment. Instead, LHCb is a forward spectrometer, where the two beams collide at the front of the detector. This allows for the LHCb experiment to cover a very different area of particle decays, in particular the pseudorapidity range is 2 to 5 and the nominal acceptance is 300 mrad in the horizontal bending plane and 250 mrad in the vertical plane, whereas the barrel detectors can detect in pseudorapidity ranges of less than 2.5. Thus, LHCb is able to see the shower of particles flying along the axis of the beams. This is very important because when protons collide creating  $b\bar{b}$  quark pairs, the pairs predominantly fly at a shallow angle, in the same forward cone very close to the axis of the beams, illustrated in the histogram of figure 2.2. Since bottom or beauty physics is main priority for the LHCb experiment, it is relevant and imperative that particles containing b and c quarks enter the detector.

LHCb is comprised of many subdetectors, each with different and important roles. All pieces together create images of cacophony when protons collide. As illustrated in figure 2.3, the collision area is around the (0, 0) coordinate on the  $yz$ -plane, which is the front of the experiment and all subdetectors follow to the right in the  $z$ -direction. All subdetectors are used in this analysis except for one which will not be discussed in detail (the electron calorimeter).

### **2.2.2 Tracking: VELO, Magnet, ST and OT**

The complete tracking system in LHCb consists of the VERtEX LOcator (VELO), a dipole magnet, the Silicon Tracker (ST) and the Outer Tracker (OT) stations, which work together to reconstruct particle movement through space.

A key sub-detector is the silicon strip vertex detector, the VELO. The job of the VELO is to measure the positions of vertices, which are the locations in space where particles decay or break apart into other particles, occurring very close to the collision point. The collision

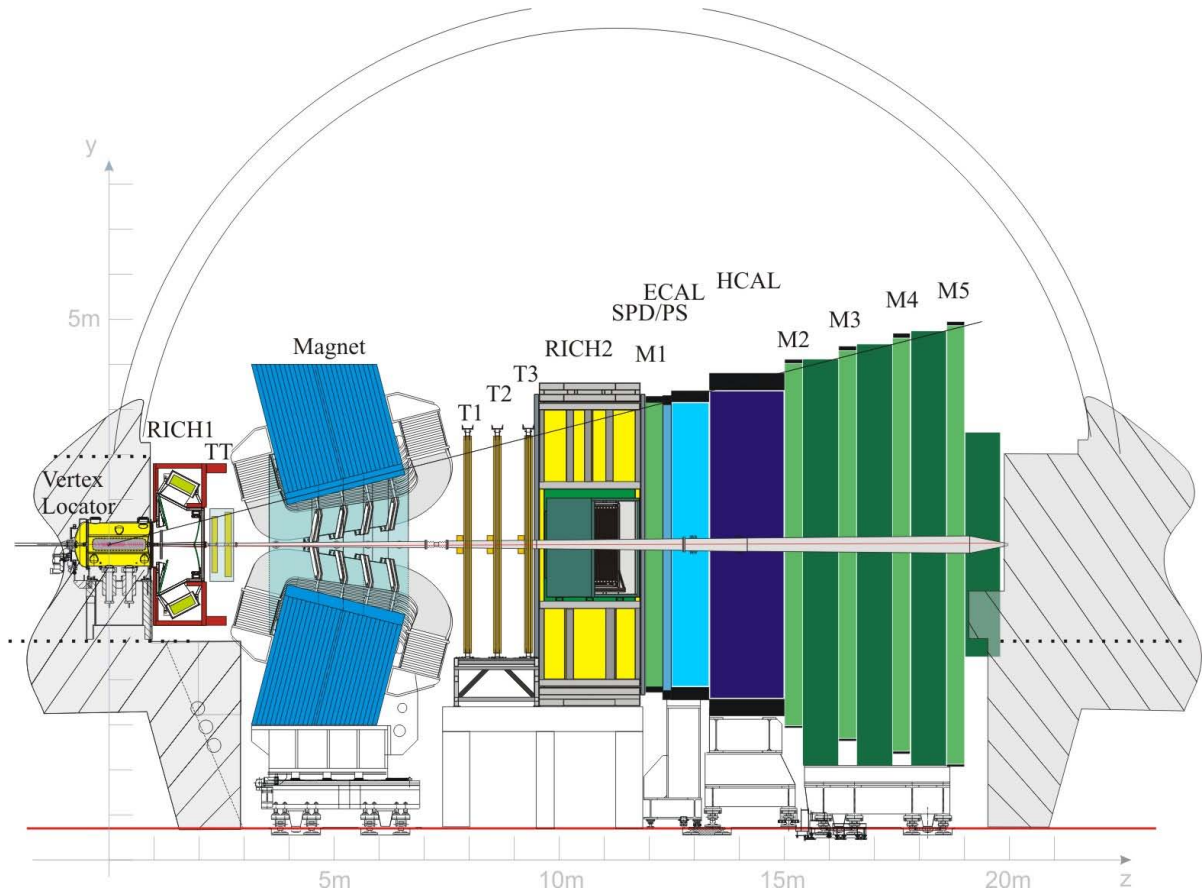


Figure 2.3: An illustration of the LHCb Detector at the LHC.

zone of the two head-on proton beams is near the front of the VELO subdetector and because the particles of interest fly at a shallow angle with respect to the direction from which they came, they travel and decay directly in the VELO. For this reason, a very important aspect of the VELO detector is its resistance to radiation damage.

The VELO is comprised of 84  $n^+n$  silicon strip sensors of  $300\mu\text{m}$  thickness that measure  $R$  and  $\phi$  coordinates. The VELO is split into two halves with 42 sensors on each side, such that it can move to within millimeters of the circulating proton beams. This allows for precise measurements of the position of decay vertices. Initially the VELO sits in a retracted position from the beam pipe when the beams are not stable, preventing possible damage. Once the beams are stable, having a very small diameter and being clean (no errant particles or tails of particles), the VELO is brought to the *closed* position and collisions proceed. *Open*

and *closed* positions are shown in figure 2.4, along with the locations of the sensors along the beam line. In addition to the 84 sensors of the main VELO, there are four “pile-up” sensors that are used in the Level-0 Trigger (L0) (discussed in section 2.2.4).

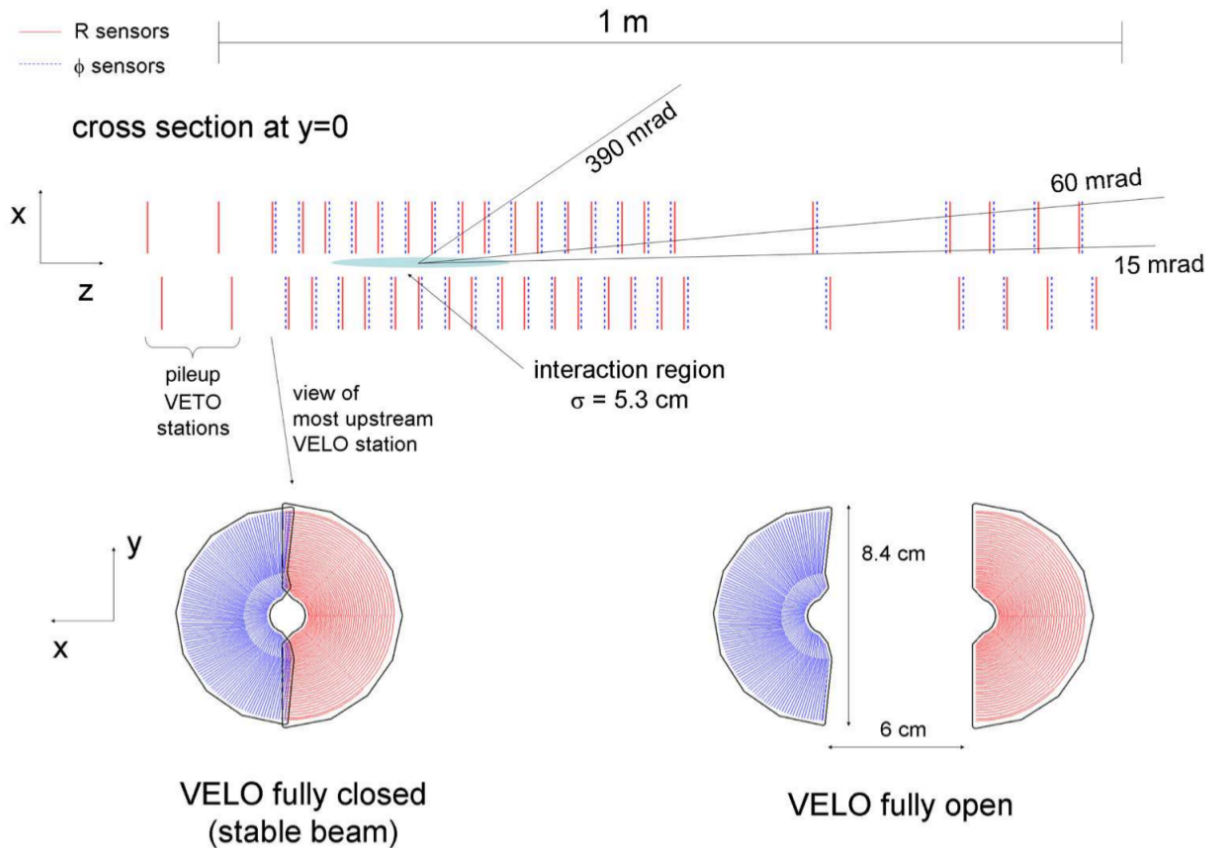


Figure 2.4: A drawing of the VELO viewed from overhead.

Each VELO sensor is semicircular in shape with 2048 silicon strips attached. The spacing of the strips on the bulk of the material of the sensor, called the pitch, is an important quantity in order to attain precision position measurement and potentially momentum measurement as well [23]. The pitch of the strips in the VELO varies linearly from the center area closest to the beam out towards the edge of each semicircular sensor. For the  $R$  sensors, the pitch range is  $40\mu\text{m}$  to  $102\mu\text{m}$  and for the  $\phi$  sensors the pitch range is  $38\mu\text{m}$  to  $96\mu\text{m}$ . These have been chosen such that the measurements of a track will contribute to the impact parameter precision with roughly equal weight as a particle traverses each sensor plane along

this track.

A simplified explanation of a semiconductor sensor (e.g.,  $\text{SiO}_2$  used here for each strip) is that the sensor converts energy that has been deposited by a passing particle to an electrical signal [24]. The energy is absorbed by the semiconductor material, which produces electron-hole pairs. An electric field exists in the material as a result of outside applied voltage across the bulk of the material, and this causes the electrons to move in the direction of the positive voltage/electric field and the holes in the opposite direction. Since the silicon is of type  $n^+n$ , this means that electrons are the mobile charge carriers within the sensor [24]. This is what occurs when particles traverse the VELO, except each strip is the silicon sensor material. Thus this occurs on a large scale.

Attached to these sensors are copious amounts of supporting material, for instance carbon fiber support structures to hold the sensors perpendicular to the beam axis, cooling blocks, as well as electronics such as analogue to digital converters (ADCs), which are programmed by VELO firmware and read via data acquisition software. A diagram of connections is shown in figure 2.5. The VELO sensors are read out into the front-end electronics called beetle chips. These chips are bonded via pitch adapters to the strips. Each sensor has 16 beetle chips, thus each chip accounts for 128 channels from the sensors. The beetle chips are very useful and flexible pieces of electronics that are also used in two of the other subdetectors of the LHCb experiment: the RICH detector and the Silicon Tracker. The beetle chips are able to accept and store data in the form of an analogue signal or a binary signal. The readout for the signal is analog rather than digital, which gives better hit resolution and better monitoring of radiation damage that occurs over time.

The VELO tracks are reconstructed using projected tracks from the other subdetectors in the tracking system. These tracks are extrapolated back towards the point of proton-proton collision to create vertices of many interactions. The tracks are reconstructed well enough such that primary and secondary vertices are discerned from one another. Thus vertex resolution is important as physicists need to be able to dissect the interaction region

very well as it is incredibly busy. As shown in figure 2.6, the resolutions of the vertices are very good,  $13.1\mu\text{m}$  and  $12.5\mu\text{m}$  in the  $x$  and  $y$  directions respectively. Located five

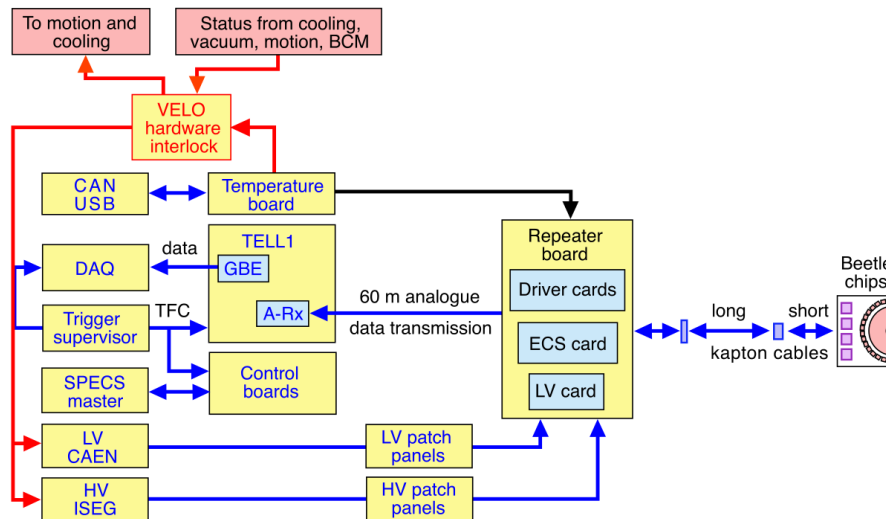


Figure 2.5: A schematic diagram of one sensor and all the components necessary to read out data.

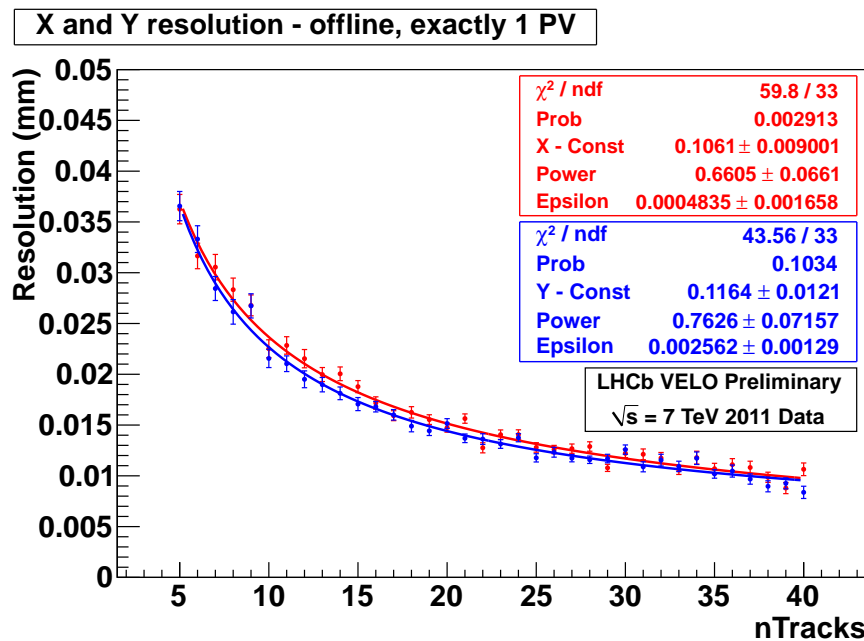


Figure 2.6: A plot of the VELO's  $x$  and  $y$  vertex resolutions. For a single primary vertex (PV) at the interaction point and for 25 tracks, the  $x$  and  $y$  vertex resolutions are  $13.1\mu\text{m}$  and  $12.5\mu\text{m}$  respectively.

meters downstream from the VELO is a large dipole magnet which bends the particles trajectory as they fly. The magnet covers the nominal LHCb acceptance of  $\pm 300$  mrad horizontally and  $\pm 250$  mrad vertically. It is a warm magnet rather than superconducting, as the latter is very expensive and not necessary. The design is based on the need to have a 4Tm integrated field for tracks that are 10m in length, a field as high as possible between tracking stations for better track separation and also to have the field low near the Ring Imaging Cherenkov Detector (RICH) [25]. The magnet is made of two sets of saddle-shaped coils located in a window-frame yoke. The coils are located across from one another above and below the central beam-pipe location, as illustrated in figure 2.7. Within these coils is a cooling channel of 25mm diameter as heating is the main stress for this system since the coils' current reach  $\sim 5.8$ kA [26]. The conductor has a specific ohmic resistance below  $28\Omega\text{m}$  at  $20^\circ\text{C}$ . The structure on which the coils are located is part of older experiment, DELPHI. In particular, the magnet sits on a platform made of the old rails and magnet carriages from this experiment, which is done for economic purposes.

The magnet bends a charged particle's direction of travel through the magnet. This allows for separation of the differently charged particles and ease in tracking that the tracking stations must perform.

After passing through the magnet, the particles pass through the Tracking stations (T-stations) for track reconstruction of the particle flight. Each station measures the positions of passing particles to then create projected tracks. This allows the analysts to determine many things: where the final state particles originate, their energies and momenta. The T-stations refer to the ST and the OT stations together.

The ST is made up of two detectors: the Tracking Turicensis<sup>6</sup> (TT) and the Inner Tracker (IT). The TT is located immediately between the RICH1 and the magnet at the front of the detector, just after the collision region. The TT is 150 cm wide and 130 cm high that covers the nominal acceptance of the LHCb detector. This allows for almost all particles

---

<sup>6</sup>Meaning "from Zurich" in Latin. The TT is formally known as the Trigger Tracker.

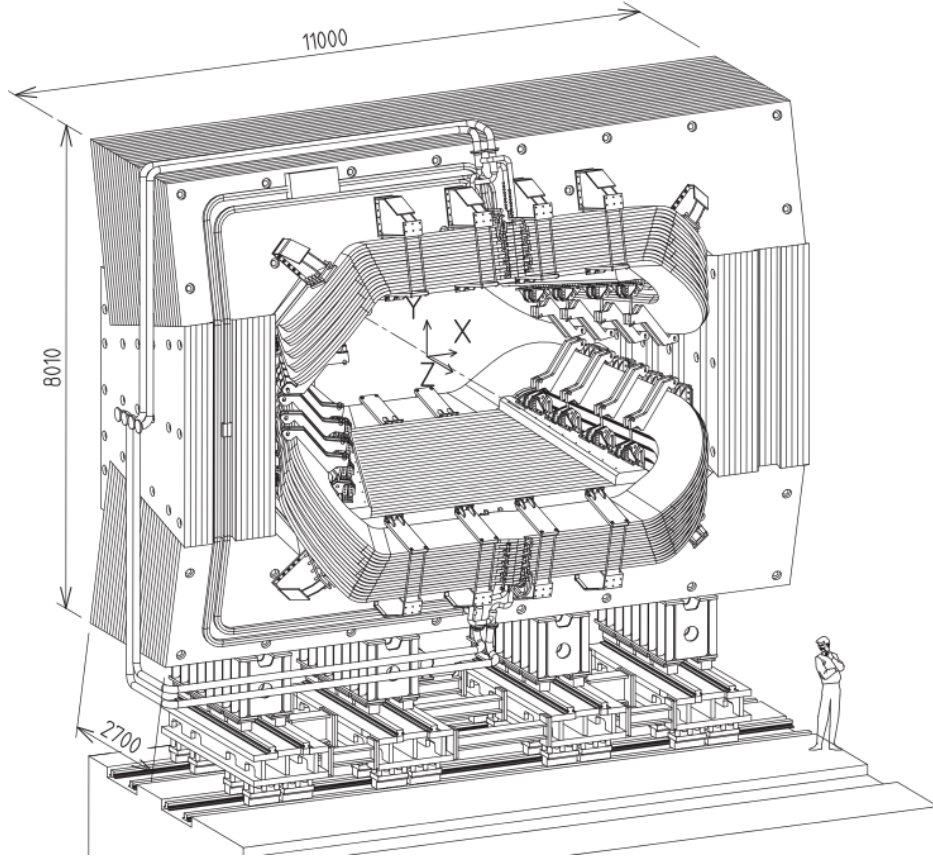


Figure 2.7: Illustration of the magnet located in the LHCb experiment. The  $+z$ -direction is coming out of the page at the reader.

that enter the TT to be detected, with over 99% efficiency [27]. It is made up of four layers each consisting of a row of seven silicon sensors organized into two or three readout sectors with a readout hybrid containing electronics mounted at the end. Figure 2.8 illustrates two layers of the TT, where the colored regions represent different readout sectors. The first and last layers have vertical read-out silicon strips that measure in the  $x$ -direction, while the second and third layers have strips rotated at an angle of  $+5^\circ$  ( $u$ -axis) and  $-5^\circ$  ( $v$ -axis) with respect to the  $x$ -axis, respectively [28]. This layout provides a precise measurement of track positions for momentum determination in the bending plane of the magnet. The  $400\mu\text{m}$  thick silicon strips have a pitch of  $183\mu\text{m}$ , giving a spatial hit resolution of around  $50\mu\text{m}$ .

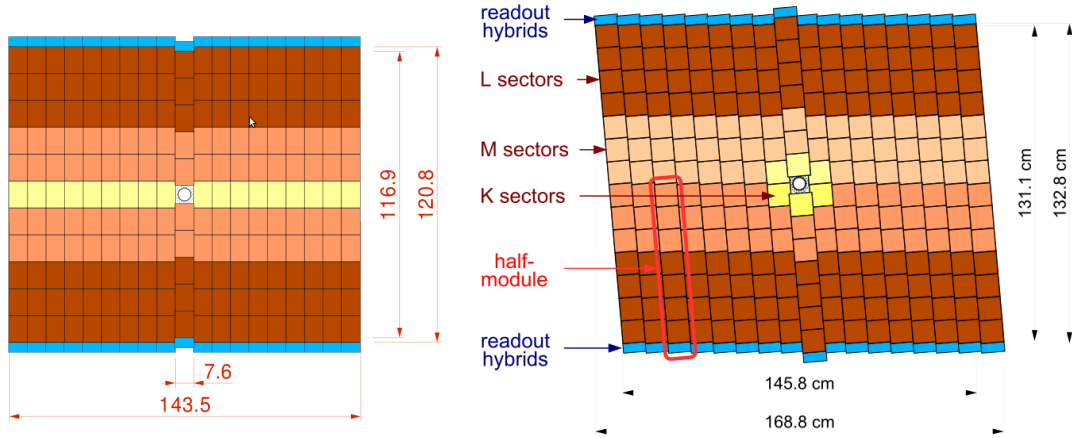


Figure 2.8: A drawing of the first and third TT station planes, where the latter is set at an angle of  $-5^\circ$ . The colored regions mark different readout sectors.

The IT consists of three tracking stations: T1, T2 and T3. They are located just after the magnet in the middle section of the experiment, closest to the beam pipe. The IT covers a 120 cm wide and 40 cm high cross-shaped region around the beam pipe, shown in figure 2.9. Each tracking station is made of four boxes that are located above, below and to the sides of the beam pipe. A box contains four layers with silicon readout microstrips at a pitch of around  $200\mu\text{m}$ . A layer consists of seven staggered silicon ladders. The layers are assembled as long ladders connected to a readout at one end, where the layers are either one-sensor or two-sensors wide. The one-sensor ladders are used in the top and bottom boxes, while the two-sensor ladders are used in the side boxes, again illustrated in figure 2.9. The two types of sensors, which are the same in all ways except thickness, one-sensor modules and two-sensor modules, are  $320\mu\text{m}$  and  $410\mu\text{m}$  thick respectively. The different thicknesses are chosen to ensure a high enough signal to noise ratio while trying to keep the cost down. Following the same method of the TT, the first and last layer of each tracking station measures in the x-direction using vertical readout strips. Again the second and third layer of each tracking station are rotated at an angle of  $+5^\circ$  ( $u$ -axis) and  $-5^\circ$  ( $v$ -axis), respectively.

The inner tracking system takes care of the region around the beam pipe, where the particle density is at its highest. The silicon strip technology here works the same as described



for the VELO. However, since pitch and sensor thickness are larger here the precision is not as good as for the VELO. This is acceptable as precision does not need to be as good as the VELO at this point in the tracking. The IT material also must withstand high amounts of radiation.

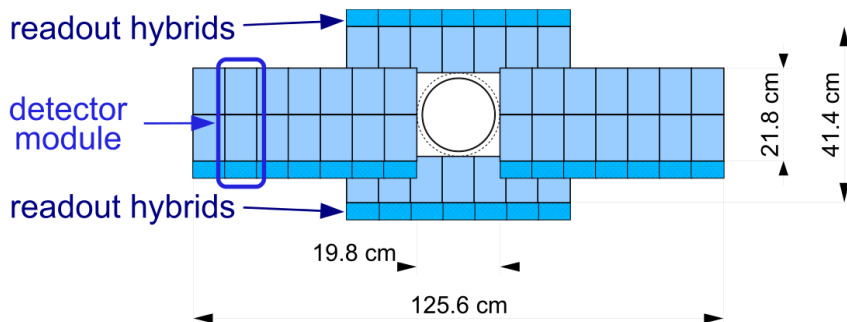


Figure 2.9: A schematic of the Inner Tracker. Each light-colored rectangle represents a sensor. The darker, smaller rectangles are readout hybrids. The central circle is the beam pipe.

The OT consists of three tracking stations, each with four detection layers which are arranged in the familiar  $x - u - v - x$  geometry used in the ST. The OT stations sit around the IT stations, illustrated in figure 2.10. The OT is made up of an array of gas-tight straw-tube modules. There are 64 straw-tubes per module that go in the detector. The tubes sit in two layers, one layer offset slightly from the other for maximum coverage, illustrated in figure 2.11.

The OT is a drift-time detector used to track charged particles and measure their momentum over a large acceptance area. The basic principles behind this type of detector, also known as drift tubes, is easy to understand. A tube or cylindrical chamber<sup>7</sup> is filled with gas with a wire along the center of it [29]. The wire (anode) is kept at a positive voltage while the outer cylinder (cathode) is kept at an equally negative voltage, or ground. When radiation passes through the tube, it ionizes the gas releasing electrons that are accelerated (drift) towards the wire, creating an electrical signal. This signal is carried from the wire to

<sup>7</sup>Of course this can be simplified to planar anodes and cathodes, but LHCb utilizes cylinders, so this type is discussed.

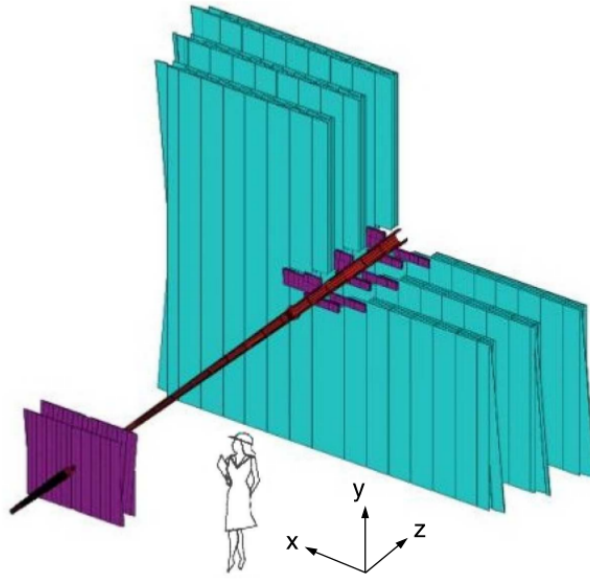


Figure 2.10: A cut-away illustration of the Outer Tracker. The OT are in blue while the IT are the purple inner sections of the image.

electronics outside the detector. In figure 2.12, a zoomed cross-section of stacked drift tubes is illustrated with the wires going into the page. A particle's trajectory crossing the array of tubes is marked by the red arrow. As this particle passes, gas is ionized at the position where the particle passes through the chamber, which occurs at some radius away from the central wire, denoted by the green lines. The time it takes for an ionized electron to drift from this point of ionization to the wire is related to the radius and velocity with which it traveled.

Each tube has a cylindrical chamber made of a strip of  $40\mu\text{m}$  carbon-doped polyamide foil wound simultaneously with a  $37.5\mu\text{m}$  thick kapton-aluminum laminate, the latter for gas-tightness, for fast signal transmission and good shielding against noise. The wire inside is made of gold-plated tungsten and has a diameter of  $25.4\mu\text{m}$ . The ionizing gas in the chamber is a mixture of 70% Argon and 30%  $\text{CO}_2$ , which gives a fast drift time of  $\sim 50\text{ ns}$ . As there are 128 tubes per short module, 256 per long module, with 96 short modules total and 198 long modules total, there are over 55000 single tube channels in the entire OT. A

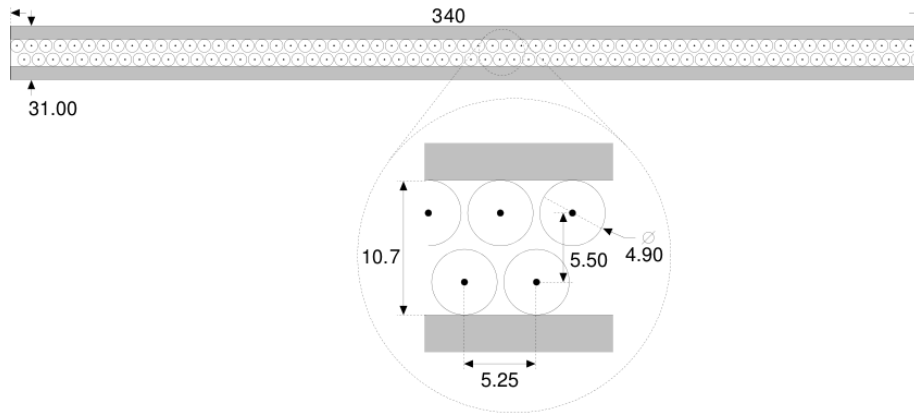


Figure 2.11: A cross-sectional view of the Outer Tracker straw drift tubes in two layers that are slightly offset. Units are in millimeters.

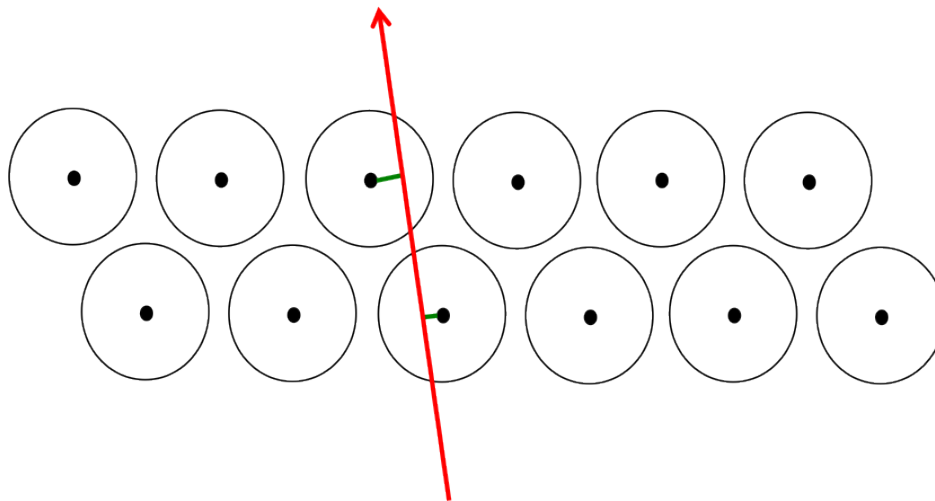


Figure 2.12: A zoomed-in illustration of a particle passing through stacked drift tubes.

cross-sectional view of one chamber is shown in figure 2.11.

Track reconstruction is done with the entire tracking system. It begins with track seeds or initial candidates in the VELO and the T-stations that have low magnetic field. Tracks are located between these two detectors and then they are fit with a Kalman filter, which takes into account multiple scattering with detector material and corrects for  $dE/dx$  energy losses. Figure 2.13 illustrates the many type of tracks that one identifies in the experiment. This

allows physicists to manipulate the criteria of the tracking system, which reduces background and enhances signal. In this work the principle tracks used are “long tracks”, which utilize each sub-detector of the tracking system as shown in figure 2.13.

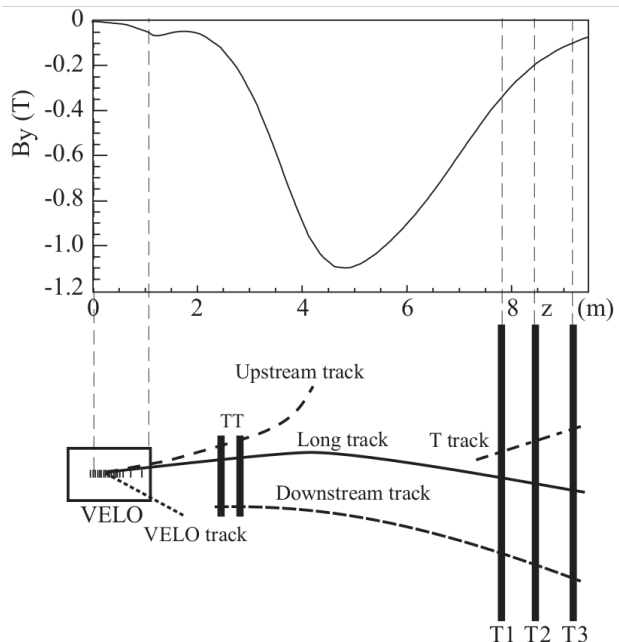


Figure 2.13: A schematic drawing of multiple types of tracks through the LHCb experiment and the magnetic field profile in the  $y$ -direction (bending plane) along the experiment.

### 2.2.3 Identification: RICH1, RICH2, the Calorimeters and Muon System

Located after the VELO is the first of two Ring Imaging CHerenkov detectors (RICH1), while the second (RICH2) is located further away from the interaction point.

RICH detectors have the task of identifying passing charged particles. This is done by utilizing Cherenkov light emission that occurs when a charged particle travels faster than the speed of light in a medium. When the particle travels at these speeds, it emits radiation in the shape of a cone in the direction of the particle’s flight. This gives access to the particle’s velocity. With the velocity, and the mass and energy measurements from the calorimeters,

identification of the particle is acquired. Particle identification is an integral part of this experiment as it reduces background in any interesting final states and allows physicists to separate interesting decays from contamination. The momenta of the particles detected by the RICH1 are between 1 and 60 GeV, while RICH2 detects particles with momentum of 15 GeV and greater.

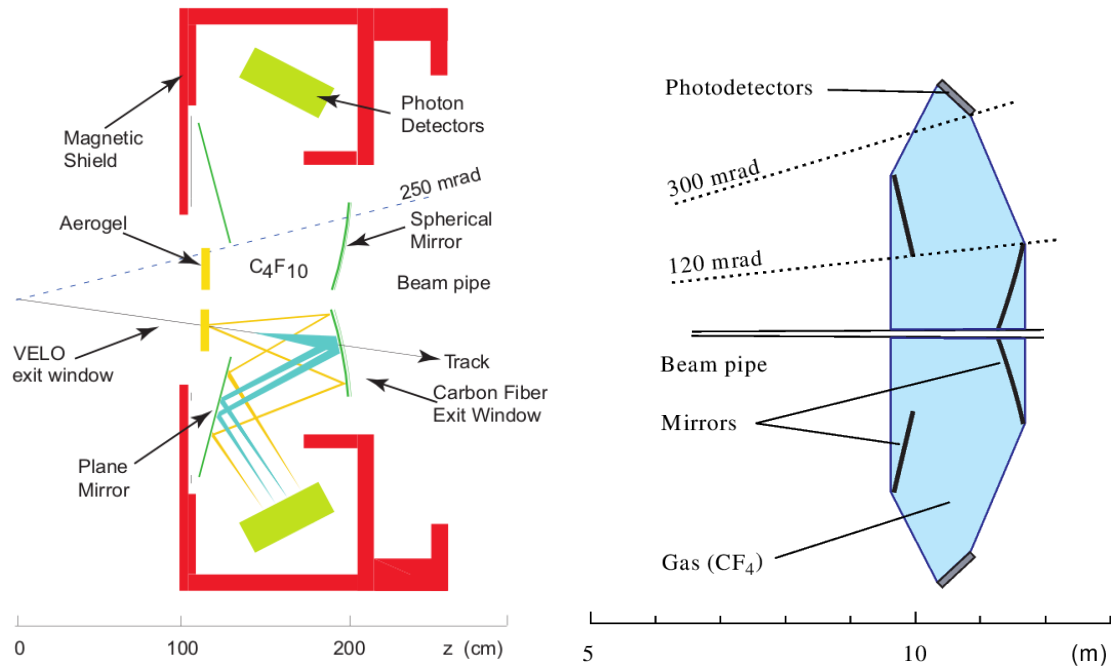


Figure 2.14: A schematic of RICH1 and RICH2.

The base components necessary for a RICH detector are a cavity filled with a medium, mirrors and photon detectors. The RICH detectors must contain some medium, also called radiators, in which the particles can enter and travel faster than the speed of light. In RICH1 this is in the form of a thin layer of aerogel followed by a larger volume of  $C_4F_{10}$  gas. Silica aerogel is chosen as the first layer radiator because it has a tunable refractive index between 1.01 – 1.10 and is ideal for detecting particles with low momenta, as low as a few GeV. There is some loss of photons due to Rayleigh scattering in the aerogel and it is particularly dominating at high energies, so a 330 $\mu$ m thick plane of glass is placed between the aerogel and the next layer of gas to absorb photons that cause chromatic aberration. The second

radiator,  $C_4F_{10}$ , is chosen because its refractive index,  $n = 1.0014$  at  $\lambda = 400$  nm, is well matched to the momentum spectrum of resulting B decays that occur in LHCb. Similarly, in RICH2 the radiator is in the form of  $CF_4$  and chosen for the same reason. The index of refraction is  $n = 1.0005$  at  $\lambda = 400$  nm for  $CF_4$ . Illustrations of RICH1 and RICH2 are seen in figure 2.14.

For RICH1, the Cherenkov light is reflected off two mirrors, a spherical and planar, which is then directed into the photon detectors. In RICH2, the double reflection process is the same, however both mirrors are planar.  $Al + SiO_2 + HfO_2$  coating is used for all RICH glass mirrors in LHCb, which is optimized for the different mean angles of incidence,  $25^\circ$  for the spherical mirror,  $45^\circ$  for the flat mirror in RICH1 and  $30^\circ$  for RICH2 mirrors [25].

Both RICH systems contain many Hybrid Photon Detectors (HPD) setup as an array located in an upper area and a lower area, shown in figure 2.14, noted as photon detectors. These collect Cherenkov photons with wavelengths between 200 nm and 600 nm. Figure 2.15 shows a drawing of an HPD, where a photon hits the photo-cathode HPD window converting it into a photoelectron. The photoelectron is emitted in the vacuous interior and accelerated towards the pixelated silicon sensor. This acceleration is due to an applied voltage of about 20kV, which creates an electrostatic field in the vacuum tube of the HPD. This corresponds to  $\sim 5000$  electron-hole pairs released in the silicon sensor.

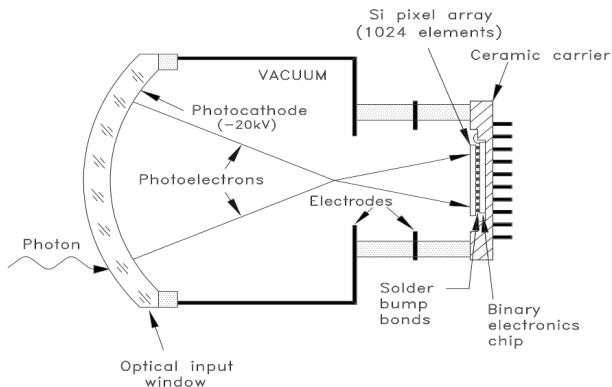


Figure 2.15: A schematic of an HPD, a component of the RICH detectors.

The photons that land on the mirrors and then the HPDs form rings of deposited energy. From the radii of each ring and the known focal lengths of the mirrors, the angles of the cherenkov light can be determined and so can the velocities of the particles. Once the velocities, energies and momenta are known, a probability likelihood distribution is created for each type of particle and compared to a probability likelihood of pions in the RICH. This delta log likelihood (DLL) distribution is defined as

$$\text{DLL}_{X\pi} = \log\left(\frac{P_X}{P_\pi}\right), \quad (2.1)$$

where  $P$  is momentum, the  $\pi$  denotes a pion used as the comparison particle as they are found copiously, and the  $X$  represents the particle whose identification is in question. From here one can determine, for example, if a kaon candidate in offline analysis is closer to being a kaon or closer to being a pion. Figure 2.16 shows the efficiencies of pions (kaons) being misidentified as electrons, muons and pions as a function of momentum, which illustrates that the RICH system does a very good job at particle identification. In order to determine likelihood functions, it is necessary to take pure samples of copiously made particles at the LHC, such as pions and kaons, and reconstruct them with the system. For instance, to get a pure sample of muons,  $J/\psi \rightarrow \mu^+\mu^-$  can be used; for kaons,  $\phi \rightarrow K^+K^-$  can be used.

One of the challenges for the RICH1 detector is the fringe magnetic field from the magnet that sits just behind it (see figure 2.3). As seen in figure 2.17, this causes the otherwise straightforward measurement of particles' positions on an HPD (black dots) to become distorted (spiral plot of red dots). This has been overcome by creating a Magnetic Distortion Calibration System (MDCS)<sup>8</sup> [30].

The MDCS is made up of two light bars, one for each set of HPDs, upper and lower. On the light bar are nineteen LED PCB units, each LED unit consisting of a six-layer PCB on which are mounted four LED arrays. Also on each LED unit is an on-board addressable micro-controller, a driver circuit to control each LED, and a collimator unit. Each LED

---

<sup>8</sup>Designed and constructed by Syracuse University with pieces from SenSyr LLC.

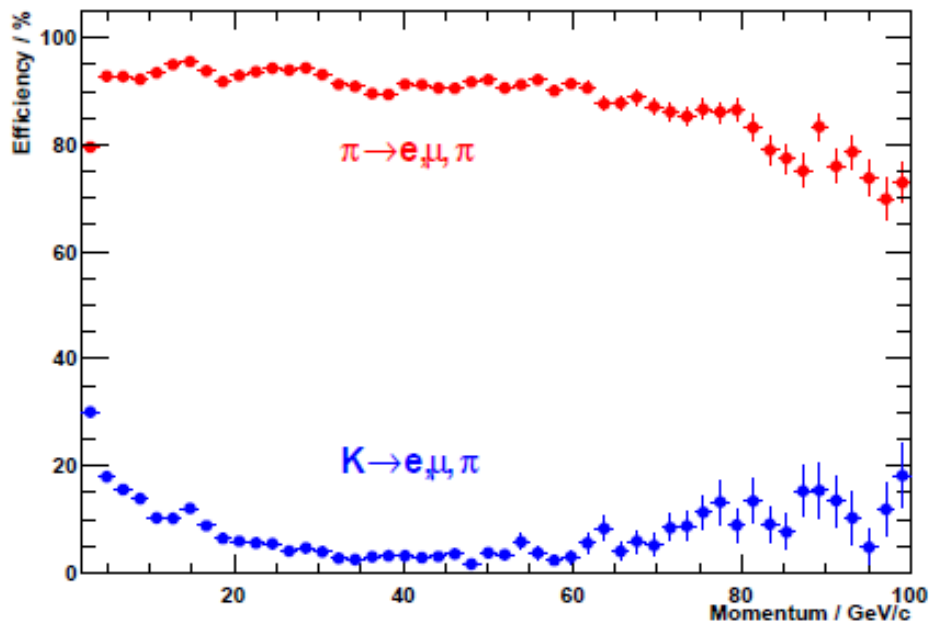


Figure 2.16: Efficiencies of a pion (kaon) being misidentified as an electron, a muon or a pion.

array consists of a  $5 \times 7$  matrix of green LEDs. The system produces many light spots on each HPD, which are then moved to scan the HPD array in two dimensions. This type of scan produces a direct mapping of the distortion at a given magnetic field. The system also creates an inverse mapping, assigning a given distorted pixel hit to its real position on the photocathode. RICH2 does not need calibration as it sits far enough from the magnet not to be affected. Figure 2.18 illustrates where the MDCS light bar is located with respect to the HPDs in RICH1.

As with all of the detectors, it is incredibly important that the measurement of a quantity be precise. This precision can be understood via the resolution of the measurement. For the RICH detectors, the resolutions prior to the use of the calibration system is unacceptable as shown by the dashed lines in figure 2.19. However, after the application of this system the resolution improves by a factor of 3.7, shown by the solid histogram lines in the same figure [30]. Further performance of the RICH system is located in the paper by the RICH Group [31].



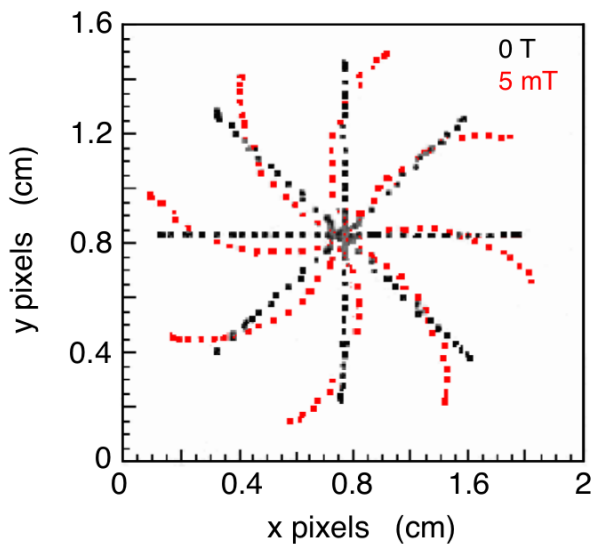


Figure 2.17: A plot of the output of RICH1 with and without the  $\vec{B}$  field, illustrating the incredible benefits of the calibration system.

In addition to the RICH detectors, calorimeters provide particle identification. Calorimeters however have the task of identifying electrons and hadrons for trigger and offline analysis as well as measurements of particle positions and energies. They provide identification of neutral particles such as photons and  $\pi^0$ 's which cannot be detected elsewhere. Calorimeters are also the last stop for most particles created during initial collisions. This means that electrons and hadrons will deposit all their remaining energy onto these devices and so this requires calorimeters to withstand a high amount of radiation.

In the LHCb experiment there are two main calorimeters, the Electron Calorimeter (ECAL) and the Hadron Calorimeter (HCAL). In addition to two calorimeters measuring electrons and hadrons, there are two detectors called the Scintillator Pad Detector (SPD) and the PreShower detector (PS). The latter two are located just after the last T-station and just in front of the ECAL, and the HCAL sits just after the ECAL.

All calorimeters follow the same basic principle in structure: scintillation light transmitted to a Photo-Multiplier Tube (PMT) by wavelength-shifting (WLS) fibers. When charged particles move through material, they lose energy through electromagnetic interaction with

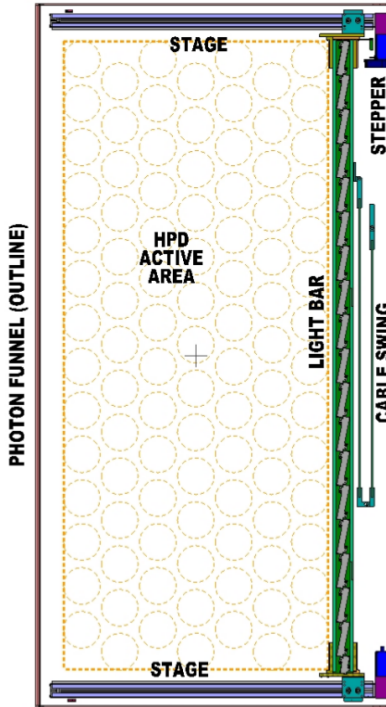


Figure 2.18: An image of an HPD array of a RICH1 box. The HPDs are noted by grey circles and a MDCS light bar is in parked position at the right edge of the box. During calibration the bar moves to the left in steps and light spots from the LED are produced onto the HPDs to calibrate the hit positions.

Coulomb fields. This ionizes atoms or molecules of the material through which it passes bringing them to an excited state. These excited atoms try to go back down to their ground state and thus release their energy in the form of photons. When this excited energy released is in the visible domain of the electromagnetic spectrum, it is called scintillation [32].

PMTs are utilized in the ECAL and HCAL and work very similarly to the HPDs described earlier. However, in PMTs the photoelectrons inside the vacuum are multiplied many times over by focusing the particles onto stacked multipliers such that a large electrical signal is emitted [29], which is not the case in HPDs. Wavelength shifting fibers absorb scintillation light and re-emit it at a lower energy (longer wavelength) [32]. This is important as PMTs have a higher quantum efficiency for blue light ( $\sim 400$  nm) than green light [29].

The purpose of the SPD and PS is to signal the presence of a charged particle prior to

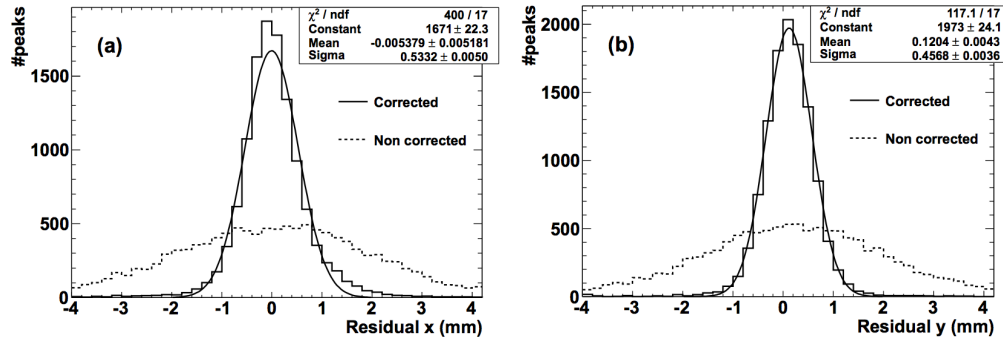


Figure 2.19: Spatial residuals demonstrating the resolution with which the light spots of the test pattern in RICH1 are identified. The plots show the distance from the measured light spot center to the nearest test point. Residuals of the  $x$  and  $y$  direction of the RICH system before (dashed lines) and after (solid histogram) the application of the MDCS. The solid curved line is a Gaussian fit to the calibrated data.

it entering the ECAL as well as to reduce the high background of neutral pions with high transverse energy. These particles then pass into the ECAL to be identified.

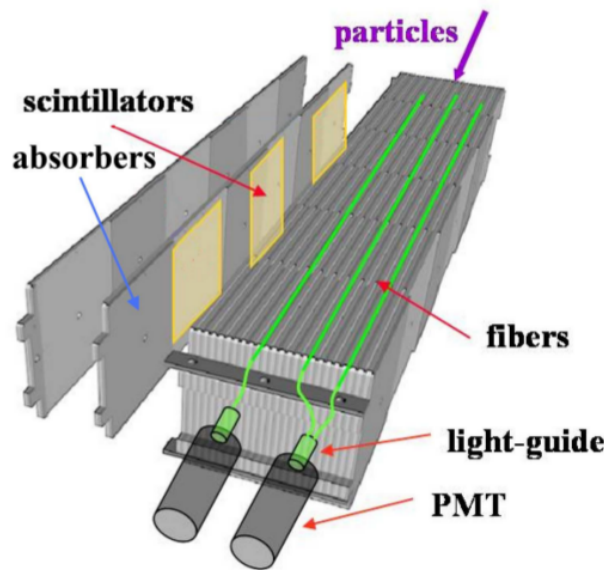


Figure 2.20: An illustration of the Hadron Calorimeter structure. The layers of absorber (iron) and scintillating tiles are placed parallel to the beam axis as opposed to perpendicular as in the ECAL. Shown, is only one-quarter of the detector.

The HCAL is a large rectangular structure that is 8.4m in height, 6.8m in width<sup>9</sup> and 1.65m in depth. It is made of layered 16mm thick iron and 4mm thick scintillating tiles, with each tile wrapped in 120 – 150 $\mu$ m of TYVEK. The TYVEK serves to enhance the light collection of the WLS fibers, reduce cross-talk between adjacent tiles as well as protecting the optical reflective surface of the tiles. The layers of iron and scintillator run parallel to the beam axis as shown in figure 2.20, which makes the HCAL unique in terms of calorimeters. WLS fibers are utilized to readout the light from the scintillators via total internal reflection. The fibers have a diameter of 1.2mm and length of 1.6m, and run parallel along the edges of the tiles towards the back of the HCAL. They are connected to PMTs for readout to the electronics. Each WLS fiber collects light from three tiles which are arranged along the hadron shower development direction, and each PMT reads out one cell of tiles. Due to the high energy particles that hit the calorimeters in general and in particular at the central region around the beam pipe<sup>10</sup>, the HCAL is subdivided into three areas as seen in figure 2.21. This allows the outer regions' functionality to be unaffected when the central regions become highly irradiated and damaged. The segmentation of the calorimeters provides physicists with precision position measurements and angle of incident particle measurements, which allows for better identification.

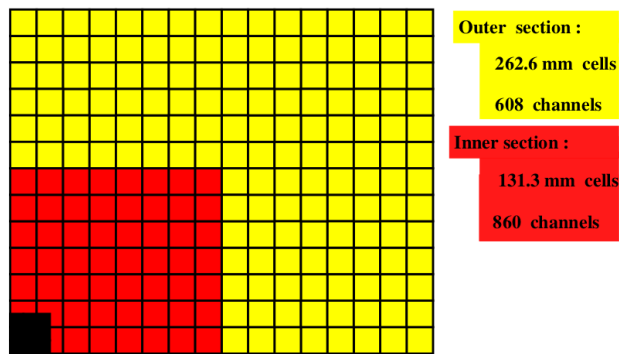


Figure 2.21: The HCAL is subdivided into two regions, the inner region and the outer region.

<sup>9</sup>This is about 57m<sup>2</sup>. For scale, this is slightly larger than the size of the apartment in which I lived while working at CERN.

<sup>10</sup>The hit density increases by two orders of magnitude over the surface area of the HCAL.

Hadronic cascades are similar to electromagnetic (EM) showers but are more complex. The hadrons travel very fast and penetrate the material of the detector causing nuclear interactions with the material. The hadrons produce multiple particles, mostly in the form of pions and nucleons. Then these secondary particles interact with the material of the detector. This continues as a cascade of interactions until all the energy is expended. These showers have been studied thoroughly and so the length of a shower is known as it is dependent on its energy. The maximum shower length can be measured from the beginning of the calorimeter in which the shower takes place and is approximated by the following,

$$L_{max}(\lambda) \simeq 0.2 \ln(E) + 2.5 \lambda E^{0.13} + 0.7, \quad (2.2)$$

where  $E$  is energy in GeV and  $\lambda$  is the absorption length of the material [33]. All pieces of the calorimetry system are used in the L0 trigger to reduce the amount of uninteresting events. The electron L0 trigger is required to reject 99% of the inelastic proton-proton interactions. This is discussed in more detail in section 2.2.4.

The muon system provides the identification of the muons for L0 trigger as well as offline analysis. Muon identification is important because they are present in the final states of many CP-sensitive B decays, including  $B_s^0 \rightarrow D_s \mu \nu$ , which is of interest in this work. The acceptance is  $\pm 300$  mrad horizontally and  $\pm 200$  mrad vertically. Muons are selected in the L0 trigger by trying to match hits in the muon stations with tracks reconstructed via the tracking system. The RICH detectors are also used to identify particles as muons to reduce misidentification causing background.

As shown in figure 2.22, the muon system is made up of five rectangular muon stations (M1-M5) with 80cm thick iron absorber walls in between each, and all but M1 are located after the calorimeters. Each muon station is split into four regions, R1 to R4, where R1 is closest to the beam pipe (see figure 2.22 and 2.23) and thus getting hit with very high amounts of radiation, and R4 is the furthest corner of the muon station rectangle. Regions R1, R2, R3 and R4 in muon stations M2, M3 and M4 utilize Multi-Wire Proportional

Chambers (MWPC), whereas the R1 region in muon station M1 utilizes triple Gas Electron Multiplier detectors (GEM). The area closest to the beam on the first muon station is where the most radiation is deposited. Thus this area must be able to withstand very high amounts of radiation without exhibiting symptoms of damage<sup>11</sup>. GEMs are consequently chosen for this region because they are shown to be robust and have the ability to tolerate the dose which is given by the LHC machine.

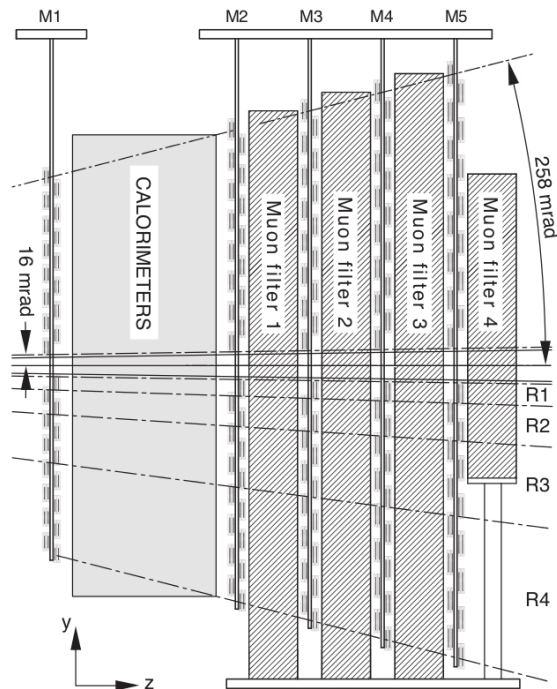


Figure 2.22: A side view schematic of the muon system.

MWPCs are very similar to drift-tubes, where instead of a cathode cylinder there are two cathode planes and rather than one wire there is a plane of wires along the center space of the two planes. Also, there is gas in the areas between the wires, and here the mixture is  $\text{Ar}/\text{CO}_2/\text{CF}_4 \simeq 40/55/5$ , having been tested for optimization [34]. When a negative voltage is applied to the cathode planes the electric field produced is effectively parallel to the wires, except when very close to the wires where the field is distorted due to their finitely cylindrical

<sup>11</sup>This occurs in the form of dead detector pieces, etc.

nature. When radiation crosses through the chamber, the electrons in the gas are ionized and drift towards the wires. Once they get close enough they are accelerated due to the distortion mentioned and produce an avalanche of electron-ion pairs, which means that the already ionized electrons produce another ionization and so on. This avalanche usually takes the shape of a teardrop with the faster moving electrons near the wide part accelerating towards the wire and the slower moving positive ions near the point of the teardrop. This leads to electrons, where the radiation passed through, to drift towards a wire creating a negative signal and surrounding wires to also acquire a signal, but instead these signals are positive. Consequently, it is unambiguous which wire has been passed by the particle.

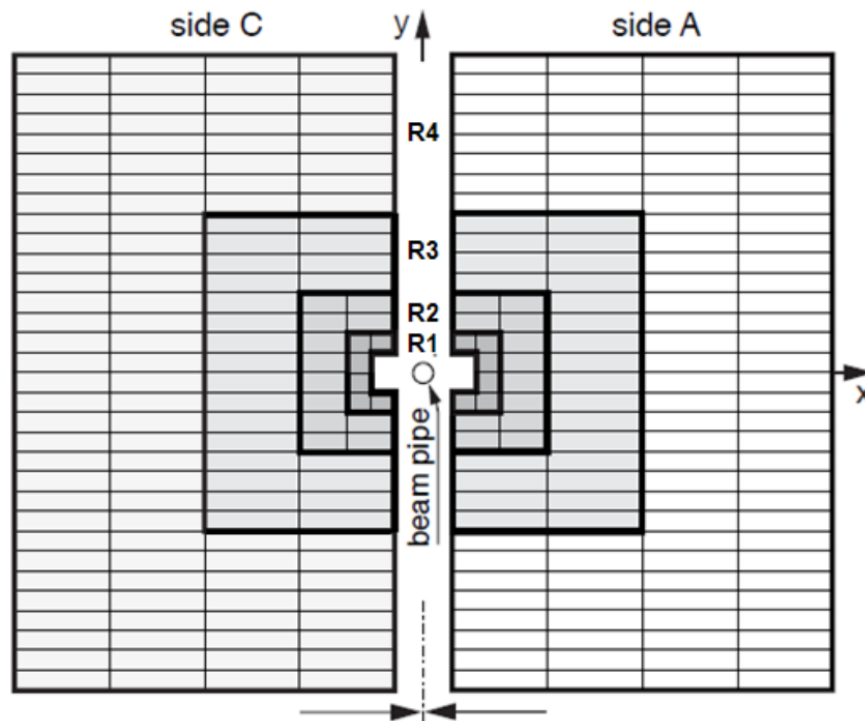


Figure 2.23: A diagram of a muon station with the four regions indicated.

A GEM is another type of detector that is chosen for the area of the muon station closest to the beam. It is made up of a  $50\mu\text{m}$  copper clad kapton foil that has a high surface density of holes. Each hole has an hourglass structure with external and internal diameter of  $70\mu\text{m}$  and  $50\mu\text{m}$  respectively, where the hole pitch is  $140\mu\text{m}$ . The unique shape of the

hole minimizes the effect of charging-up the kapton inside the holes. A triple GEM detector consists of three gas electron multiplier foils sandwiched between anode and cathode planes, where the gas is the same optimized mixture of Ar/CO<sub>2</sub>/CF<sub>4</sub> but with a different ratio of 45/15/40. This is effectively used as a tracking detector, with good time and position resolution performances [35]. A voltage is applied to one side of the planes and so an electric field is produced between the planes as well as inside the holes. The holes act as electron multiplication channels for electrons released by ionizing radiation in the gas [36].

Station M1 is placed in front of the calorimeters in order to improve the  $p_T$  measurement in the trigger and thus information from M1 is only used in the L0 trigger. Information from stations M2- M5 is used to identify and trace muons in online as well as offline analyses.

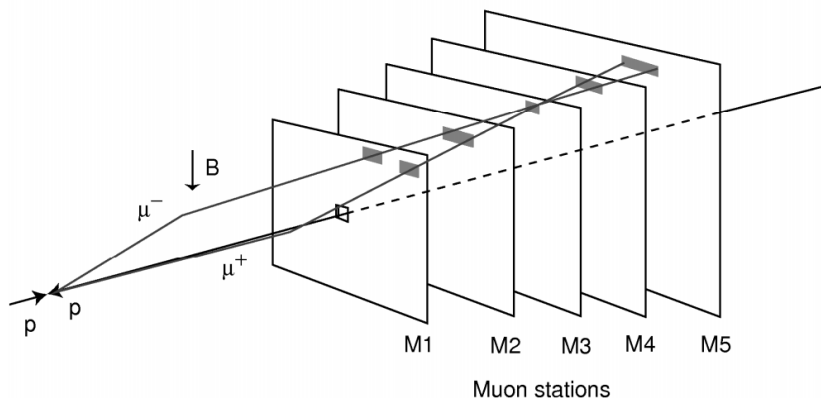


Figure 2.24: An example of track finding in the muon stations. After  $pp$  collision, two muons are produced and enter into the muon sub-detector where their hits are examined by an algorithm. The grey boxes represent the field of interest.

The L0 Muon trigger reconstructs muon candidate tracks by searching for hits in a field of interest (FOI) projective to the interaction point using M2 through M5. If hits are aligned in these four stations then the hits of M2 and M3 are used to predict the track hit position in M1. If there is a hit matching the predicted hit position in M1 in another FOI then this hit and the hit in M2 are used to define the track after the magnet deflection [34]. Figure 2.24 illustrates an example of two muons being produced from the interaction point and entering



the muon sub-detector [37].

In particular there is a specific boolean that is required of muon tracks, called “IsMuon”. For a track that is reconstructed in the tracking system, the software algorithm looks for hits in the muon stations around some field of interest. This “IsMuon” boolean is satisfied when there is at least one hit in this FOI in the muon stations [38]. The required number of muon stations is dependent on the muon momentum, which are listed in table 2.1.

Table 2.1: Number of muon stations required to pass the “IsMuon” boolean cut. This cut is dependent on the muon momentum.

Momentum Range	Muon Stations
$3 \text{ GeV} < p < 6 \text{ GeV}$	M2+M3
$6 \text{ GeV} < p < 10 \text{ GeV}$	M2+M3+(M4.or.M5)
$p > 10 \text{ GeV}$	M2+M3+M4+M5

## 2.2.4 2011 Data Taking and Trigger

The luminosity at which LHCb operates is  $2 \times 10^{32} \text{ cm}^{-2} \text{ s}^{-1}$ , which produces massive amounts of information. All the data are produced within LHCb cannot be saved, much to the physicist’s chagrin. In a perfect world, there would be infinitely fast electronics and unlimited storage, but this is not the case. LHCb *has* speedy electronics at the front-end as well as behind the scenes to pass the data from the detector to the analysts. At the front, since the LHC outputs data at a rate of 40 MHz, LHCb’s electronics read in data at this frequency. As data is read in it is passed through a Level-0 hardware trigger that identifies and sorts the particles into three categories: photons, leptons or hadrons.

The L0 trigger is divided into three components: the pile-up system (VELO), the L0 calorimeter trigger (HCAL and ECAL) and the L0 muon trigger (muon system), as illustrated in figure 2.25. Each part is connected to one detector (in parentheses) and to the L0 Decision Unit (L0DU), the latter which collects all information calculated by the trigger systems to evaluate the final decision. This makes the L0 trigger the first step to removing unwanted

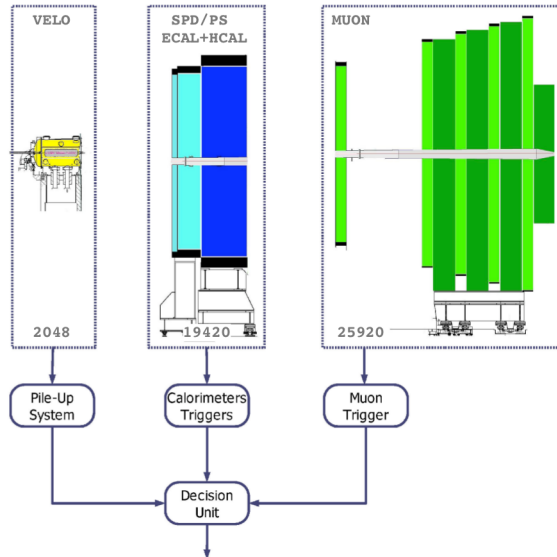


Figure 2.25: A schematic of the L0 Trigger and how all the components are connected.

and uninteresting events, reducing the data flow to 1 MHz.

The pile-up system consists of four R-coordinate measuring VELO sensors that are located at the very front of the detector, upstream of the interaction region. The system's job is to determine how many bunch crossings there are during collisions, whether it be one bunch crossing another or multiple bunches (for LHCb, 1 bunch by 1 bunch is best for clean events). The sensors do this by measuring the vertices of the proton interactions.

The calorimeter trigger system looks for particles with high transverse energy ( $E_T$ ), such as electrons, photons,  $\pi_0$ 's or hadrons. The software forms clusters and they are selected based on which clusters have greater  $E_T$ . The information provided by the SPD, PS, ECAL and HCAL yield what type of particle it is. A measure of the charged track multiplicity in the crossing is determined by information from the SPD hits.

The muon system reconstructs muon tracks with its five stations, reconstructing with a  $p_T$  resolution of about 20%. Track finding is performed by combining the strip and pad data from all muon stations to form areas pointing towards the interaction region. Then the L0 muon trigger selects two muons with the highest  $p_T$  for each quadrant of the muon detector, searching for hits defining a straight line through the five muon stations and pointing towards

the interaction point. The position of a track in the first two stations allows the determination of its  $p_T$ .

The data is funneled from the three sub-detector units to the L0DU, which makes the final decision to accept or reject events. The time it takes for the interaction to occur, the data to be read through each detector and the L0DU to make the decisions is  $4\mu\text{s}$ . Data is then quickly output from the L0 trigger into High Level Trigger 1 (HLT1).

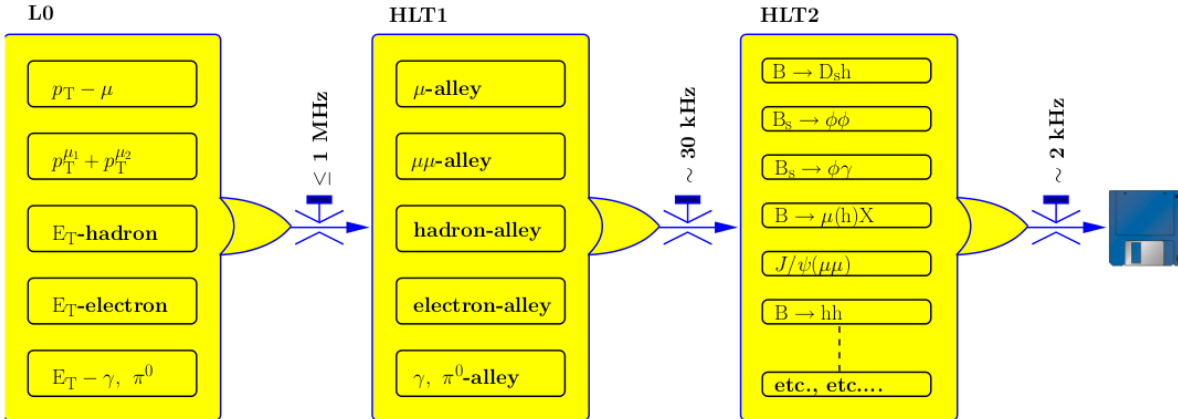


Figure 2.26: A flow chart of the data through the trigger.

The purpose of HLT1 is to reconstruct particles in the VELO and T-stations corresponding to the L0 objects. HLT1 output rate is about 30 kHz, which allows events to be small enough to begin reconstructing in HLT2. Figure 2.26 illustrates the data flow from L0 to disk.

When the data enters High Level Trigger 2 (HLT2), simple final states such as  $\phi \rightarrow K^+K^-$  and  $J/\psi \rightarrow \mu^+\mu^-$  are reconstructed and further uninteresting events are rejected, while keeping the events that are to be used in analyses. Also in HLT2 some invariant mass cuts are made, as well as other quality track cuts on final state particles.

All trigger lines are broken into two main categories: events that (1) trigger independent of signal (TIS) and events that (2) trigger on signal (TOS) with respect to the user defined signal. Therefore, if one is to search for a B decay, requiring TOS on the B hadron and its

final state particles, then one is sure to have triggered on the signal desired. However, if one requires TIS on this same B hadron, then the signal desired is not the source of triggering and it must be something else (most likely background, which includes the other B that decays from the pp collisions).

The final data output rate is around 2 kHz and this is the maximum that can be handled and saved onto disk. At this moment in the process, data acquisition is complete and offline analysis begins.

# Chapter 3

## Measurement of $a_{\text{sl}}^s$

**with**  $B_s^0 \rightarrow (D_s^\mp \rightarrow \phi \pi^\mp) \mu^\pm \nu_\mu$

CP violation in B mixing can show up in  $\phi_{12}$  in the  $a_{\text{sl}}^s$  quantity. This is important as new physics can be found in these developments. Specifically, if the value of  $a_{\text{sl}}^s$  departs from zero than it is possible that new physics exists. The Standard Model prediction of  $a_{\text{sl}}^s = (0.0019 \pm 0.0003)\%$  shows that there is no asymmetry.

The formalism of  $a_{\text{sl}}^s$  has been discussed in the section 1, however it is important to review the quantity that is being measured, namely

$$A_{\text{meas}} = A_\mu^c - A_{\text{track}} - A_{\text{bkg}}, \quad (3.1)$$

with

$$A_\mu^c = \frac{N(D_s^- \mu^+) - N(D_s^+ \mu^-) \times \frac{\epsilon(\mu^+)}{\epsilon(\mu^-)}}{N(D_s^- \mu^+) + N(D_s^+ \mu^-) \times \frac{\epsilon(\mu^+)}{\epsilon(\mu^-)}}, \quad (3.2)$$

$$A_{\text{track}} = A^{\mu\pi} + A^{KK}, \quad (3.3)$$

and

$$A_{\text{bkg}} = A_{\text{prompt}} + A_{\text{fakes}} + A_{\text{peaking}}. \quad (3.4)$$

$N(D_s^- \mu^+)$  and  $N(D_s^+ \mu^-)$  in equation 3.2 represent the raw yields of the final state decays denoted in parentheses, while  $\epsilon(\mu^-)$  and  $\epsilon(\mu^+)$  represent the efficiency corrections including trigger and identification effects. In equation 3.3, the two quantities are the asymmetry in tracking between the pion-muon pair and the kaon pair.  $A_{bkg}$  is the asymmetry result from any background contribution in equation 3.4. As mentioned, the production asymmetry of the  $B_s^0$  system multiplied by the small integral value is very small with respect to the measured quantity and thus it is ignored. Consequently,

$$a_{sl}^s = 2A_{meas}, \quad (3.5)$$

is the final result.

### 3.1 Stripping and Reconstruction

After data is taken, all triggers are applied and the data is saved on disk, the data must undergo a final step called *stripping*. This is a CPU intensive offline task that is applied to all the data. This means that only the most interesting and very important decay processes are kept and the remainder are thrown away. The stripping algorithms contain kinematic cuts to remove backgrounds of certain channels in which one may be interested.

The stripping used for this analysis is mainly of the 17<sup>th</sup> iteration. However there is one set of data that has been done through the 18<sup>th</sup> iteration of stripping, which is called 17b<sup>1</sup>. Table 3.1 shows the amount of data per magnet polarity and the stripping line and iteration associated. In the signal stripping line, cuts applied have stemmed from work on a measurement of the  $b$ -hadron production fractions previously done [39].

The analysis is done with DaVinci v29r2(3), a C++ based analysis software in LHCb, and with MC11a<sup>2</sup> Monte Carlo events. During the analysis process, the magnet polarities

---

<sup>1</sup>This is simply a re-stripping of the data for only dramatically updated lines.

<sup>2</sup>The number in MC11a denotes the year of collection of the data.

Table 3.1: List of 2011 data samples used in this analysis.

Stripping	Iteration	Luminosity[ pb <sup>-1</sup> ] Magnet Up	Magnet Down
<b>Signal Samples</b>			
<i>Semileptonic/Strippingb2DsMuXPhiPi</i>	17	447	595
<i>Semileptonic/Strippingb2DsMuX</i>	17	447	595
<b>Muon Efficiency Studies Samples</b>			
<i>PID/MuIDCalib_JpsiFromBNoPIDNoMip</i>	17	447	595
<b>Pion Efficiency Studies Samples</b>			
<i>CharmCompleteEvent/StrippingD0ForBXX</i>	17	447	595
<i>Charm/StrippingPromptCharm</i>	17	447	595
<i>Charm/D2hhh_KKPLine</i>	17	447	595
<b>Background Studies Samples</b>			
<i>Semileptonic/Strippingb2DsMuXPhiPi_fakes</i>	17b	447	595

are kept separated, such that they are effectively separate sets of data. With the DaVinci framework, one has access to all information needed to analyze all decay channels. This framework reconstructs the decays back to the final state particles' origin, then outputs all the information into an n-tuple in ROOT form for offline analysis by a user. At this point, the user can apply kinematic cuts, multivariate cuts and so on, in order to whittle down the background and amplify the signal even more. The offline analysis in this work has been done via several C++ ROOT macros with rectangular kinematic cuts. The stripping cuts applied are listed in table 3.2 and are discussed below.

For a particle to be identified as a muon, it is required that the momentum be larger than 3 GeV, the transverse momentum be greater than 800 MeV, the  $\chi^2$  of the impact parameter (IP) be greater than 4, where IP is defined as the smallest distance between the track path and the primary vertex (PV) position. The  $\chi^2$  per degree of freedom of the muon candidate track must be less than 5. It is also required that the Delta Log Likelihood (DLL) of the comparison pion minus the candidate muon be greater than 0 (meaning it must be identified by the RICH system to be more like a muon than a pion), and finally the muon candidate track must pass the "IsMuon" cut, which requires that the muon has passed through a certain number of muon stations where the track is matched within some area around an

Table 3.2: Stripping cuts on the  $B_s^0$  signal.

Muon Selection Criteria	
$p$	$> 3 \text{ GeV}$
$p_T$	$> 0.8 \text{ GeV}$
IP $\chi^2$	$> 4$
Track $\chi^2/\text{NDF}$	$< 5$
Muon Identification	IsMuon = 1 & PIDmu $> 0$
$D_s$ daughter hadrons	
$p$	$> 2 \text{ GeV}$
$p_T$	$> 300 \text{ MeV}$
IP $\chi^2$	$> 4$
Track $\chi^2/\text{NDF}$	$< 4$
Kaon Identification	PIDK $> -5$
$\phi$ Meson	
Vertex fit $\chi^2/\text{NDF}$	$< 25$
$ m(K^+K^-) - m(\phi) $	$\leq 50 \text{ MeV}$
$D_s$ Meson Selection Criteria	
$p(\phi\pi)$	$> 800 \text{ MeV}$
Sum of IP $\chi^2$	$> 4$
Vertex fit $\chi^2/\text{NDF}$	$< 6$
FD $\chi^2$	$> 100$
$DIRA$	$> 0.99$
$ m(D_s) - m(D_s)_{PDG} $	$\leq 200 \text{ MeV}$
$B_s^0(D_s\mu)$ Selection Criteria	
$m(B_s^0)$	$[2.5, 6.0] \text{ GeV}$
Vertex fit $\chi^2/\text{NDF}$	$< 6$
$DIRA$	$> 0.999$
$z(D_s) - z(B_s^0)$	$> 0$



extrapolated line of the track direction [40].

For the  $D_s$  final state particles, the kaons and pions, to be identified as such, the momentum of each must be larger than 2 GeV, the transverse momentum of each must be greater than 300 MeV, each  $\chi^2$  value of the IP must be greater than 4, and the  $\chi^2$  per degree of freedom of each track must be less than 4. Specifically to be identified as a kaon, it is required that the DLL of the reference pion minus the kaon be greater than  $-5$ . The latter identification cut is very loose and left this way in stripping as it has high efficiency, and virtually no bias. Note that there are no identification cuts required for the pions as any bias may create a false asymmetry. The kaons are reconstructed as a  $\phi(1020)$  particle which also has requirements to pass. The  $K^+K^-$  vertex fit  $\chi^2$  per degree of freedom must be less than 25 and the invariant mass must be within 50 MeV of the  $\phi$  mass.

To be identified as a  $D_s$  particle, the combination of the pion and the two kaons all together must have a transverse momentum greater than 800 MeV, the  $\chi^2$  of the IP of the  $\phi$  and the pion must be greater than 4, the  $\chi^2$  per degree of freedom of the vertex fit (vertex of the  $\phi\pi$ ) must be less than 6 (i.e. very good), the vertex separation  $\chi^2$  of the  $D_s$  with respect to the PV must be greater than 100, the cosine of the angle between the momentum of the  $D_s$  and the direction vector from the PV must be greater than 0.99, and the mass of the  $KK\pi$  candidate must be within 200 MeV of the  $D_s$  invariant mass value. The latter is left very loose such that the  $D^\pm$  may be selected as well.

Finally, to create a  $B_s^0$  candidate, the mass of the aggregate particles must be between 2.5 GeV and 6.0 GeV, the  $\chi^2$  per degree of freedom of the vertex fit (vertex of the  $D_s\mu$ ) must be less than 6 (again, very good), the cosine of the angle between the momentum of the  $B_s^0$  and the direction vector from the PV must be greater than 0.999, and finally the z-coordinate of the vertex of the  $B_s^0$  subtracted from the z-coordinate of the vertex of the  $D_s$  must be greater than 0, i.e. the  $D_s$  must fly forward with respect to the  $B_s^0$ .

On top of these cuts, the clone killer is applied for all  $B_s^0$  final state particle tracks, in order to remove any repetitive tracking, i.e. hits in the detector that make up a single track

multiple times.

## 3.2 Offline Selection

Table 3.3 shows the additional cuts applied to the signal samples to cut out more background.

Again the cuts are discussed below.

Table 3.3: Offline selections on the  $B_s^0$  signal.

Muon Selection Criteria	
$p$	$\geq 6$ GeV and $< 100$ GeV
$p_T$	$> 1.5$ GeV
Track $\chi^2/\text{NDF}$	$< 3$
$\eta$	[2,5]
IP $\chi^2$	$> 4$
Muon Identification	IsMuon=1 & nShare= 0 & PIDmu> 0
$D_s$ daughter hadrons	
IP $\chi^2$	$> 9$
Kaon Identification	PIDK> 4
sum of $p_T$	$> 2.1$ GeV
$p$	$> 2$ GeV
$p_T$	$> 0.3$ GeV
Track $\chi^2/\text{NDF}$	$< 4$
$\phi$ Meson	
$ m(K^+K^-) - m(\phi) $	$\leq 20$ MeV
$D_s$ Meson Selection Criteria	
$ m(D_s) - m(D_s)_{PDG} $	$\leq 160$ MeV
IP	$< 7.4$ mm
Vertex fit	$\chi^2/\text{NDF} < 6$
$DIRA$	$> 0.99$
FD $\chi^2$	$> 100$
$B_s^0(D_s\mu)$ Selection Criteria	
$m(B_s^0)$	[3.1,5.1] GeV
$\eta$	[2,5]
Vertex fit	$\chi^2/\text{NDF} < 6$
$DIRA$	$> 0.999$
$z(D_s) - z(B_s^0)$	$> 0$
Global Event Cut	n(longTracks)< 250

Now that the muon candidate has been loosely identified, more strict cut requirements are

applied. The momentum range is now from 6 GeV to 100 GeV, the transverse momentum cut is increased to 1.5 GeV, the  $\chi^2$  per degree of freedom of the track is tightened to be less than 3. The pseudorapidity of the muon is required to be between 2 and 5, a newly introduced cut. The IP  $\chi^2$  cut remains the same. And finally an additional cut is applied for the muon identification, the number of shared tracks with the muon track is required to be 0, reducing multiplicity. For the final kaons and pions, the  $\chi^2$  of the IP cut has increased to a value of 9. The DLL of the reference pion minus the kaon, for the kaon identification<sup>3</sup>, has increased to 4. The sum of the final state particle transverse momentum must now be greater than 2100 MeV. All other final state particle cuts remain the same as in the stripping cuts. The  $K^+K^-$  invariant mass is tightened to be within 20 MeV of the  $\phi$  mass. The mass of the  $KK\pi$  candidate must now be within 160 MeV of the  $D_s$  invariant mass value. Also, the  $D_s$  IP must be less than 7.4mm. The other cuts on the  $D_s$  remain the same as in stripping. The  $B_s^0$  candidate's cuts have tightened as well. The mass must now be between 3.1 GeV and 5.1 GeV. The pseudorapidity of the  $B_s^0$  candidate is required to be between 2 and 5, another newly introduced cut. Also included here is a new cut on long tracks, removing 250 or greater long tracks.

In addition to these kinematic offline cuts, there are higher level trigger cuts that are applied. The trigger lines used are listed in table 3.4. It is required that the muon pass the hardware L0MuonTOS trigger, a logical OR of three HLT1 triggers: HLT1TrackAllL0TOS, HLT1TrackMuonTOS and HLT1SingleMuonHighPTTOS, and a logical OR of four HLT2 triggers: HLT2TopoMu2BodyBBDTTOS, HLT2TopoMu3BodyBBDTTOS, HLT2TopoMu4BodyBBDTTOS, and HLT2IncPhiTOS.

The topological trigger decisions are not simple rectangular cuts<sup>4</sup>. Also for the muon topological lines, a muon is specifically required, i.e. at least one of the particles passing through each decision must be a muon. This is implemented via the “IsMuon” cut [42].

---

<sup>3</sup>There is still no identification cut required for the final state pion.

<sup>4</sup>The “BBDT” stands for Boosted Bonsai Decision Tree, more information can be found here [41], as it is not incredibly pertinent to this work. This is due to the fact that the code implementing these criteria is a centralized production in the experiment and thus cannot be changed on a whim.

Table 3.4: List of triggers used in this analysis.

Trigger Level	Triggers Used
Level-0	L0MuonTOS
HLT1	HLT1TrackAllL0DecisionTOS HLT1TrackMuonDecisionTOS HLT1SingleMuonHighPTDecisionTOS
HLT2	HLT2TopoMu2BodyBBDTDecisionTOS HLT2TopoMu3BodyBBDTDecisionTOS HLT2TopoMu4BodyBBDTDecisionTOS HLT2IncPhiDecisionTOS

### 3.3 Analysis Method

There are several parts to this analysis: signal extraction, muon correction for identification and trigger, particle tracking corrections, and background corrections. For the signal extraction and muon ID and trigger corrections, the datasets are fitted in fine kinematic binning as a function of muon momentum, then the final answer,  $A_\mu^c$ , is a weighted result of each individual fit. The particle tracking corrections are done in bins of muon momentum only, with the final measurement,  $A_{track}$ , being a weighted average of each momentum bin. The background correction,  $A_{bkg}$  is done in the same way as the tracking correction. For all parts, the analysis is done with magnet up polarity and magnet down polarity data treated as two separate datasets. The final result,  $A_{meas}$ , is then calculated, with the magnet up and down polarities averaged together.

### 3.4 Signal Extraction

There are two ways that the yields are extracted in this work. Primarily this is done by performing a one-dimensional maximum-likelihood fit to the mass of the  $D^+$  ( $D^-$ ) and the  $D_s^+$  ( $D_s^-$ ), to include all regions of background on the sides of the  $D_s$  mass peak. A second way is by performing a two-dimensional maximum-likelihood fit of the mass and natural

logarithm of the IP (lnIP) of  $D_s^\pm$ .

All fits are done in five bins of muon momentum (standard in this work):  $6 \leq p < 20$  GeV,  $20 \leq p < 30$  GeV,  $30 \leq p < 40$  GeV,  $40 \leq p < 50$  GeV and  $50 \leq p < 100$  GeV. This binning is chosen thusly because it gives enough detail to understand any dependencies as a function of muon momentum, which gives a good handle on the  $B_s^0$  candidate dependencies and of course  $D_s$  momentum dependencies, yet still each bin has enough events to provide reasonable fits of good  $\chi^2/NDF$ .

Within the two fitting methods is an internal check for robustness of each fit. This is done by fitting the opposite sign charm mesons,  $D_s^+$  and  $D_s^-$ , simultaneously, which means keeping all signal parameters the same between the two charm mesons but letting the background parameters float separately, from now on called *simultaneous fitting*. Then they are fitted separately, allowing all parameters to float and differ separately, from here on called *separate fitting*.

### 3.4.1 One Dimensional Fitting

For this method, the  $D$  and  $D_s$  mass plots are fit with a double Gaussian probability distribution function (P.D.F.) with a common mean between the two Gaussians for each peak. This is described below by

$$f(m) = f_1 \text{Gauss}(\mu_1, \sigma_1, m) + (1 - f_1) \text{Gauss}(\mu_1, \sigma_2, m), \quad (3.6)$$

where  $m$  indicates the observable, invariant mass  $m(KK\pi)$ ,  $\text{Gauss}(\mu, \sigma, m)$  is the Gaussian function of  $m$  with mean as  $\mu$ , width as  $\sigma$  and  $f_1$  a constant.

The background is characterized by a second order Chebychev polynomial P.D.F.. Fits with linear background shape have been performed as well and have proven to be inadequate, however they are considered in the systematic uncertainties.

Again, these fits are completed in the five muon momentum bins, separately and simul-

taneously. In figure 3.1, the four plots are fit results from separate and simultaneous fitting over the muon momentum spectrum of  $6 \leq p < 100$  GeV and muon transverse momentum spectrum of  $1.5 \leq p_T < 10$  GeV, which is the entire set of data considered. From these fit results and the quantitative results listed in table 3.6, it is clear that both methods are consistent with one another, however the better and more robust fits are produced from the separate method. Henceforth, the separate fit method results will only be shown.

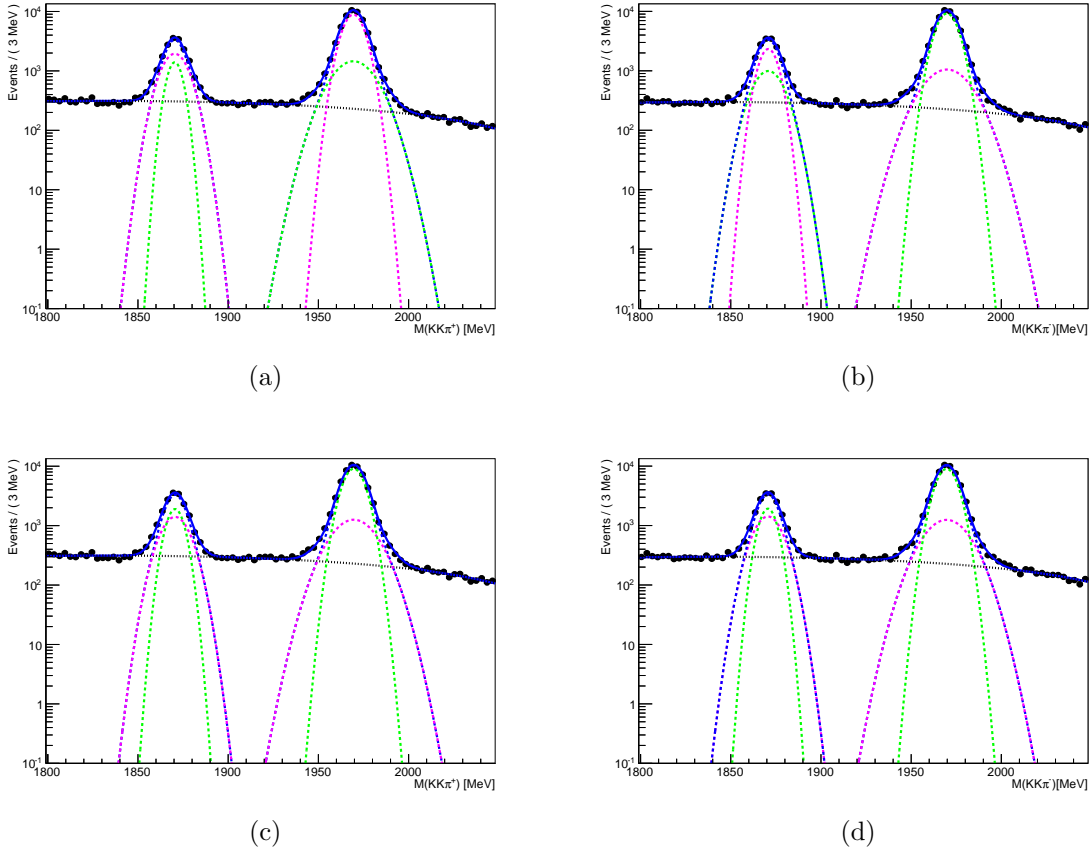


Figure 3.1: Two plots of the overall muon momentum from 6–100 GeV. (a) and (b) show the separate fit method results for  $D_s^+$  and  $D_s^-$  respectively. (c) and (d) show the simultaneous fitting between  $D_s^+$  and  $D_s^-$ . Results are shown for magnet down polarity only. The solid blue curve is the overall fit, the green and magenta dotted lines are the two Gaussians that share a mean and the black dashed line is the background.

Table 3.5: A listing of the parameters for the one dimensional fits in overall muon momentum region for both magnet down and magnet up.

Magnet Down	$D_s^+$	$D_s^-$
$\mu_1 = \mu_2$	$1969.41 \pm 0.03$	$1969.82 \pm 0.03$
$\sigma_1$	$5.56 \pm 0.08$	$4.96 \pm 0.43$
$\sigma_2$	$10.90 \pm 0.42$	$11.89 \pm 0.60$
$f$	$0.76 \pm 0.03$	$0.81 \pm 0.02$
$\sigma_{mean}$	$6.86 \pm 0.18$	$6.27 \pm 0.39$
Magnet Up	$D_s^+$	$D_s^-$
$\mu_1 = \mu_2$	$1969.90 \pm 0.04$	$1969.57 \pm 0.04$
$\sigma_1$	$5.47 \pm 0.12$	$9.84 \pm 0.52$
$\sigma_2$	$10.66 \pm 0.62$	$6.78 \pm 0.42$
$f$	$0.75 \pm 0.04$	$0.31 \pm 0.05$
$\sigma_{mean}$	$6.79 \pm 0.27$	$7.72 \pm 0.36$

Table 3.6: Signal yields for magnet down in the entire muon momentum region considered only (6 – 100 GeV) for one-dimensional fits (after  $L0p_T > 1.640$  GeV).

$D_s$ Charge	Fit Type	Signal Yield	Background Yield	$\chi^2/NDF$
$D_s^+$	Separate	$56400 \pm 263$	$21746 \pm 223$	1.26
$D_s^-$	Separate	$55809 \pm 271$	$21124 \pm 246$	1.58
$D_s^+$	Simultaneous	$56391 \pm 258$	$21769 \pm 208$	2.00
$D_s^-$	Simultaneous	$55785 \pm 257$	$21147 \pm 206$	2.50

### Fitting in Different Kinematic Binning

Included in the one-dimensional fitting method is an individual finer kinematic binned fitting procedure. This is necessary to do in conjunction with the muon momentum bins to determine if there are dependencies on other quantities. Particularly, there is a  $p_T$ -kick that charged particles receive when traveling in the detector. This affects where the final state particles traverse the detector and is likely to create asymmetries. Similarly, particles in the detector bend more in one direction due to the magnetic field. For example, muons hitting the third muon station (MS3) are dispersed differently depending on their momenta at that point in the detector. In the two left-hand plots of figure 3.2,  $\mu^-$  particles are pushed left or

right with respect to the beam pipe depending on the magnetic field polarity (top left plot is magnet up and bottom left plot is magnet down). In this same figure, the left plots illustrate the distribution of muons hitting MS3 when they are measured to have low momenta, while the right plots illustrate the same quantity but for high momenta. The spread is quite different depending on the momentum of the muon and so it is very important to consider this in the final measurement. Figure 3.3 illustrates the same scatter plots for  $\mu^+$ . The structure seen, acceptance hole and vertical/horizontal lines, is present also in the calibration sample and corresponds to region where the overlap between chambers is not perfect. For example, at  $x \sim 2700$  mm the overlap between chambers three and four is partial. A study of applying special cuts to these specific areas of high asymmetry (near 100%) has been done and reduces the sample by almost 10%. However, in this study, the resulting raw asymmetry is changed by 0.01% with these cuts, thus it is of small consequence not to introduce them (this is discussed in Appendix 5).

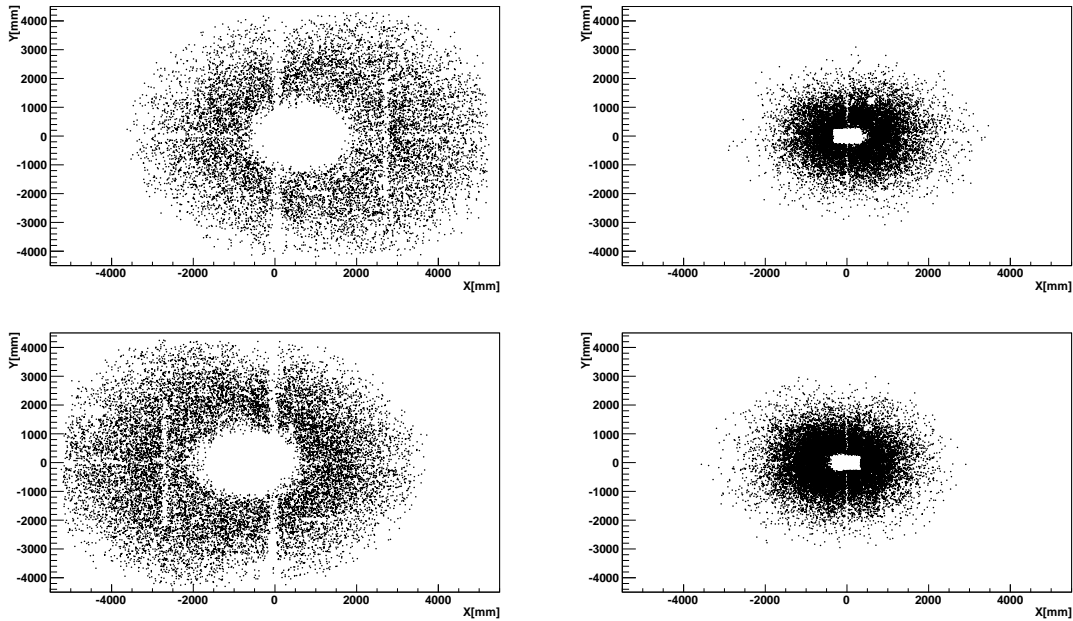


Figure 3.2: Two-dimensional scatter plots of muons in the third Muon Station. The top plots are magnet up with  $\mu^-$  and the bottom plots are magnet down with  $\mu^-$ . The left plots are the first muon momentum bin (6 – 20 GeV) and the right plots are the last and highest muon momentum bin (50 – 100 GeV).



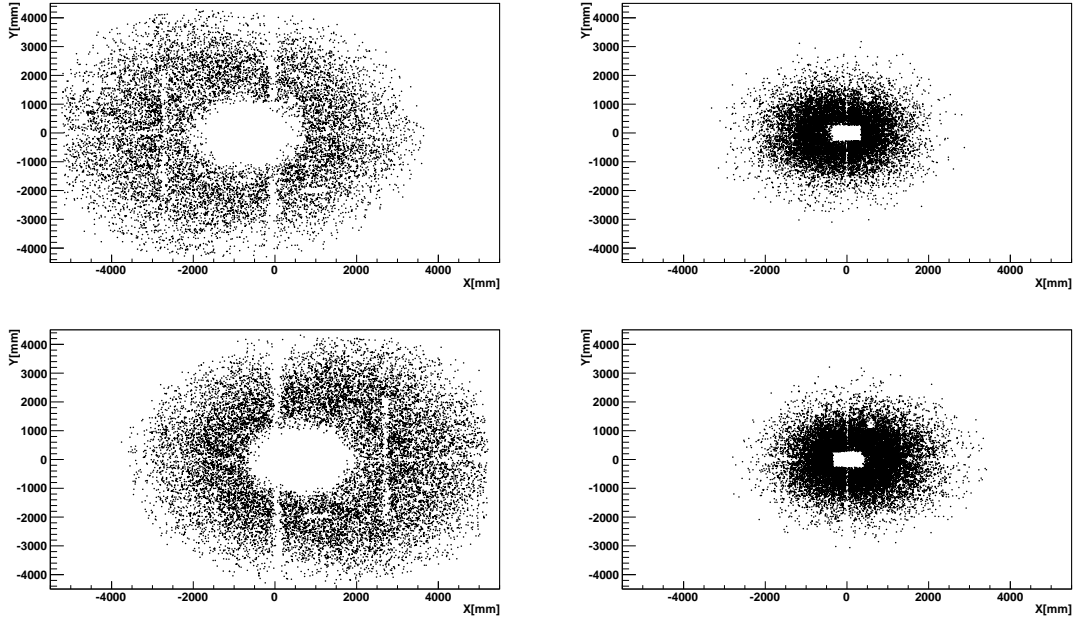


Figure 3.3: Two-dimensional scatter plots of muons in the third Muon Station. The top plots are magnet up with  $\mu^+$  and the bottom plots are magnet down with  $\mu^+$ . The left plots are the first muon momentum bin (6 – 20 GeV) and the right plots are the last and highest muon momentum bin (50 – 100 GeV).

Consequently, two sets of finer kinematic binning are implemented, in ten bins of muon  $q \times p_x$  vs  $p_y$  and in eight bins of muon  $q \times \varphi$  vs  $p_T$ , where  $q$  is the charge of the muon,  $-1$  or  $+1$ .  $p_x$  and  $p_y$  are the  $x$  and  $y$  components of the muon momentum,  $p_T$  is the transverse momentum and  $\varphi$  is the angle  $\tan^{-1}(p_y/p_x)$ .

For all fits, most P.D.F. parameters are taken from each muon momentum bin fit, discussed in the previous section, and constrained to be constant for each individual  $q \times p_x$  vs  $p_y$  and  $q \times \varphi$  vs  $p_T$  bin. The only items that are assigned to vary are the yields and the background shapes.

### $q \times p_x$ vs $p_y$ Fitting

Larger bins are focused on the outer region of the detector while smaller bins are focused on the inner region of the detector. The area near the beam pipe has a high density of hits so finer binning is necessary. Figure 3.4 illustrates the binning used to probe this space. Figure

3.5 illustrates the ten fits for the lowest muon momentum bin, where each fit represents a  $q \times p_x$  vs  $p_y$  bin. The corresponding yields to figure 3.5 are located in table 3.7. These

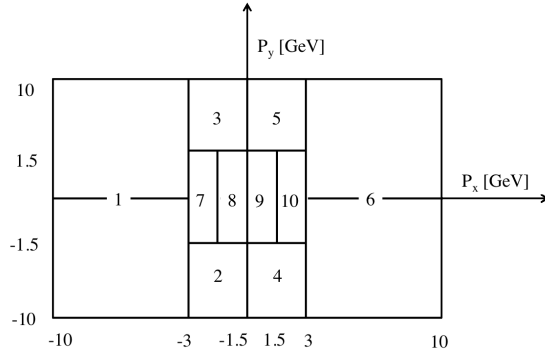


Figure 3.4: The  $q \times p_x$  vs  $p_y$  binning chosen in which the mass of the  $D_s$  is fitted.

are just one set of yields as a result of this one-dimensional fitting in five bins, only for the lowest muon momentum bin in  $q \times p_x$  vs  $p_y$  individual kinematic binning. Figure 3.6 shows the fits for each muon momentum bin over the entire  $q \times p_x$  vs  $p_y$  space. The remaining plots and corresponding yields can be found in Appendix 1.

### $q \times \varphi$ vs $p_T$ Fitting

All bins in the  $q \times \varphi$  vs  $p_T$  binning are the same size since the “pie-slice” bins illustrated in figure 3.7 allow for more evenly distributed events throughout the phase space. Table 3.8 refers to the  $p_T$  bins chosen to fit the masses with respect to the  $\varphi$  variable.

Figure 3.8 represents the fits in all eight fine kinematic bins. The corresponding yields to figure 3.8 are located in table 3.9. These are just one set of yields as a result of this one-dimensional fitting in five bins, only for the lowest muon momentum bin in  $q \times p_x$  vs  $p_y$  individual kinematic binning. The remaining plots and corresponding yields can be found in Appendix 2.

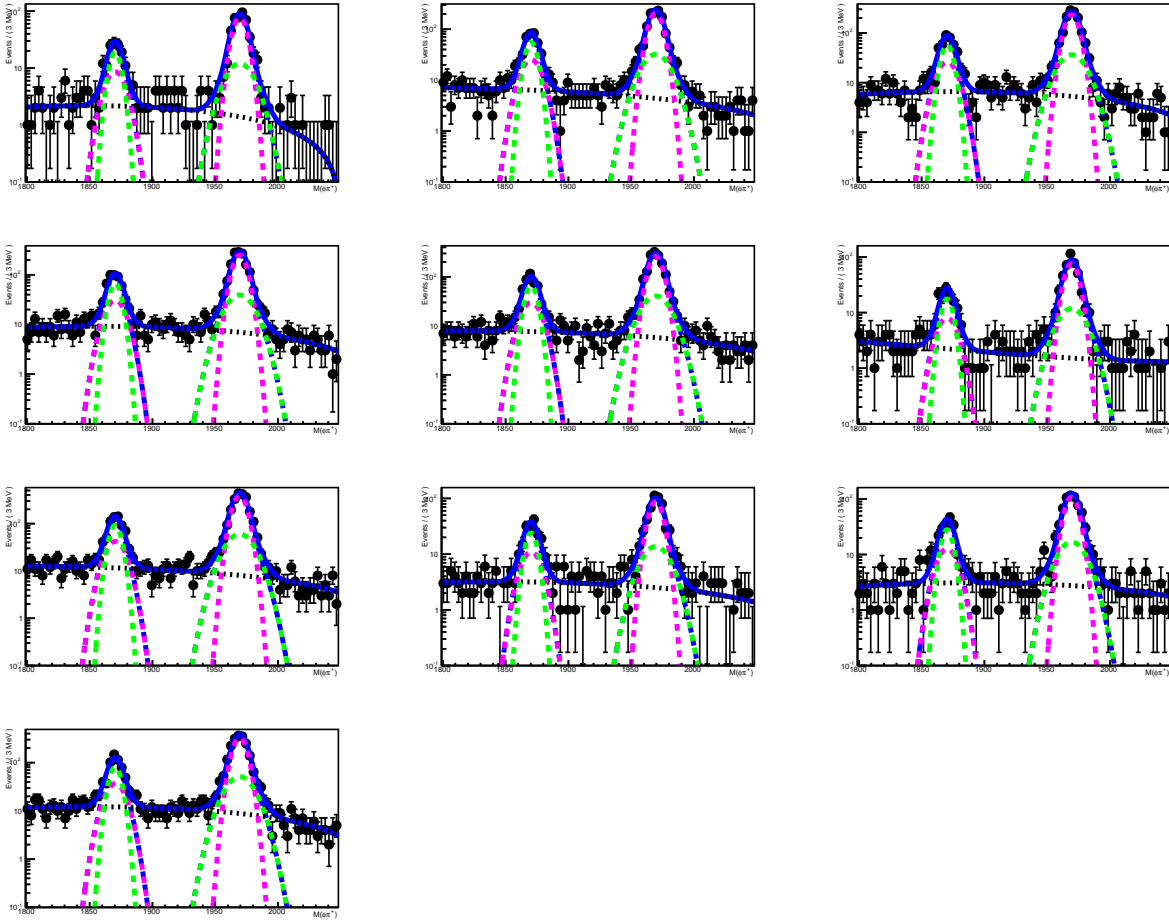


Figure 3.5: From left to right starting from 1 ending with 10, these are the resulting fits for each bin in  $q \times p_x$  vs  $p_y$ . These fits are for the first muon momentum bin 6 – 20 GeV for magnet down only. The black points are data, the solid blue curve is the overall fit, the green and magenta dotted lines are the two Gaussians that share a mean and the black dashed line is the background.

### 3.4.2 Two Dimensional Fitting

The method of two-dimensional fitting originates from the  $b$ -hadron production fraction measurement [39] where the  $D_s$  mass and logarithm of the impact parameter ( $\ln\text{IP}$ ) of the  $D_s$  are fitted simultaneously. This was originally done to allow for very good separation between a specific type of background, namely prompt  $D_s$ , and signal. Prompt  $D_s$  events are produced directly from  $pp \rightarrow c\bar{c}X$  interactions, where the X denotes the sum over all possible final state particles. In the small amount of data used in the analysis of the  $b$ -hadron production

Table 3.7: Signal yields for magnet down in the lowest momentum (6 – 20 GeV) bin for the individual kinematic bins of  $q \times p_x$  vs  $p_y$  only.

Fitted Yields	$q \times p_x$ vs $p_y$ Bin	Magnet Down
$D_s^+ \mu^-$	1	$446 \pm 22$
	2	$1192 \pm 36$
	3	$1355 \pm 39$
	4	$1458 \pm 40$
	5	$1512 \pm 41$
	6	$441 \pm 22$
	7	$2229 \pm 50$
	8	$510 \pm 24$
	9	$627 \pm 27$
	10	$1906 \pm 46$
$D_s^- \mu^+$	1	$402 \pm 21$
	2	$1275 \pm 38$
	3	$1208 \pm 37$
	4	$1464 \pm 40$
	5	$1503 \pm 41$
	6	$409 \pm 21$
	7	$1936 \pm 46$
	8	$520 \pm 24$
	9	$613 \pm 27$
	10	$1893 \pm 46$

Table 3.8: List of kinematic binning for the fine  $q \times \varphi$  vs  $p_T$  bins.

$p_T$	$p$
1.5 – 2.0 GeV	6 – 20 GeV
2.0 – 10 GeV	20 – 30 GeV
	30 – 40 GeV
	40 – 50 GeV
	50 – 100 GeV

fraction, this was necessary as the background is very high. In this work the background is very well suppressed and so this technique is not completely necessary. However it provides a complimentary confirmation of the one-dimensional fit method’s reliability.

In the two-dimensional fits here, there are three components:  $D_s$  signal coming from a  $B_s^0$  (DfB), prompt  $D_s$  coming from the primary vertex or nearby (Prompt), and false  $D_s$

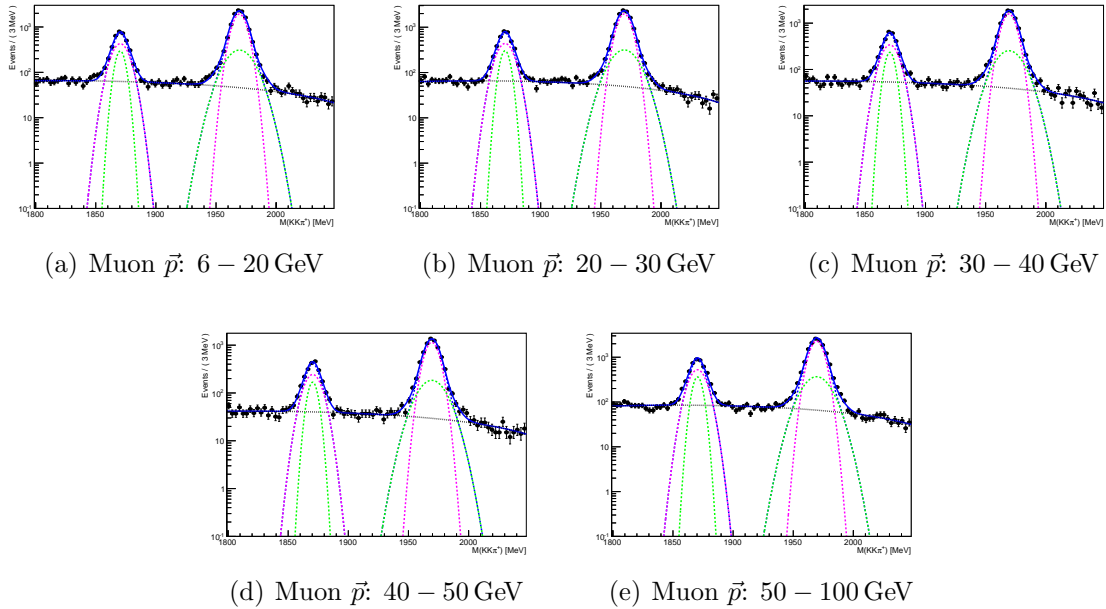


Figure 3.6: Five muon momentum bin fits of the  $D_s^+$  mass. Only magnet down polarity results are shown. The black points are data, the solid blue curve is the overall fit, the green and magenta dotted lines are the two Gaussians that share a mean and the black dashed line is the background.

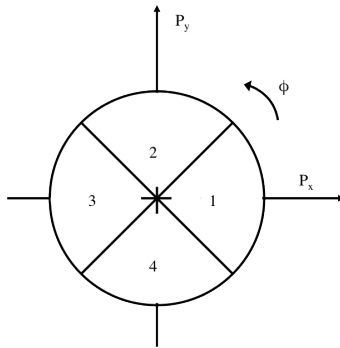


Figure 3.7: A drawing to show the bins in the  $\varphi$  variable chosen.

combinations (BKG). Each component has its own shape, all of which are taken from data, except for the signal shape, which is based on signal Monte Carlo. In the case of the Prompt, the shape is taken from a special stripped sample which is discussed in section 3.7.

These fits are completed in all five muon momentum bins as well as in overall muon momentum from 6 – 100 GeV. The individual finer kinematic binned fitting is not applied

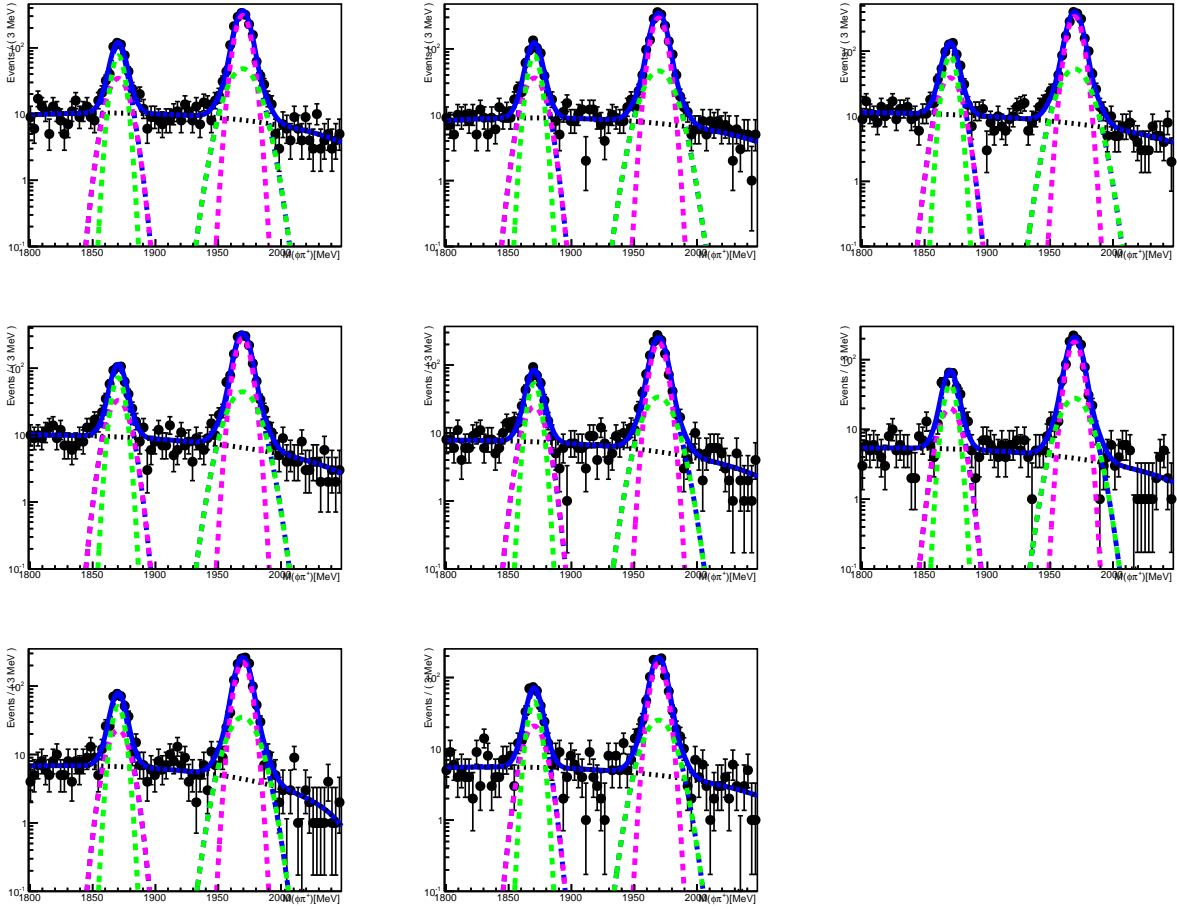


Figure 3.8: From left to right, starting from 1 and ending with 8, these are the resulting fits for each bin in  $q \times \varphi$  vs  $p_T$ . Shown is only fits for the lowest muon momentum bin, 6–20 GeV, for magnet down. The black points are data, the solid blue curve is the overall fit, the green and magenta dotted lines are the two Gaussians that share a mean and the black dashed line is the background.

here as it is much more difficult to fit with so many parameters<sup>5</sup> and converge on a final result. The same cross-check of separate and simultaneous fitting is applied in these two-dimensional fits. For separate fits, all parameters are left floating between the two signed charm meson. For simultaneous fitting the mass shapes are kept the same as are the prompt hIP shapes between the  $\phi^+\pi^-$  and the  $\phi^-\pi^+$ . However, once again the separate fit method provides a better match to the data as compared with the simultaneous fitting procedure.

<sup>5</sup>There are 15 parameters for each sign of  $D_s$ .

Table 3.9: Signal yields for magnet down in the lowest momentum (6 – 20 GeV) bin for the individual kinematic bins of  $q \times \varphi$  vs  $p_T$ .

Fitted Yields	$q \times \varphi$ vs $p_T$ Bin	Magnet Down
$D_s^+ \mu^-$	1	$1791 \pm 45$
	2	$1714 \pm 44$
	3	$1986 \pm 47$
	4	$1651 \pm 43$
	5	$1253 \pm 37$
	6	$1039 \pm 34$
	7	$1306 \pm 38$
	8	$936 \pm 33$
$D_s^- \mu^+$	1	$1722 \pm 44$
	2	$1696 \pm 44$
	3	$1741 \pm 44$
	4	$1713 \pm 43$
	5	$1246 \pm 37$
	6	$994 \pm 33$
	7	$1167 \pm 36$
	8	$942 \pm 33$

Thus the separate fit will only be used in the final result. However, the simultaneous results will be considered in systematic error evaluation.

The DfB and Prompt mass P.D.F.s are both double Gaussians where the peaks share a common mean. The BKG mass P.D.F. is a second order Chebychev polynomial. All three components' lnIP P.D.F. are single bifurcated Gaussians. Figure 3.9 shows four fit results. See Appendix 3 for the remaining plots. The wrong sign (WS) decays are also fit, where the WS decay is when the  $\pi$  from the  $D_s$  and the  $\mu$  have the same sign. The WS yields are not subtracted from the signal as this background is not asymmetric, instead the WS fits are used to give a quick handle on this background. Currently, this is at the level of sub-1%. An example of WS fits is in figure 3.10. The WS fits also give some idea of the prompt shape as in these fits the signal and the prompt are well separated. Table 3.10 has listed the yields as a result of two-dimensional fitting in five bins summed. The raw yields between the  $D_s^+$  and  $D_s^-$  results are not very far from one another, which suggests a small raw asymmetry.

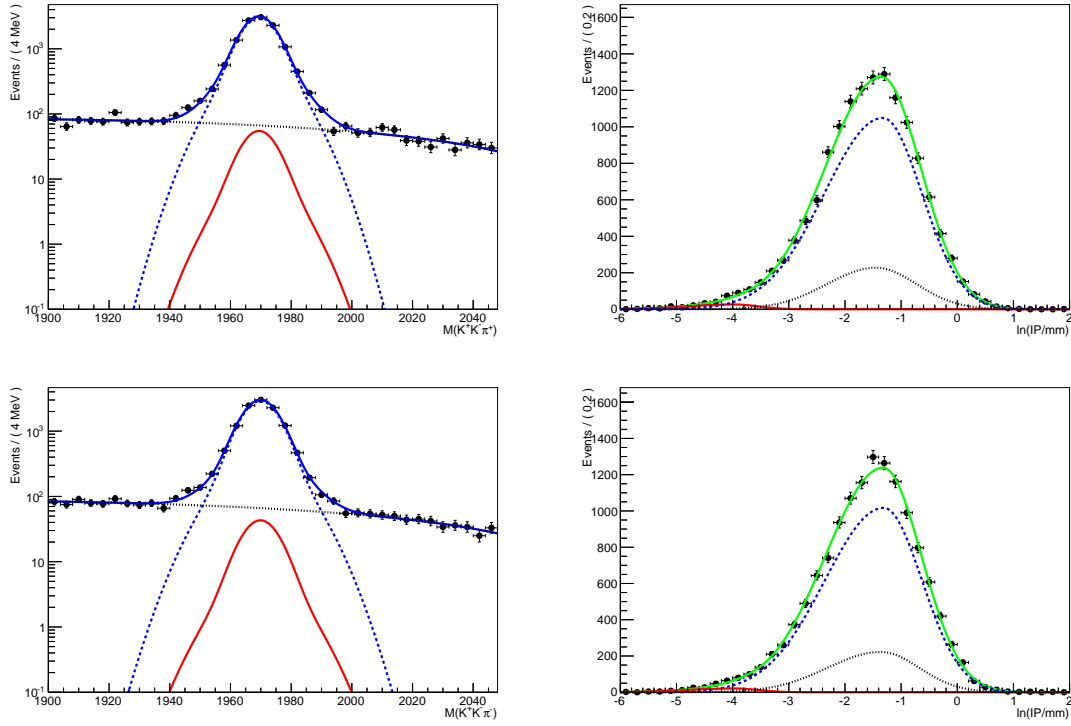


Figure 3.9: Two-dimensional fit results for magnet down data in the muon momentum bin 6 – 20 GeV. The blue dotted line is  $D_s$  signal (DfB), the red solid line is the prompt  $D_s$  background, the black dashed line is false  $D_s$  background (BKG). The top row represents fits for  $D_s^+$  and the bottom for  $D_s^-$ .

Table 3.10: Signal yields for overall fits for muon momentum range 6 – 100 GeV for 2D fits.

Fitted Yields	Magnet Down	Magnet Up
$D_s^+ \mu^-$	$55468 \pm 290$	$38788 \pm 248$
$D_s^- \mu^+$	$54805 \pm 306$	$39314 \pm 238$

From these two-dimensional fits, the prompt background level is calculated. This background is of the order of 1 – 1.5% of the total  $D_s$  yield. The results for magnet down and up in bins of muon momentum are listed in table 3.11 and 3.12 respectively. Since the measured production asymmetry of  $D_s^+ - D_s^-$  is  $(-0.33 \pm 0.22 \pm 0.10)\%$  [43], the total effect of this prompt background on  $a_{\text{sl}}^s$  is  $\sim 3 \times 10^{-5}$ . This is much smaller than the precision expected of this measurement.



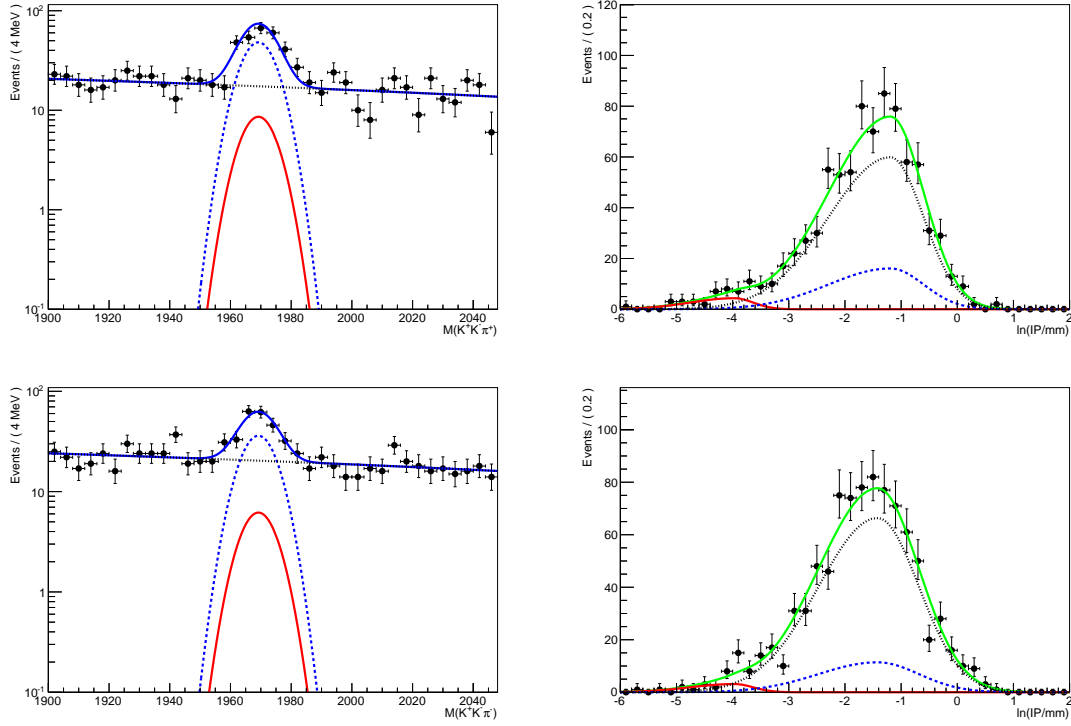


Figure 3.10: Two-dimensional fit results for wrong sign magnet down data in the muon momentum bin 6 – 20 GeV. The blue dotted line is  $D_s$  signal (DfB), the red solid line is the prompt  $D_s$  background, the black dashed line is false  $D_s$  background (BKG). The top row represents fits for  $D_s^+$  and the bottom for  $D_s^-$ .

Table 3.11: Percentages of prompt contamination in signal for magnet down.

$D_s$ Sign	Muon Momentum Bin	Prompt Percentage of Total $D_s$ Sample [%]
$D_s^+$	1	$1.8 \pm 0.2$
	2	$1.3 \pm 0.2$
	3	$1.1 \pm 0.2$
	4	$1.5 \pm 0.2$
	5	$1.1 \pm 0.1$
	Overall	$1.4 \pm 0.1$
$D_s^-$	1	$1.7 \pm 0.2$
	2	$1.0 \pm 0.1$
	3	$1.3 \pm 0.2$
	4	$1.2 \pm 0.2$
	5	$1.2 \pm 0.1$
	Overall	$1.3 \pm 0.1$

Table 3.12: Percentages of prompt contamination in signal for magnet up.

$D_s$ Sign	Muon Momentum Bin	Prompt Percentage of Total $D_s$ Sample [%]
$D_s^+$	1	$2.5 \pm 0.3$
	2	$1.3 \pm 0.2$
	3	$0.9 \pm 0.2$
	4	$0.8 \pm 0.2$
	5	$1.0 \pm 0.2$
	Overall	$1.4 \pm 0.1$
$D_s^-$	1	$1.9 \pm 0.3$
	2	$1.7 \pm 0.2$
	3	$1.5 \pm 0.2$
	4	$1.2 \pm 0.2$
	5	$1.1 \pm 0.2$
	Overall	$1.5 \pm 0.1$

Table 3.13: Raw asymmetries calculated from raw yields resulting from fits explained above for all fit methods.

Fit Method	Raw Asymm. MD [%]	Raw Asymm. MU [%]	Average [%]
1D $q \times p_x$ vs $p_y$	$-0.25 \pm 0.32$	$0.32 \pm 0.38$	$0.037 \pm 0.25$
1D $q \times \varphi$ vs $p_T$	$-0.27 \pm 0.32\%$	$0.29 \pm 0.38\%$	$0.014 \pm 0.25$
2D	$-0.67 \pm 0.38\%$	$0.52 \pm 0.47\%$	$-0.076 \pm 0.30$

### 3.5 Muon Detection Efficiency: ID and Trigger

Muon detection efficiencies are broken down into two groups, the first being the identification efficiency and the second being the trigger efficiency, including L0 and HLT1. For the measurement of these efficiencies two calibration samples have been used, as cross checks. One sample is a muon selected sample (MS, PID) utilizing a “tag and probe” method and the other sample being a kinematically chosen sample (KS, MB). Since the KS sample has the L0 fix applied (and the MS sample does not), which removes inherent asymmetry due to the detector’s physical asymmetry, only the KS sample is considered.

### 3.5.1 Criteria, Fitting and Results

The KS sample is used to determine the muon efficiency ratio of the trigger and the identification done with a  $J/\psi \rightarrow \mu\mu$  sample. This sample is taken from the *BeautyToCharm* hadron stripping line where  $J/\psi$  combinations in events including trigger selected hadronic B decays are included. The trigger selection is applied to the  $b$ -hadron signal and then it is kinematically required that the other  $b$ -hadron decays into a  $J/\psi$ , which then decays into a  $\mu^+\mu^-$  pair (“TOS” on L0 and HLT1 required of the  $b$ -hadron). This method removes any possible bias that may come from the trigger. The offline cuts applied to the two muon tracks are listed in table 3.14.

Table 3.14: Quality and background suppression cuts applied to the two  $\mu$  candidate tracks to select a minimum bias  $J/\psi$ , for the KS (a.k.a. MB) sample.

Variable	Requirement
$p$	$< 3 \text{ GeV}$
$p_T$	$< 1.2 \text{ GeV}$
Track $\chi^2$	$< 3$
IP $\chi^2$	$> 4$
$\eta$	$\geq 2$ and $< 5$
$m(\mu^-\mu^+)$	Within 150 MeV of $J\psi$ mass
Vertex $\chi^2/NDF$	$< 11$
Event Multiplicity (Long Tracks)	$< 250$
CloneKiller	True
“Probe” $\mu$	Required TIS on all lines
“Tag” $\mu$	Required to pass muon ID cuts (same as signal channel)

Studies on the momentum and transverse momentum spectra are completed to assess the similarities or disparities between the signal and this sample. Figures 3.11 and 3.12 illustrate the muon momentum and transverse momentum detected in the detector from three data samples: signal, KS and MS. The three samples are in good agreement with one another. However it is evident that there are some discrepancies. These differences evoke additional reasoning to execute fits in binning of muon momentum as well as fine kinematic binning in

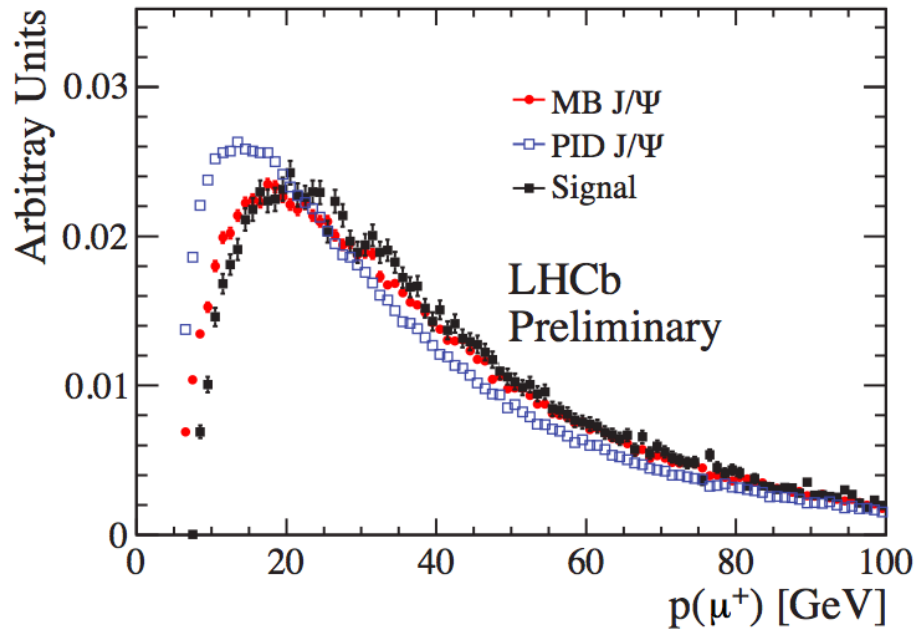


Figure 3.11: Muon momentum plots of the two muon specific samples illustrated in red and blue, and signal data in black.

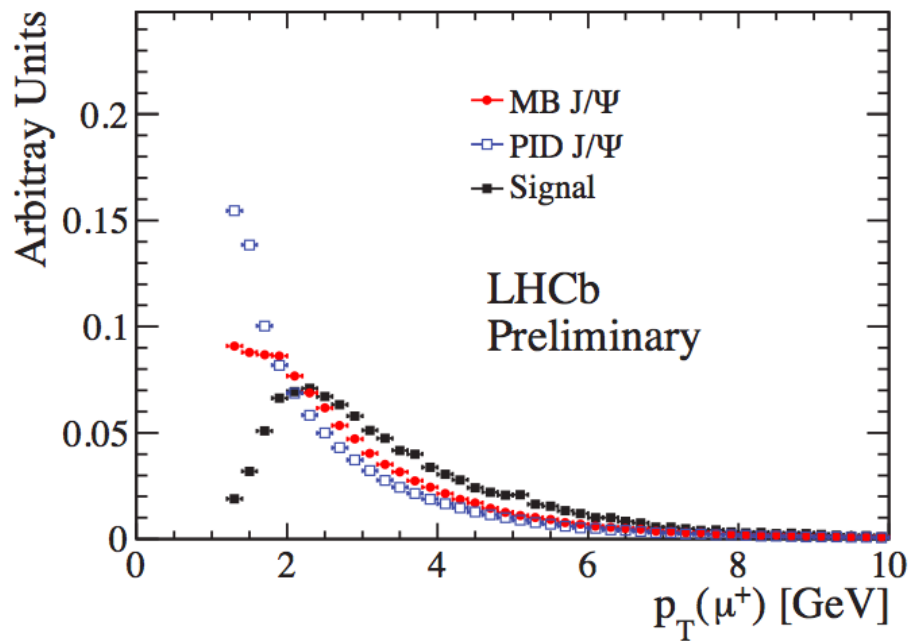


Figure 3.12: Muon transverse momentum plots of the two muon specific samples illustrated in red and blue, and signal data in black.

$q \times p_x$  vs  $p_y$  and  $q \times p_T$  vs  $\varphi$ .

The KS sample is thus divided into two groups, one that passes a certain criteria and one that fails it. For instance, the ratio between the  $J/\psi$  signal yields for the “probe” muons passing the identification criteria and the yields in the original sample gives the measurement of the identification efficiency. To get these yields, a one-dimensional fit on the  $J/\psi$  resonance is done on both groups of the sample. The shape used to model the resonance is a double Crystal Ball P.D.F. [44], and a linear function is used to model the background shape. The results for one fit are shown in figure 3.13, with yields of overall muon momentum fit located in table 3.15. Similar methods are used to determine the other efficiencies, such as the L0 and HLT2 trigger efficiencies (see Appendix 4). Table 3.16 lists all the efficiencies for the

Table 3.15: Signal yields for the KS sample, where muons are required to have a momentum between 6 – 100 GeV and transverse momentum of 1.5 – 10 GeV.

Muon Charge	Magnet Up	Magnet Down
KS Sample		
$\mu^+$	$633931 \pm 2314$	$906517 \pm 2766$
$\mu^-$	$632411 \pm 2377$	$903825 \pm 2687$
after TIS on probe $\mu$		
$\mu^+$	$256840 \pm 1502$	$372268 \pm 2124$
$\mu^-$	$261667 \pm 1454$	$363036 \pm 1809$
after ID required on tag $\mu$		
$\mu^+$	$246770 \pm 826$	$357448 \pm 987$
$\mu^-$	$252282 \pm 844$	$350892 \pm 952$

muons for magnet up and down in the first muon momentum bin, for the fine  $q \times p_x$  vs  $p_y$  binning method. The remaining momentum bins are in Appendix 1. The values for the muon corrected asymmetry for magnet up and down for both individual fine kinematic bin methods are listed in table 3.17. Clearly the asymmetry in the yields with muon corrections is very small. However, there are more asymmetries to determine whether the final answer deviates from zero.

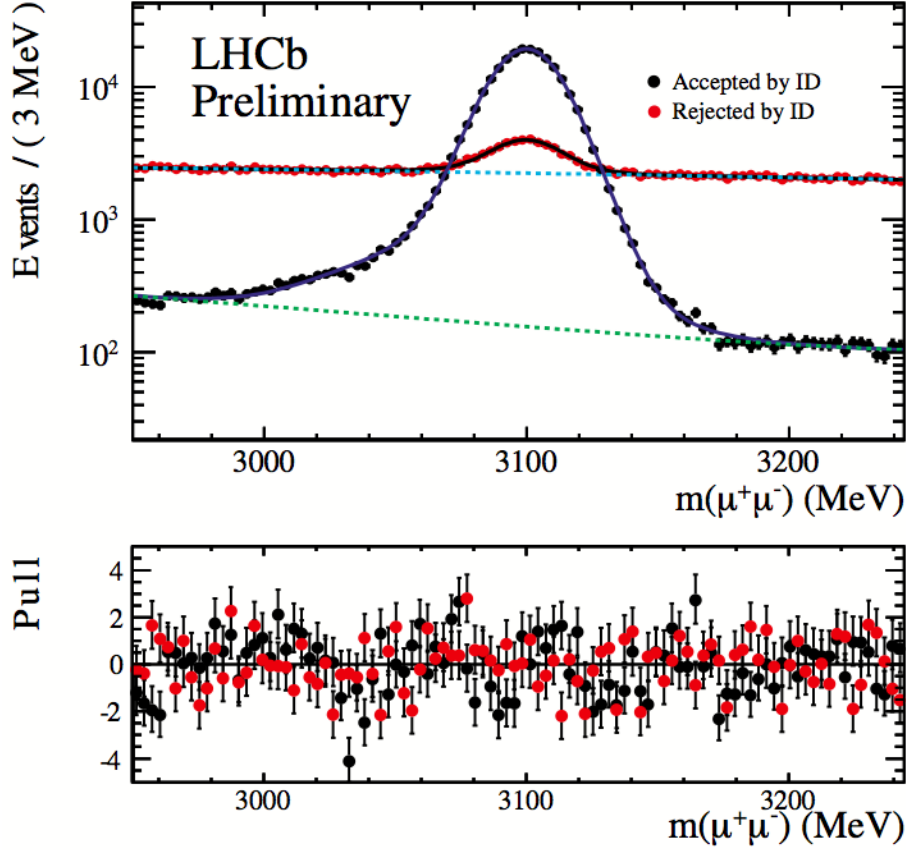


Figure 3.13: The invariant mass of the  $\mu^+ \mu^-$  pair for the KS sample of  $J/\psi$  events. Probe muons are required to pass TIS, while tag muons are required to pass ID cuts. The red points represent the events rejected by the muon ID requirements and the black represent those accepted by this requirement.

### 3.6 Final State Particle Tracking Corrections

The pion detection efficiency is also crucial to this work because any asymmetries that are inherent in the detector affects the final asymmetry measurement, which is very sensitive to these issues.

Asymmetry measurements in general, include cancellations of efficiencies that take place between positively and negatively charged hadrons. However it is enough to measure the relative efficiency for detecting  $\pi^+$  to  $\pi^-$ , denoted as  $\epsilon(\pi^+)/\epsilon(\pi^-)$ , as a function of pion momentum.

This measurement is done using data from LHCb, with checks from MC. The method has

Table 3.16: Overall muon efficiency table using KS sample after the operation  $q \times p_x$  vs  $p_y$  for muon momentum bin 6 – 20 GeV.

	Mag Up		Mag Down	
$q \times p_x$ vs $p_y$ bin	$\epsilon(\mu^+)$	$\epsilon(\mu^-)$	$\epsilon(\mu^+)$	$\epsilon(\mu^-)$
1	$65.6 \pm 1.7$	$62.4 \pm 1.7$	$66.9 \pm 1.4$	$67.7 \pm 1.4$
2	$55.6 \pm 0.8$	$53.3 \pm 0.8$	$49.0 \pm 0.7$	$47.2 \pm 0.7$
3	$56.3 \pm 0.8$	$52.3 \pm 0.8$	$50.1 \pm 0.7$	$50.0 \pm 0.7$
4	$47.7 \pm 0.8$	$49.4 \pm 0.8$	$54.0 \pm 0.7$	$54.8 \pm 0.7$
5	$48.7 \pm 0.8$	$50.2 \pm 0.8$	$55.5 \pm 0.7$	$53.4 \pm 0.7$
6	$69.8 \pm 1.7$	$69.1 \pm 1.7$	$65.7 \pm 1.4$	$65.4 \pm 1.5$
7	$48.5 \pm 0.7$	$47.9 \pm 0.6$	$50.1 \pm 0.5$	$52.3 \pm 0.5$
8	$33.1 \pm 0.9$	$31.9 \pm 0.8$	$28.4 \pm 0.6$	$27.7 \pm 0.6$
9	$28.3 \pm 0.8$	$27.2 \pm 0.8$	$32.5 \pm 0.7$	$32.4 \pm 0.7$
10	$51.8 \pm 0.6$	$50.3 \pm 0.6$	$49.1 \pm 0.5$	$50.0 \pm 0.5$

Table 3.17: List of the asymmetries in the signal with muon identification and trigger, in the two fine kinematic binning methods used. Errors are only statistical.

Binning Method	Magnet Polarity	$A_\mu^C[\%]$
$q \times p_x$ vs $p_y$	Down	$-0.25 \pm 0.32$
	Up	$0.32 \pm 0.38$
	Average	$0.037 \pm 0.25$
$q \times p_T$ vs $\varphi$	Down	$-0.27 \pm 0.32$
	Up	$0.29 \pm 0.38$
	Average	$0.014 \pm 0.25$

been applied first in the measurement of the production asymmetry between  $D_s^+$  and  $D_s^-$  [43]. Using the decay sequence  $D^+ \rightarrow D^0 \pi_s$ ,  $D^0 \rightarrow K^- \pi^+ \pi^- \pi^+$  (and the charge conjugate), the efficiency ratio is measured. This decay can be fully reconstructed in the detector as each particle has a charge. However, since there are sufficient kinematic constraints, it is possible to detect the entirety of this decay, even if one pion is missed. Both approaches are utilized to determine the efficiency ratio, the former being the *fully reconstructed* method and the latter being the *partially reconstructed* method. The ratio of fully reconstructed to the partially

reconstructed decays, each defined as

$$\epsilon(\pi^+) = N_{full}(D^0\pi_s^+)/N_{part}(D^0\pi_s^+) \quad (3.7)$$

$$\epsilon(\pi^-) = N_{full}(\bar{D}^0\pi_s^-)/N_{part}(\bar{D}^0\pi_s^-), \quad (3.8)$$

where  $N_{partORfull}(D^0\pi)$  are the measured yields for the decay in question<sup>6</sup>, provides a measurement of the pion reconstruction efficiency. For the partially reconstructed sample, the mass  $m(K^-\pi^+\pi^-)$  and the mass difference  $m(\pi_s^+K^-\pi^+\pi^-) - m(K^-\pi^+\pi^-)$  are examined, and for the fully reconstructed sample the invariant mass  $m(K^-\pi^+\pi^-\pi^+)$  and the mass difference  $m(\pi_s^+K^-\pi^+\pi^-\pi^+) - m(K^-\pi^+\pi^-\pi^+)$  are examined.

### 3.6.1 Criteria, Fitting and Results

The data on which these studies are performed are different from the semileptonic data used for the main analysis. The data used are available in the stripping lines noted in table 3.1. This data sample must go through rigorous background suppression done by applying the stripping and offline selections. This information is located in Appendix 5. Shown here is only the data sample taken with magnet polarity down as an example to illustrate the fitting procedure and how the systematic uncertainty is estimated. The remaining fits and numbers are located in the same appendix. In order to determine the yields in equation 3.7, the mass and mass differences mentioned above must be examined. The method is done by performing a binned maximum likelihood fit to the right-sign (RS) and wrong-sign (WS)<sup>7</sup>  $D^0$  and  $\bar{D}^0$  distributions simultaneously. The signal P.D.F. used in fitting the partial reconstructed sample is procured from empirical data, by simply trying many shapes until one gives the best  $\chi^2/NDF$  result. The shapes are then tested on an MC sample, listed in table 3.26.

Figure 3.14 shows data distributions, denoted by black points, of the mass difference

---

<sup>6</sup>Includes the complex conjugate.

<sup>7</sup>RS is defined as  $D^{*\pm} \rightarrow D^0\pi_s^\pm$  and WS is defined as  $D^{*\pm} \rightarrow D^0\pi_s^\mp$ .



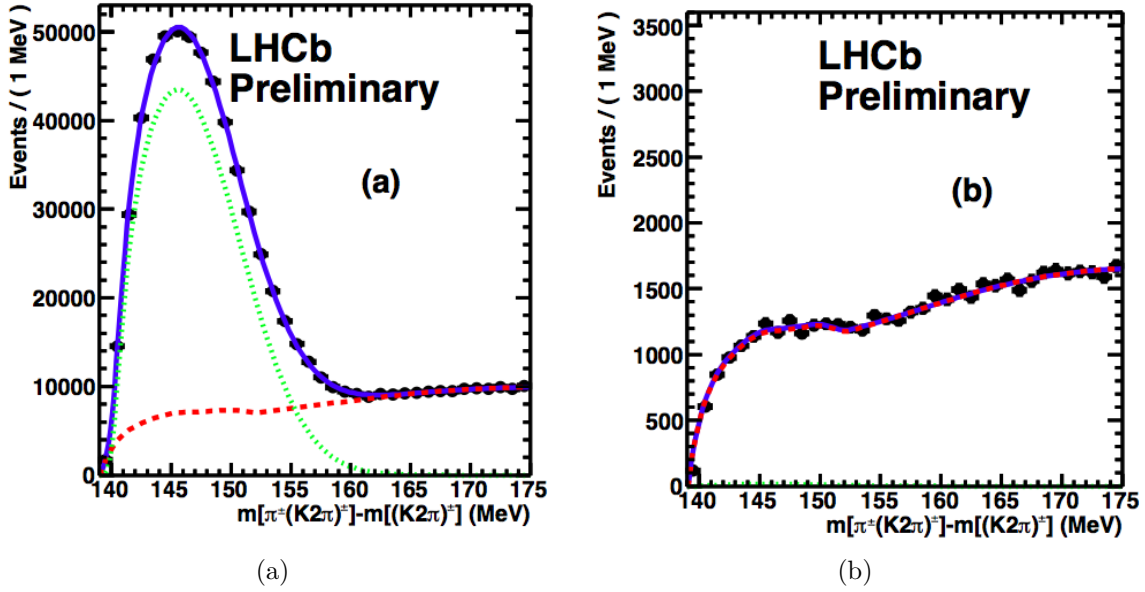


Figure 3.14: Distributions of mass differences  $m(\pi_s^+ K^- \pi^+ \pi^-) - m(K^- \pi^+ \pi^-)$  in partial reconstruction for (a) RS ( $D^{*+} \rightarrow D^0 \pi_s^+$ ) and (b) WS ( $D^{*+} \rightarrow D^0 \pi_s^-$ ) events.

for  $D^{*+}$ , defined as  $\Delta m_{part} = m(\pi_s^+ K^- \pi^+ \pi^-) - m(K^- \pi^+ \pi^-)$ . Figure 3.15 contains two plots of the same fitting procedure, but for the opposite signed charm meson,  $D^{*-}$ . The total P.D.F. is denoted by the thick blue lines on both plots of figures 3.14 and 3.15. The background is fit with a different P.D.F., which has been taken from the WS combinations, illustrated in the right-hand plots of figures 3.14 and 3.15. The signal shape of the mass difference  $\Delta m_{full} = m(\pi_s^+ K^- \pi^+ \pi^- \pi^+) - m(K^- \pi^+ \pi^- \pi^+)$  is a bit more complicated and is treated specially. Different P.D.F.s are used to fit the  $\Delta m_{full}$  distribution, the differences on the efficiency ratio are taken as the systematic uncertainty. Again to determine yields, a binned maximum likelihood fit to  $D^0$  and  $\bar{D}^0$ , both RS and WS, simultaneously is performed. Results of these full reconstruction fits is presented in figures 3.16 for  $D^{*+}$  and 3.17 for  $D^{*-}$ .

As stated earlier, it is necessary to obtain this ratio as a function of the missing pion's momentum and transverse momentum. This cannot be done by simply binning and fitting as is done for the signal extraction. In particular, for the partial reconstruction, a kinematic fitting method, different from above, is used to *infer* the missing pion's momentum. The

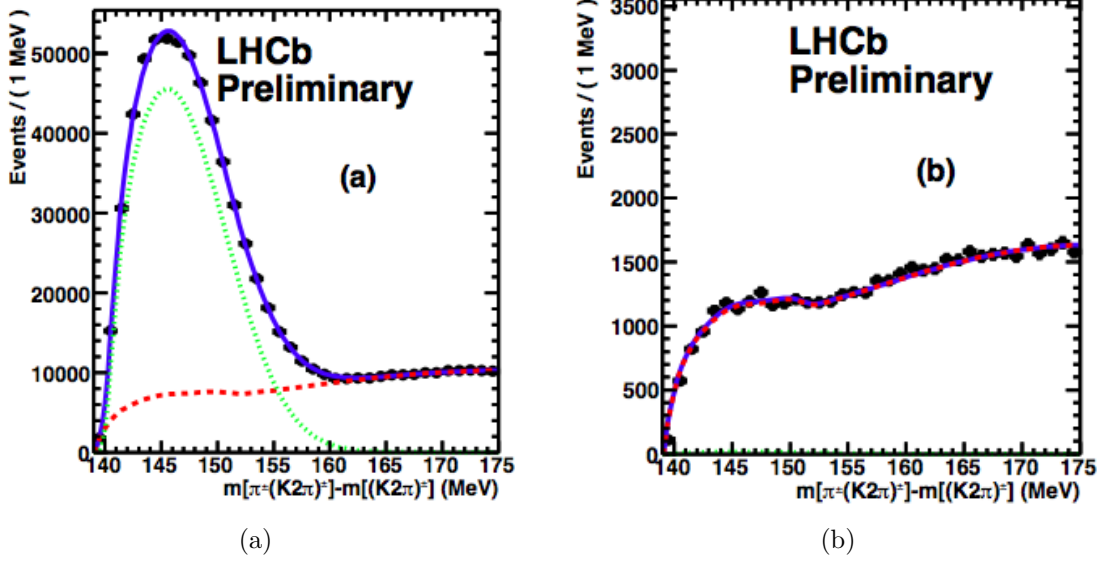


Figure 3.15: Distributions of mass differences  $m(\pi_s^- K^+ \pi^- \pi^+) - m(K^+ \pi^- \pi^+)$  in partial reconstruction for (a) RS ( $D^{*-} \rightarrow D^0 \pi_s^-$ ) and (b) WS ( $D^{*-} \rightarrow D^0 \pi_s^+$ ) events.

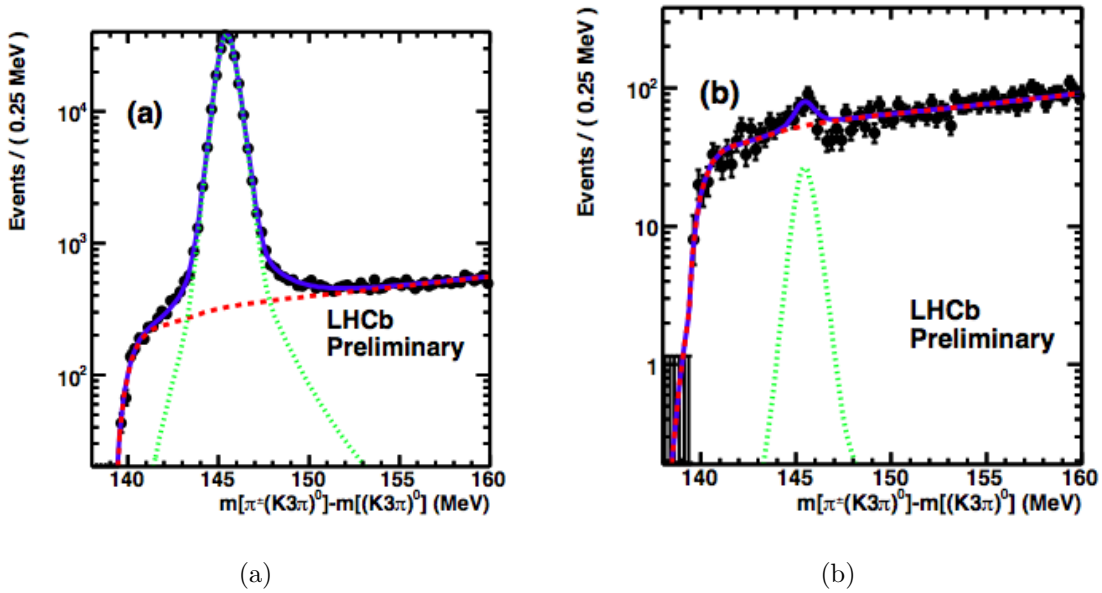


Figure 3.16: Distributions of mass differences  $m(\pi_s^+ K^- \pi^+ \pi^- \pi^+) - m(K^- \pi^+ \pi^- \pi^+)$  in partial reconstruction for (a) RS ( $D^{*+} \rightarrow D^0 \pi_s^+$ ) and (b) WS ( $D^{*+} \rightarrow D^0 \pi_s^-$ ) events.

inferred momentum is not exact so the efficiency versus momentum function is corrected by taking into account the finite momentum resolution via a process called “unfolding”.

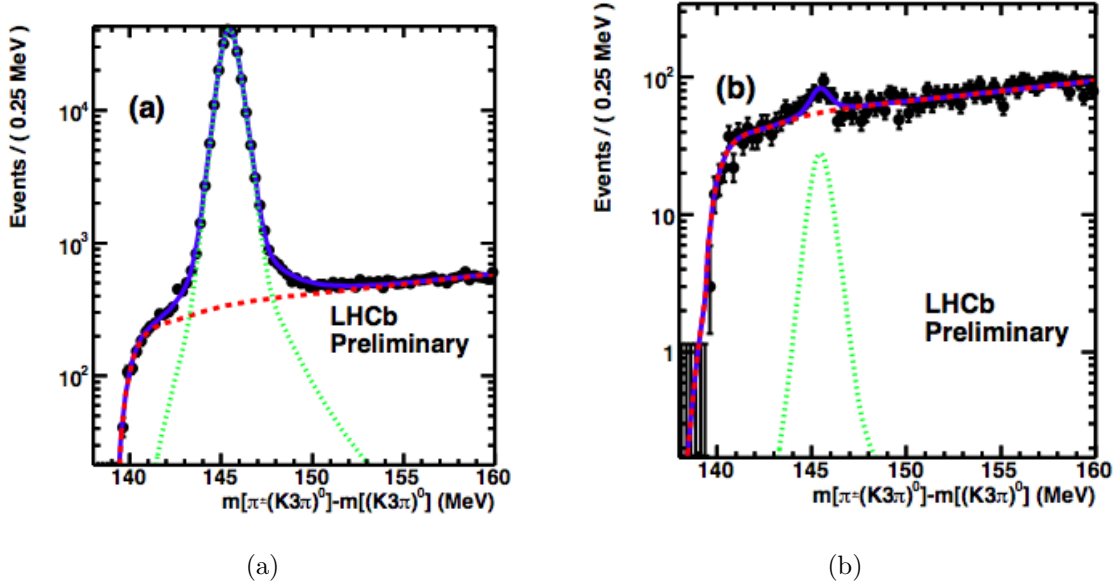


Figure 3.17: Distributions of mass differences  $m(\pi_s^- K^+ \pi^- \pi^+ \pi^-) - m(K^+ \pi^- \pi^+ \pi^-)$  in partial reconstruction for (a) RS ( $D^{*-} \rightarrow D^0 \pi_s^-$ ) and (b) WS ( $D^{*-} \rightarrow D^0 \pi_s^+$ ) events.

The unfolding matrix is estimated using the fully reconstructed sample. Comparing the measured momentum of a found pion that is then ignored and its momentum inferred using a kinematic fit. The absolute bin-by-bin pion-muon detection efficiency is determined, using

Table 3.18: A table of bins and the corresponding inferred and detected momentum ranges for the pion efficiencies.

Bin $i$ (or $j$ )	Range[GeV]
1	2-6
2	6-20
3	20-30
4	30-40
5	40-50
6	50-100

the following equation,

$$\epsilon(\pi^- \mu^+) = \frac{\sum_{i,j} N_{ij}(D_s^- \mu^+)}{\sum_{i,j} N_{ij}(D_s^- \mu^+) / \epsilon_{ij}}, \quad (3.9)$$

where  $i$  and  $j$  are the bins of muon momentum listed in table 3.18 for the muon sum and the

pion sum, respectively. These are not the standard muon momentum bins used through the analysis.  $N_{ij}(D_s^- \mu^+)$  is the signal yield in each of the 2D correlated bins mentioned earlier, and  $\epsilon_{ij} = \epsilon_i(\text{track}^+) \times \epsilon_j(\text{track}^-)$ , where  $\epsilon_i(\text{track}^+)$  and  $\epsilon_j(\text{track}^-)$  are measured using the full and partial reconstruction method above. The charge conjugate of equation 3.9 is

$$\epsilon(\pi^+ \mu^-) = \frac{\sum_{i,j} N_{ij}(D_s^+ \mu^-)}{\sum_{i,j} N_{ij}(D_s^+ \mu^-) / \epsilon_{ij}^*}, \quad (3.10)$$

where  $\epsilon_{ij}^* = \epsilon_i(\text{track}^-) \times \epsilon_j(\text{track}^+)$ . These results are located in table 3.19.

The final ratio of the efficiencies is shown in figure 3.18. It is clear that there are no dependences on the momentum of the undetected pion momentum. Figure 3.19 illustrates

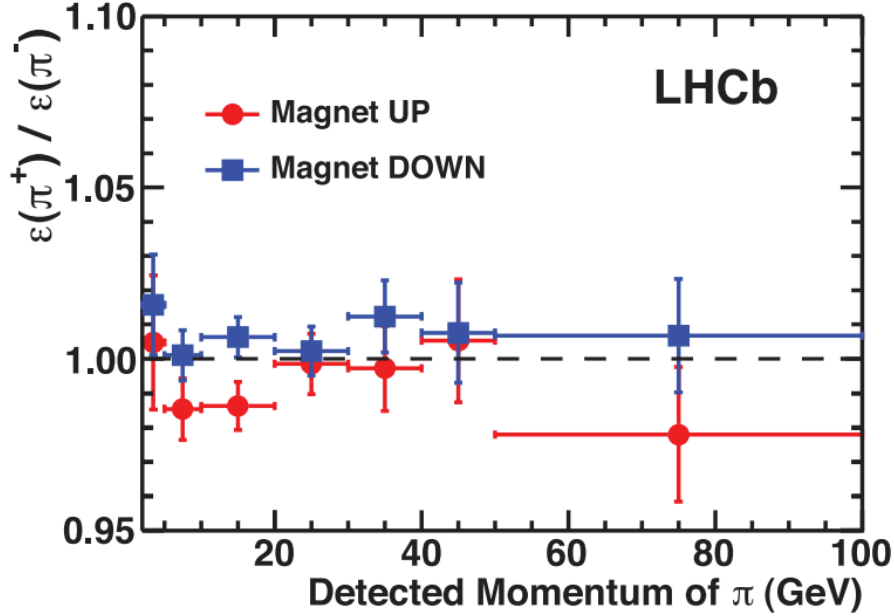


Figure 3.18: The detection efficiency ratio of  $\pi^+$  to  $\pi^-$  as a function of the undetected pion momentum. The red points are the data sample with magnet polarity up and the blue points are the data sample with magnet polarity down. The errors on the points are statistical only.

the dependence of the efficiency ratio on the undetected pion track's transverse momentum in bins of momentum. It is evident here as well that there is no dependence of the efficiency ratio on  $p_T$ . The result for the tracking asymmetry of the pion and muon is thus  $A^{\mu\pi} = (0.01 \pm 0.13)\%$ .

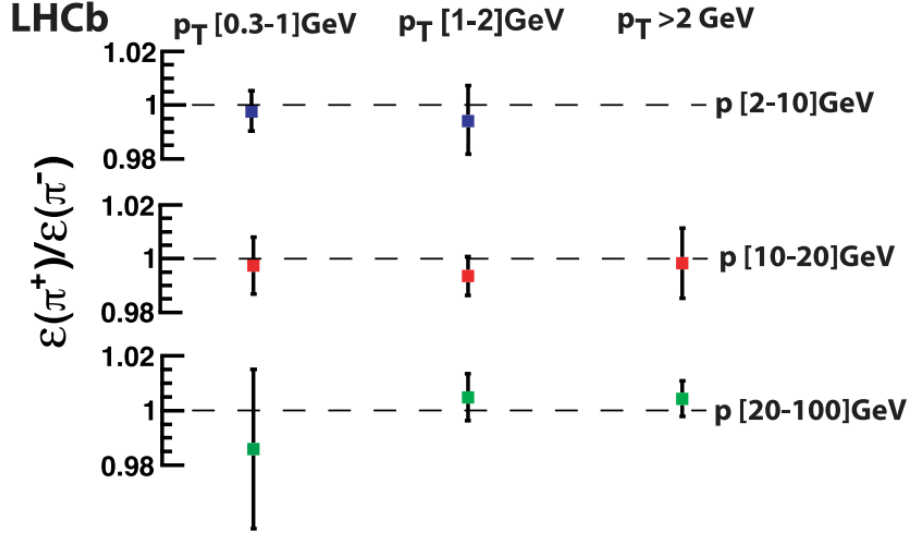


Figure 3.19: The tracking efficiency ratio of  $\pi^+$  to  $\pi^-$  as a function of pion transverse momentum in three momentum bins.

A second method is used to measure the KK pair asymmetry. Here, the track efficiency asymmetry is coupled to the difference between momentum distributions of both kaon pair,

$$A^{KK} = \int [P_{OS}(p) - P_{SS}(p)] \times A_K(p) dp, \quad (3.11)$$

where

$$A_K(p) = \frac{\epsilon(K^+) - \epsilon(K^-)}{\epsilon(K^+) + \epsilon(K^-)}. \quad (3.12)$$

$P_{OS}(p)$  is the P.D.F. for the momentum spectra for kaons with opposite signs,  $K^+K^-$  and the complex conjugate, while  $P_{SS}(p)$  is the P.D.F. for the momentum spectra for kaons with same signs,  $K^+K^+$  and the complex conjugate. Equation 3.12 contains  $\epsilon(K^\pm)$ , which are the  $K$  efficiencies and are calculated as a function of the kaon momentum [45]. The asymmetry of KK pair result is measured to be  $A^{KK} = (0.012 \pm 0.004)\%$ . Thus the combination gives a total tracking asymmetry of  $A_{track} = (0.02 \pm 0.13)\%$ .

Table 3.19: A table summarizing the tracking efficiency percentages in the six momentum bins for each magnet polarity and track sign. Only diagonal elements of the covariance matrix are shown as the errors.

Momentum bin ( GeV)	Up track <sup>+</sup>	Up track <sup>-</sup>	Down track <sup>+</sup>	Down track <sup>-</sup>
2-6	48.68 ± 0.31	49.30 ± 0.31	47.88 ± 0.26	47.95 ± 0.26
6-20	59.11 ± 0.22	59.96 ± 0.22	60.24 ± 0.17	59.85 ± 0.17
20-30	59.07 ± 0.35	59.10 ± 0.34	59.85 ± 0.28	59.95 ± 0.27
30-40	57.17 ± 0.49	56.97 ± 0.47	57.66 ± 0.41	57.65 ± 0.40
40-50	54.89 ± 0.64	54.51 ± 0.62	55.65 ± 0.54	55.76 ± 0.53
50-100	51.52 ± 0.62	51.45 ± 0.61	53.70 ± 0.55	54.80 ± 0.55

## 3.7 Background Studies

There are many types of background that can contaminate the  $B_s^0$  semileptonic decays. Combinatoric fake  $D_s$  background (FakeDs), tends to be flat underneath the  $D_s$  mass peak. Prompt background peaks underneath the  $D_s$  mass peak and thus is a larger challenge to understand. There are also other sources of background when a  $B^+$  or a  $B^0$  hadron decays via different intermediate states into the final state of the signal channel studied. This source is also a type of peaking background and thus involves more work to understand. These are all considered and are taken into account when calculating the final asymmetry value.

### 3.7.1 Prompt and Fake Background Studies

There are some background sources that have not been considered in this analysis up until now. Firstly, the prompt  $D_s$  decay, which has been mentioned. To further understand these types of background a special stripping line has been written and implemented for stripping 17b data samples. The stripping line is exactly the same as the signal line for the  $B_s^0$  and  $D_s$  requirements, however the muon track requirement is different. The muon track is now required to be a hadron track that accompanies the  $D_s$ . For this, it is required that the  $DLL(\pi - \mu)$  of this hadron track be less than zero, opposite to that of the signal stripping line. The combinations are required to pass the HLT2IncPhi trigger decision in the stripping

line.

Offline, the same cuts are applied to this sample as are for the signal sample, however any of the specific muon cuts regarding identification are no longer applied<sup>8</sup>. The hadron tracks (kaons and pions) are separated and analyzed so, by requiring that the  $DLL(\pi - K)$  is less than or greater than 0, respectively. These samples are fit using the same method as the two-dimensional signal fits, using the same P.D.F. shapes as well. These fits are done in the five muon momentum bins. In total, there are ten parameters for each magnet polarity. A weighted mean of each parameter is calculated and these together become the final prompt lnIP shape, a bifurcated Gaussian, with one mean and two sigmas. In the signal fit, these parameters are constrained to be constant in the signal fit for each momentum bin. Figure 3.20 shows four fit results for magnet down in the first muon momentum bin. Tables 3.20 through 3.23 list the signal, prompt and background yields for each muon momentum bin.

Using the prompt yields in each bin as the numerator in a raw asymmetry calculation and normalizing with the signal yields in each bin, an asymmetry due to this background is calculated. With the equation

$$A_{prompt} = \frac{N(D_s^- \mu^+)_{prompt} - N(D_s^+ \mu^-)_{prompt}}{N(D_s^- \mu^+)_{signal} + N(D_s^+ \mu^-)_{signal}}, \quad (3.13)$$

calculated per each bin then averaged with weights, the asymmetry due to the prompt background is,  $A_{prompt} = (0.03 \pm 0.05)\%$ . A second background that must be taken into account is a “fake background signal”. This is when the muon accompanying the  $D_s$  creating the  $B_s^0$  candidate is misidentified as a pion or a kaon. This can occur, for instance, when the  $B_s^0$  decays into a  $D_s \pi$  final state, where then the pion is misidentified as a muon and the final state becomes the signal channel. The probabilities that a pion or kaon is mistaken for a muon are measured using a sample of  $D^{*+} \rightarrow \pi^+ D^0$ , with  $D^0$  decaying into a  $K^- \pi^+$  [46]. Studies are done in the same five muon momentum bins to determine the momentum dependent

---

<sup>8</sup>This occurs primarily because during the processing a bug in the code gives random results for muon identification variables on tracks that are not muons. This affects the “isMuon” cut, and thus not incorporated here.

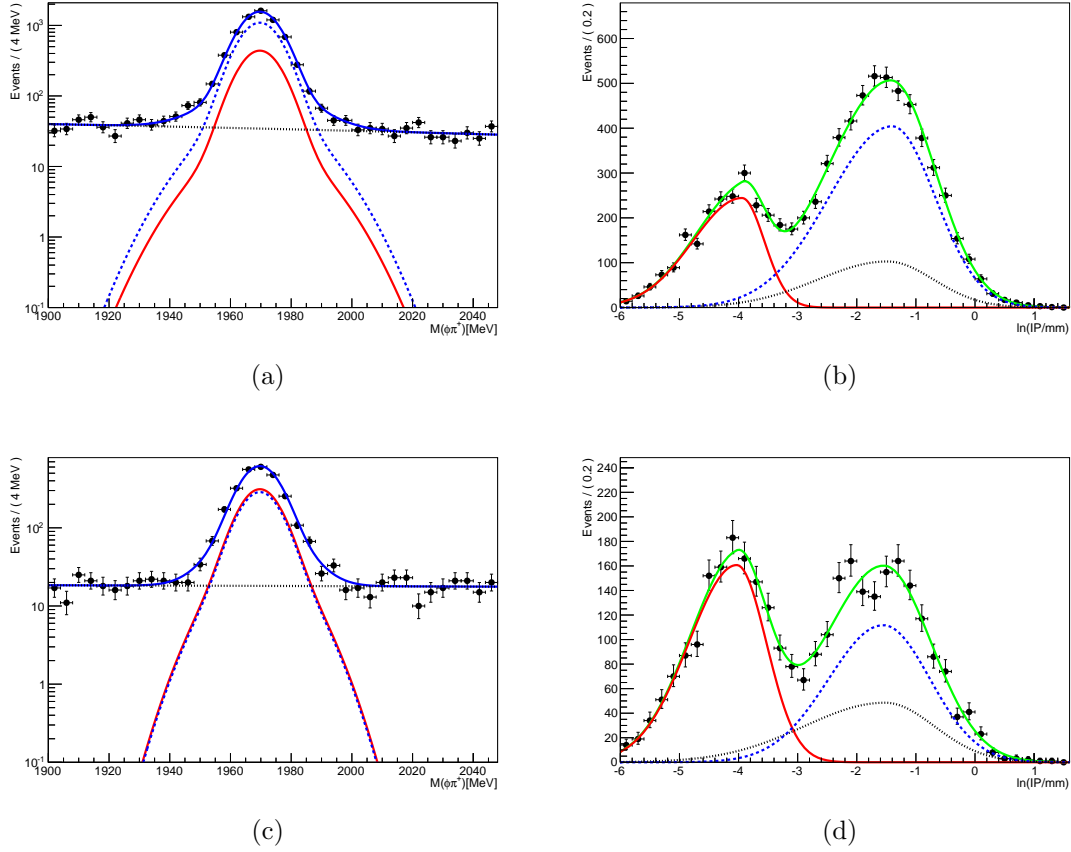


Figure 3.20: Resulting plots of mass and  $\ln IP$  from two-dimensional fits for magnet down in the first muon momentum bin  $6 - 20$  GeV. The top two plots, (a) and (b), refer to events occurring when the hadron accompanying the  $D_s$  is a pion. Plots (c) and (d) refer to when the hadron is a kaon. The blue dotted line is DfB, the red solid line is Prompt, the black dashed line is BKG.

fake rates. The results for kaons and pions are shown on the left and right of figure 3.21, respectively. From these plots it is clear that these backgrounds are very small. One would expect a difference between  $K^+$  and  $K^-$  since they interact differently in matter [1]. There *is* a difference for both the pion and the kaon, however it is very small. The total number of fakes is of the order of 1% thus the net affect on the final measurement of  $a_{s1}^s$  is of the order of  $10^{-4}$ , which results in  $A_{fake} = (0.00 \pm 0.00)\%$ . This result has been calculated in the same way as the prompt asymmetry. The results of the fake rates multiplied by the yields from the fits are shown in table 3.24 and 3.25.



Table 3.20: Fake yields presented for magnet down in all momentum bins for  $D_s^+$  and  $D_s^-$ , for kaons faking muons.

$D_s^+$	$p$ bin	Signal	Prompt	Background
	1	$1255 \pm 73$	$1248 \pm 70$	$678 \pm 33$
	2	$925 \pm 41$	$714 \pm 34$	$674 \pm 32$
	3	$805 \pm 43$	$516 \pm 36$	$542 \pm 29$
	4	$759 \pm 48$	$337 \pm 40$	$467 \pm 27$
	5	$2035 \pm 69$	$714 \pm 54$	$1122 \pm 46$
	Overall	$5736 \pm 114$	$3562 \pm 96$	$3493 \pm 99$
$D_s^-$	$p$ bin	Signal	Prompt	Background
	1	$1214 \pm 63$	$1442 \pm 63$	$683 \pm 35$
	2	$1041 \pm 48$	$715 \pm 39$	$650 \pm 33$
	3	$853 \pm 78$	$541 \pm 76$	$534 \pm 30$
	4	$720 \pm 34$	$332 \pm 23$	$381 \pm 25$
	5	$1984 \pm 70$	$795 \pm 55$	$1139 \pm 47$
	Overall	$5869 \pm 120$	$3783 \pm 104$	$3375 \pm 76$

Table 3.21: Fake yields presented for magnet up in all momentum bins for  $D_s^+$  and  $D_s^-$ , for kaons faking muons.

$D_s^+$	$p$ bin	Signal	Prompt	Background
	1	$892 \pm 69$	$876 \pm 67$	$511 \pm 30$
	2	$743 \pm 48$	$500 \pm 43$	$427 \pm 27$
	3	$664 \pm 32$	$300 \pm 22$	$398 \pm 24$
	4	$591 \pm 31$	$219 \pm 18$	$343 \pm 24$
	5	$1370 \pm 64$	$567 \pm 57$	$780 \pm 34$
	Overall	$4286 \pm 103$	$2487 \pm 86$	$2411 \pm 64$
$D_s^-$	$p$ bin	Signal	Prompt	Background
	1	$968 \pm 70$	$858 \pm 69$	$470 \pm 36$
	2	$820 \pm 41$	$486 \pm 33$	$457 \pm 28$
	3	$667 \pm 41$	$314 \pm 36$	$409 \pm 25$
	4	$535 \pm 37$	$282 \pm 29$	$290 \pm 23$
	5	$1491 \pm 57$	$615 \pm 45$	$815 \pm 39$
	Overall	$4411 \pm 114$	$2631 \pm 95$	$2442 \pm 75$

Table 3.22: Fake yields presented for magnet down in all momentum bins for  $D_s^+$  and  $D_s^-$ , for pions faking muons.

$D_s^+$	$p$ bin	Signal	Prompt	Background
	1	$4617 \pm 106$	$1819 \pm 90$	$1237 \pm 47$
	2	$4624 \pm 94$	$1085 \pm 67$	$1395 \pm 50$
	3	$3586 \pm 87$	$755 \pm 63$	$1135 \pm 47$
	4	$2512 \pm 63$	$511 \pm 35$	$877 \pm 41$
	5	$4876 \pm 131$	$870 \pm 112$	$1552 \pm 69$
	Overall	$20174 \pm 202$	$5097 \pm 148$	$6184 \pm 105$
$D_s^-$	$p$ bin	Signal	Prompt	Background
	1	$4411 \pm 93$	$1760 \pm 71$	$1240 \pm 51$
	2	$4583 \pm 112$	$1306 \pm 91$	$1372 \pm 56$
	3	$3740 \pm 85$	$776 \pm 61$	$1104 \pm 45$
	4	$2649 \pm 64$	$441 \pm 36$	$840 \pm 38$
	5	$4852 \pm 86$	$852 \pm 49$	$1430 \pm 52$
	Overall	$20287 \pm 199$	$5133 \pm 134$	$5935 \pm 122$

Table 3.23: Fake yields presented for magnet up in all momentum bins for  $D_s^+$  and  $D_s^-$ , for pions faking muons.

$D_s^+$	$p$ bin	Signal	Prompt	Background
	1	$3018 \pm 95$	$1230 \pm 83$	$995 \pm 42$
	2	$3350 \pm 72$	$768 \pm 44$	$1034 \pm 43$
	3	$2510 \pm 66$	$574 \pm 42$	$796 \pm 45$
	4	$1852 \pm 55$	$415 \pm 34$	$574 \pm 33$
	5	$3302 \pm 75$	$606 \pm 50$	$1112 \pm 45$
	Overall	$13965 \pm 161$	$3644 \pm 110$	$4529 \pm 101$
$D_s^-$	$p$ bin	Signal	Prompt	Background
	1	$2980 \pm 132$	$1474 \pm 125$	$850 \pm 45$
	2	$3396 \pm 77$	$797 \pm 52$	$981 \pm 42$
	3	$2626 \pm 67$	$498 \pm 44$	$764 \pm 37$
	4	$1848 \pm 74$	$340 \pm 64$	$593 \pm 33$
	5	$3399 \pm 117$	$703 \pm 107$	$1126 \pm 46$
	Overall	$14312 \pm 189$	$3727 \pm 151$	$4337 \pm 92$

### 3.7.2 $b$ -Backgrounds

In this section fake  $D_s$  backgrounds that can possibly come from other B mesons is discussed. These backgrounds can peak under the real  $D_s$  mass peak. Table 3.26 lists all Monte Carlo

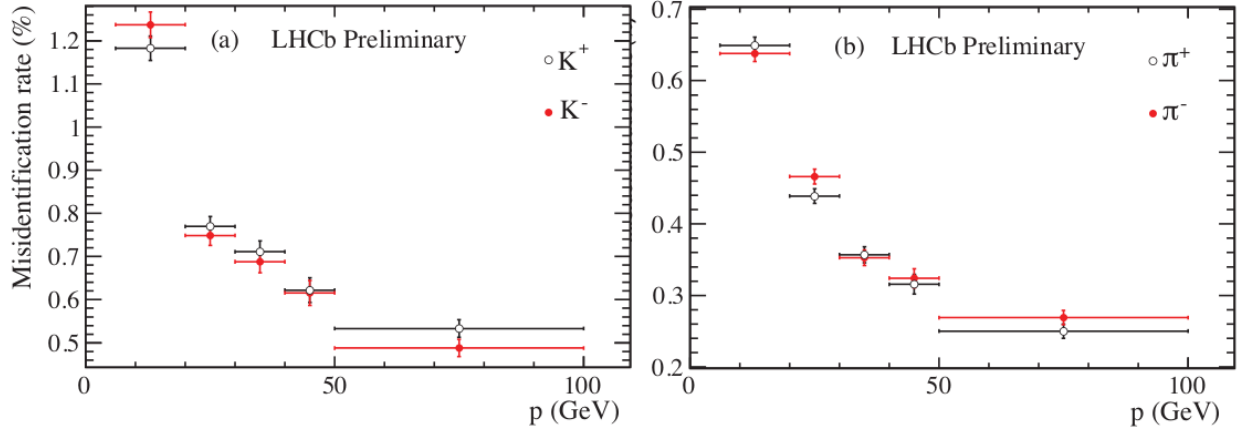


Figure 3.21: Mis-identification of kaons and pions as a muon. This is an important background to understand as it can create asymmetries in the signal.

Table 3.24: Results of the 2D fake fits. The yields are multiplied by the fake rates, then they are added together to get a final number for a total fake number of hadrons accompanying the  $D_s$ . The results are show for all muon momentum bins, for magnet down only, for  $D_s^+$  and  $D_s^-$  respectively. Fake Rates is represented with FR.

$p$ bin	$(\pi^- + K^-)$ Fake Signal $\times$ FR	$(\pi^+ + K^+)$ Fake Signal $\times$ FR
1	$43 \pm 1$	$44 \pm 1$
2	$28 \pm 1$	$28 \pm 1$
3	$18 \pm 1$	$19 \pm 1$
4	$13 \pm 1$	$13 \pm 1$
5	$23 \pm 1$	$22 \pm 1$

Table 3.25: Results of the 2D fake fits. The yields are multiplied by the fake rates, then they are added together to get a final number for a total fake number of hadrons accompanying the  $D_s$ . The results are show for all muon momentum bins, for magnet up only, for  $D_s^+$  and  $D_s^-$  respectively. Fake Rates is represented with FR.

$p$ bin	$(\pi^- + K^-)$ Fake Signal $\times$ FR	$(\pi^+ + K^+)$ Fake Signal $\times$ FR
1	$30 \pm 1$	$31 \pm 4$
2	$21 \pm 1$	$21 \pm 1$
3	$13 \pm 1$	$14 \pm 1$
4	$9 \pm 1$	$9 \pm 1$
5	$15 \pm 1$	$16 \pm 1$

samples used in this analysis to understand certain kinematic properties better and more importantly used for background studies.

The case of a decay when the charm hadron originates from the  $W$  boson instead of the  $B$  hadron is a source of background. Rather than the diagram in figure 1.2, the charm hadron switches places with the muon and neutrino. Any  $B$  hadron, as well as even the  $\Lambda_b$  hadron, can contribute to these types of events. This decay type,  $B^+/B^0 \rightarrow D_s D^0/D^+$ , is a source of peaking background, in that the  $D^0$  and the  $D^+$  decay into  $X\mu\nu$ , where they peak under the signal making it difficult to disentangle from the true signal. This cannot be studied in data so Monte Carlo is used.

Similarly,  $B^+ \rightarrow D_s K \mu \nu$  with the  $D_s K$  forming an excited  $D^{*0}$  resonance is a source of background. This channel is much more prominent than the  $D_s D^0/D^+$  final states mentioned since there is less separation between the muon and the  $D_s$ . Also, the  $D_s$  and the muon originate from the same vertex, whereas in the  $D_s D^0/D^+$  final state the muon comes from a completely separate vertex from the  $D_s$ . This allows for high suppression for the  $D_s D^0/D^+$  channel and low suppression for the  $D_s K$  channel. The Monte Carlo samples are examined

Table 3.26: List of Monte Carlo samples used in the analysis.

Event type	Events Generated	Type
13774002	20M	$B_s^0$ signal cocktail
13873201	5M	$B_s^0$ background cocktail
12775001	5M	$B^+ \rightarrow D_s K \mu \nu$
11774001	5M	$B^0 \rightarrow D_s K \mu \nu$
12875601	5M	$B^+ \rightarrow D^0 D_s$
11876001	5M	$B^0 \rightarrow D^0 / D D_s$
15894301	10M	$\Lambda_b^0$ background cocktail
27265000	5M	$D^{*+} \rightarrow D^0 \pi, D^0 \rightarrow K \pi \pi \pi$

to determine the efficiency at which the decays are reconstructed in the detector. This is done by defining the quantity,

$$\epsilon_{reco} = \frac{\epsilon(\text{ReconstructedParticles} + \text{OfflineCuts})}{\epsilon(\text{GeneratorLevelMCParticles})}. \quad (3.14)$$

From here, the efficiency of each background sample is compared to that of the MC signal sample. The results are listed in table 3.27. The next table, table 3.28, are the measured branching fractions for all possible peaking backgrounds (to upper charm), as well as production asymmetries estimated from the branching fractions and the final asymmetries. This method utilizes the inverse of the  $b$ -hadron production fraction measured by LHCb [39], which is  $3.75 \pm 0.29$ , while the inverse of the  $\Lambda_b$  production fraction measured by LHCb is  $2.32 \pm 0.63$  [39]. It is assessed using the following

$$A_{peaking, DD_s X} = -a_p f_p \mathcal{D} \frac{\mathcal{B}(B^+(B^0) \rightarrow DD_s^+ X) \mathcal{B}(D \rightarrow \mu X)}{\mathcal{B}(B_s^0 \rightarrow D_s^+ \mu \nu X)} \cdot \frac{\epsilon_{reco, bkg}}{\epsilon_{reco, sig}} \quad (3.15)$$

$$A_{peaking, KD_s X \mu \nu} = a_p f_p \mathcal{D} \frac{\mathcal{B}(B^+(B^0) \rightarrow D_s^- K \mu^+)}{\mathcal{B}(B_s^0 \rightarrow D_s^+ \mu \nu X)} \cdot \frac{\epsilon_{reco, bkg}}{\epsilon_{reco, sig}}, \quad (3.16)$$

where  $a_p$  is the production asymmetry,  $f_p$  is the production fraction, the  $\mathcal{D}$  is the dilution factor for the  $B^+$  and  $B^0$ , and the  $D$  terms in each decay represent the relevant charm hadron and the terms with decays in parentheses are the resulting yields of the decay. The negative sign in equation 3.15 comes from the difference in  $D_s$  sign between the upper-vertex charm decays and the  $D_s K \mu$  final state.

Table 3.27: MC reconstruction efficiencies for multiple types of backgrounds as well as the signal channel (last row).

Signal Type	Efficiency[%]
$B^+ \rightarrow D^0 D_s^+ X$	$0.101 \pm 0.002$
$B^0 \rightarrow D^0 D_s^+ X$	$0.067 \pm 0.001$
$B^0 \rightarrow D^- D_s^+ X$	$0.101 \pm 0.002$
$\Lambda_b^0 \rightarrow D_s^+ \Lambda_c X$	$0.097 \pm 0.001$ [47]
$B^+ \rightarrow D_s^- K X \mu^+ \nu$	$0.646 \pm 0.006$
$B^0 \rightarrow D_s^- K X \mu^+ \nu$	$0.688 \pm 0.006$
$B_s^0 \rightarrow D_s^- X \mu^+ \nu$	$1.344 \pm 0.004$

The  $B^0$  decays are split into final states including a  $D^0$  and a  $D^-$  according to the  $D^{*+}/D^+$  ratio in the measured exclusive final states. An uncertainty of 20% is assigned

Table 3.28: MC reconstruction branching fractions, signal to background ratios and production asymmetries for multiple types of backgrounds.

Signal Type	B.F. [%]	S/B	$a_p$ [%]	$A_{peaking}$ [%]
$B^+ \rightarrow D^0 D_s^+ X$	$(7.9 \pm 1.4)$	13	$(+0.3 \pm 0.9)$	$+0.005 \pm 0.014$
$B^0 \rightarrow D^0 D_s^+ X$	$(5.7 \pm 1.2)$	13	$(-0.1 \pm 1.0)$	$0.000 \pm 0.004$
$B^0 \rightarrow D^- D_s^+ X$	$(4.6 \pm 1.0)$	20	$(-0.1 \pm 1.0)$	$-0.001 \pm 0.005$
$\Lambda_b^0 \rightarrow D_s^+ \Lambda_c X$	$(10 \pm 2)$	14	$(-1.0 \pm 4.0)$	$-0.006 \pm 0.023$
$B^+ \rightarrow D_s^- K X \mu^+ \nu$	$(6.1 \pm 1.2) \times 10^{-4}$	2	$(+0.3 \pm 0.9)$	$0.004 \pm 0.012$
$B^0 \rightarrow D_s^- K X \mu^+ \nu$	$(6.1 \pm 1.2) \times 10^{-4}$	2	$(-0.1 \pm 1.0)$	$0.000 \pm 0.004$

Table 3.29: Included in this table are the branching fractions of the signal channel for this analysis as well as the charm decays used.

Decay Type	$\mathcal{B}$ [%]
$B_s^0 \rightarrow D_s \mu^+ \nu$	$8.9 \pm 0.4$
$B^+(B^0) \rightarrow K D_s^- \mu^+ \nu$	$(6.1 \pm 1.2) \times 10^{-2}$
$D^0 \rightarrow X \mu^+ \nu$	$6.5 \pm 0.1$
$D^+ \rightarrow X \mu^+ \nu$	$16.1 \pm 0.3$
$\Lambda_c \rightarrow X \mu^+ \nu$	$3.1 \pm 0.3$

to this model used, by varying this fraction and reevaluating this background component. Taking into account the 33% weight factor for the  $B^0$  component due to mixing, the peaking background asymmetry is equal to  $A_{peaking} = (0.01 \pm 0.03)\%$ . Finally, adding all components, the background asymmetry is  $A_{bkg} = (0.04 \pm 0.05)\%$ .

## 3.8 Final Results

Thus far, each piece of the  $A_{meas}$  quantity has been measured and calculated with some statistical error. Sources of systematic uncertainties are considered and are discussed below. First, for signal extraction, a systematic uncertainty must be assigned for the methods used. The systematic uncertainty on the signal modeling and muon correction comes from a few places. For signal modeling, the simultaneous fitting method is used to assess the uncertainty, as is the two fine binning methods. Examining the change in  $A_\mu^c$  for each

Table 3.30: A listing of systematic uncertainties on quantities that enter into  $A_{meas}$ .

Sources	$\sigma(A_{meas})\%$
Signal modeling and muon corrections	0.07
Backgrounds	0.05
HLT2 efficiency corrections in muon topological triggers	0.05
Statistical uncertainty on the efficiency ratios	0.08
Tracking	0.13
Varying run conditions	0.01
Total	0.18

method, the uncertainty is determined to be 0.07%. The systematic on the background is extracted from the errors on the numbers discussed in section 3.7, which is 0.05%.

The systematic uncertainty associated with the HLT2 bias in muon topological trigger is obtained by taking the statistical error in the assessment of this quantity, weighted by a factor of 0.5. The latter is correspondent to the fraction of the number of events triggered solely by the HLT2 muon topological algorithm. The systematic attributed to this is 0.05%. The trigger bias on the muon are discussed in Appendix 4. The statistical error on the efficiency ratios is 0.08%. The tracking is discussed in the section 3.6 and is 0.13%.

Over the year of data-taking in 2011, it was not possible to keep the datasets of magnet up and magnet down polarities equal, thus they are not fully compatible to cancel out completely. The uncertainty is determined by first taking difference between the up and down  $A_{meas}$  and then multiplying it by a scale factor, which is obtained by comparing separate field signal yields with luminosity difference between the two samples. The uncertainty obtained is 0.01%.

This leads to a final result of  $(-0.03 \pm 0.25 \pm 0.18)\%$ , which implies

$$a_{sl}^s = (-0.06 \pm 0.50 \pm 0.36)\%, \quad (3.17)$$

where the first error is statistical and the second is systematic. This measured result is consistent with the prediction of the Standard Model, recalling that the SM predicts

$a_{\text{sl}}^s$  to be  $(0.0019 \pm 0.0003)\%$  and  $a_{\text{sl}}^d$  to be  $(-0.041 \pm 0.006)\%$ . The D0 collaboration has measured the semileptonic asymmetries, one analysis that is exact to the work presented here, and another, which is based on a di-muon final state. The former D0 results  $a_{\text{sl}}^s$  and  $a_{\text{sl}}^d$  based on  $D^\pm \mu^\mp$  events in a  $10.4 \text{ fb}^{-1}$  sample are  $a_{\text{sl}}^s = (-1.12 \pm 0.74 \pm 0.17)\%$  [20] and  $a_{\text{sl}}^d = (0.68 \pm 0.45 \pm 0.14)\%$  [21]. The  $a_{\text{sl}}^d$  quantity is predicted by the SM to be  $a_{\text{sl}}^d = (-0.041 \pm 0.006)\%$  [18]. It is clear that these results diverge from the SM predictions by  $\sim 1.5\sigma$  for both asymmetries. The D0 measured asymmetries in di-muon decays in 1.96 TeV  $pp$  collisions of  $A_{\text{sl}}^b = (-0.787 \pm 0.172 \pm 0.093)\%$  [19].

The LHCb measurement and the D0 measurements, along with the Standard Model prediction and the HFAG  $\Upsilon(4S)$  average are shown in figure 3.22 [19] [20] [21] [48]. Since the measurement in LHCb of  $a_{\text{sl}}^s$  results in an agreement with the SM prediction, this implies that there is *no new physics* in this sector of study. However with the divergence of the D0 measurements, this implication is not validated.

The CP-violating asymmetry,  $a_{\text{sl}}^s$ , currently measured by LHCb is the most precise measurement in the world and is in very good agreement with the Standard Model prediction.



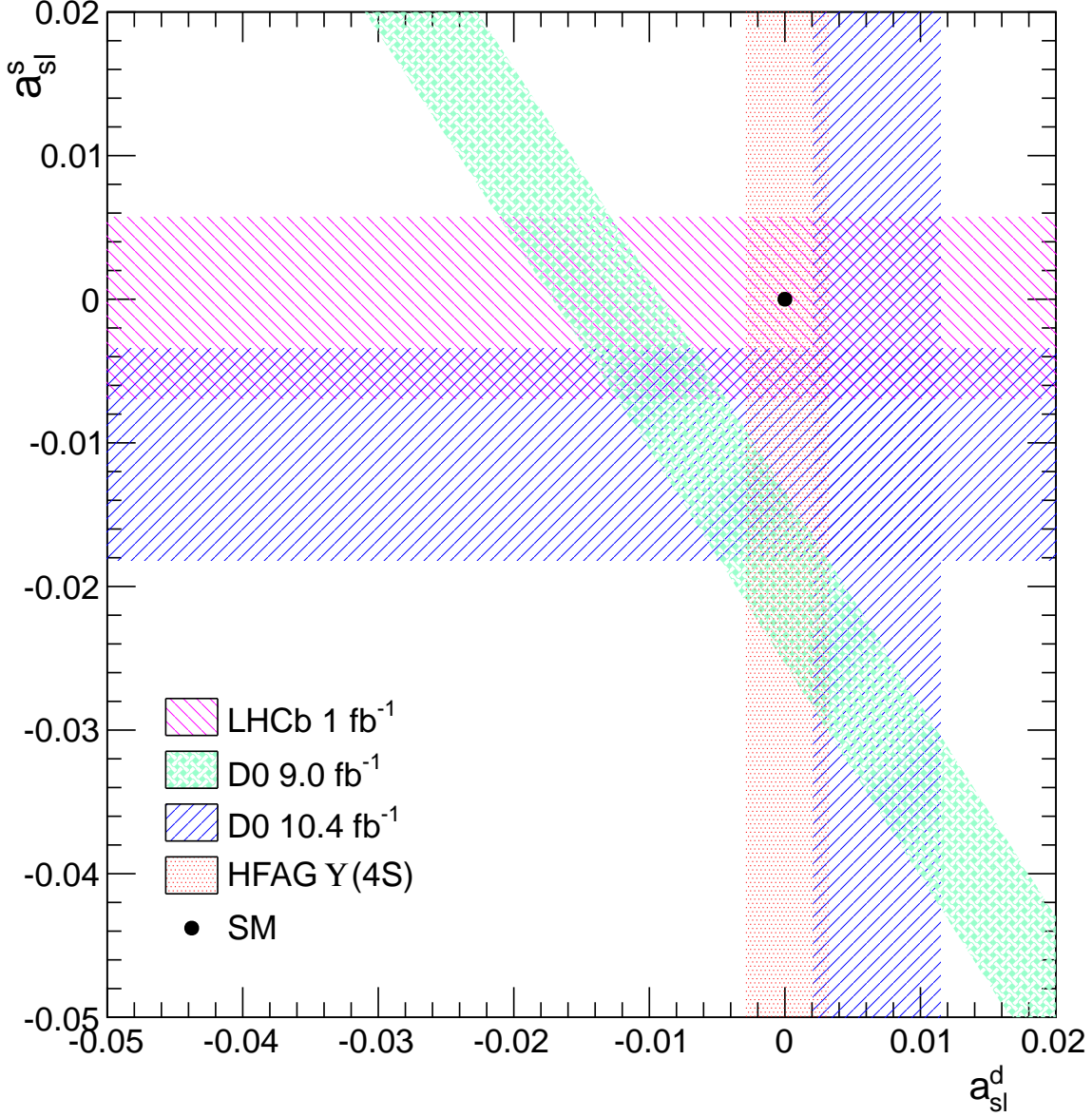


Figure 3.22: This is a plot with  $a_{sl}^d$  on  $x$ -axis and  $a_{sl}^s$  on  $y$ -axis. The black dot represents the Standard Model prediction, the magenta backslash-band represents the LHCb measurement presented in this work, the blue forwardslash-bands and the green diamond-band represent the D0 results, and finally the red dotted-band represents a recent average result from  $b$ -factories. The bands represent the sum in quadrature of the statistical and systematic errors on each central value result.

# Chapter 4

## Conclusions

The asymmetry  $a_{\text{sl}}^s$  is measured, which is twice the measured asymmetry between  $D_s^- \mu^+$  and  $D_s^+ \mu^-$  yields, as

$$a_{\text{sl}}^s = (-0.06 \pm 0.50 \pm 0.36)\%. \quad (4.1)$$

Figure 3.22 shows this result with the D0 collaboration's measurements in 1.96 TeV  $pp$  collisions in di-muon decays of  $A_{\text{sl}}^b = (-0.787 \pm 0.172 \pm 0.093)\%$  [19], in  $D_s \mu$  final state as  $a_{\text{sl}}^s = (-1.12 \pm 0.74 \pm 0.17)\%$  [20] and in the  $D \mu$  final state as  $a_{\text{sl}}^d = (0.68 \pm 0.45 \pm 0.14)\%$  [21]. Included also in the figure is the most recent and current best measurement from the  $e^+e^-$  B-factories, namely  $a_{\text{sl}}^d = (0.02 \pm 0.31)\%$ . The LHCb result for  $a_{\text{sl}}^s$  is currently the most precise measurement and is consistent with the Standard Model.

Studies are continuing in this realm by investigating a dataset which includes the 2012 data. This will triple the dataset to  $3 \text{ fb}^{-1}$  and means that there will be around three times the amount signal which can reduce the statistical error by almost a factor of two. New methods may allow the systemic error to be lower as well. A higher precision measurement may put some constraints elsewhere in the SM.

Further high precision measurements in the  $B$  mixing sector of physics mentioned in section 1.4 may illuminate why nature is the way it is, or if there is new physics hiding somewhere.

# Appendix 1

## $q \times p_x$ vs $p_y$ Binned Signal Fits

### 1.1 Magnet Down

All figures in this section show the fit results for the magnet down polarity data for the individual fine kinematic binning in  $q \times p_x$  vs  $p_y$ . In each figure, the dashed green and pink lines are the two Gaussian shapes.

Figures 1.1 through 1.10 illustrate the fits for  $D_s^-$ . Figures 1.1 and 1.2 show the fits in muon momentum bin 1. Figures 1.3 and 1.4 show the fits in muon momentum bin 2. Figures 1.5 and 1.6 show the fits in muon momentum bin 3. Figures 1.7 and 1.8 show the fits in muon momentum bin 4. Figures 1.9 and 1.10 show the fits in muon momentum bin 5.

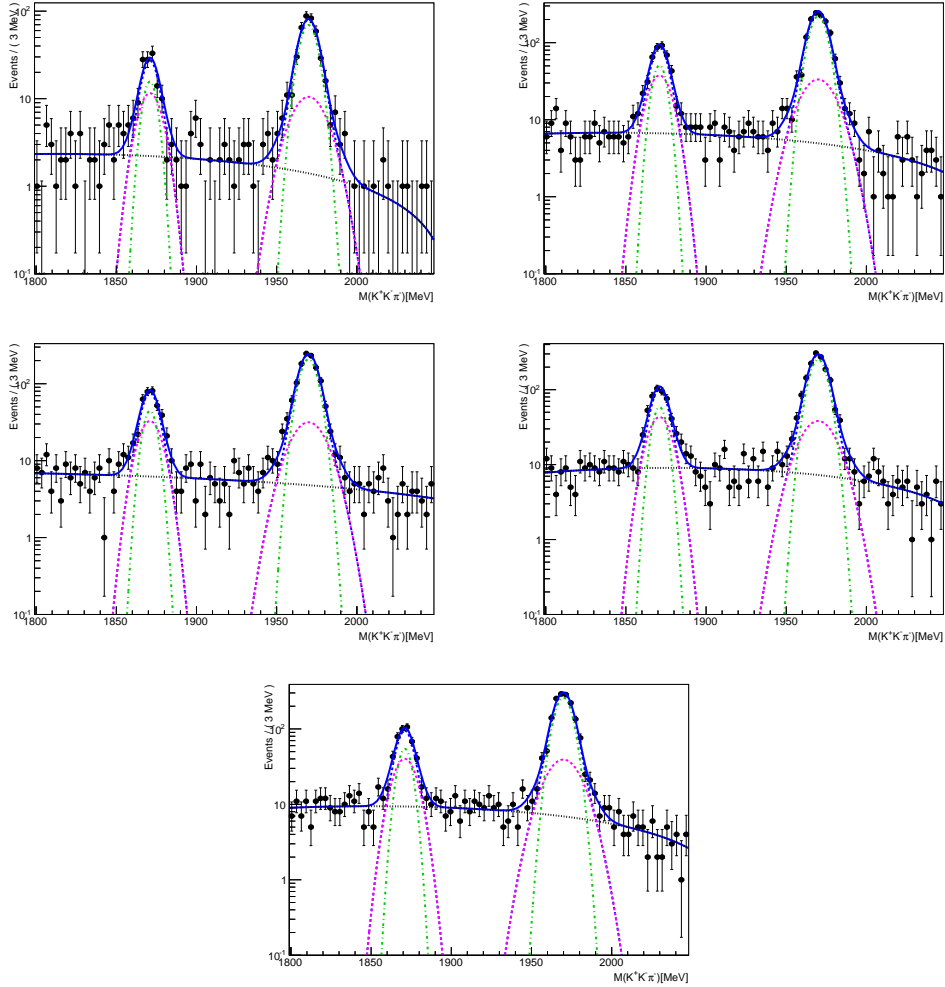


Figure 1.1: Signal data 1D fit results for magnet down, muon momentum bin 6 – 20 GeV, for  $D_s^-$ . The blue dotted line is DfB and the black dashed line is BKG. The bins in each plot are the bins of  $q \times p_x$  vs  $p_y$  with respect to the muon. The upper left is bin 1, upper right is bin 2, middle left is bin 3, middle right is bin 4, and lowest plot is bin 5.

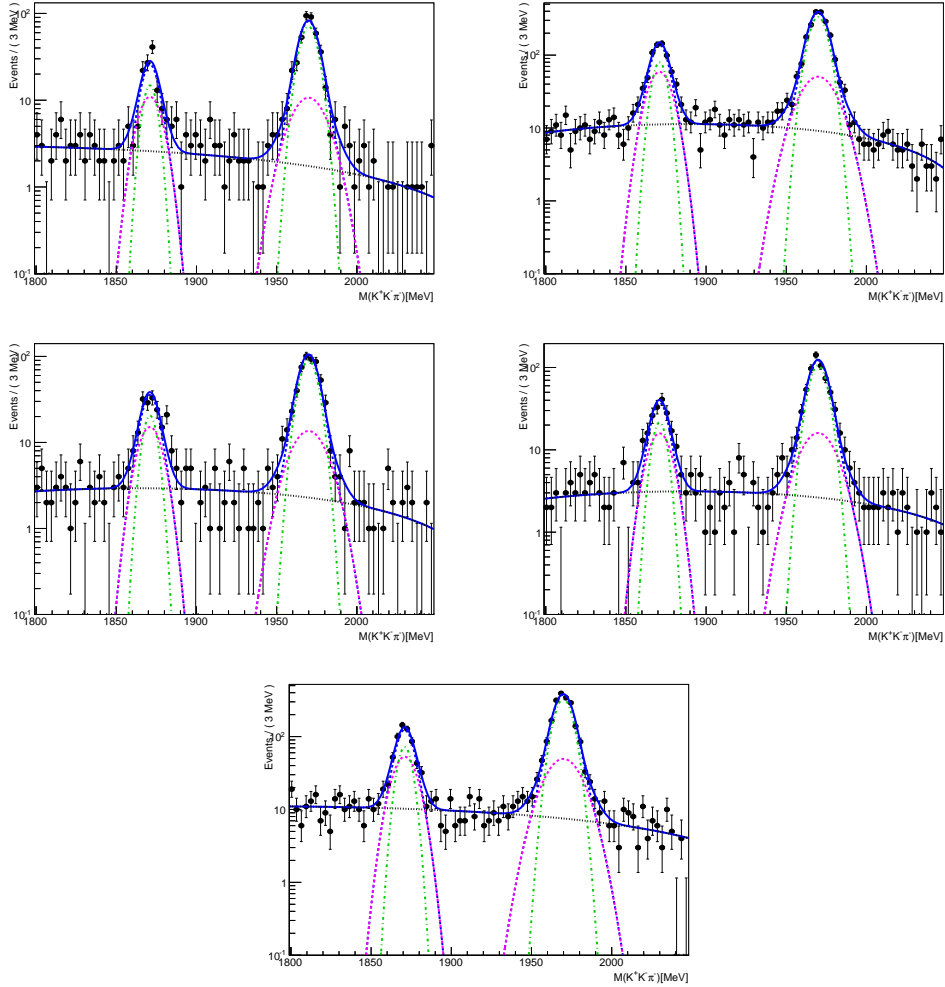


Figure 1.2: Signal data 1D fit results for magnet down, muon momentum bin 6 – 20 GeV for  $D_s^-$ . The blue dotted line is DfB and the black dashed line is BKG. The bins in each plot are the bins of  $q \times p_x$  vs  $p_y$  with respect to the muon. The upper left is bin 6, upper right is bin 7, middle left is bin 8, middle right is bin 9, and lowest plot is bin 10.

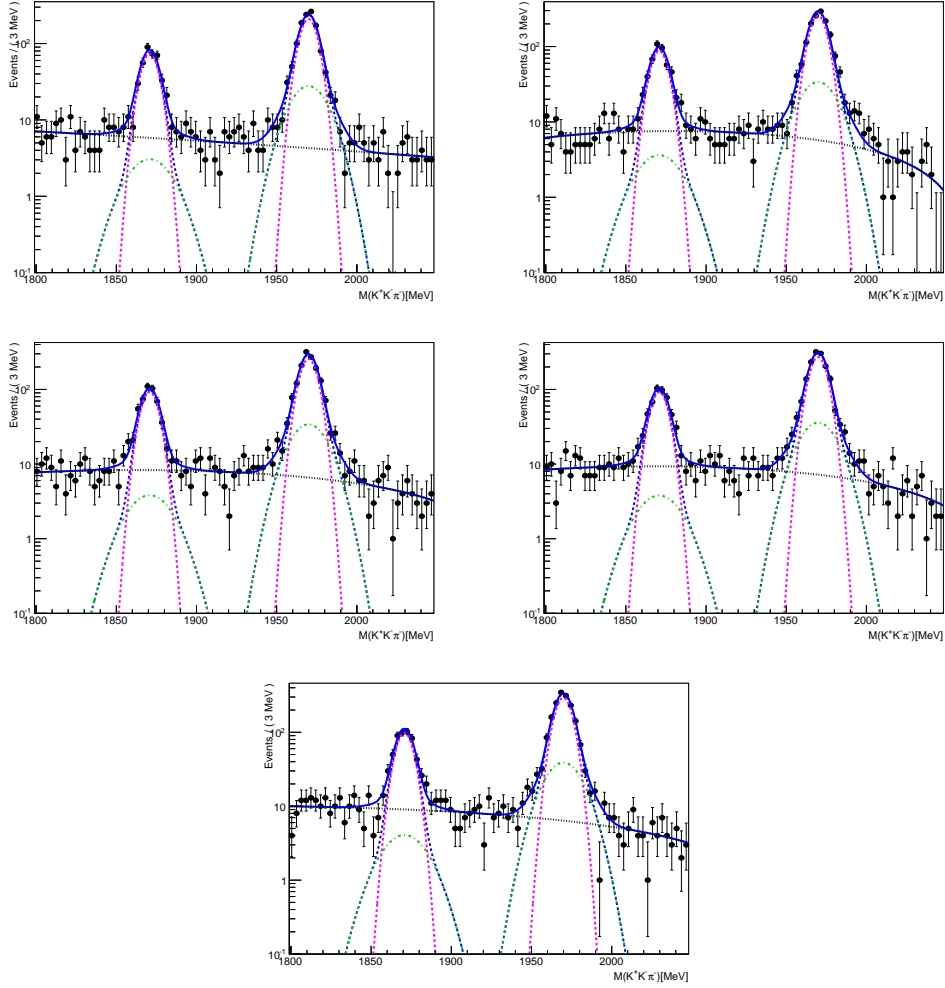


Figure 1.3: Signal data 1D fit results for magnet down, muon momentum bin 20 – 30 GeV, for  $D_s^-$ . The blue dotted line is DfB, the red solid line is PMT, the black dashed line is BKG. The bins in each plot are the bins of  $q \times p_x$  vs  $p_y$  with respect to the muon. The upper left is bin 1, upper right is bin 2, middle left is bin 3, middle right is bin 4, and lowest plot is bin 5.

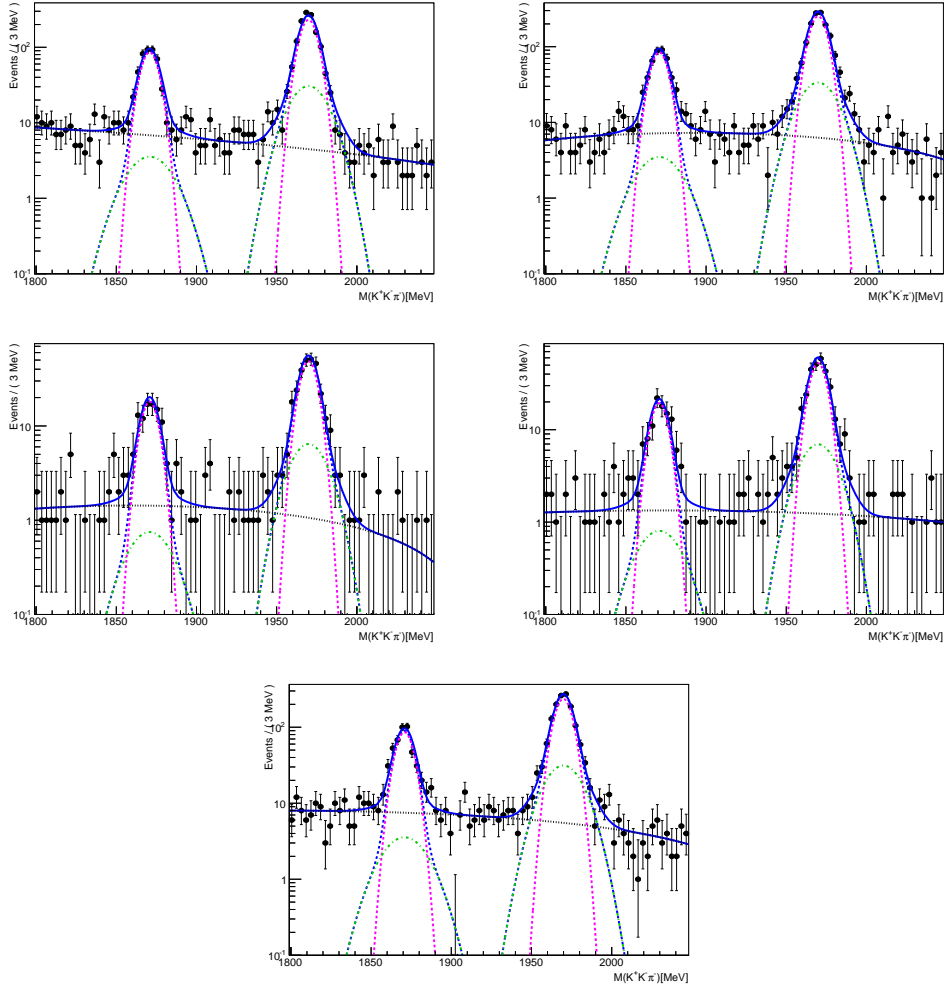


Figure 1.4: Signal data 1D fit results for magnet down, muon momentum bin 20 – 30 GeV, for  $D_s^-$ . The blue dotted line is DfB and the black dashed line is BKG. The bins in each plot are the bins of  $q \times p_x$  vs  $p_y$  with respect to the muon. The upper left is bin 6, upper right is bin 7, middle left is bin 8, middle right is bin 9, and lowest plot is bin 10.

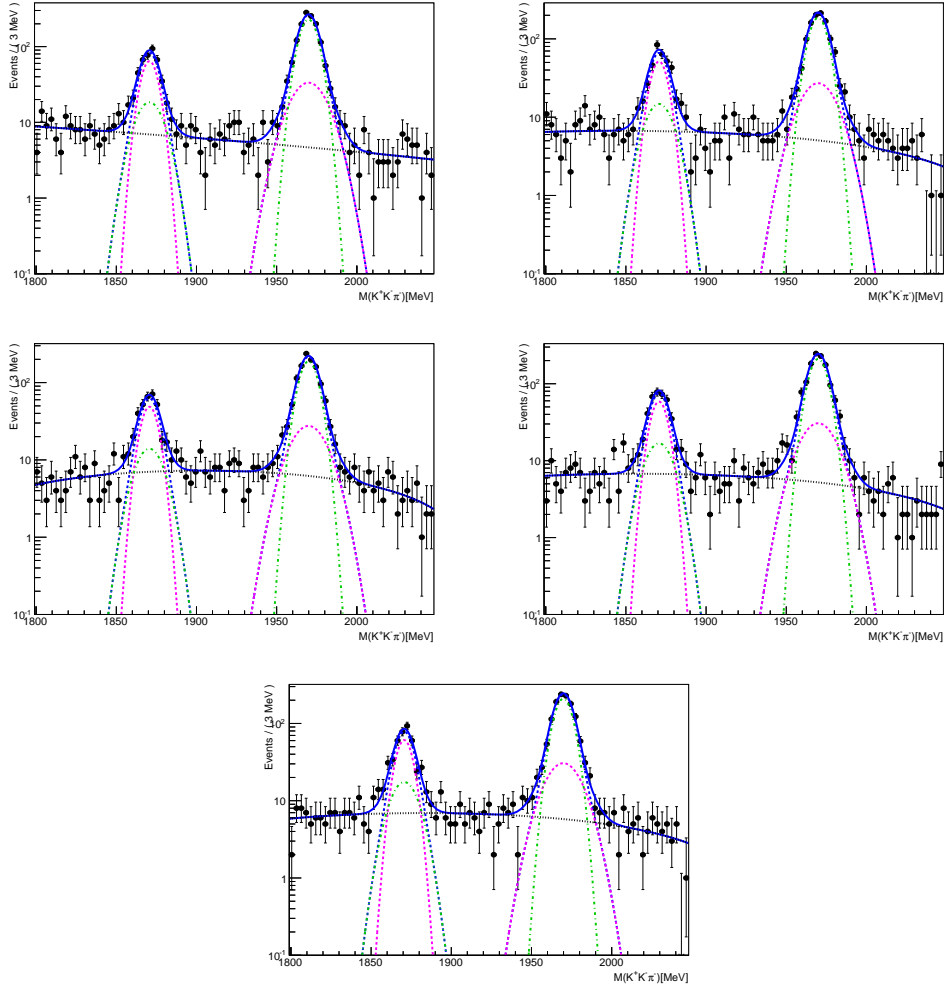


Figure 1.5: Signal data 1D fit results for magnet down, muon momentum bin 30 – 40 GeV, for  $D_s^-$ . The blue dotted line is DfB and the black dashed line is BKG. The bins in each plot are the bins of  $q \times p_x$  vs  $p_y$  with respect to the muon. The upper left is bin 1, upper right is bin 2, middle left is bin 3, middle right is bin 4, and lowest plot is bin 5.



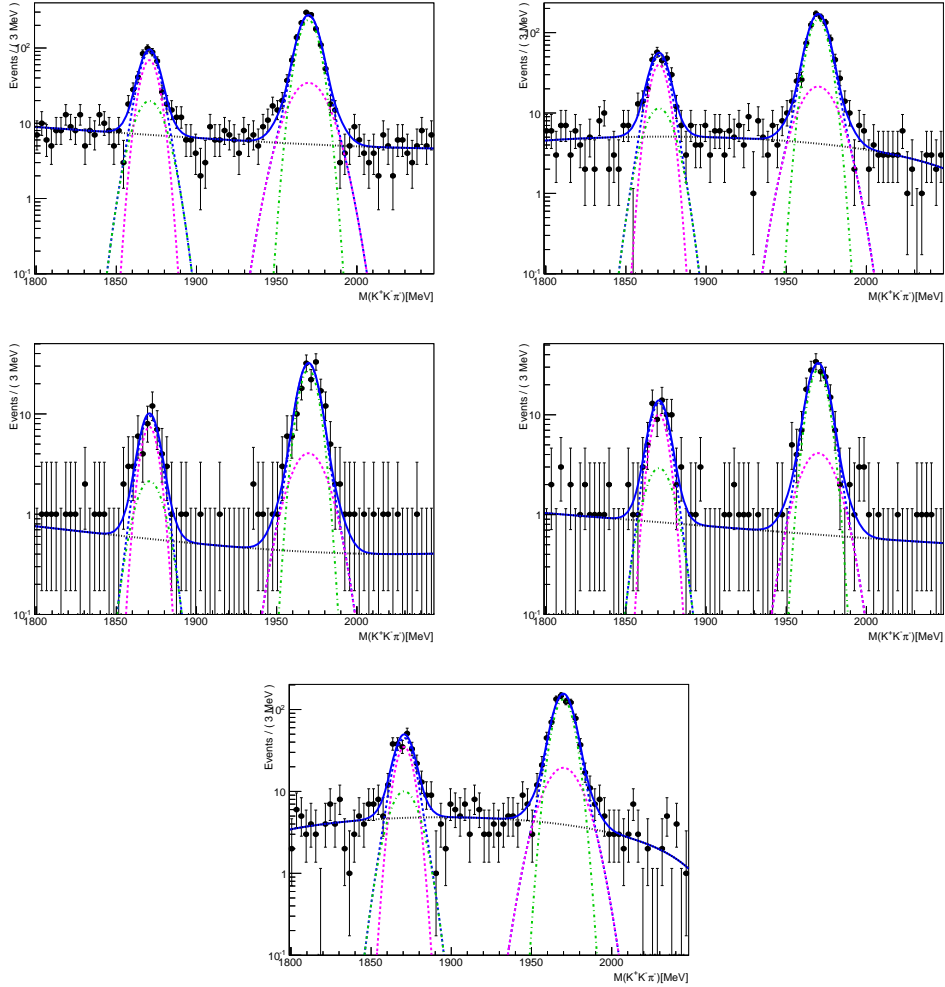


Figure 1.6: Signal data 1D fit results for magnet down, muon momentum bin 30 – 40 GeV, for  $D_s^-$ . The blue dotted line is DfB and the black dashed line is BKG. The bins in each plot are the bins of  $q \times p_x$  vs  $p_y$  with respect to the muon. The upper left is bin 6, upper right is bin 7, middle left is bin 8, middle right is bin 9, and lowest plot is bin 10.

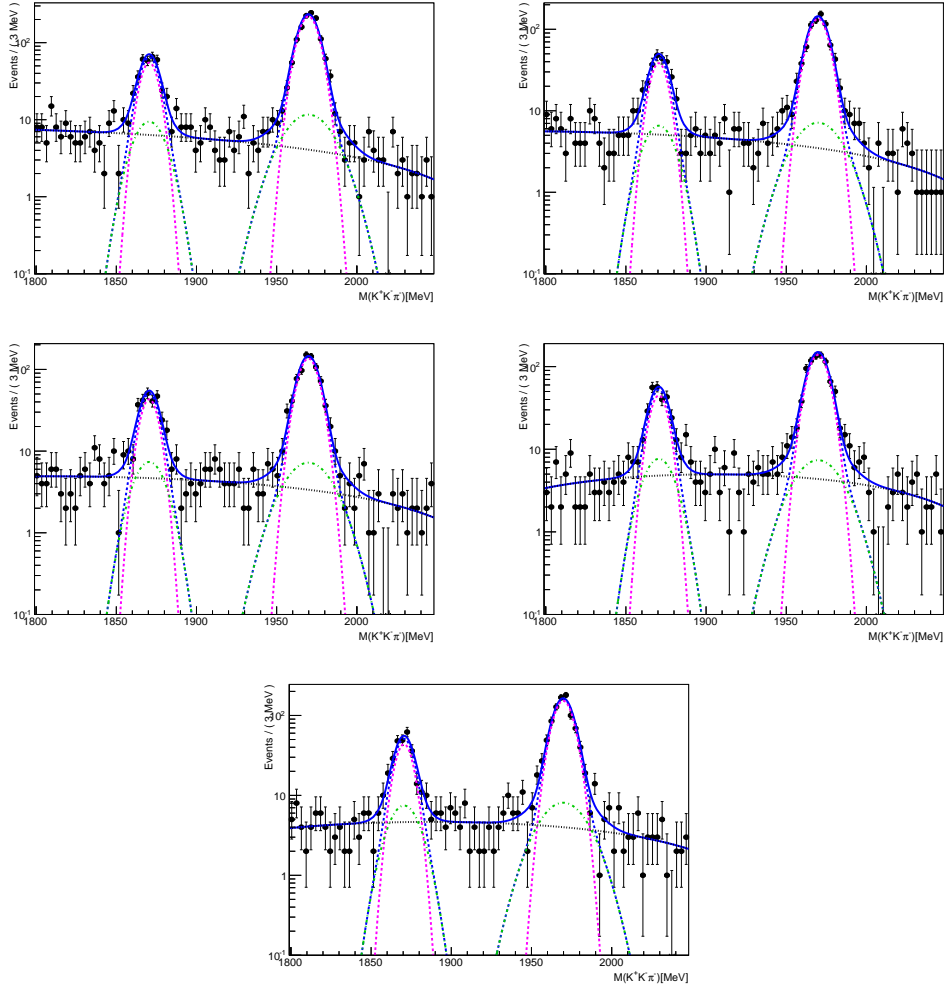


Figure 1.7: Signal data 1D fit results for magnet down, muon momentum bin 40 – 50 GeV, for  $D_s^-$ . The blue dotted line is DfB and the black dashed line is BKG. The bins in each plot are the bins of  $q \times p_x$  vs  $p_y$  with respect to the muon. The upper left is bin 1, upper right is bin 2, middle left is bin 3, middle right is bin 4, and lowest plot is bin 5.

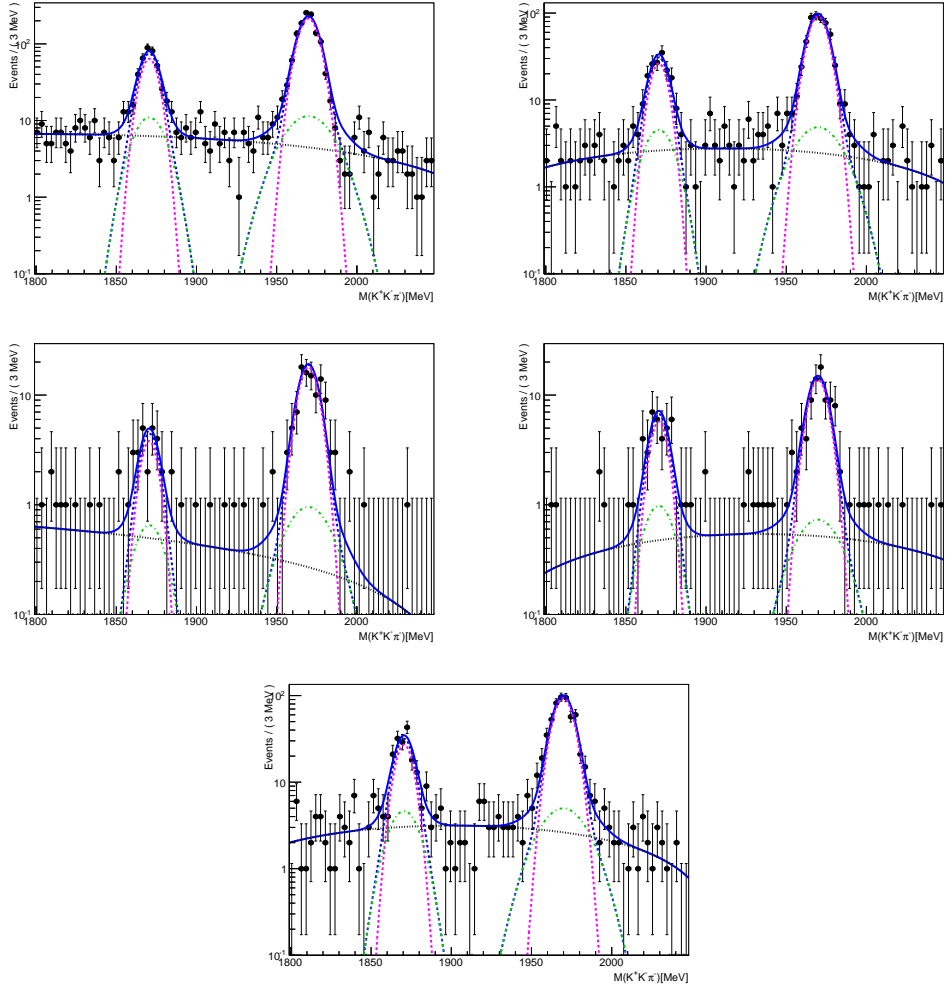


Figure 1.8: Signal data 1D fit results for magnet down, muon momentum bin 40 – 50 GeV, for  $D_s^-$ . The blue dotted line is DfB and the black dashed line is BKG. The bins in each plot are the bins of  $q \times p_x$  vs  $p_y$  with respect to the muon. The upper left is bin 6, upper right is bin 7, middle left is bin 8, middle right is bin 9, and lowest plot is bin 10.

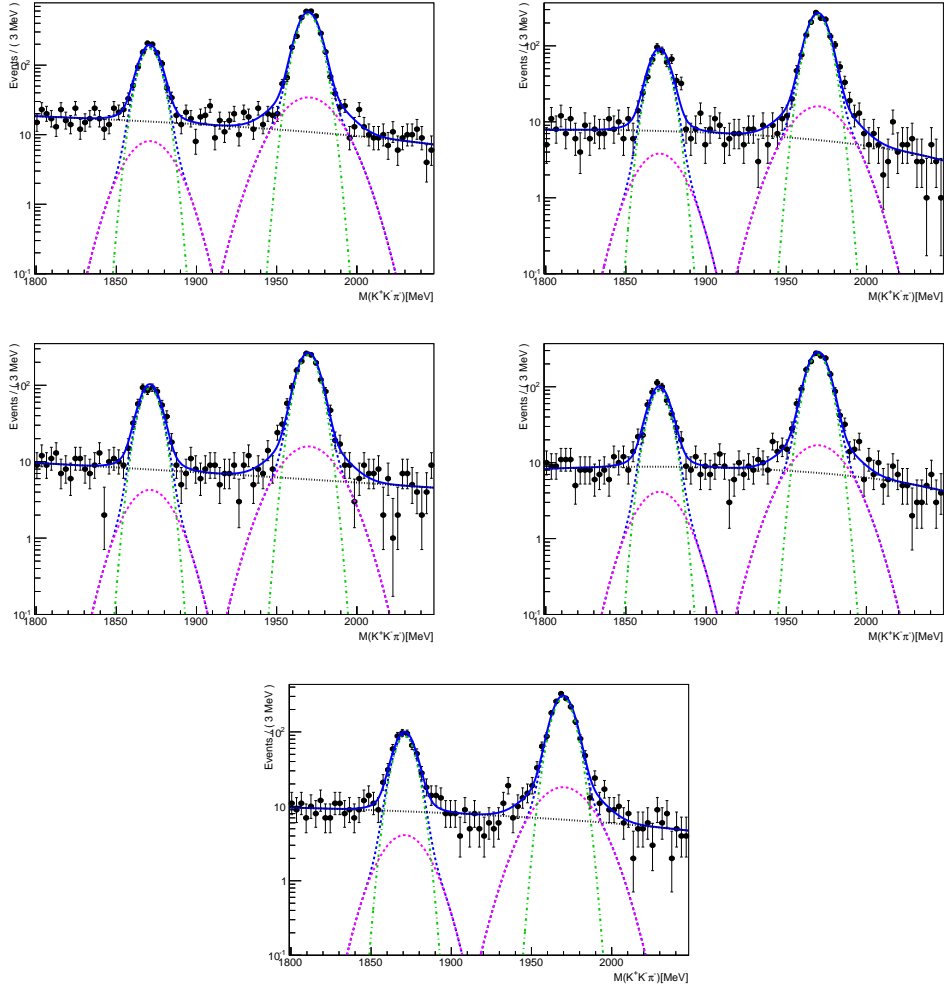


Figure 1.9: Signal data 1D fit results for magnet down, muon momentum bin 50 – 100 GeV, for  $D_s^-$ . The blue dotted line is DfB and the black dashed line is BKG. The bins in each plot are the bins of  $q \times p_x$  vs  $p_y$  with respect to the muon. The upper left is bin 1, upper right is bin 2, middle left is bin 3, middle right is bin 4, and lowest plot is bin 5.

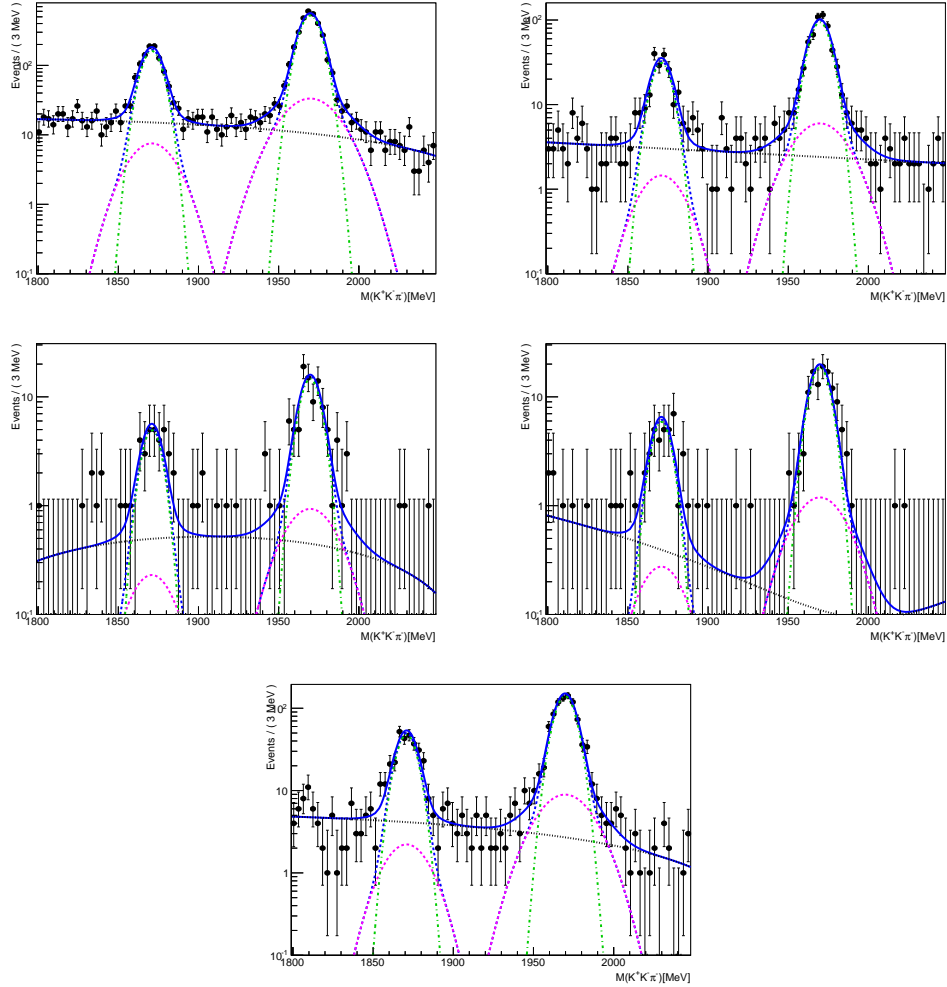


Figure 1.10: Signal data 1D fit results for magnet down, muon momentum bin 50 – 100 GeV, for  $D_s^-$ . The blue dotted line is DfB and the black dashed line is BKG. The bins in each plot are the bins of  $q \times p_x$  vs  $p_y$  with respect to the muon. The upper left is bin 6, upper right is bin 7, middle left is bin 8, middle right is bin 9, and lowest plot is bin 10.

Figures 1.11 through 1.20 illustrate the fits for  $D_s^+$ . Figures 1.11 and 1.12 show the fits in muon momentum bin 1. Figures 1.13 and 1.14 show the fits in muon momentum bin 2. Figures 1.15 and 1.16 show the fits in muon momentum bin 3. Figures 1.17 and 1.18 show the fits in muon momentum bin 4. Figures 1.19 and 1.20 show the fits in muon momentum bin 5.

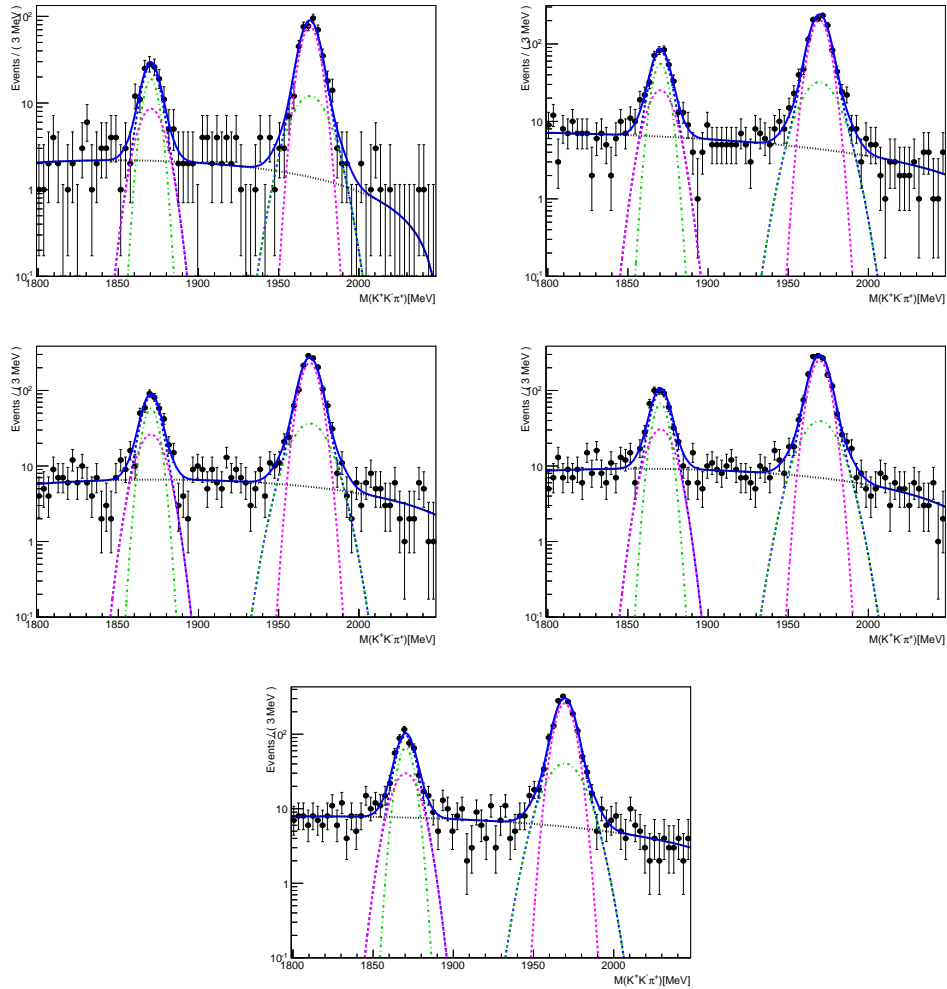


Figure 1.11: Signal data 1D fit results for magnet down, muon momentum bin 6 – 20 GeV, for  $D_s^+$ . The blue dotted line is DfB and the black dashed line is BKG. The bins in each plot are the bins of  $q \times p_x$  vs  $p_y$  with respect to the muon. The upper left is bin 1, upper right is bin 2, middle left is bin 3, middle right is bin 4, and lowest plot is bin 5.

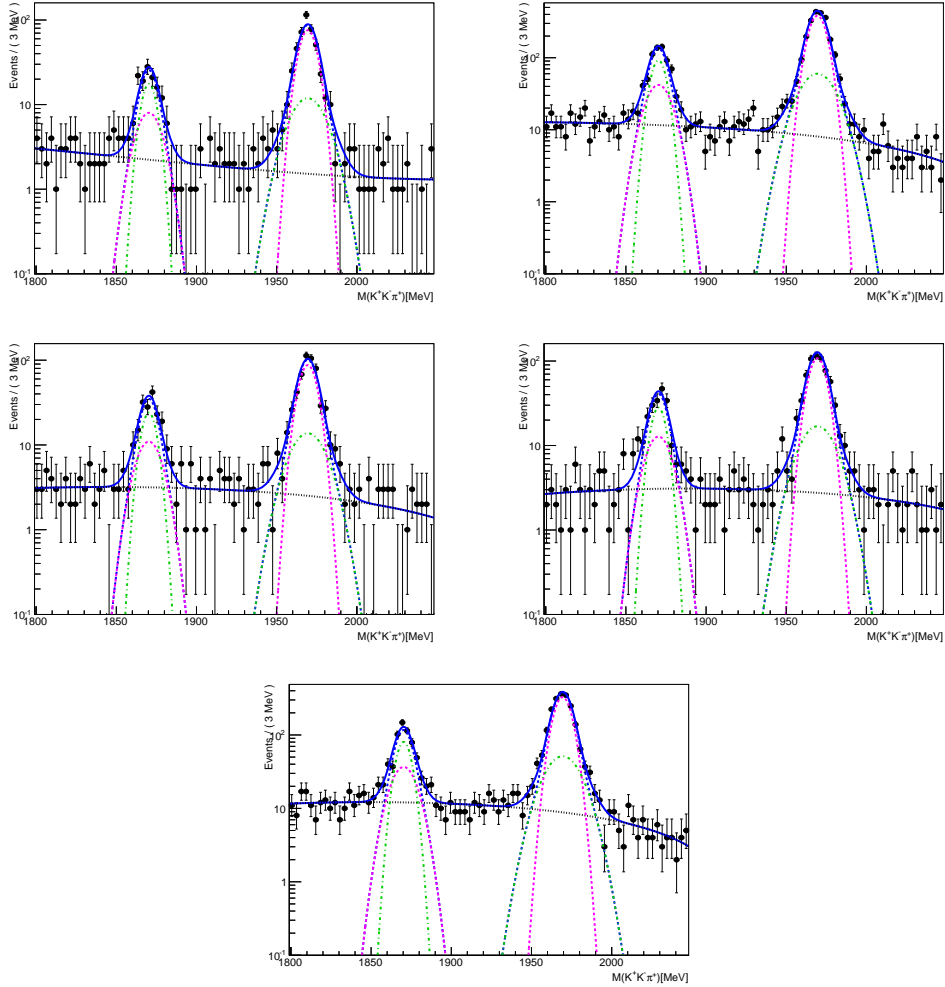


Figure 1.12: Signal data 1D fit results for magnet down, muon momentum bin 6 – 20 GeV for  $D_s^+$ . The blue dotted line is DfB and the black dashed line is BKG. The bins in each plot are the bins of  $q \times p_x$  vs  $p_y$  with respect to the muon. The upper left is bin 6, upper right is bin 7, middle left is bin 8, middle right is bin 9, and lowest plot is bin 10.

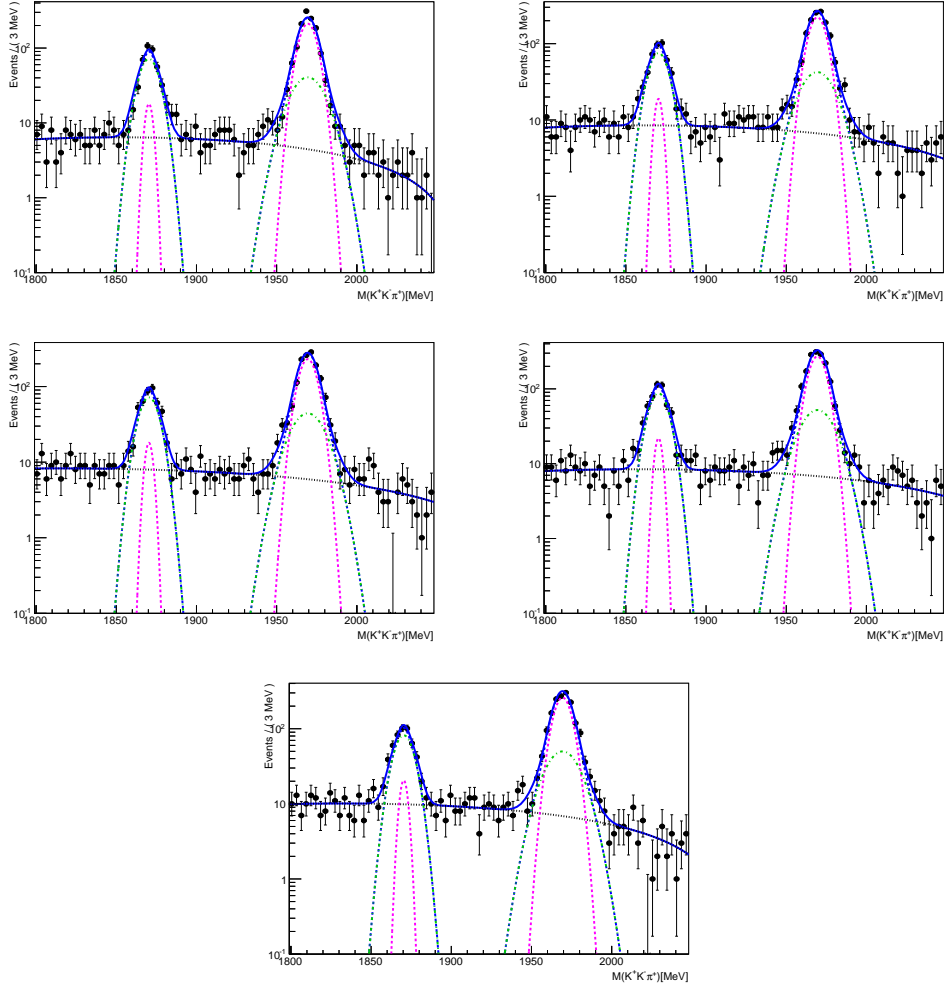


Figure 1.13: Signal data 1D fit results for magnet down, muon momentum bin 20 – 30 GeV, for  $D_s^+$ . The blue dotted line is DfB, the red solid line is PMT, the black dashed line is BKG. The bins in each plot are the bins of  $q \times p_x$  vs  $p_y$  with respect to the muon. The upper left is bin 1, upper right is bin 2, middle left is bin 3, middle right is bin 4, and lowest plot is bin 5.



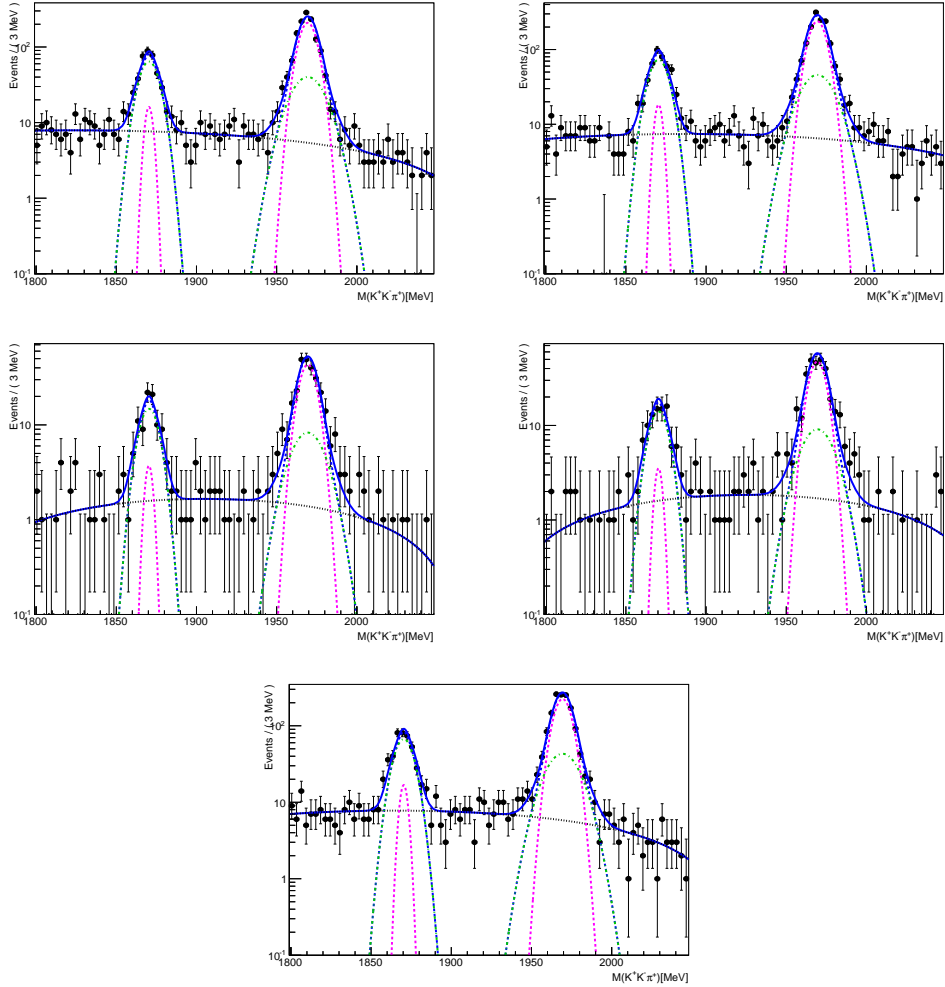


Figure 1.14: Signal data 1D fit results for magnet down, muon momentum bin 20 – 30 GeV, for  $D_s^+$ . The blue dotted line is DfB and the black dashed line is BKG. The bins in each plot are the bins of  $q \times p_x$  vs  $p_y$  with respect to the muon. The upper left is bin 6, upper right is bin 7, middle left is bin 8, middle right is bin 9, and lowest plot is bin 10.

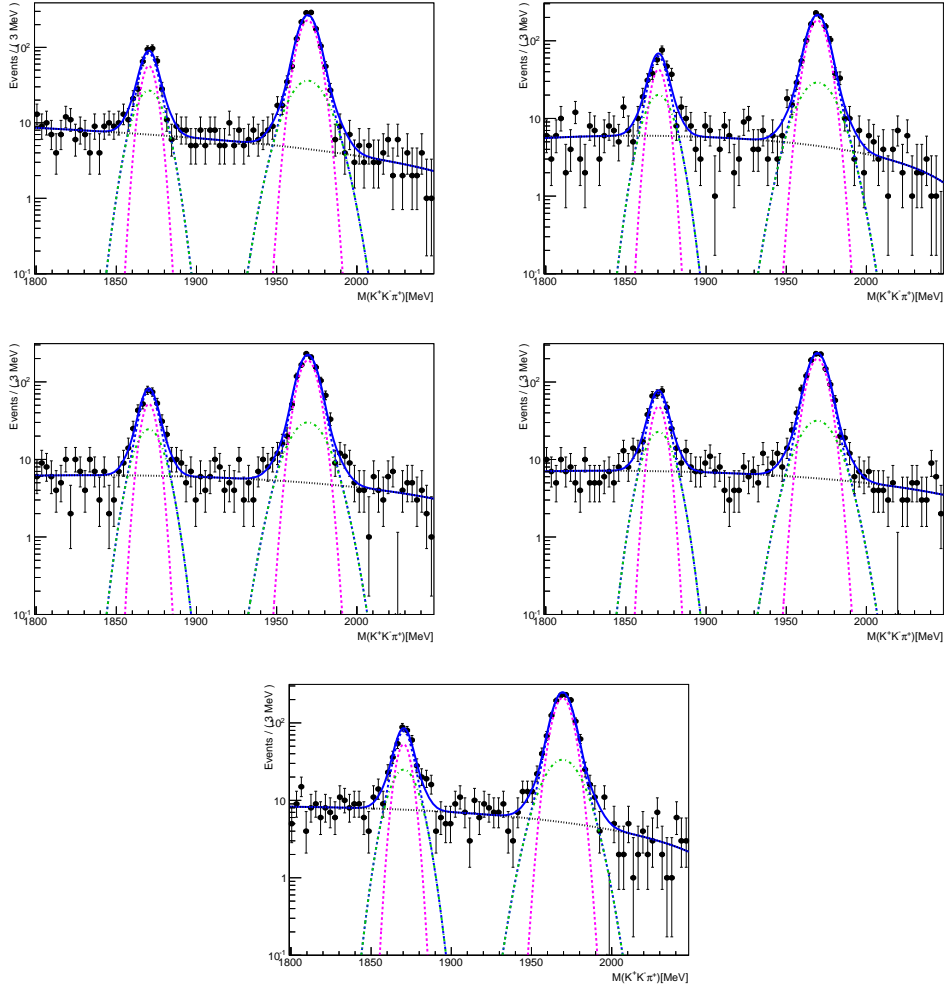


Figure 1.15: Signal data 1D fit results for magnet down, muon momentum bin 30 – 40 GeV, for  $D_s^+$ . The blue dotted line is DfB and the black dashed line is BKG. The bins in each plot are the bins of  $q \times p_x$  vs  $p_y$  with respect to the muon. The upper left is bin 1, upper right is bin 2, middle left is bin 3, middle right is bin 4, and lowest plot is bin 5.

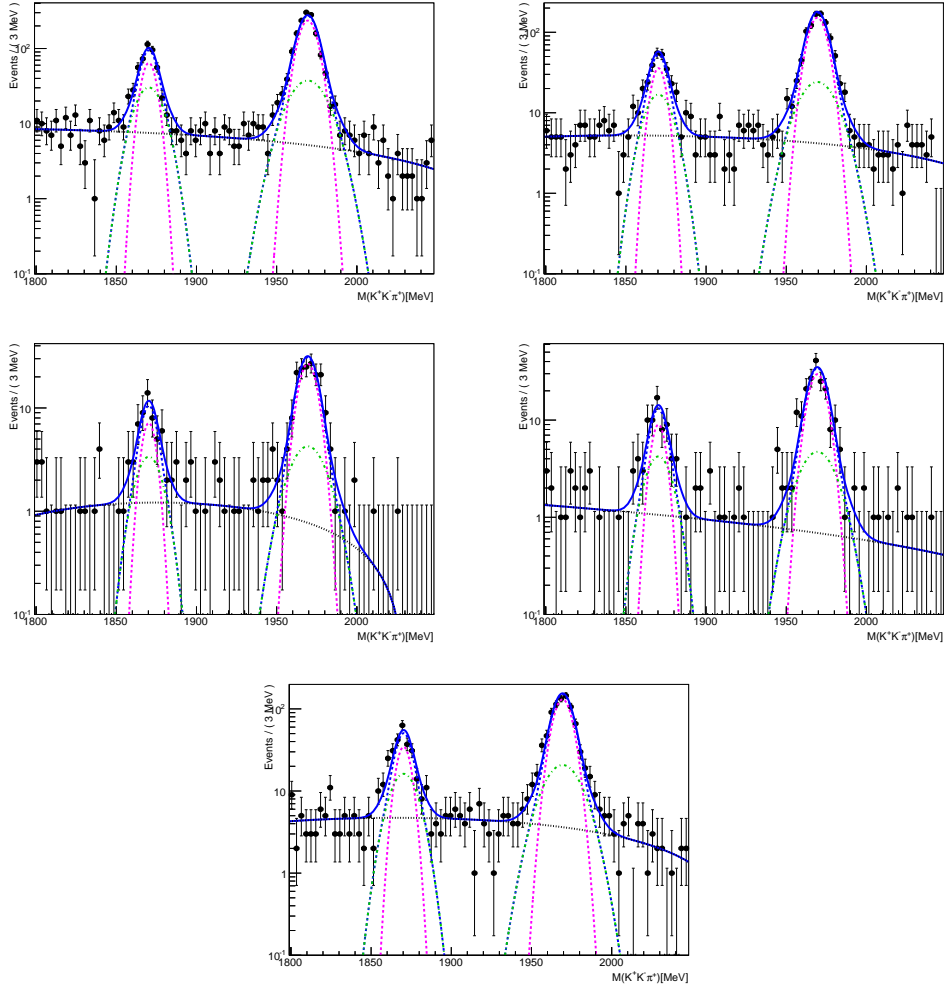


Figure 1.16: Signal data 1D fit results for magnet down, muon momentum bin 30 – 40 GeV, for  $D_s^+$ . The blue dotted line is DfB and the black dashed line is BKG. The bins in each plot are the bins of  $q \times p_x$  vs  $p_y$  with respect to the muon. The upper left is bin 6, upper right is bin 7, middle left is bin 8, middle right is bin 9, and lowest plot is bin 10.

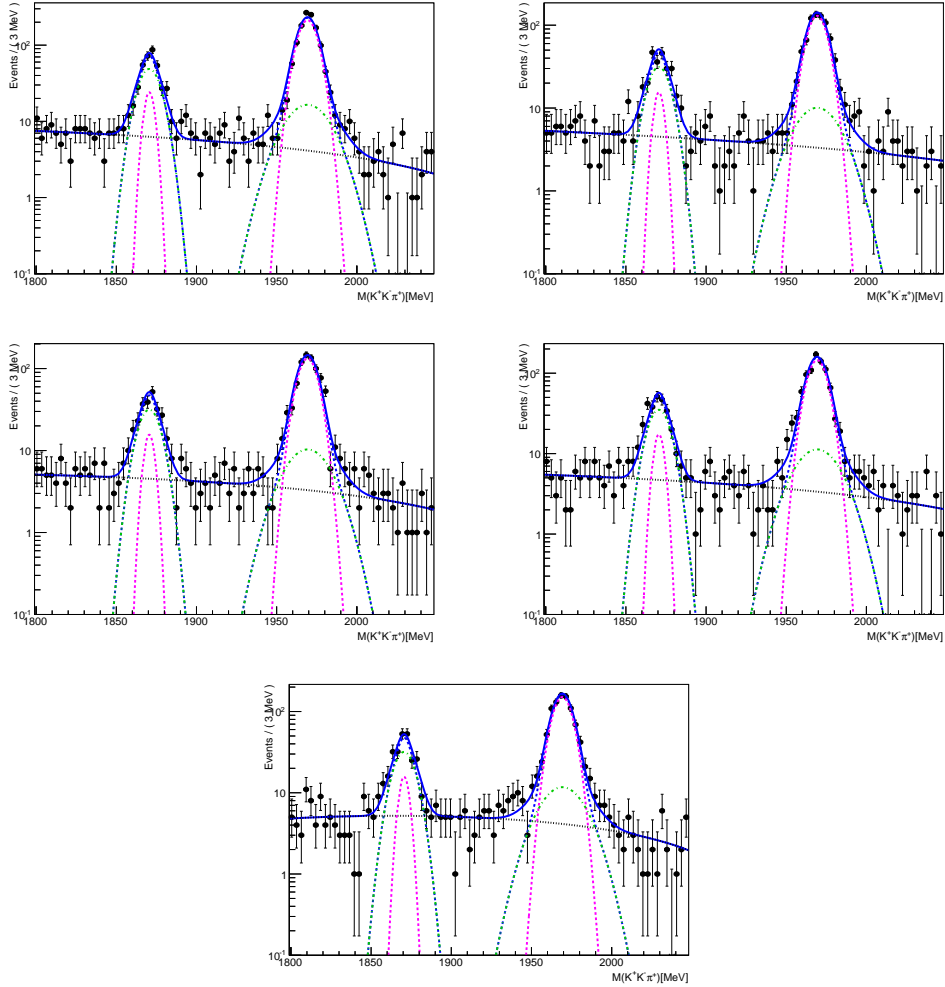


Figure 1.17: Signal data 1D fit results for magnet down, muon momentum bin 40 – 50 GeV, for  $D_s^+$ . The blue dotted line is DfB and the black dashed line is BKG. The bins in each plot are the bins of  $q \times p_x$  vs  $p_y$  with respect to the muon. The upper left is bin 1, upper right is bin 2, middle left is bin 3, middle right is bin 4, and lowest plot is bin 5.

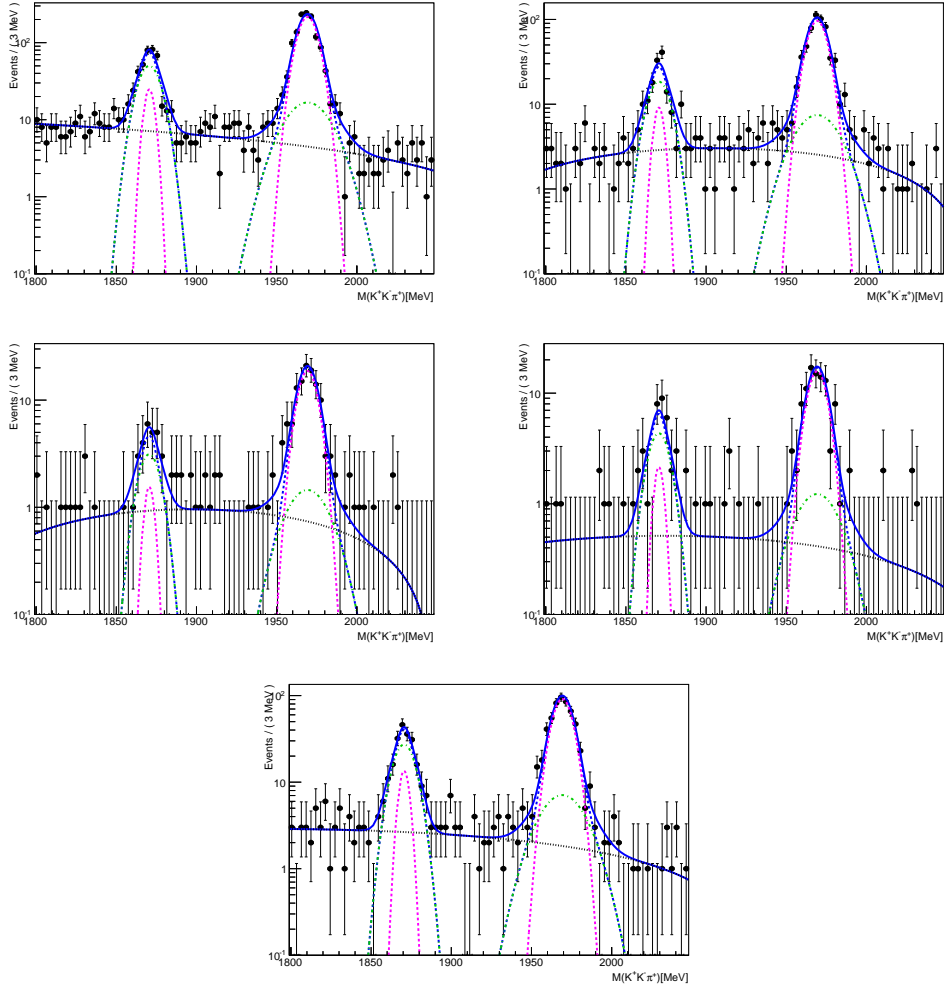


Figure 1.18: Signal data 1D fit results for magnet down, muon momentum bin 40 – 50 GeV, for  $D_s^+$ . The blue dotted line is DfB and the black dashed line is BKG. The bins in each plot are the bins of  $q \times p_x$  vs  $p_y$  with respect to the muon. The upper left is bin 6, upper right is bin 7, middle left is bin 8, middle right is bin 9, and lowest plot is bin 10.

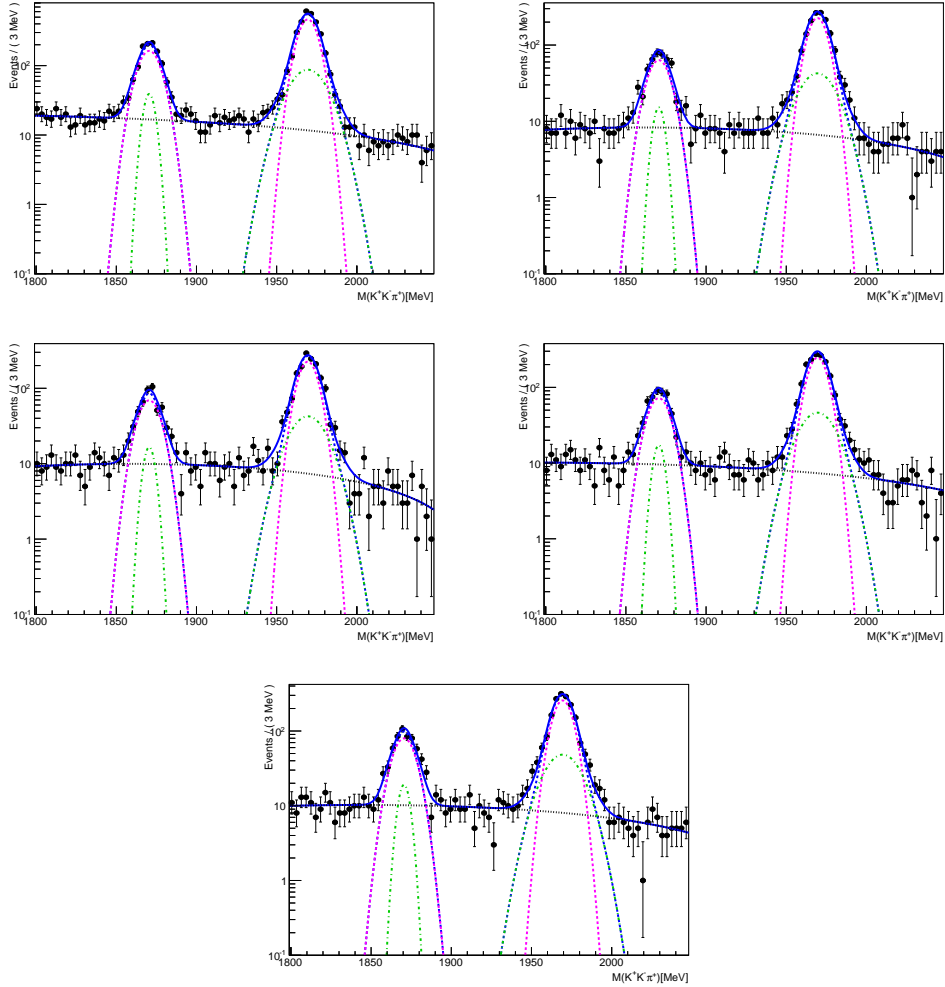


Figure 1.19: Signal data 1D fit results for magnet down, muon momentum bin 50 – 100 GeV, for  $D_s^+$ . The blue dotted line is DfB and the black dashed line is BKG. The bins in each plot are the bins of  $q \times p_x$  vs  $p_y$  with respect to the muon. The upper left is bin 1, upper right is bin 2, middle left is bin 3, middle right is bin 4, and lowest plot is bin 5.

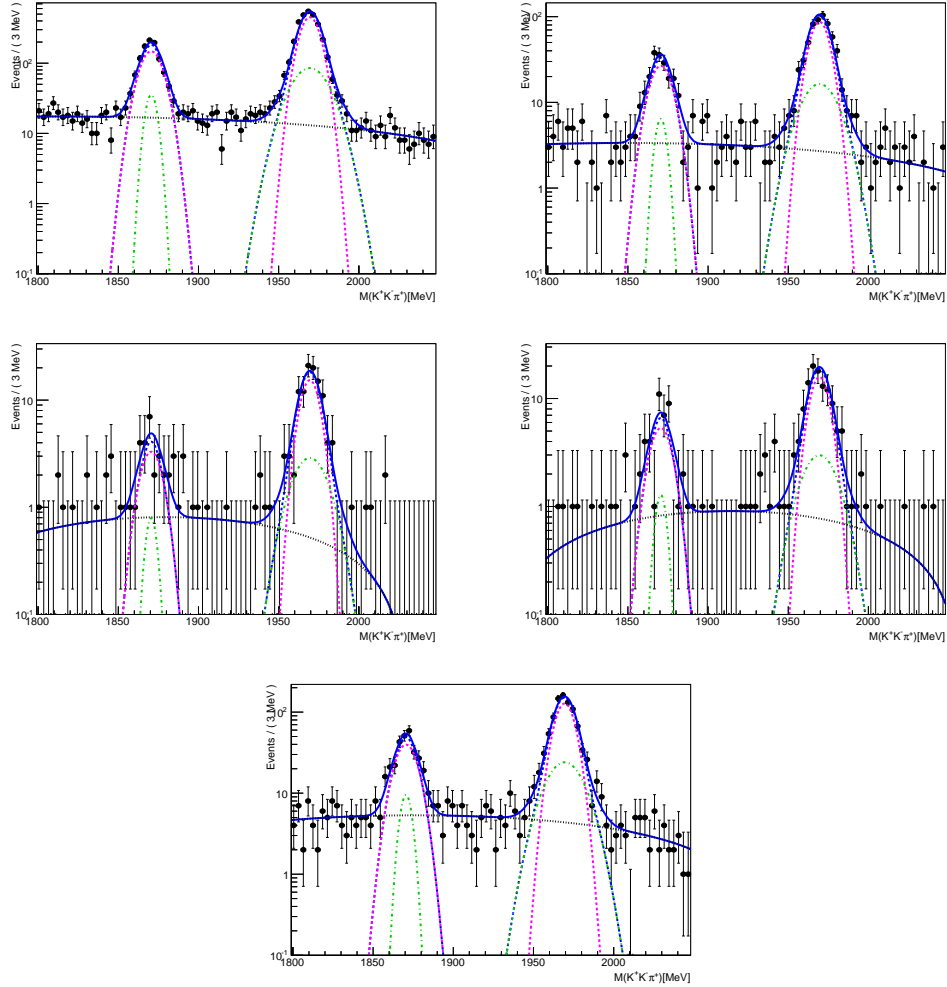


Figure 1.20: Signal data 1D fit results for magnet down, muon momentum bin 50 – 100 GeV, for  $D_s^+$ . The blue dotted line is DfB and the black dashed line is BKG. The bins in each plot are the bins of  $q \times p_x$  vs  $p_y$  with respect to the muon. The upper left is bin 6, upper right is bin 7, middle left is bin 8, middle right is bin 9, and lowest plot is bin 10.

## 1.2 Magnet Up

All figures in this section show the fit results for the magnet up polarity data for the individual fine kinematic binning in  $q \times p_x$  vs  $p_y$ . In each figure, the dashed green and pink lines are the two Gaussian shapes.

Figures 1.21 through 1.30 illustrate the fits for  $D_s^-$ . Figures 1.21 and 1.22 show the fits in muon momentum bin 1. Figures 1.23 and 1.24 show the fits in muon momentum bin 2. Figures 1.25 and 1.26 show the fits in muon momentum bin 3. Figures 1.27 and 1.28 show the fits in muon momentum bin 4. Figures 1.29 and 1.30 show the fits in muon momentum bin 5.



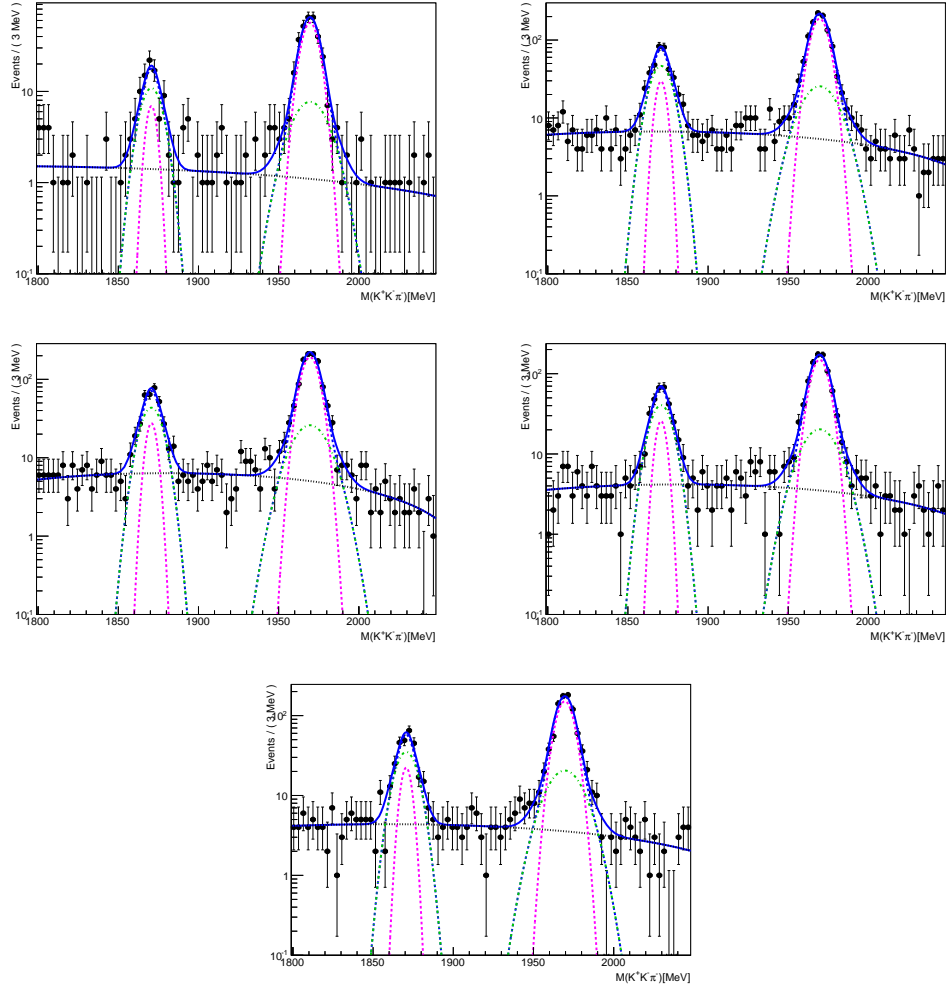


Figure 1.21: Signal data 1D fit results for magnet up, muon momentum bin 6 – 20 GeV, for  $D_s^-$ . The blue dotted line is DfB and the black dashed line is BKG. The bins in each plot are the bins of  $q \times p_x$  vs  $p_y$  with respect to the muon. The upper left is bin 1, upper right is bin 2, middle left is bin 3, middle right is bin 4, and lowest plot is bin 5.

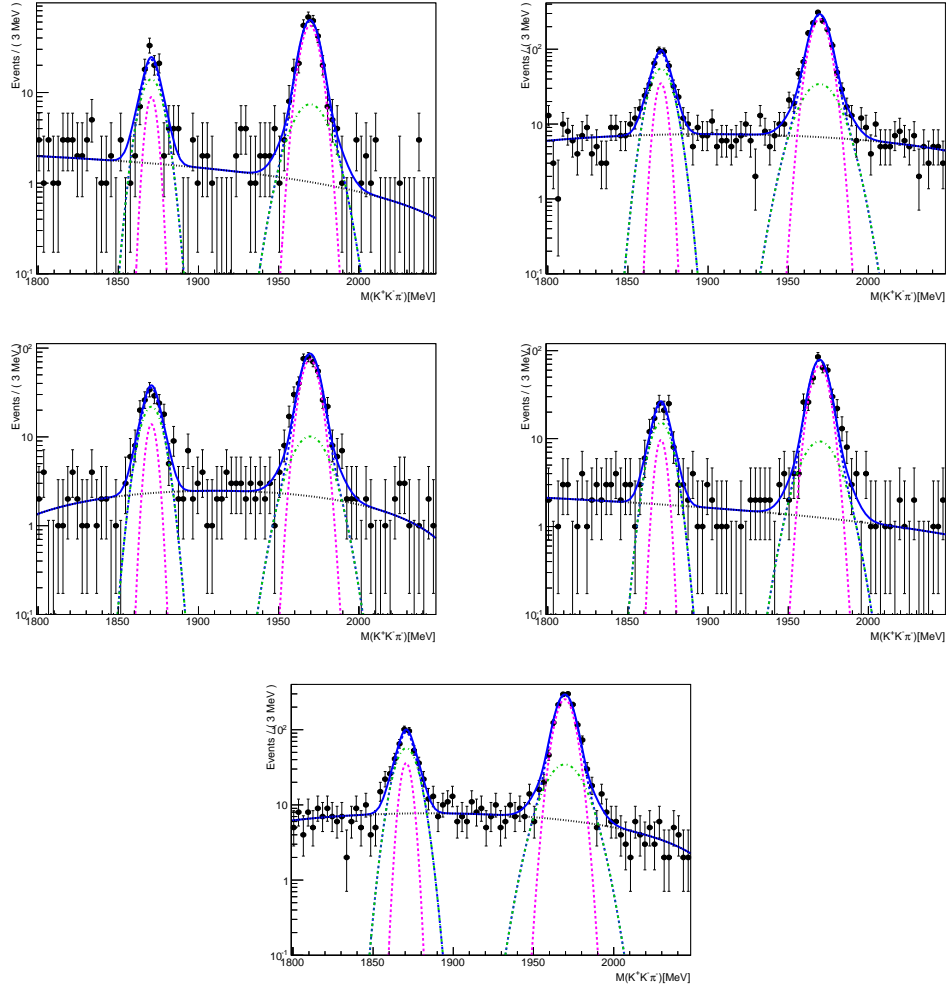


Figure 1.22: Signal data 1D fit results for magnet up, muon momentum bin 6 – 20 GeV for  $D_s^-$ . The blue dotted line is DfB and the black dashed line is BKG. The bins in each plot are the bins of  $q \times p_x$  vs  $p_y$  with respect to the muon. The upper left is bin 6, upper right is bin 7, middle left is bin 8, middle right is bin 9, and lowest plot is bin 10.

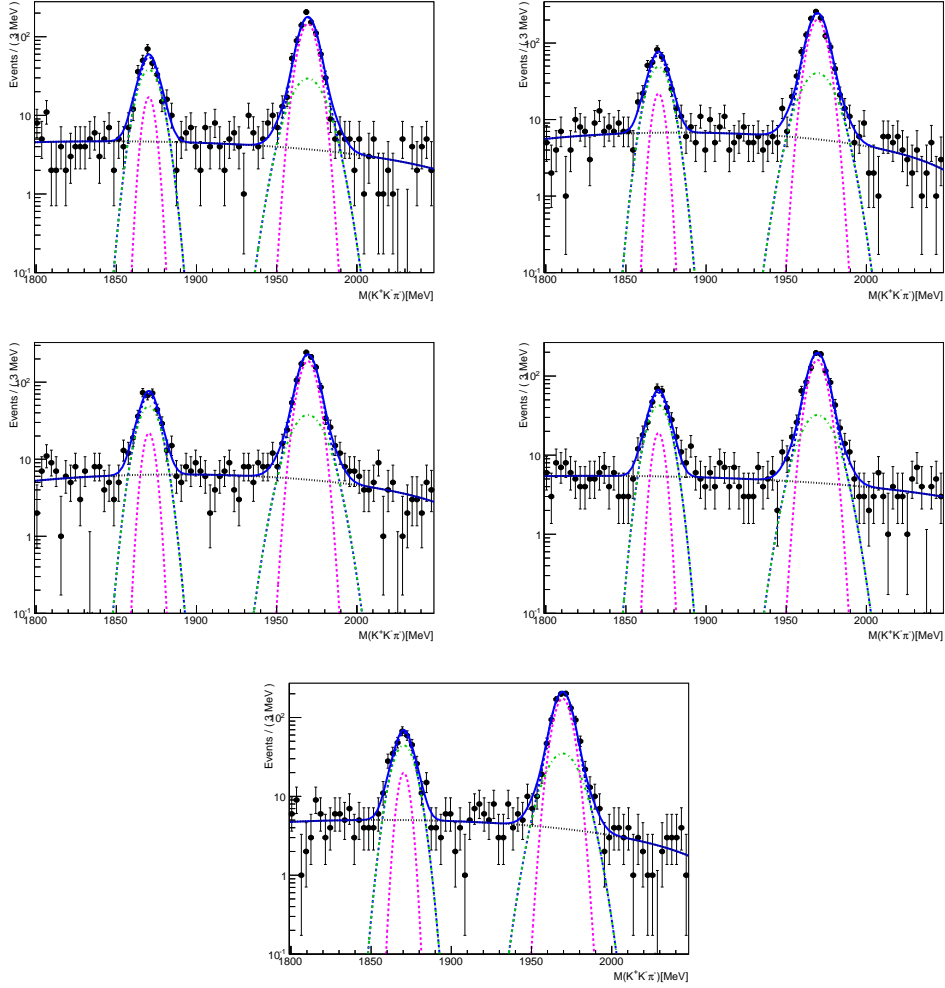


Figure 1.23: Signal data 1D fit results for magnet up, muon momentum bin 20 – 30 GeV, for  $D_s^-$ . The blue dotted line is DfB, the red solid line is PMT, the black dashed line is BKG. The bins in each plot are the bins of  $q \times p_x$  vs  $p_y$  with respect to the muon. The upper left is bin 1, upper right is bin 2, middle left is bin 3, middle right is bin 4, and lowest plot is bin 5.

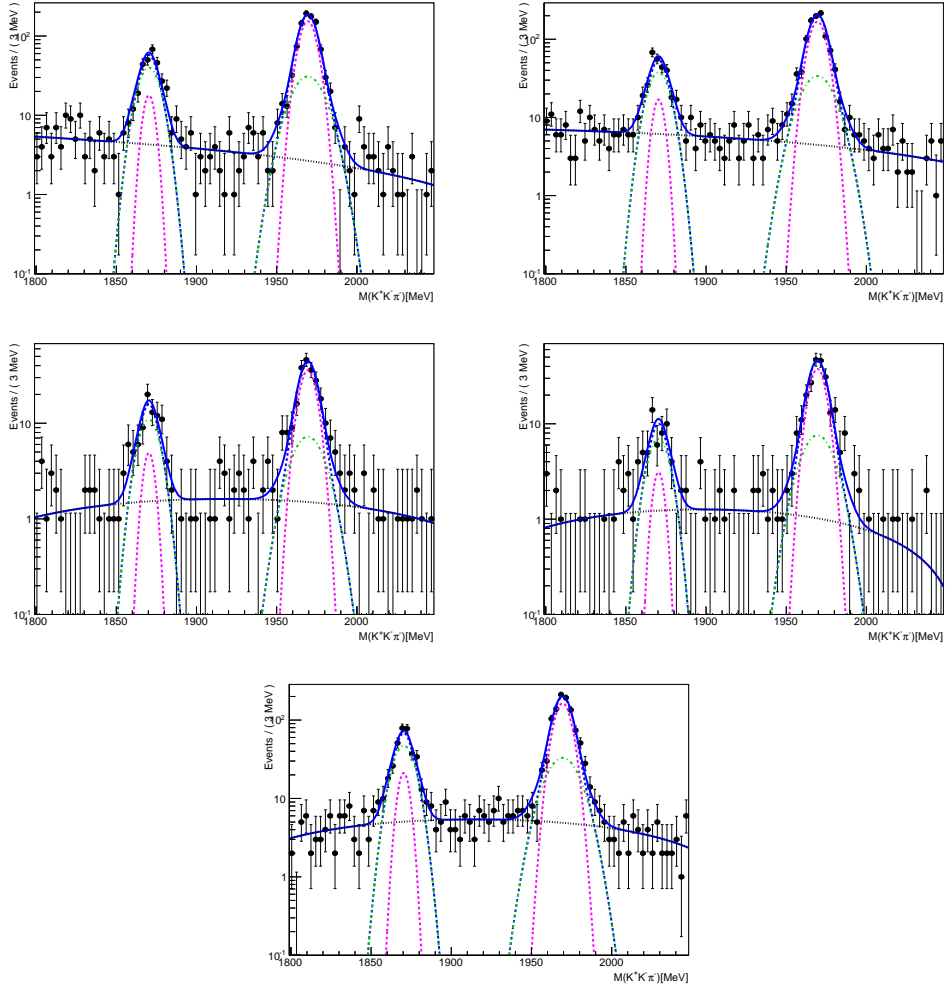


Figure 1.24: Signal data 1D fit results for magnet up, muon momentum bin 20 – 30 GeV, for  $D_s^-$ . The blue dotted line is DfB and the black dashed line is BKG. The bins in each plot are the bins of  $q \times p_x$  vs  $p_y$  with respect to the muon. The upper left is bin 6, upper right is bin 7, middle left is bin 8, middle right is bin 9, and lowest plot is bin 10.

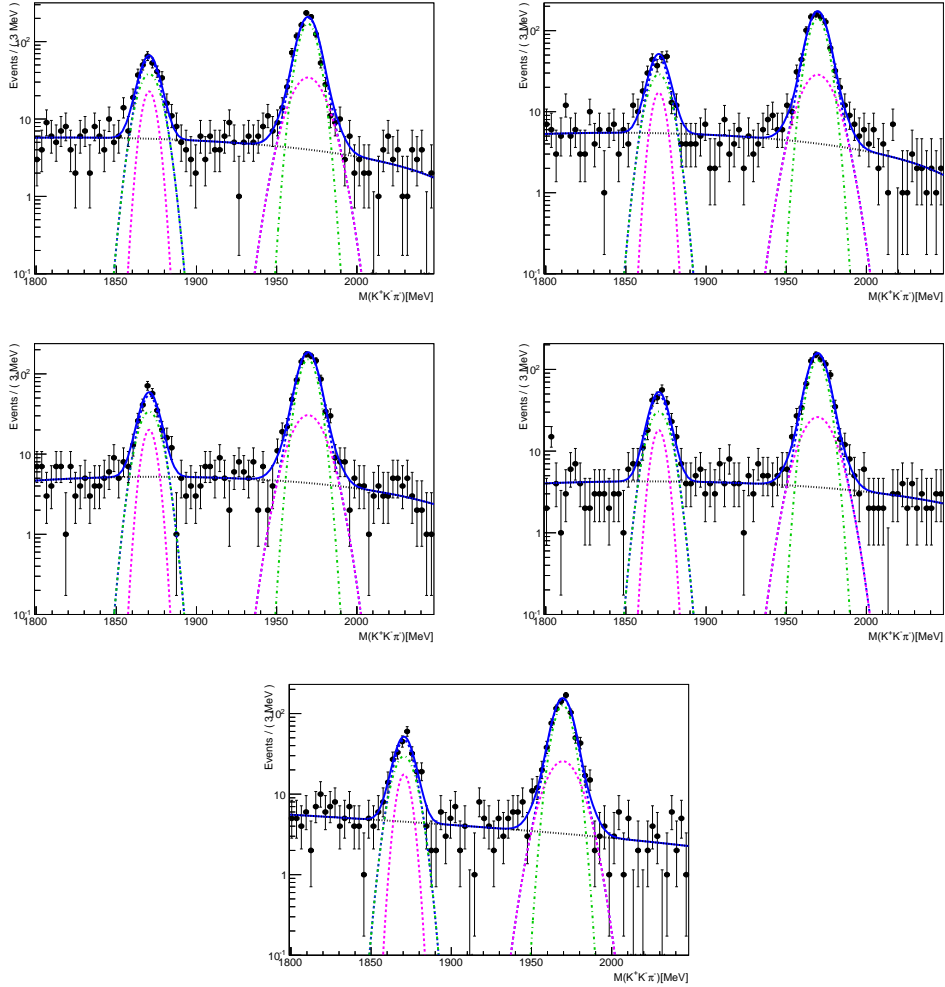


Figure 1.25: Signal data 1D fit results for magnet up, muon momentum bin 30 – 40 GeV, for  $D_s^-$ . The blue dotted line is DfB and the black dashed line is BKG. The bins in each plot are the bins of  $q \times p_x$  vs  $p_y$  with respect to the muon. The upper left is bin 1, upper right is bin 2, middle left is bin 3, middle right is bin 4, and lowest plot is bin 5.

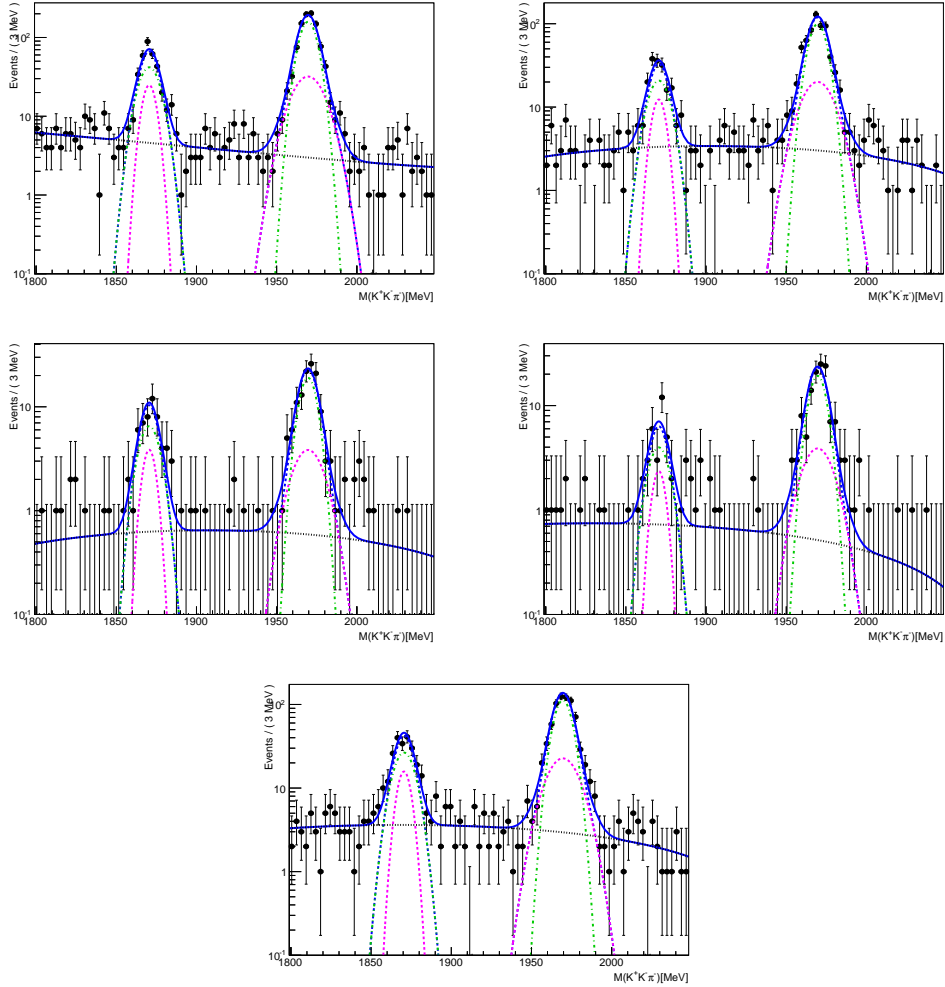


Figure 1.26: Signal data 1D fit results for magnet up, muon momentum bin 30 – 40 GeV, for  $D_s^-$ . The blue dotted line is DfB and the black dashed line is BKG. The bins in each plot are the bins of  $q \times p_x$  vs  $p_y$  with respect to the muon. The upper left is bin 6, upper right is bin 7, middle left is bin 8, middle right is bin 9, and lowest plot is bin 10.

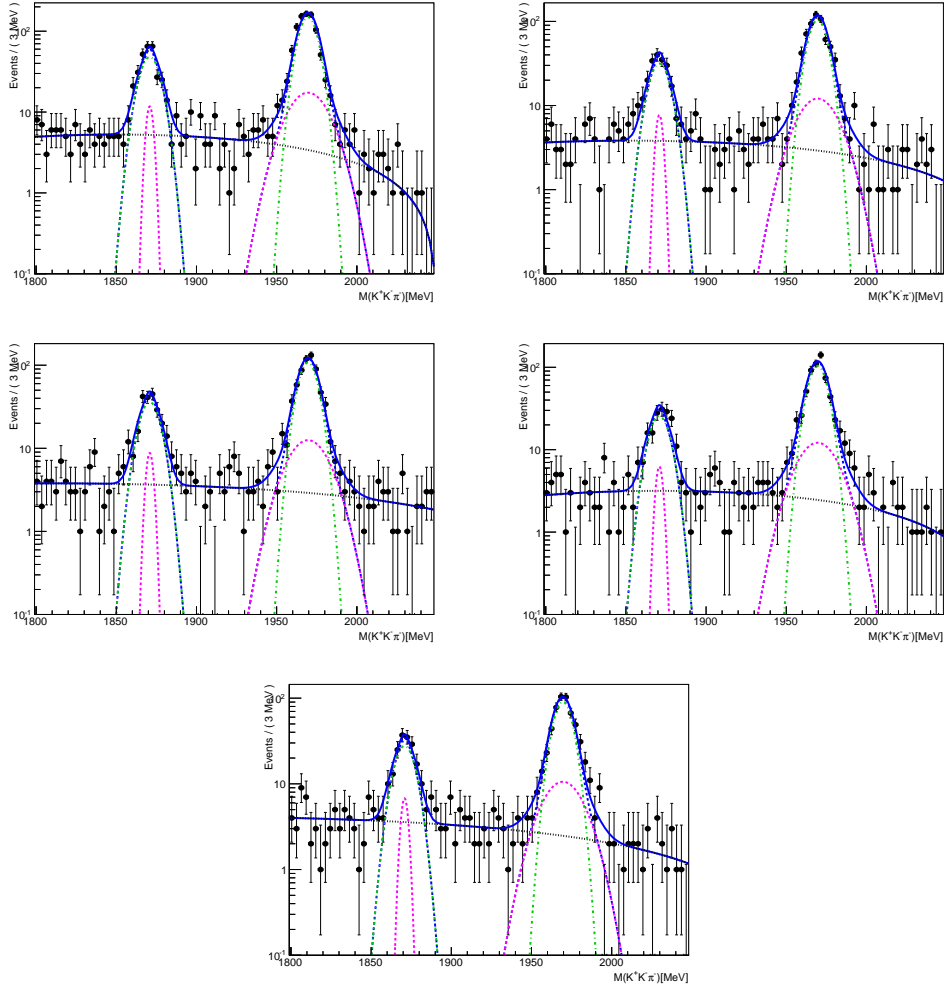


Figure 1.27: Signal data 1D fit results for magnet up, muon momentum bin 40 – 50 GeV, for  $D_s^-$ . The blue dotted line is DfB and the black dashed line is BKG. The bins in each plot are the bins of  $q \times p_x$  vs  $p_y$  with respect to the muon. The upper left is bin 1, upper right is bin 2, middle left is bin 3, middle right is bin 4, and lowest plot is bin 5.

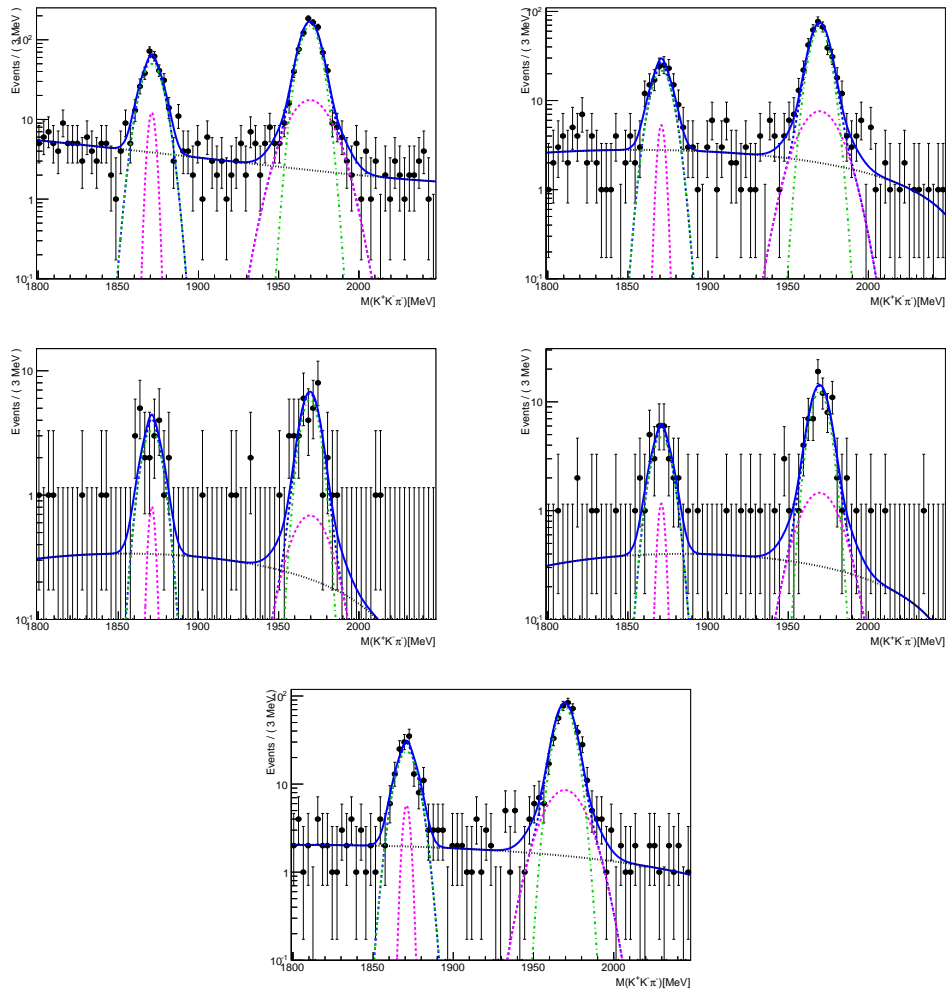


Figure 1.28: Signal data 1D fit results for magnet up, muon momentum bin 40 – 50 GeV, for  $D_s^-$ . The blue dotted line is DfB and the black dashed line is BKG. The bins in each plot are the bins of  $q \times p_x$  vs  $p_y$  with respect to the muon. The upper left is bin 6, upper right is bin 7, middle left is bin 8, middle right is bin 9, and lowest plot is bin 10.



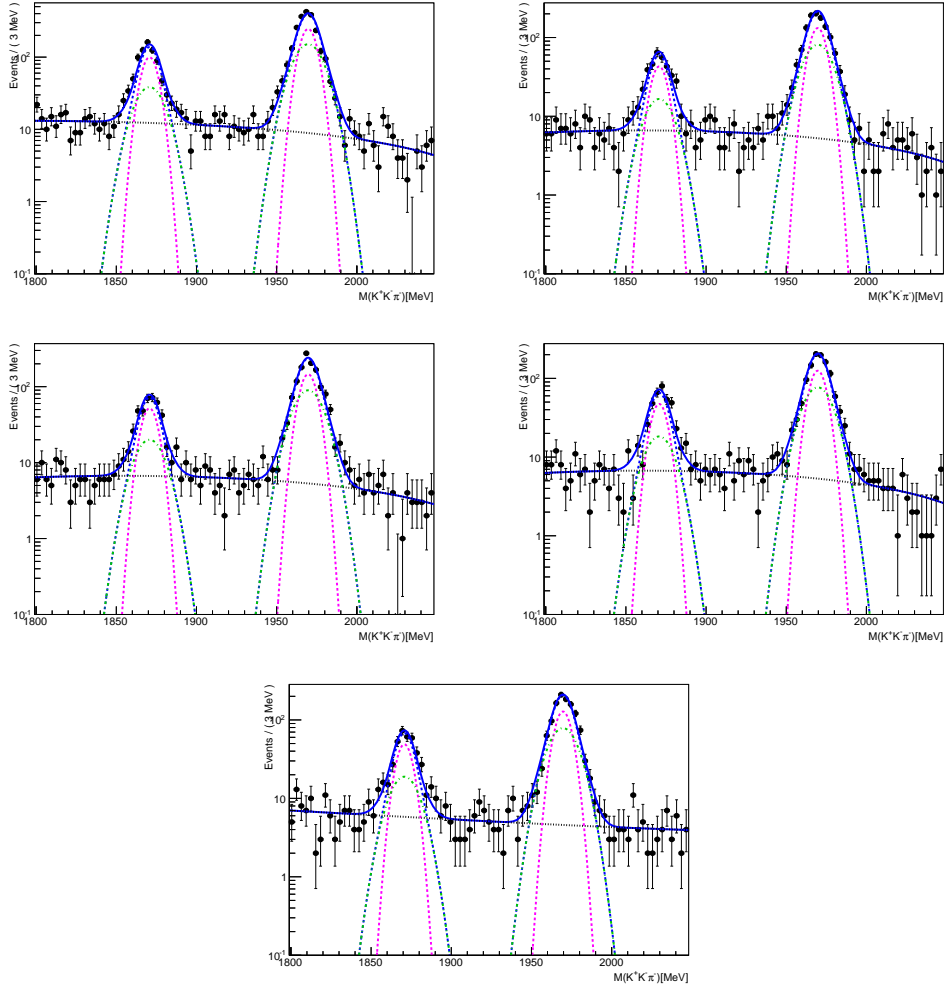


Figure 1.29: Signal data 1D fit results for magnet up, muon momentum bin 50 – 100 GeV, for  $D_s^-$ . The blue dotted line is DfB and the black dashed line is BKG. The bins in each plot are the bins of  $q \times p_x$  vs  $p_y$  with respect to the muon. The upper left is bin 1, upper right is bin 2, middle left is bin 3, middle right is bin 4, and lowest plot is bin 5.

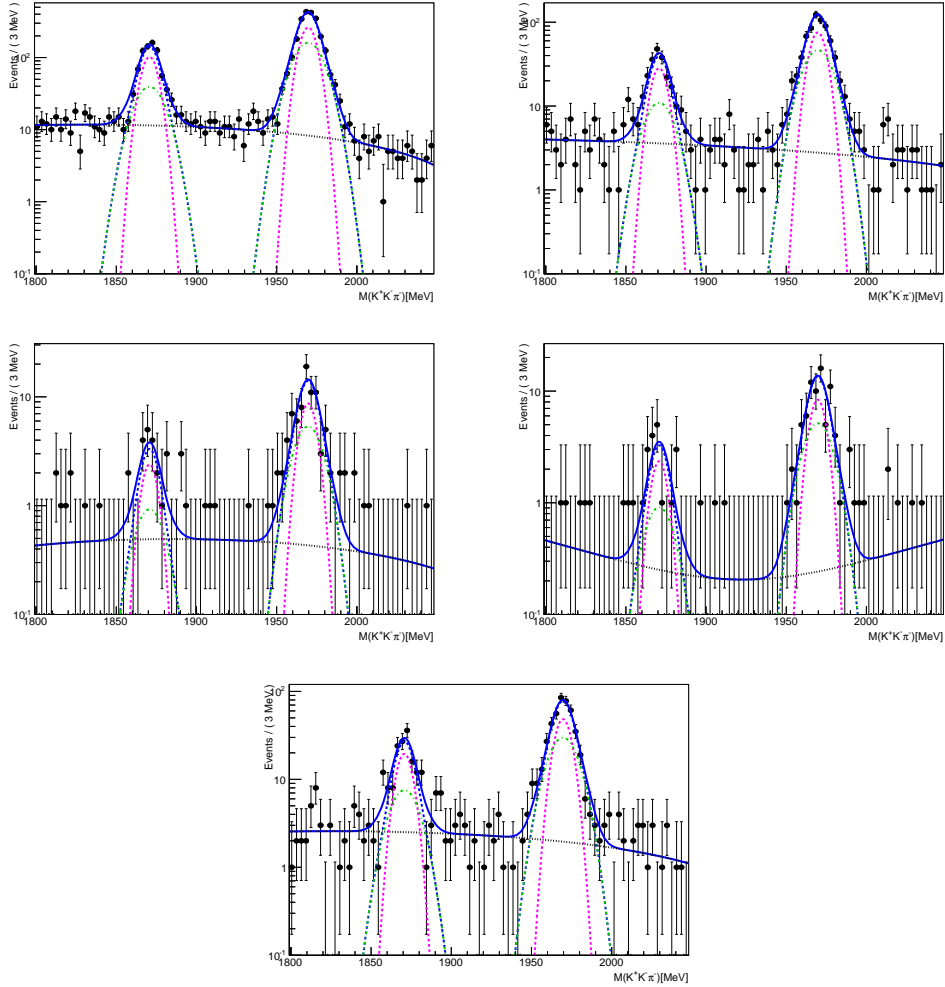


Figure 1.30: Signal data 1D fit results for magnet up, muon momentum bin 50 – 100 GeV, for  $D_s^-$ . The blue dotted line is DfB and the black dashed line is BKG. The bins in each plot are the bins of  $q \times p_x$  vs  $p_y$  with respect to the muon. The upper left is bin 6, upper right is bin 7, middle left is bin 8, middle right is bin 9, and lowest plot is bin 10.

Figures 1.31 through 1.40 illustrate the fits for  $D_s^+$ . Figures 1.31 and 1.32 show the fits in muon momentum bin 1. Figures 1.33 and 1.34 show the fits in muon momentum bin 2. Figures 1.35 and 1.36 show the fits in muon momentum bin 3. Figures 1.37 and 1.38 show the fits in muon momentum bin 4. Figures 1.39 and 1.40 show the fits in muon momentum bin 5.

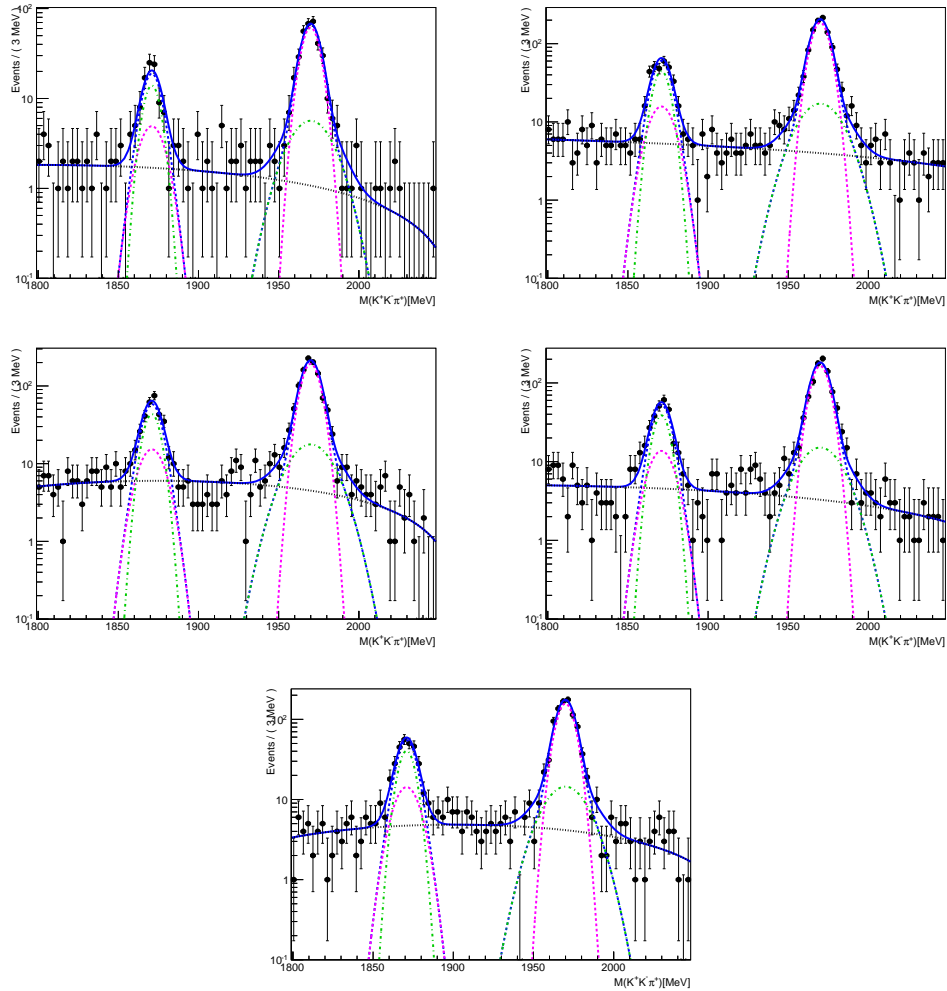


Figure 1.31: Signal data 1D fit results for magnet up, muon momentum bin 6 – 20 GeV, for  $D_s^+$ . The blue dotted line is DfB and the black dashed line is BKG. The bins in each plot are the bins of  $q \times p_x$  vs  $p_y$  with respect to the muon. The upper left is bin 1, upper right is bin 2, middle left is bin 3, middle right is bin 4, and lowest plot is bin 5.

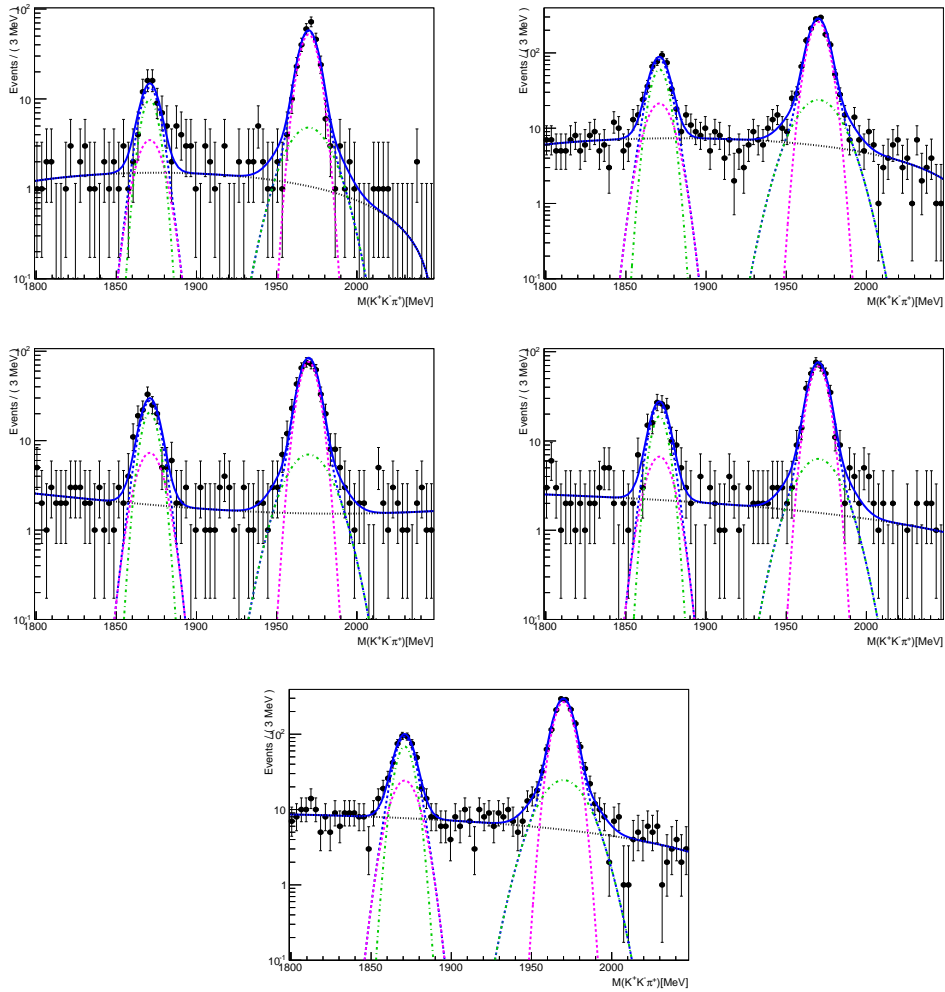


Figure 1.32: Signal data 1D fit results for magnet up, muon momentum bin 6 – 20 GeV for  $D_s^+$ . The blue dotted line is DfB and the black dashed line is BKG. The bins in each plot are the bins of  $q \times p_x$  vs  $p_y$  with respect to the muon. The upper left is bin 6, upper right is bin 7, middle left is bin 8, middle right is bin 9, and lowest plot is bin 10.

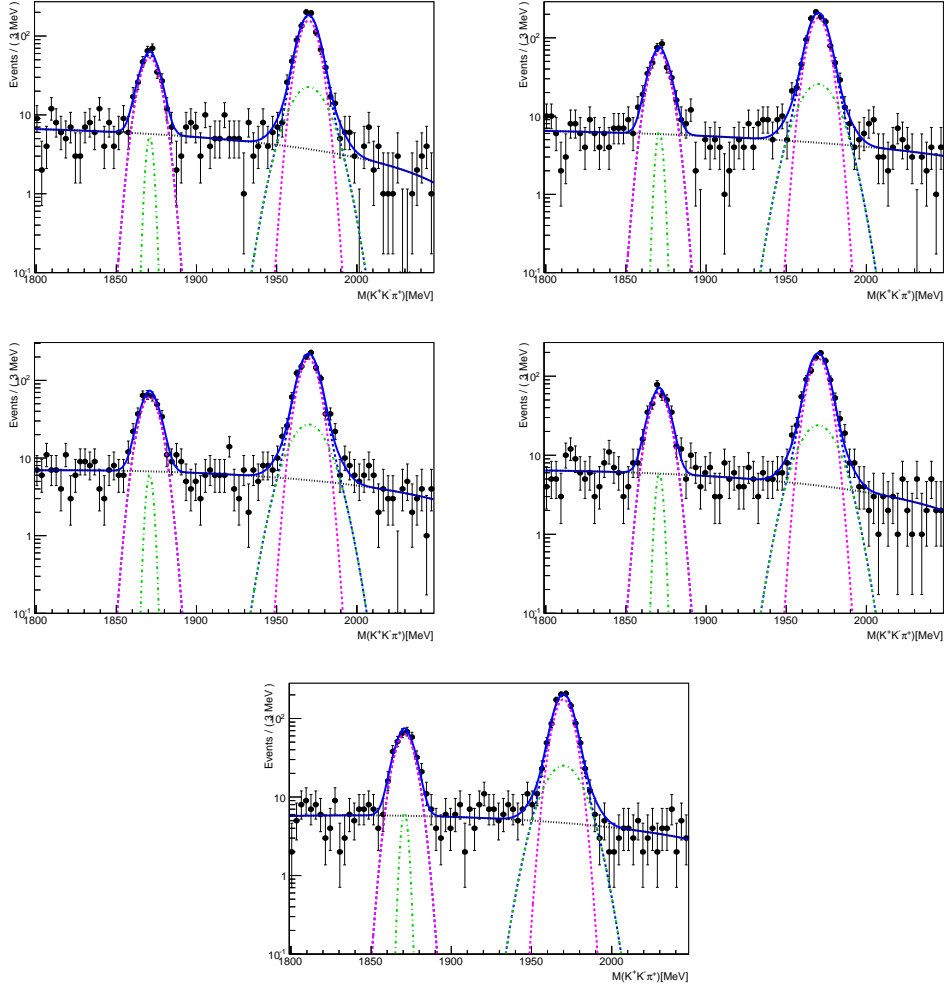


Figure 1.33: Signal data 1D fit results for magnet up, muon momentum bin 20 – 30 GeV, for  $D_s^+$ . The blue dotted line is DfB, the red solid line is PMT, the black dashed line is BKG. The bins in each plot are the bins of  $q \times p_x$  vs  $p_y$  with respect to the muon. The upper left is bin 1, upper right is bin 2, middle left is bin 3, middle right is bin 4, and lowest plot is bin 5.

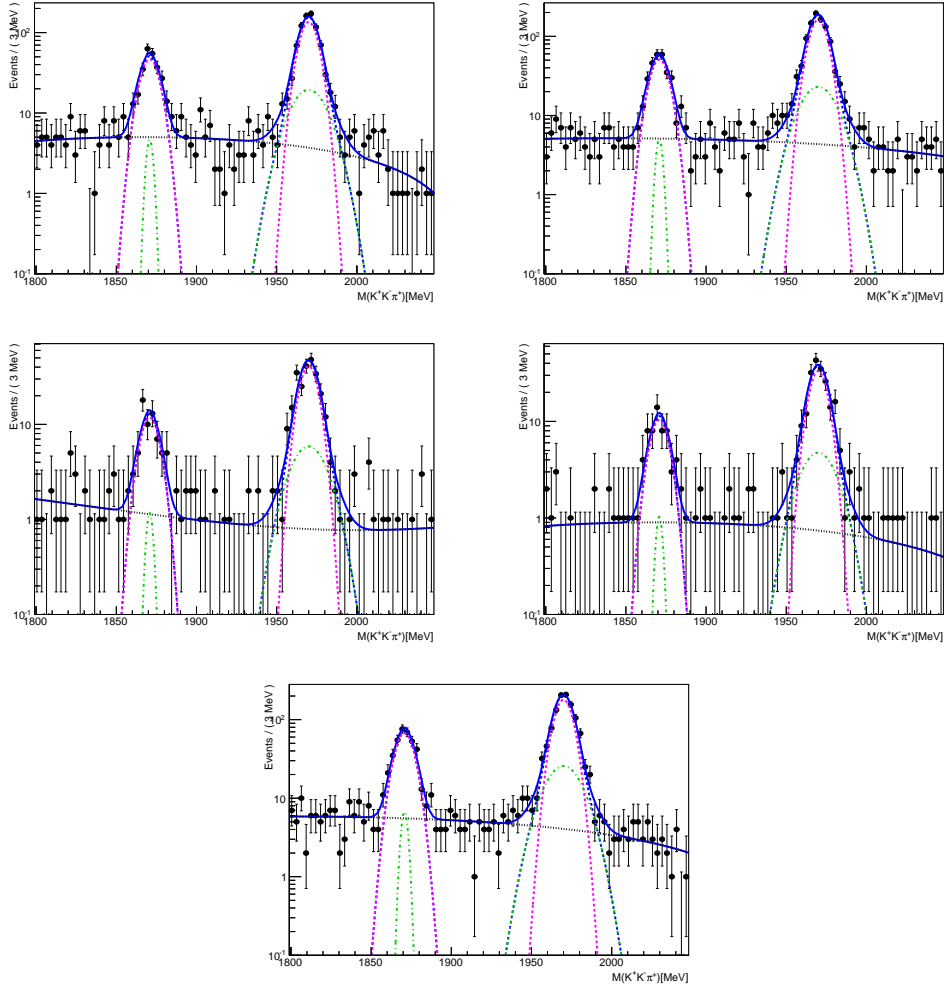


Figure 1.34: Signal data 1D fit results for magnet up, muon momentum bin 20 – 30 GeV, for  $D_s^+$ . The blue dotted line is DfB and the black dashed line is BKG. The bins in each plot are the bins of  $q \times p_x$  vs  $p_y$  with respect to the muon. The upper left is bin 6, upper right is bin 7, middle left is bin 8, middle right is bin 9, and lowest plot is bin 10.

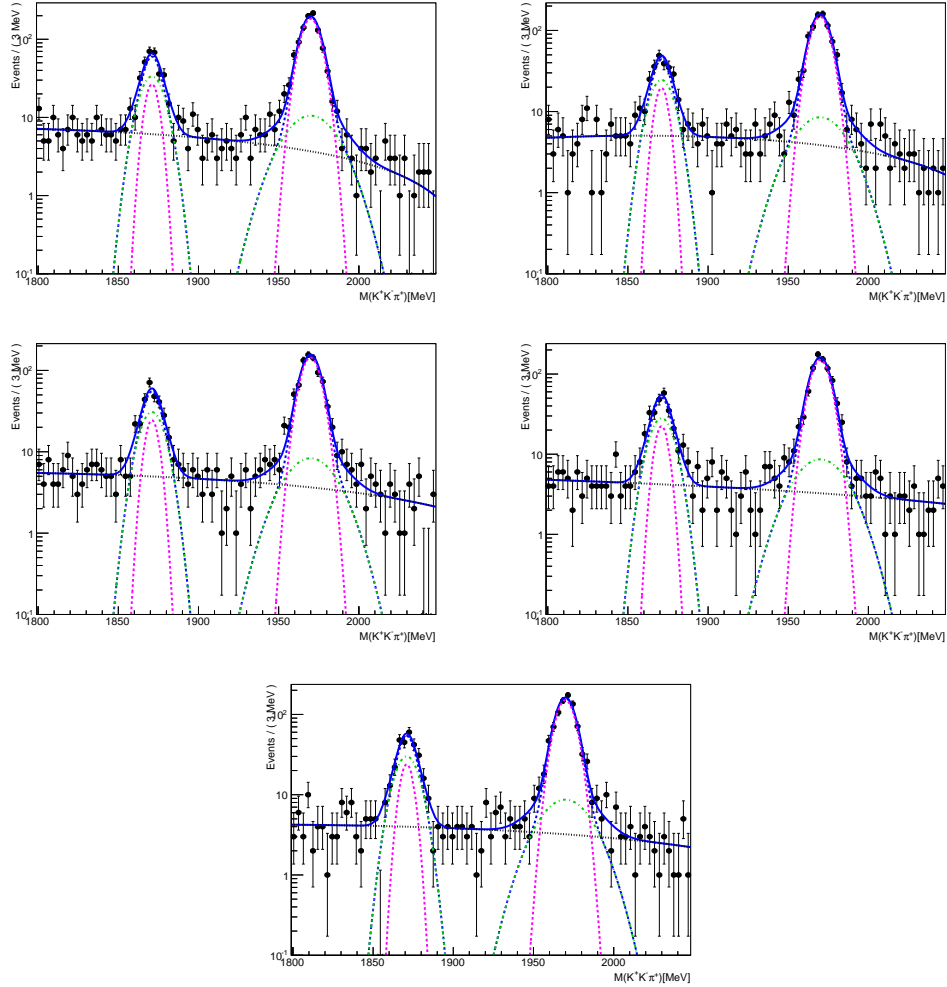


Figure 1.35: Signal data 1D fit results for magnet up, muon momentum bin 30 – 40 GeV, for  $D_s^+$ . The blue dotted line is DfB and the black dashed line is BKG. The bins in each plot are the bins of  $q \times p_x$  vs  $p_y$  with respect to the muon. The upper left is bin 1, upper right is bin 2, middle left is bin 3, middle right is bin 4, and lowest plot is bin 5.

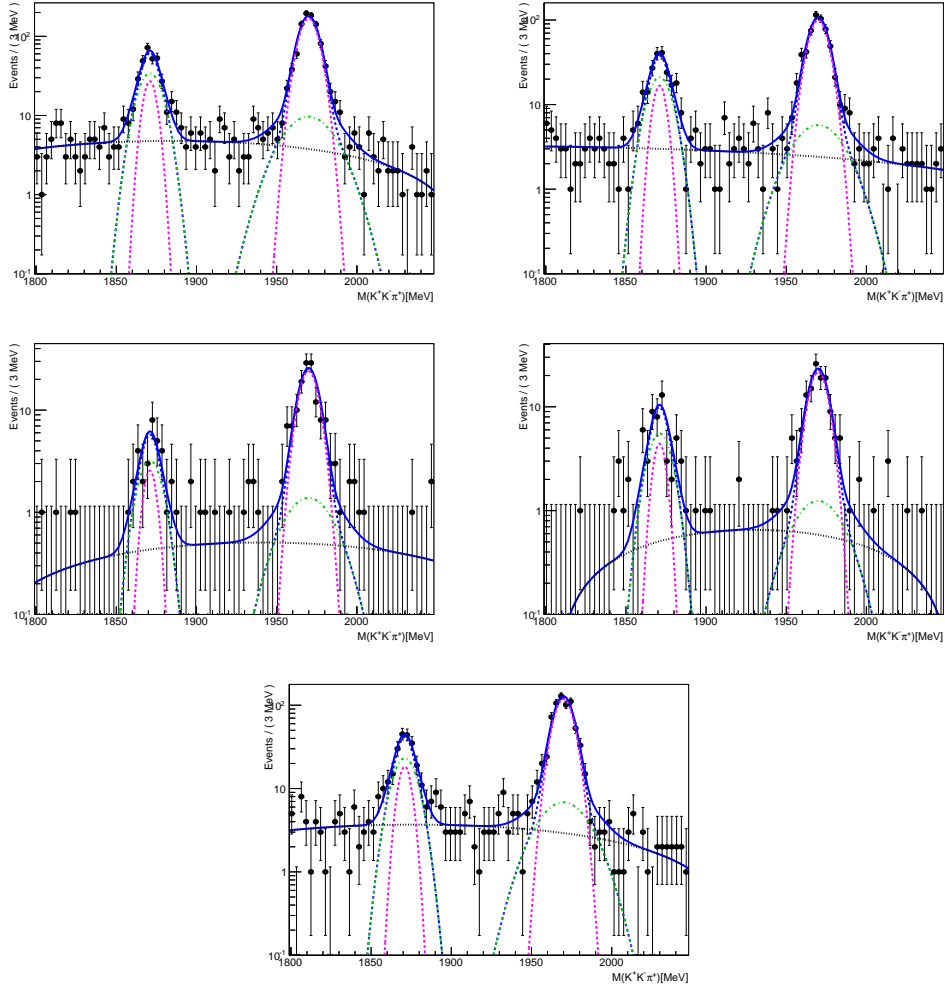


Figure 1.36: Signal data 1D fit results for magnet up, muon momentum bin 30 – 40 GeV, for  $D_s^+$ . The blue dotted line is DfB and the black dashed line is BKG. The bins in each plot are the bins of  $q \times p_x$  vs  $p_y$  with respect to the muon. The upper left is bin 6, upper right is bin 7, middle left is bin 8, middle right is bin 9, and lowest plot is bin 10.



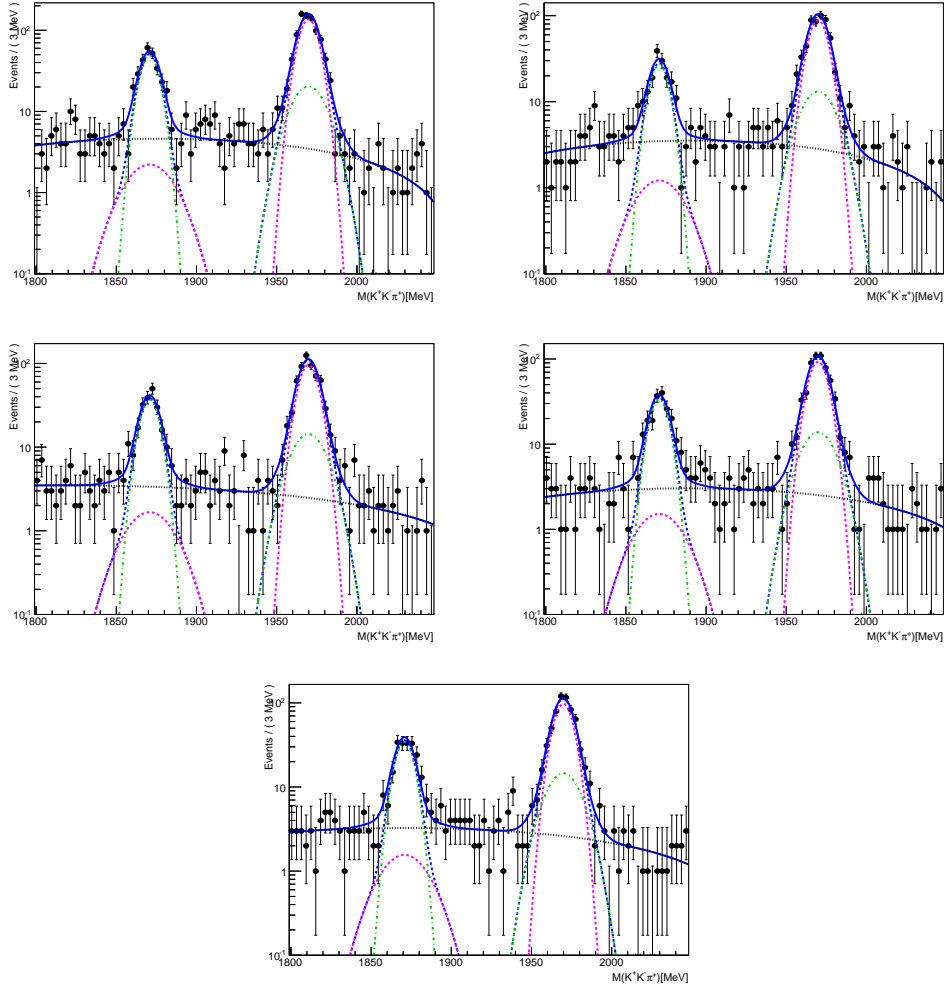


Figure 1.37: Signal data 1D fit results for magnet up, muon momentum bin 40 – 50 GeV, for  $D_s^+$ . The blue dotted line is DfB and the black dashed line is BKG. The bins in each plot are the bins of  $q \times p_x$  vs  $p_y$  with respect to the muon. The upper left is bin 1, upper right is bin 2, middle left is bin 3, middle right is bin 4, and lowest plot is bin 5.

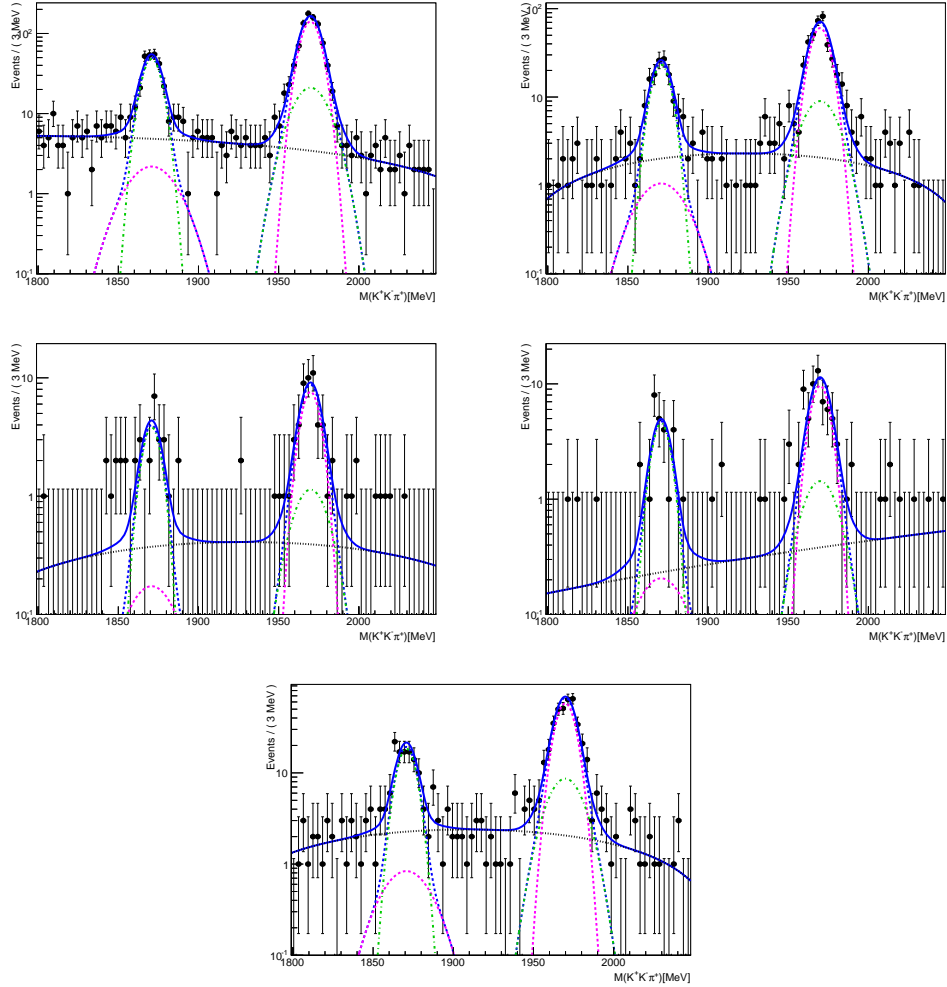


Figure 1.38: Signal data 1D fit results for magnet up, muon momentum bin 40 – 50 GeV, for  $D_s^+$ . The blue dotted line is DfB and the black dashed line is BKG. The bins in each plot are the bins of  $q \times p_x$  vs  $p_y$  with respect to the muon. The upper left is bin 6, upper right is bin 7, middle left is bin 8, middle right is bin 9, and lowest plot is bin 10.

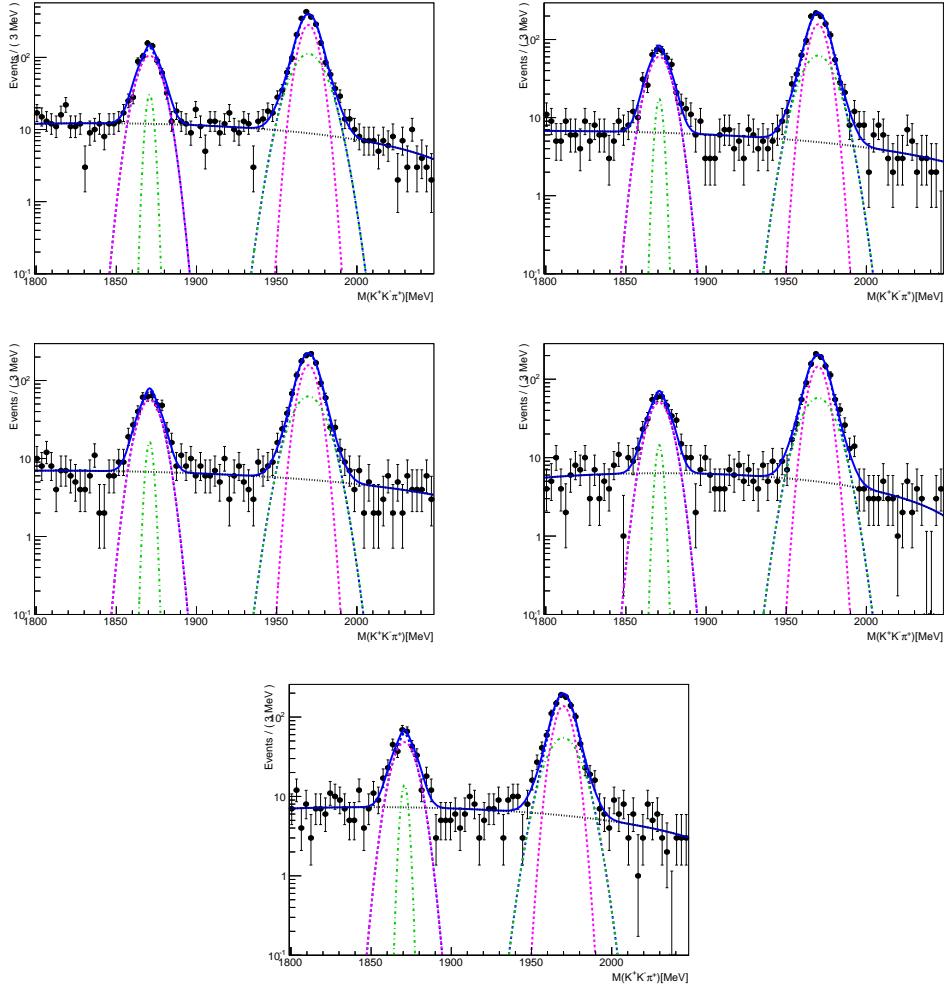


Figure 1.39: Signal data 1D fit results for magnet up, muon momentum bin 50 – 100 GeV, for  $D_s^+$ . The blue dotted line is DfB and the black dashed line is BKG. The bins in each plot are the bins of  $q \times p_x$  vs  $p_y$  with respect to the muon. The upper left is bin 1, upper right is bin 2, middle left is bin 3, middle right is bin 4, and lowest plot is bin 5.

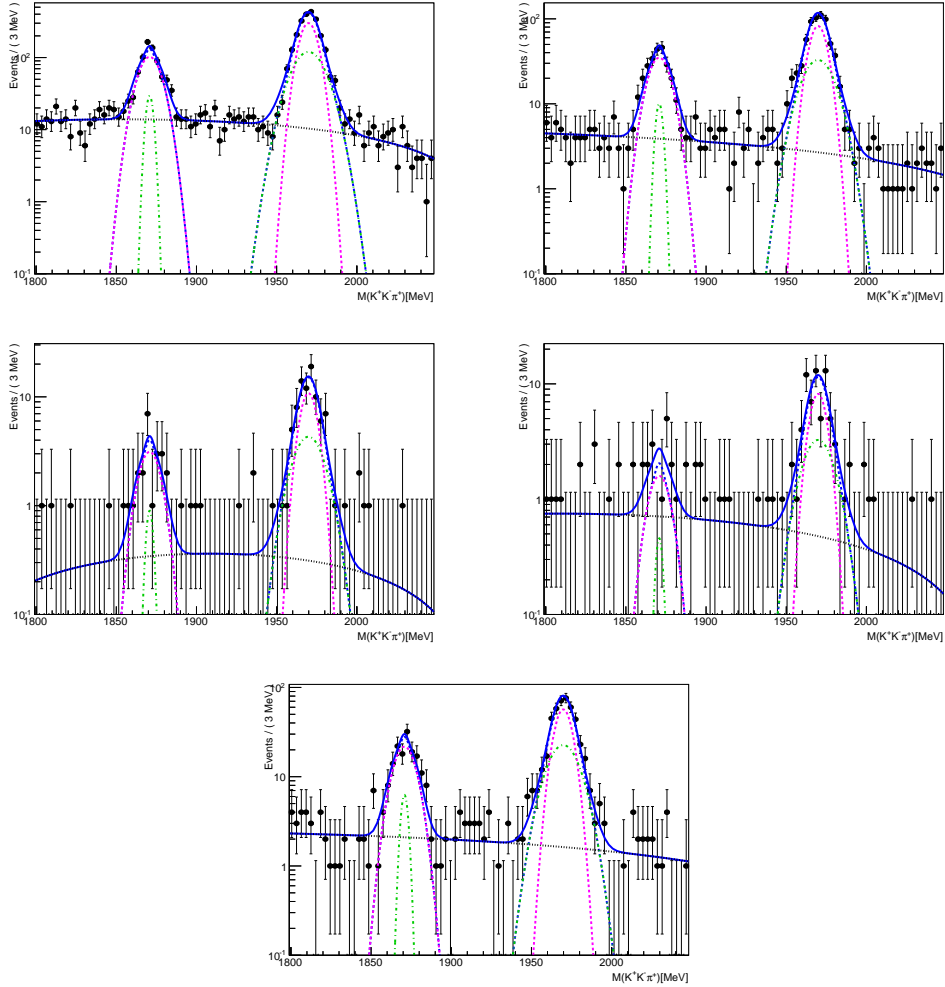


Figure 1.40: Signal data 1D fit results for magnet up, muon momentum bin 50 – 100 GeV, for  $D_s^+$ . The blue dotted line is DfB and the black dashed line is BKG. The bins in each plot are the bins of  $q \times p_x$  vs  $p_y$  with respect to the muon. The upper left is bin 6, upper right is bin 7, middle left is bin 8, middle right is bin 9, and lowest plot is bin 10.

# Appendix 2

## $q \times \varphi$ vs $p_T$ Binned Signal Fits

### 2.1 Magnet Down

All figures in this section show the fit results for the magnet down polarity data for the individual fine kinematic binning in  $q \times \varphi$  vs  $p_T$ . In each figure, the dashed green and pink lines are the two Gaussian shapes.

Figures 2.1 through 2.10 illustrate the fits for  $D_s^-$ . Figures 2.1 and 2.2 show the fits in muon momentum bin 1. Figures 2.3 and 2.4 show the fits in muon momentum bin 2. Figures 2.5 and 2.6 show the fits in muon momentum bin 3. Figures 2.7 and 2.8 show the fits in muon momentum bin 4. Figures 2.9 and 2.10 show the fits in muon momentum bin 5.

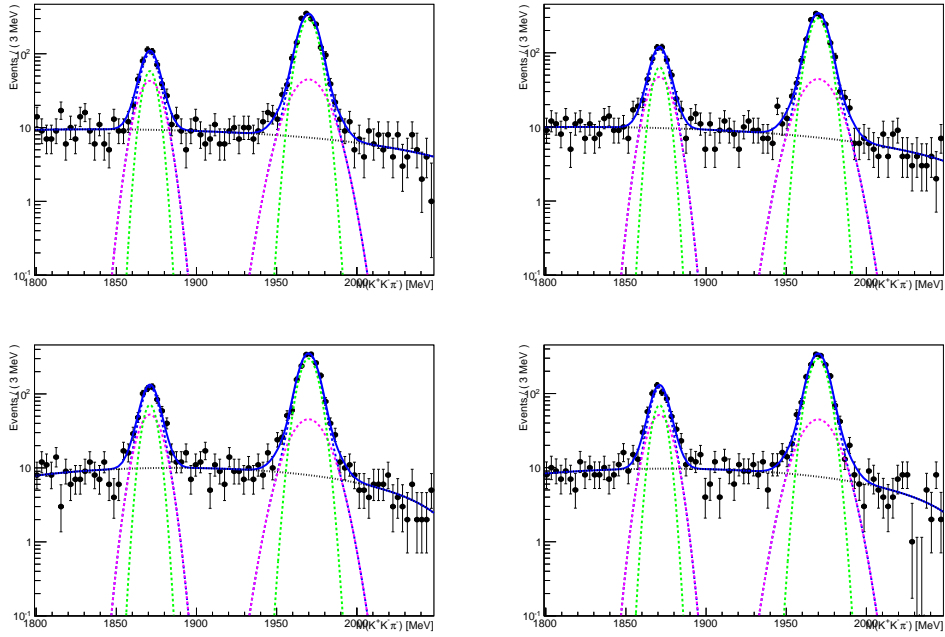


Figure 2.1: Signal data 1D fit results for magnet down, muon momentum bin 6 – 20 GeV, for  $D_s^-$ . The blue dotted line is DfB and the black dashed line is BKG. The bins in each plot are the bins of  $q \times \varphi$  vs  $p_T$  with respect to the muon. The upper left is bin 1, upper right is bin 2, bottom left is bin 3 and bottom right is bin 4.

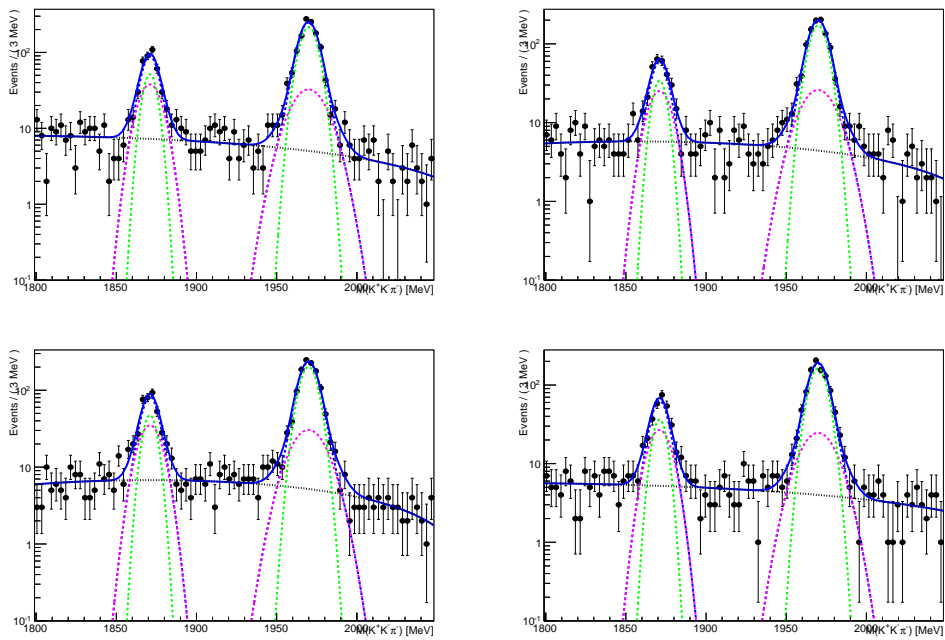


Figure 2.2: Signal data 1D fit results for magnet down, muon momentum bin 6 – 20 GeV for  $D_s^-$ . The blue dotted line is DfB and the black dashed line is BKG. The bins in each plot are the bins of  $q \times \varphi$  vs  $p_T$  with respect to the muon. The upper left is bin 6, upper right is bin 7, bottom left is bin 8 and the bottom right is bin 9.

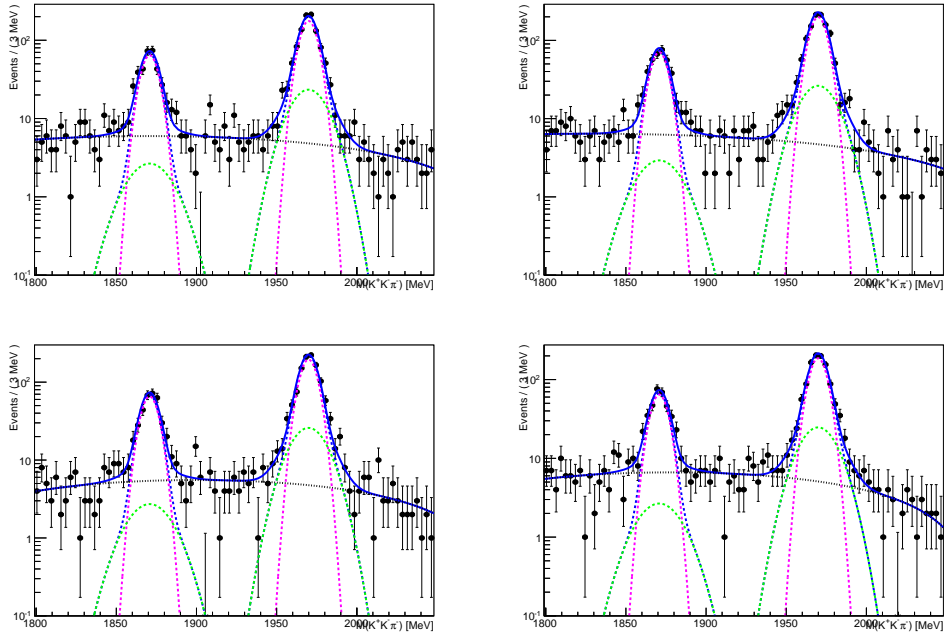


Figure 2.3: Signal data 1D fit results for magnet down, muon momentum bin 20 – 30 GeV, for  $D_s^-$ . The blue dotted line is DfB and the black dashed line is BKG. The bins in each plot are the bins of  $q \times \varphi$  vs  $p_T$  with respect to the muon. The upper left is bin 1, upper right is bin 2, bottom left is bin 3, and the bottom right is bin 4.



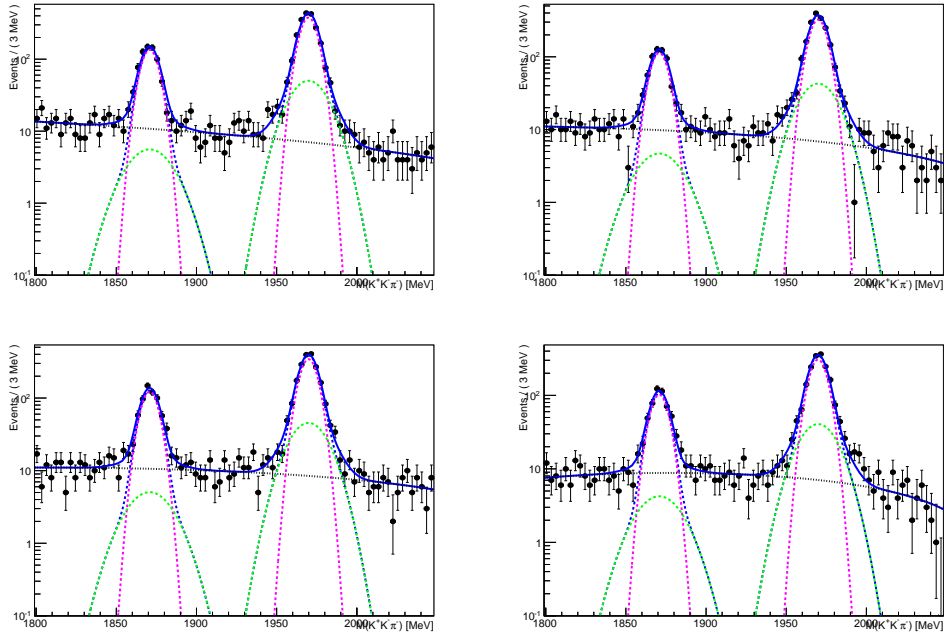


Figure 2.4: Signal data 1D fit results for magnet down, muon momentum bin 20 – 30 GeV, for  $D_s^-$ . The blue dotted line is DfB and the black dashed line is BKG. The bins in each plot are the bins of  $q \times \varphi$  vs  $p_T$  with respect to the muon. The upper left is bin 5, upper right is bin 6, bottom left is bin 7 and the bottom right is bin 8.

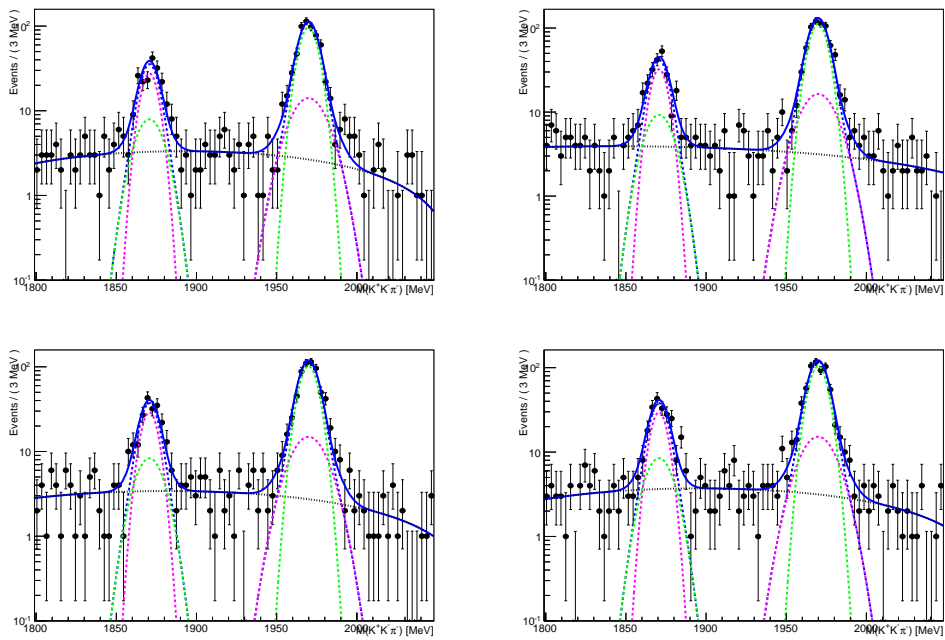


Figure 2.5: Signal data 1D fit results for magnet down, muon momentum bin 30 – 40 GeV, for  $D_s^-$ . The blue dotted line is DfB and the black dashed line is BKG. The bins in each plot are the bins of  $q \times \varphi$  vs  $p_T$  with respect to the muon. The upper left is bin 1, upper right is bin 2, bottom left is bin 3 and bottom right is bin 4.

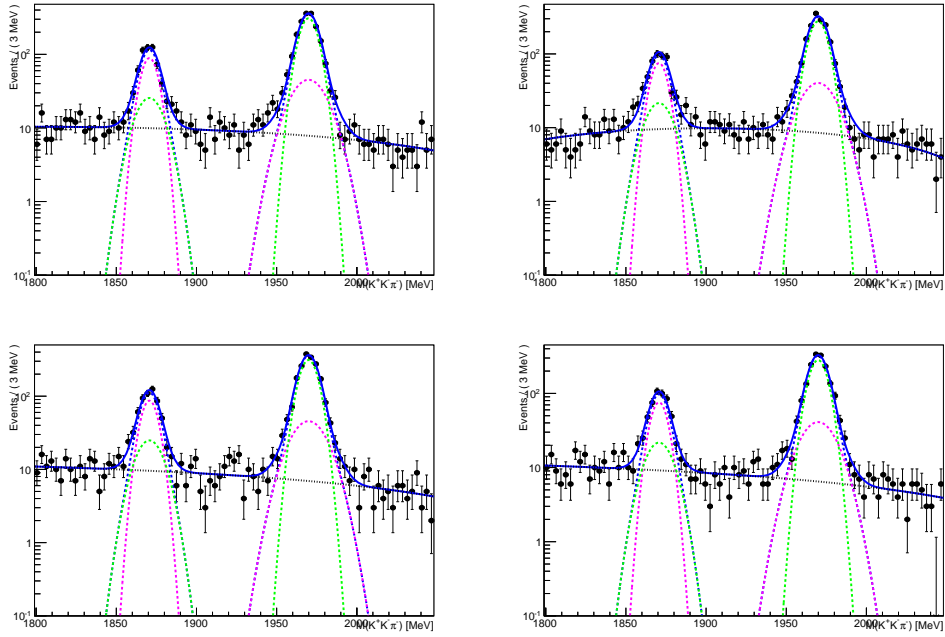


Figure 2.6: Signal data 1D fit results for magnet down, muon momentum bin 30 – 40 GeV, for  $D_s^-$ . The blue dotted line is DfB and the black dashed line is BKG. The bins in each plot are the bins of  $q \times \varphi$  vs  $p_T$  with respect to the muon. The upper left is bin 5, upper right is bin 6, bottom left is bin 7 and the bottom right is bin 8.

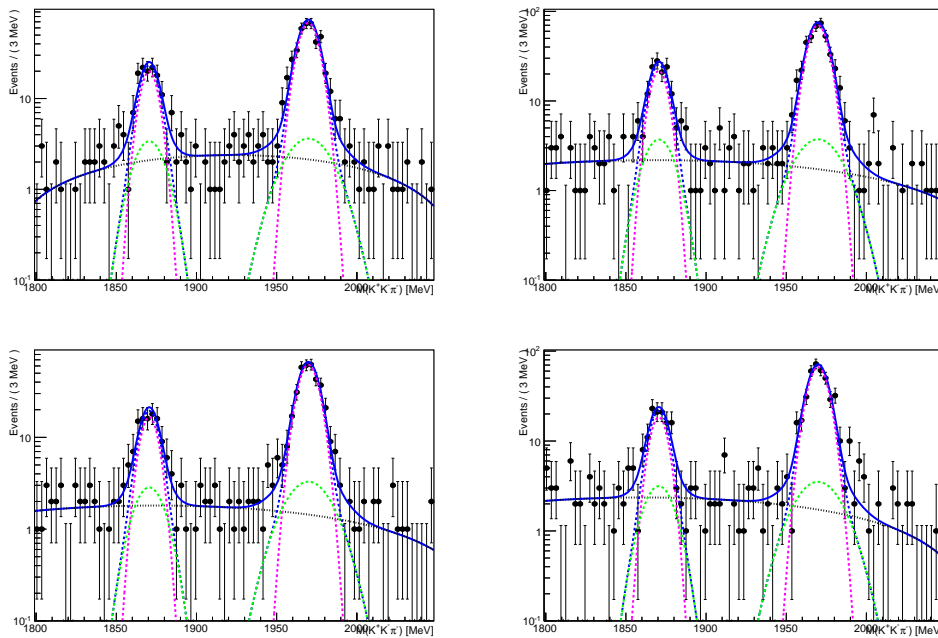


Figure 2.7: Signal data 1D fit results for magnet down, muon momentum bin 40 – 50 GeV, for  $D_s^-$ . The blue dotted line is DfB and the black dashed line is BKG. The bins in each plot are the bins of  $q \times \varphi$  vs  $p_T$  with respect to the muon. The upper left is bin 1, upper right is bin 2, bottom left is bin 3 and bottom right is bin 4.

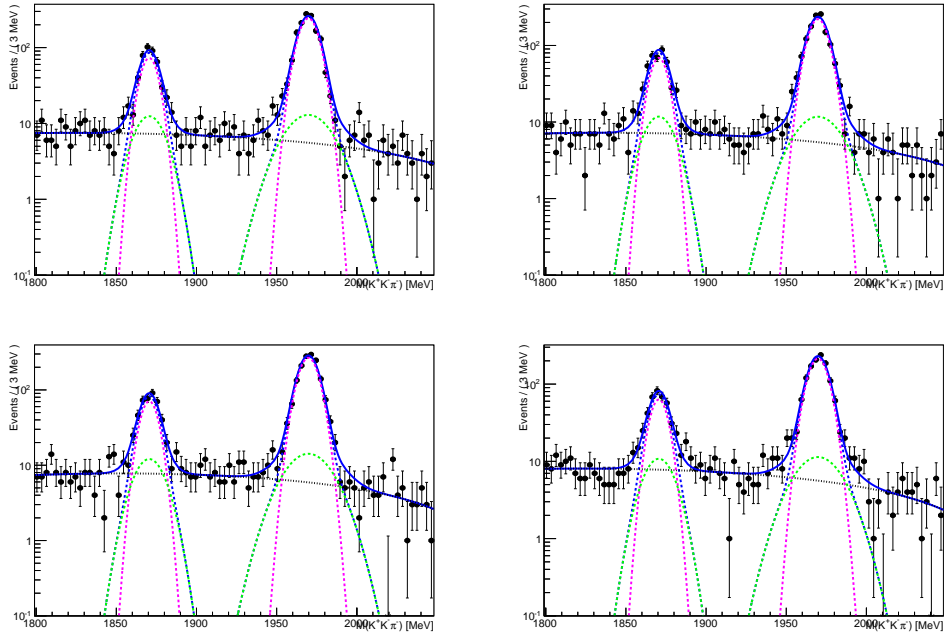


Figure 2.8: Signal data 1D fit results for magnet down, muon momentum bin 40 – 50 GeV, for  $D_s^-$ . The blue dotted line is DfB and the black dashed line is BKG. The bins in each plot are the bins of  $q \times \varphi$  vs  $p_T$  with respect to the muon. The upper left is bin 5, upper right is bin 6, bottom left is bin 7 and the bottom right is bin 8.

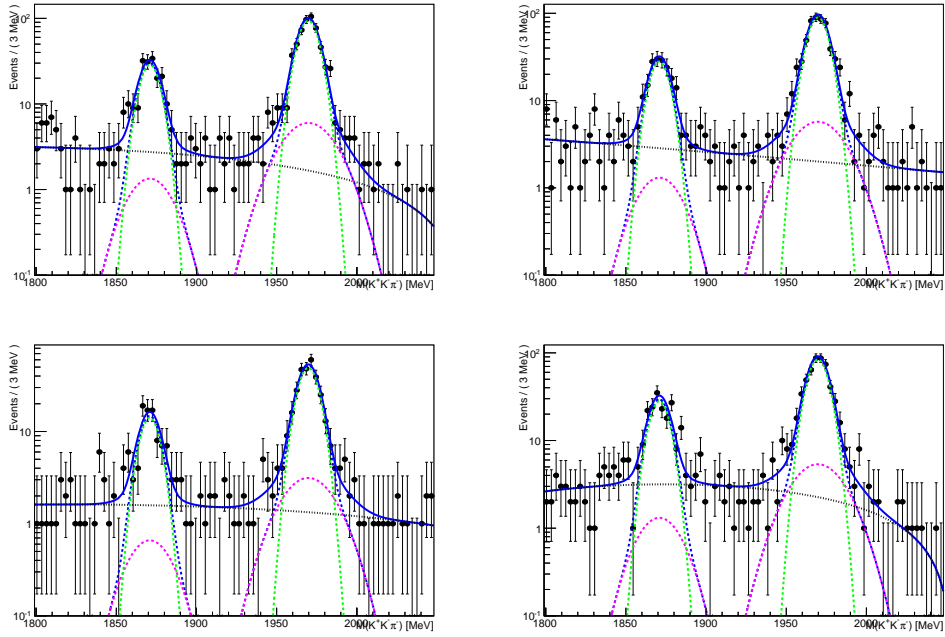


Figure 2.9: Signal data 1D fit results for magnet down, muon momentum bin 50 – 100 GeV, for  $D_s^-$ . The blue dotted line is DfB and the black dashed line is BKG. The bins in each plot are the bins of  $q \times \varphi$  vs  $p_T$  with respect to the muon. The upper left is bin 1, upper right is bin 2, bottom left is bin 3 and bottom right is bin 4.

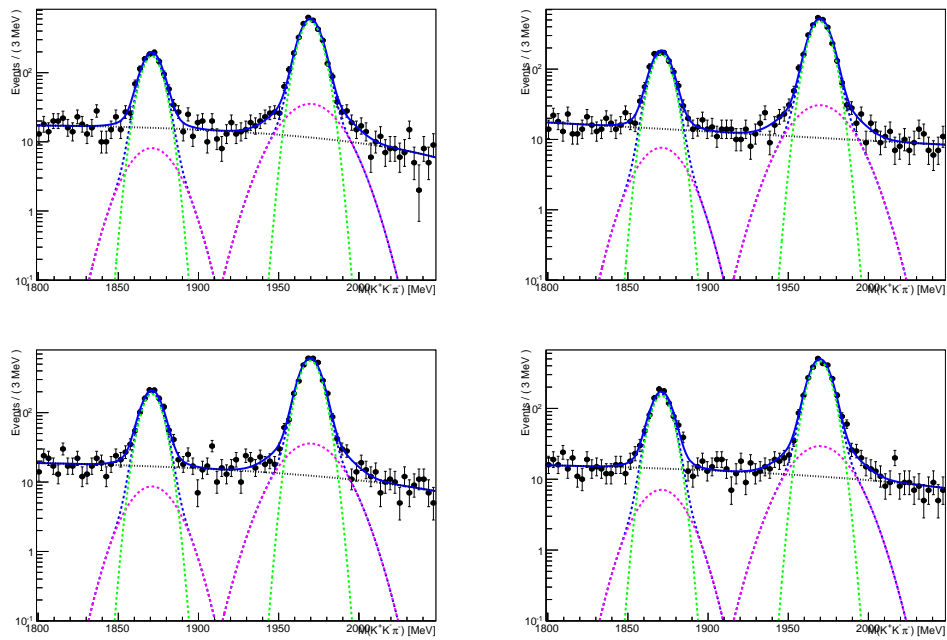


Figure 2.10: Signal data 1D fit results for magnet down, muon momentum bin 50 – 100 GeV, for  $D_s^-$ . The blue dotted line is DfB and the black dashed line is BKG. The bins in each plot are the bins of  $q \times \varphi$  vs  $p_T$  with respect to the muon. The upper left is bin 5, upper right is bin 6, bottom left is bin 7 and the bottom right is bin 8.

Figures 2.11 through 2.20 illustrate the fits for  $D_s^+$ . Figures 2.11 and 2.12 show the fits in muon momentum bin 1. Figures 2.13 and 2.14 show the fits in muon momentum bin 2. Figures 2.15 and 2.16 show the fits in muon momentum bin 3. Figures 2.17 and 2.18 show the fits in muon momentum bin 4. Figures 2.19 and 2.20 show the fits in muon momentum bin 5.

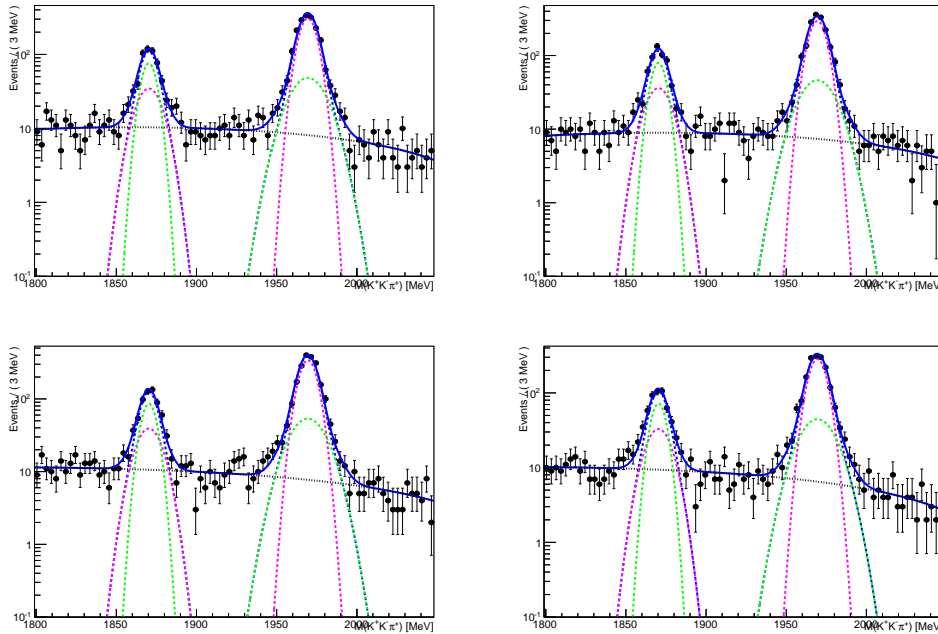


Figure 2.11: Signal data 1D fit results for magnet down, muon momentum bin 6 – 20 GeV, for  $D_s^+$ . The blue dotted line is DfB and the black dashed line is BKG. The bins in each plot are the bins of  $q \times \varphi$  vs  $p_T$  with respect to the muon. The upper left is bin 1, upper right is bin 2, bottom left is bin 3 and bottom right is bin 4.



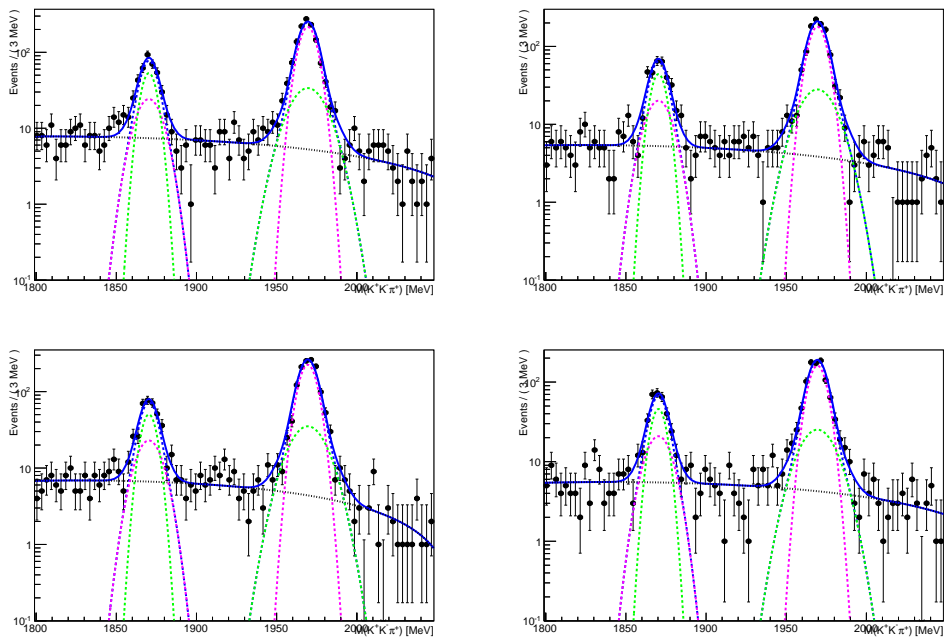


Figure 2.12: Signal data 1D fit results for magnet down, muon momentum bin 6 – 20 GeV for  $D_s^+$ . The blue dotted line is DfB and the black dashed line is BKG. The bins in each plot are the bins of  $q \times \varphi$  vs  $p_T$  with respect to the muon. The upper left is bin 5, upper right is bin 6, bottom left is bin 7 and the bottom right is bin 8.

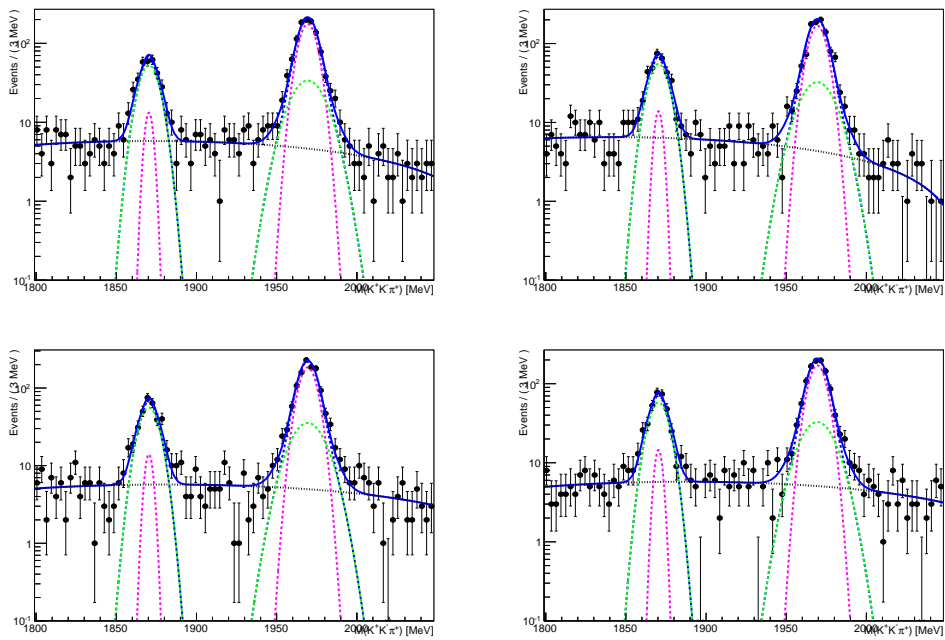


Figure 2.13: Signal data 1D fit results for magnet down, muon momentum bin 20 – 30 GeV, for  $D_s^+$ . The blue dotted line is DfB and the black dashed line is BKG. The bins in each plot are the bins of  $q \times \varphi$  vs  $p_T$  with respect to the muon. The upper left is bin 1, upper right is bin 2, bottom left is bin 3, and the bottom right is bin 4.

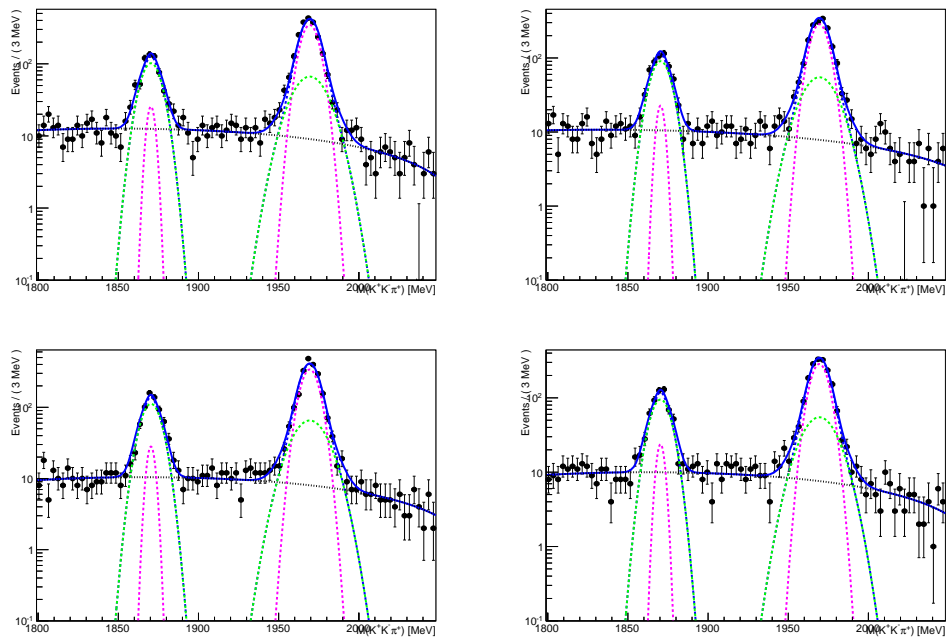


Figure 2.14: Signal data 1D fit results for magnet down, muon momentum bin 20 – 30 GeV, for  $D_s^+$ . The blue dotted line is DfB and the black dashed line is BKG. The bins in each plot are the bins of  $q \times \varphi$  vs  $p_T$  with respect to the muon. The upper left is bin 5, upper right is bin 6, bottom left is bin 7 and the bottom right is bin 8.

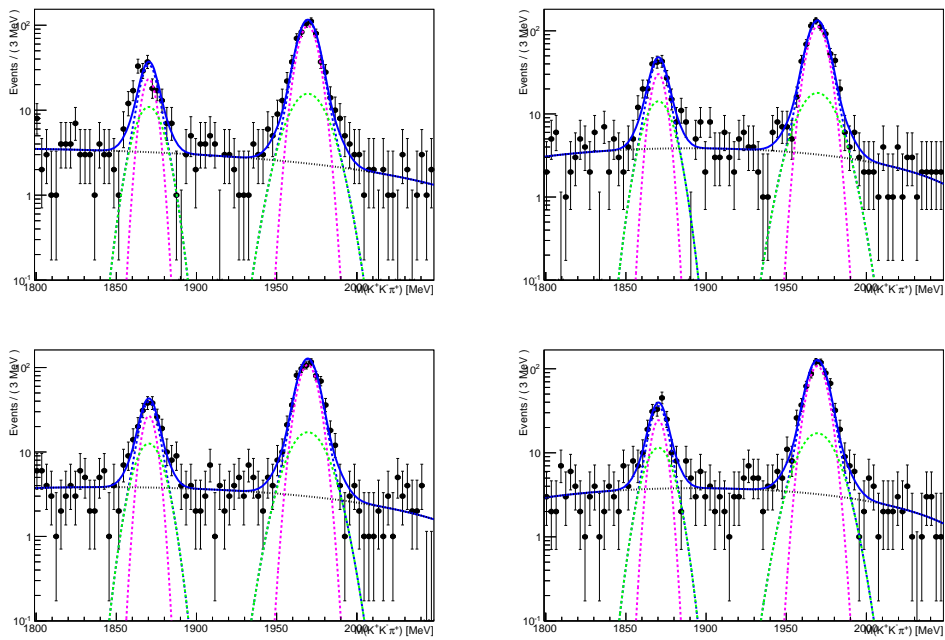


Figure 2.15: Signal data 1D fit results for magnet down, muon momentum bin 30 – 40 GeV, for  $D_s^+$ . The blue dotted line is DfB and the black dashed line is BKG. The bins in each plot are the bins of  $q \times \varphi$  vs  $p_T$  with respect to the muon. The upper left is bin 1, upper right is bin 2, bottom left is bin 3 and bottom right is bin 4.

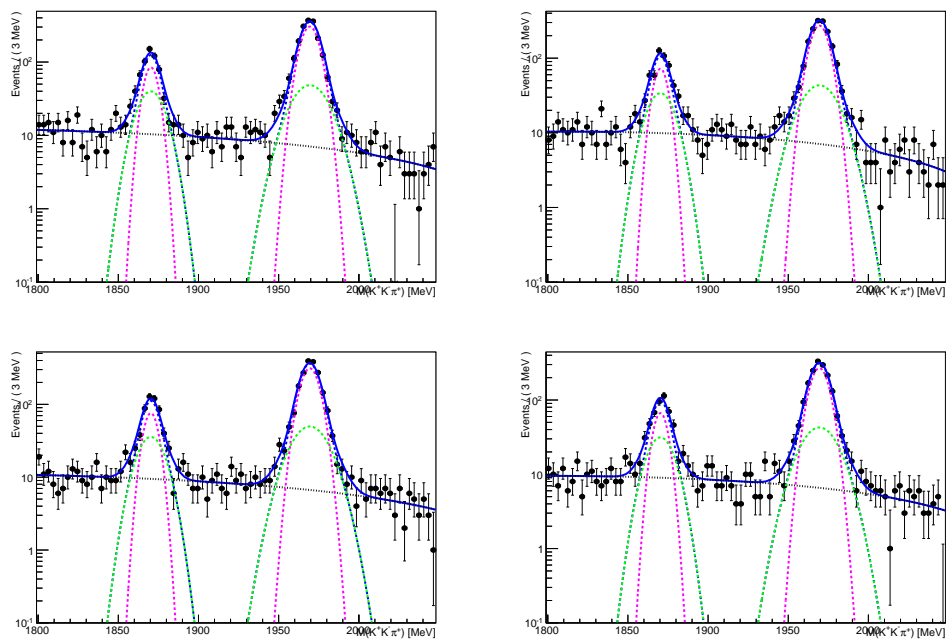


Figure 2.16: Signal data 1D fit results for magnet down, muon momentum bin 30 – 40 GeV, for  $D_s^+$ . The blue dotted line is DfB and the black dashed line is BKG. The bins in each plot are the bins of  $q \times \varphi$  vs  $p_T$  with respect to the muon. The upper left is bin 5, upper right is bin 6, bottom left is bin 7 and the bottom right is bin 8.

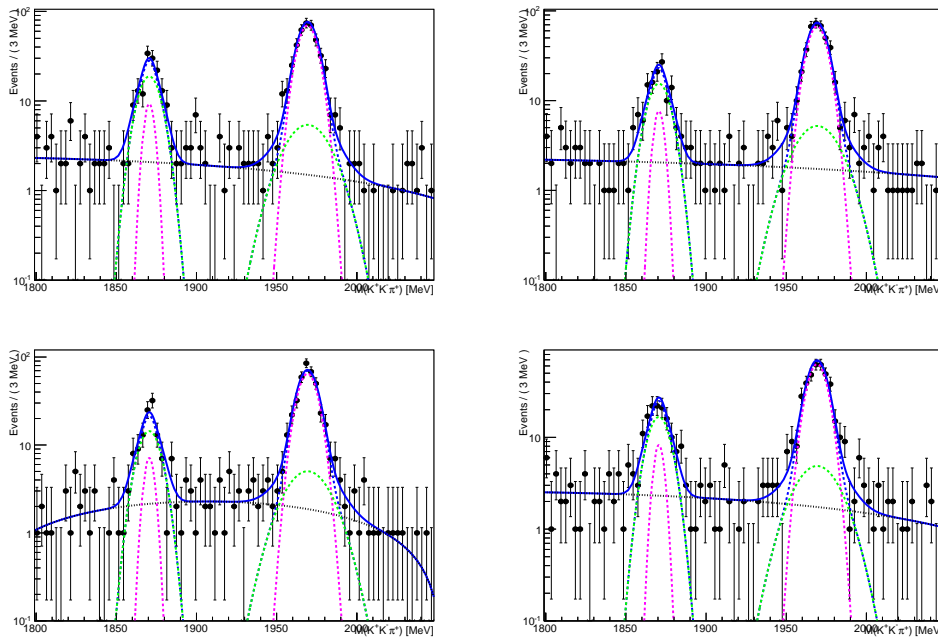


Figure 2.17: Signal data 1D fit results for magnet down, muon momentum bin 40 – 50 GeV, for  $D_s^+$ . The blue dotted line is DfB and the black dashed line is BKG. The bins in each plot are the bins of  $q \times \varphi$  vs  $p_T$  with respect to the muon. The upper left is bin 1, upper right is bin 2, bottom left is bin 3 and bottom right is bin 4.

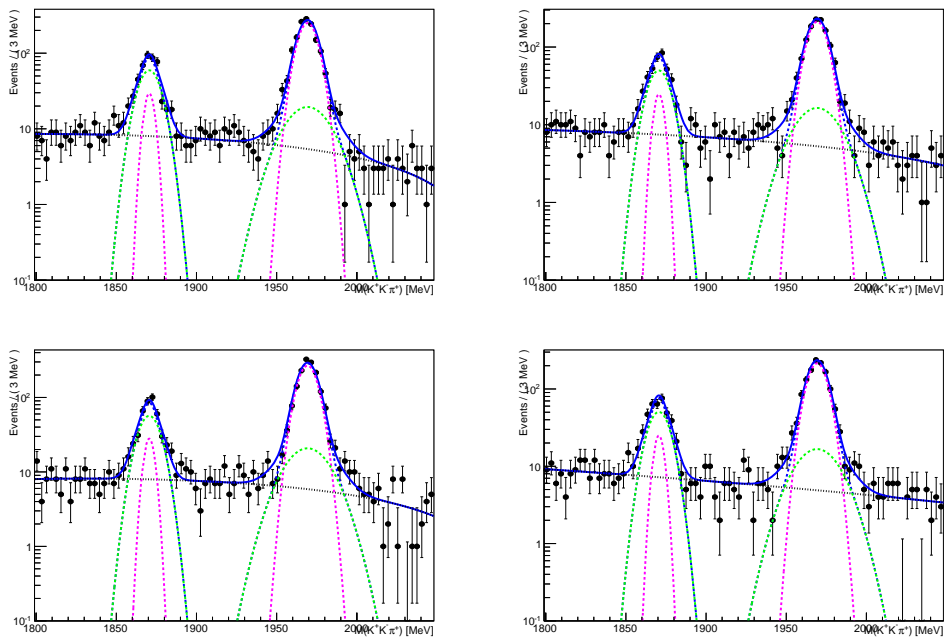


Figure 2.18: Signal data 1D fit results for magnet down, muon momentum bin 40 – 50 GeV, for  $D_s^+$ . The blue dotted line is DfB and the black dashed line is BKG. The bins in each plot are the bins of  $q \times \varphi$  vs  $p_T$  with respect to the muon. The upper left is bin 5, upper right is bin 6, bottom left is bin 7 and the bottom right is bin 8.

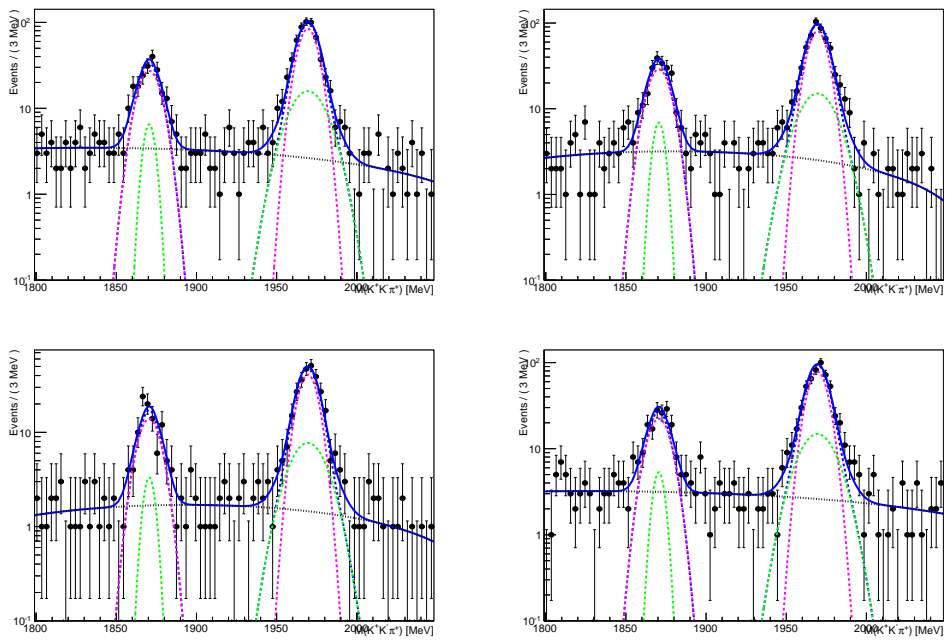


Figure 2.19: Signal data 1D fit results for magnet down, muon momentum bin 50 – 100 GeV, for  $D_s^+$ . The blue dotted line is DfB and the black dashed line is BKG. The bins in each plot are the bins of  $q \times \varphi$  vs  $p_T$  with respect to the muon. The upper left is bin 1, upper right is bin 2, bottom left is bin 3 and bottom right is bin 4.



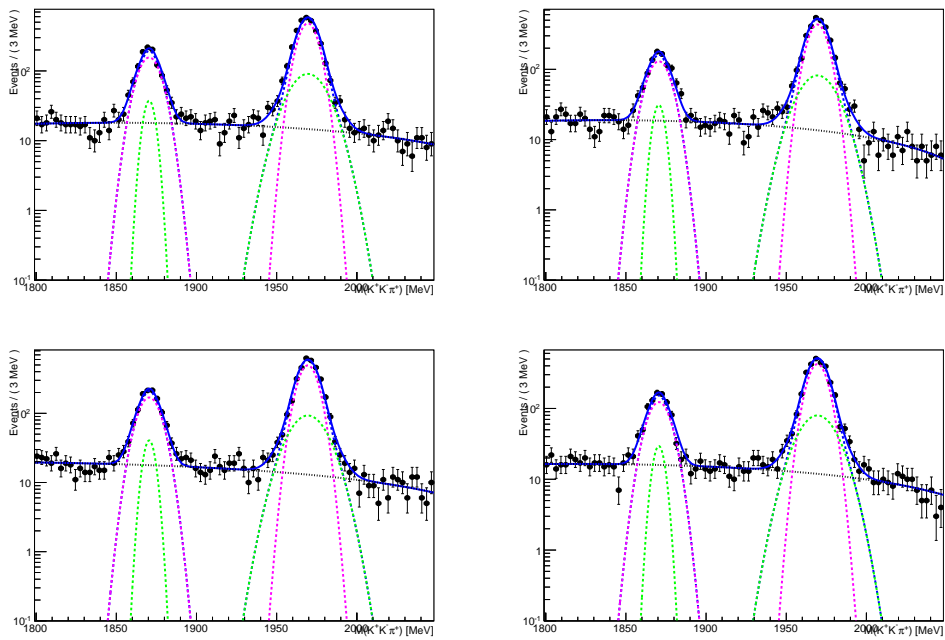


Figure 2.20: Signal data 1D fit results for magnet down, muon momentum bin 50 – 100 GeV, for  $D_s^+$ . The blue dotted line is DfB and the black dashed line is BKG. The bins in each plot are the bins of  $q \times \varphi$  vs  $p_T$  with respect to the muon. The upper left is bin 5, upper right is bin 6, bottom left is bin 7 and the bottom right is bin 8.

## 2.2 Magnet Up

All figures in this section show the fit results for the magnet up polarity data for the individual fine kinematic binning in  $q \times \varphi$  vs  $p_T$ . In each figure, the dashed green and pink lines are the two Gaussian shapes.

Figures 2.21 through 2.30 illustrate the fits for  $D_s^-$ . Figures 2.21 and 2.22 show the fits in muon momentum bin 1. Figures 2.23 and 2.24 show the fits in muon momentum bin 2. Figures 2.25 and 2.26 show the fits in muon momentum bin 3. Figures 2.27 and 2.28 show the fits in muon momentum bin 4. Figures 2.29 and 2.30 show the fits in muon momentum bin 5.

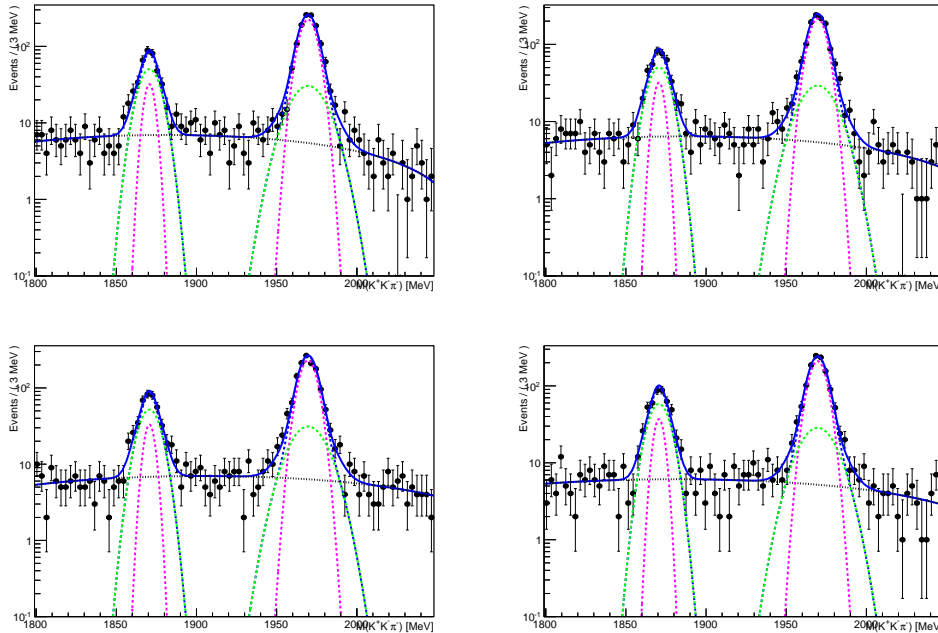


Figure 2.21: Signal data 1D fit results for magnet up, muon momentum bin 6 – 20 GeV, for  $D_s^-$ . The blue dotted line is DfB and the black dashed line is BKG. The bins in each plot are the bins of  $q \times \varphi$  vs  $p_T$  with respect to the muon. The upper left is bin 1, upper right is bin 2, bottom left is bin 3 and bottom right is bin 4.

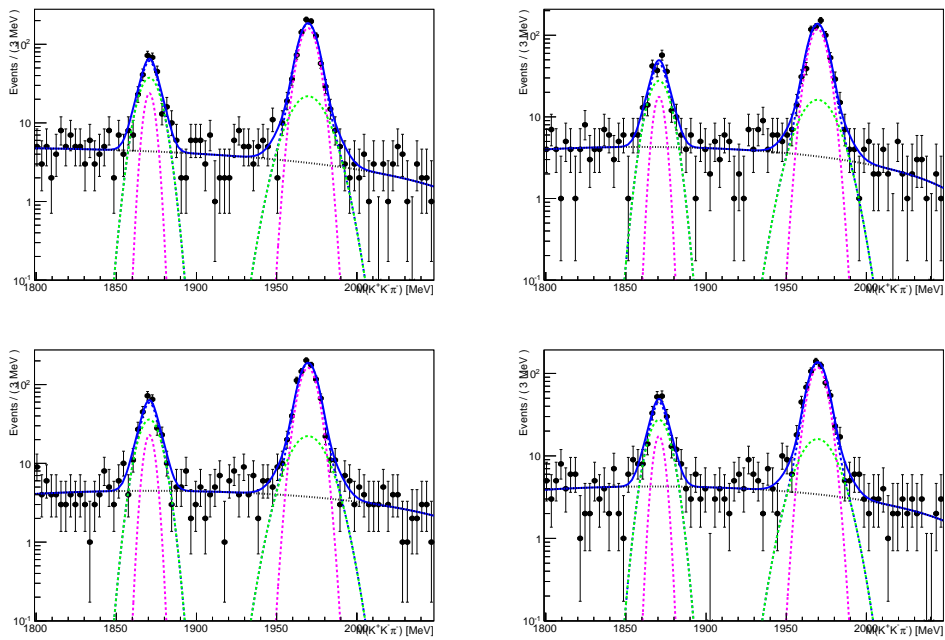


Figure 2.22: Signal data 1D fit results for magnet up, muon momentum bin 6 – 20 GeV for  $D_s^-$ . The blue dotted line is DfB and the black dashed line is BKG. The bins in each plot are the bins of  $q \times \varphi$  vs  $p_T$  with respect to the muon. The upper left is bin 5, upper right is bin 6, bottom left is bin 7 and the bottom right is bin 8.

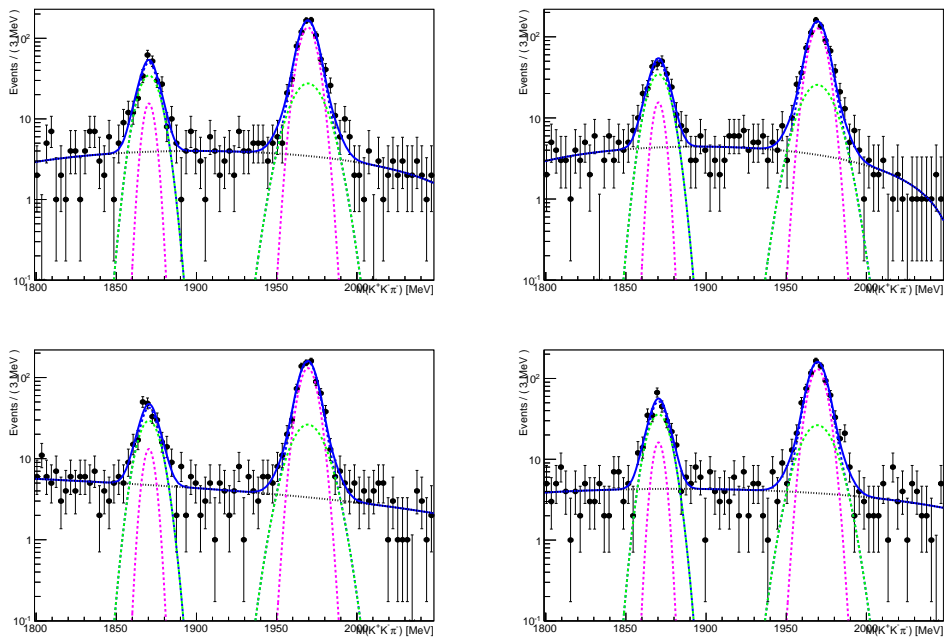


Figure 2.23: Signal data 1D fit results for magnet up, muon momentum bin 20 – 30 GeV, for  $D_s^-$ . The blue dotted line is DfB and the black dashed line is BKG. The bins in each plot are the bins of  $q \times \varphi$  vs  $p_T$  with respect to the muon. The upper left is bin 1, upper right is bin 2, bottom left is bin 3, and the bottom right is bin 4.

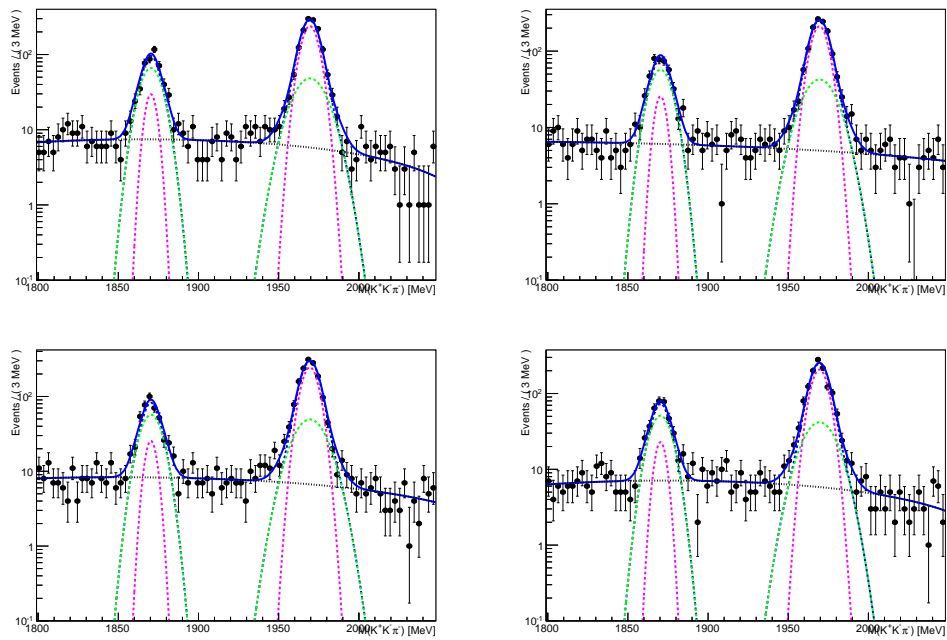


Figure 2.24: Signal data 1D fit results for magnet up, muon momentum bin 20 – 30 GeV, for  $D_s^-$ . The blue dotted line is DfB and the black dashed line is BKG. The bins in each plot are the bins of  $q \times \varphi$  vs  $p_T$  with respect to the muon. The upper left is bin 5, upper right is bin 6, bottom left is bin 7 and the bottom right is bin 8.

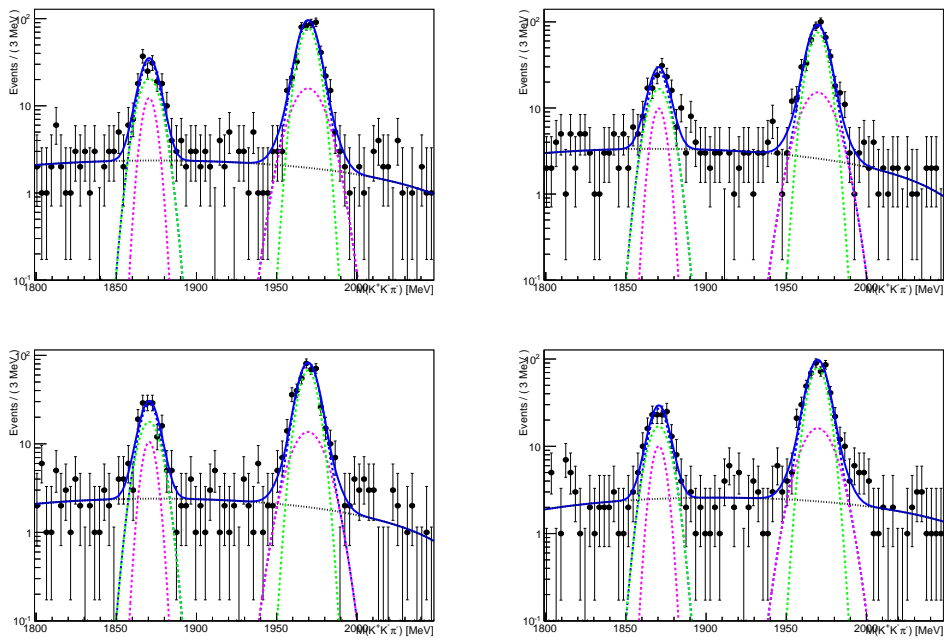


Figure 2.25: Signal data 1D fit results for magnet up, muon momentum bin 30 – 40 GeV, for  $D_s^-$ . The blue dotted line is DfB and the black dashed line is BKG. The bins in each plot are the bins of  $q \times \varphi$  vs  $p_T$  with respect to the muon. The upper left is bin 1, upper right is bin 2, bottom left is bin 3 and bottom right is bin 4.

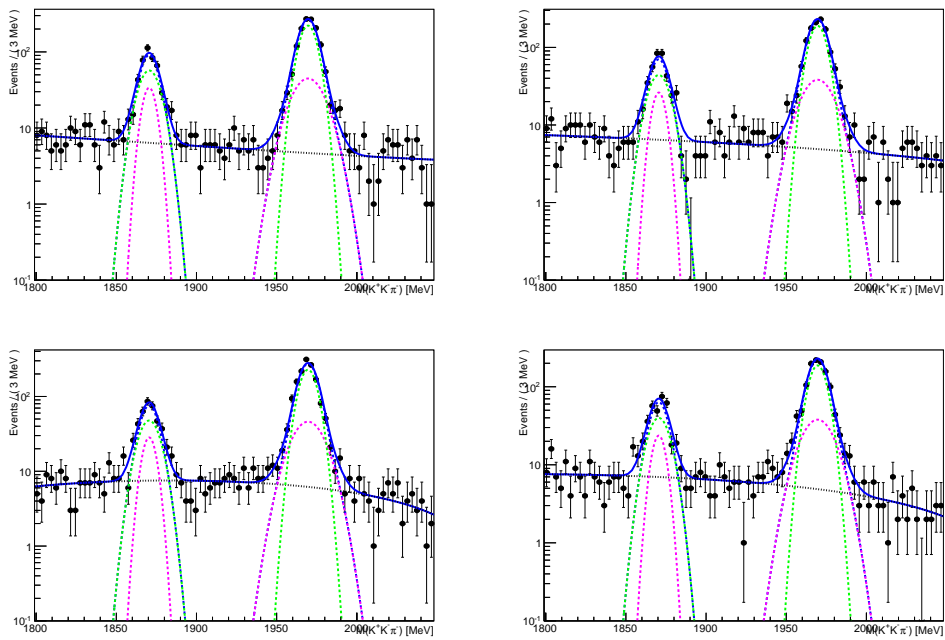


Figure 2.26: Signal data 1D fit results for magnet up, muon momentum bin 30 – 40 GeV, for  $D_s^-$ . The blue dotted line is DfB and the black dashed line is BKG. The bins in each plot are the bins of  $q \times \varphi$  vs  $p_T$  with respect to the muon. The upper left is bin 5, upper right is bin 6, bottom left is bin 7 and the bottom right is bin 8.

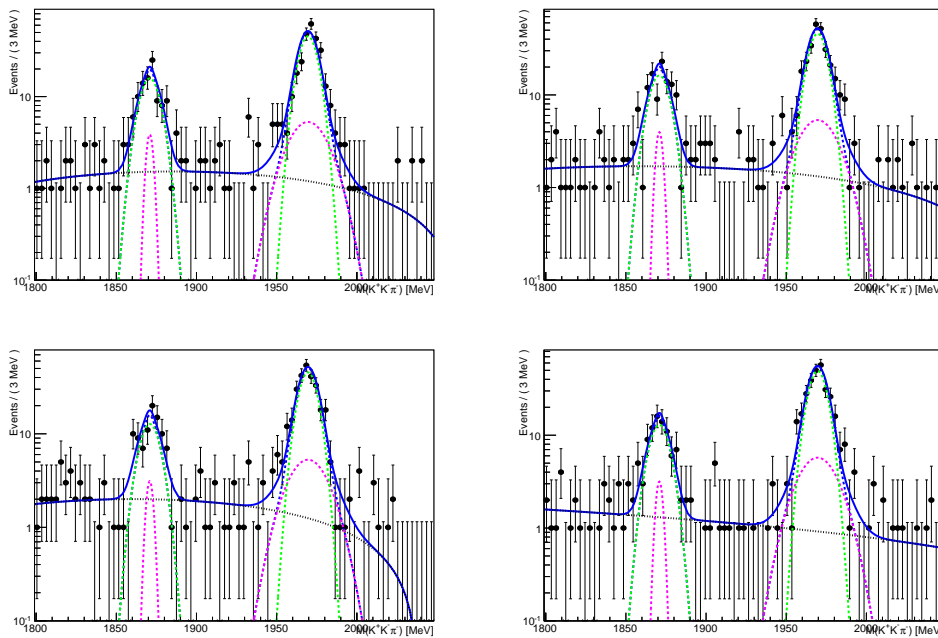


Figure 2.27: Signal data 1D fit results for magnet up, muon momentum bin 40 – 50 GeV, for  $D_s^-$ . The blue dotted line is DfB and the black dashed line is BKG. The bins in each plot are the bins of  $q \times \varphi$  vs  $p_T$  with respect to the muon. The upper left is bin 1, upper right is bin 2, bottom left is bin 3 and bottom right is bin 4.



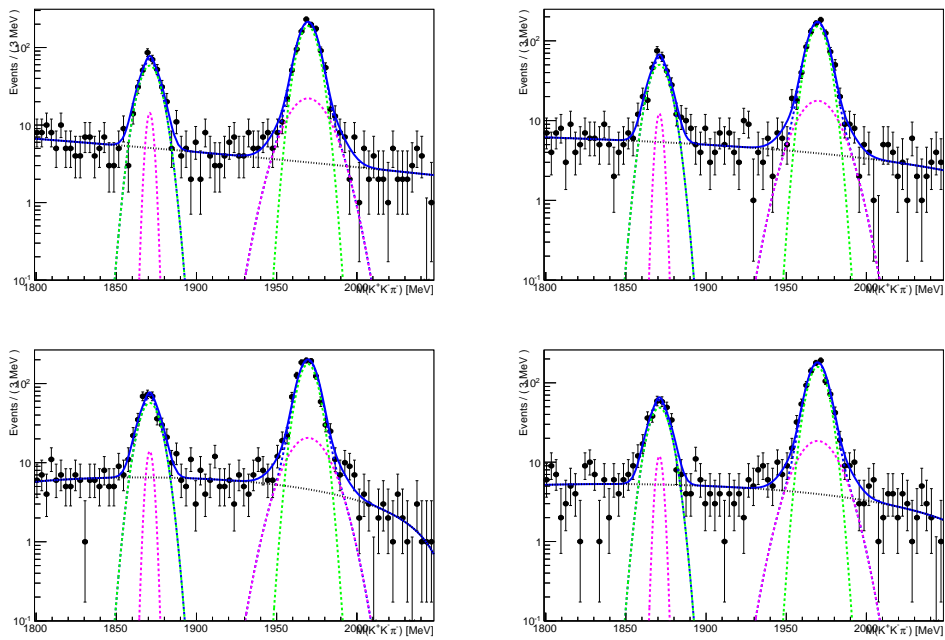


Figure 2.28: Signal data 1D fit results for magnet up, muon momentum bin 40 – 50 GeV, for  $D_s^-$ . The blue dotted line is DfB and the black dashed line is BKG. The bins in each plot are the bins of  $q \times \varphi$  vs  $p_T$  with respect to the muon. The upper left is bin 5, upper right is bin 6, bottom left is bin 7 and the bottom right is bin 8.

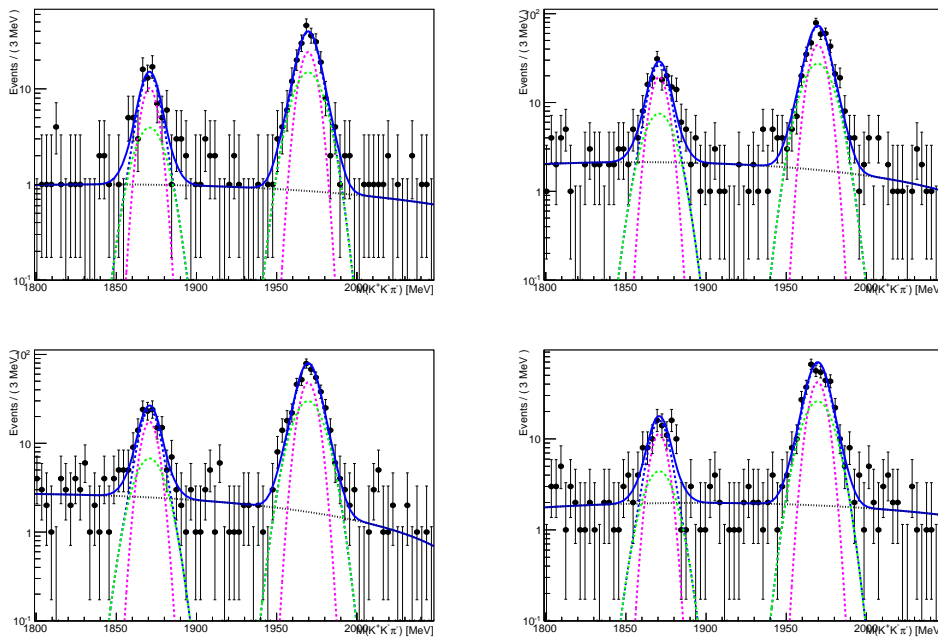


Figure 2.29: Signal data 1D fit results for magnet up, muon momentum bin 50 – 100 GeV, for  $D_s^-$ . The blue dotted line is DfB and the black dashed line is BKG. The bins in each plot are the bins of  $q \times \varphi$  vs  $p_T$  with respect to the muon. The upper left is bin 1, upper right is bin 2, bottom left is bin 3 and bottom right is bin 4.

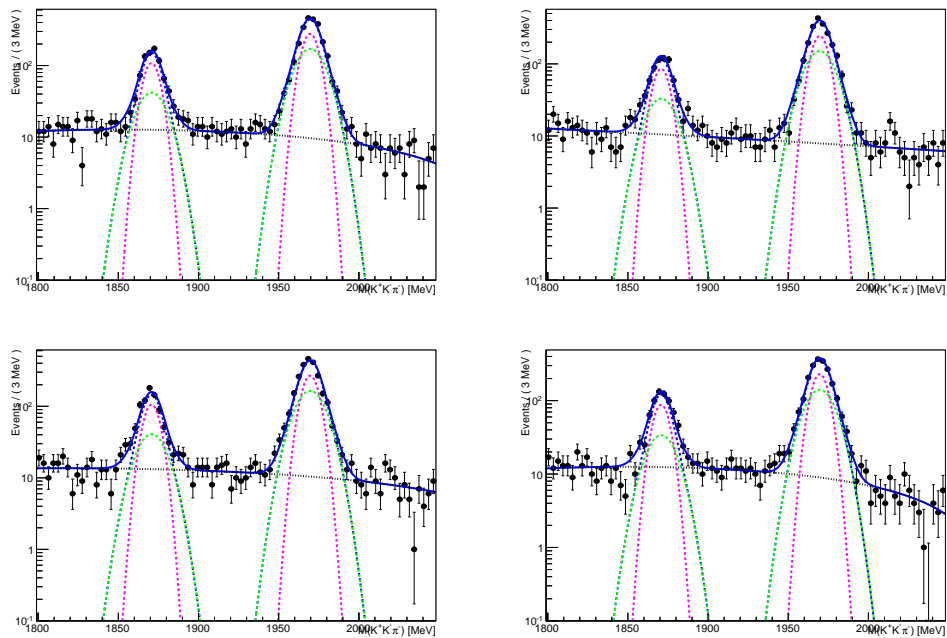


Figure 2.30: Signal data 1D fit results for magnet up, muon momentum bin 50 – 100 GeV, for  $D_s^-$ . The blue dotted line is DfB and the black dashed line is BKG. The bins in each plot are the bins of  $q \times \varphi$  vs  $p_T$  with respect to the muon. The upper left is bin 5, upper right is bin 6, bottom left is bin 7 and the bottom right is bin 8.

Figures 2.31 through 2.40 illustrate the fits for  $D_s^+$ . Figures 2.31 and 2.32 show the fits in muon momentum bin 1. Figures 2.33 and 2.34 show the fits in muon momentum bin 2. Figures 2.35 and 2.36 show the fits in muon momentum bin 3. Figures 2.37 and 2.38 show the fits in muon momentum bin 4. Figures 2.39 and 2.40 show the fits in muon momentum bin 5.

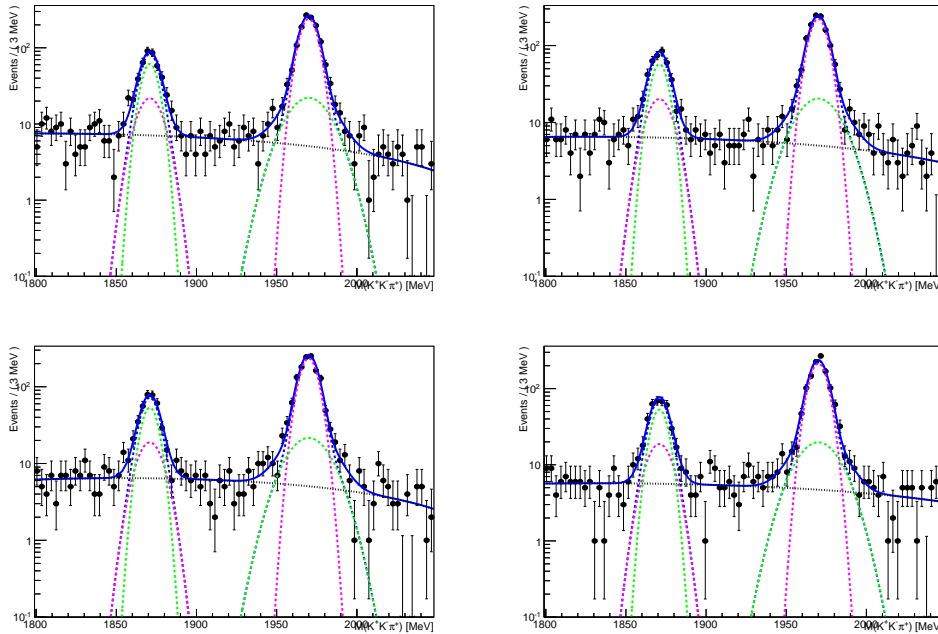


Figure 2.31: Signal data 1D fit results for magnet up, muon momentum bin 6 – 20 GeV, for  $D_s^+$ . The blue dotted line is DfB and the black dashed line is BKG. The bins in each plot are the bins of  $q \times \varphi$  vs  $p_T$  with respect to the muon. The upper left is bin 1, upper right is bin 2, bottom left is bin 3 and bottom right is bin 4.

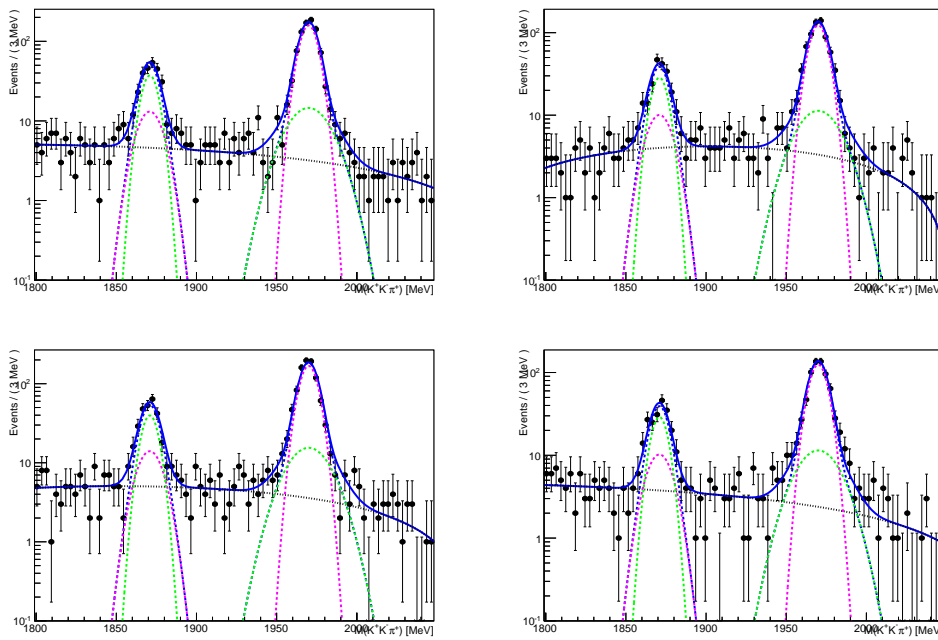


Figure 2.32: Signal data 1D fit results for magnet up, muon momentum bin 6 – 20 GeV for  $D_s^+$ . The blue dotted line is DfB and the black dashed line is BKG. The bins in each plot are the bins of  $q \times \varphi$  vs  $p_T$  with respect to the muon. The upper left is bin 5, upper right is bin 6, bottom left is bin 7 and the bottom right is bin 8.

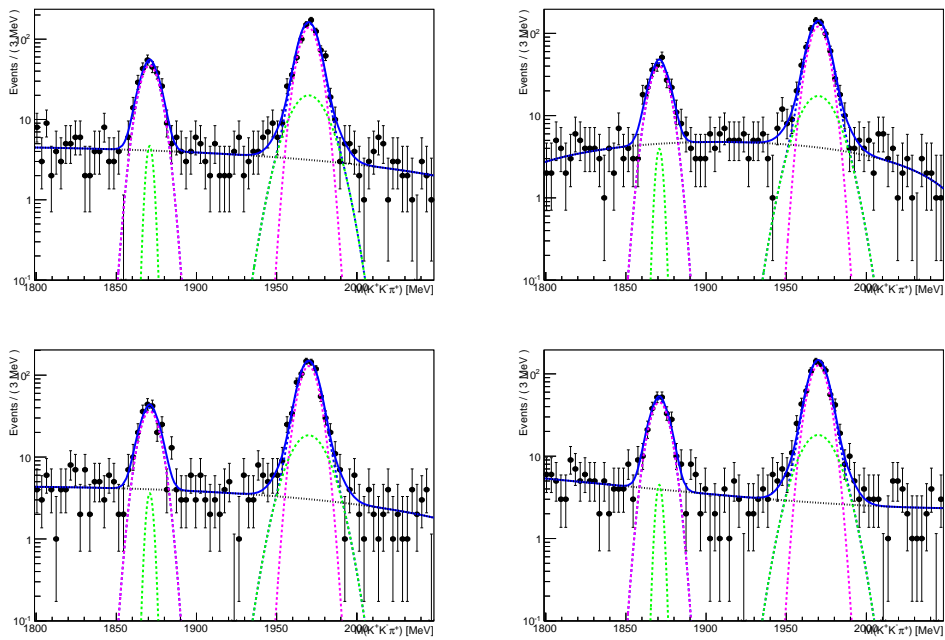


Figure 2.33: Signal data 1D fit results for magnet up, muon momentum bin 20 – 30 GeV, for  $D_s^+$ . The blue dotted line is DfB and the black dashed line is BKG. The bins in each plot are the bins of  $q \times \varphi$  vs  $p_T$  with respect to the muon. The upper left is bin 1, upper right is bin 2, bottom left is bin 3, and the bottom right is bin 4.

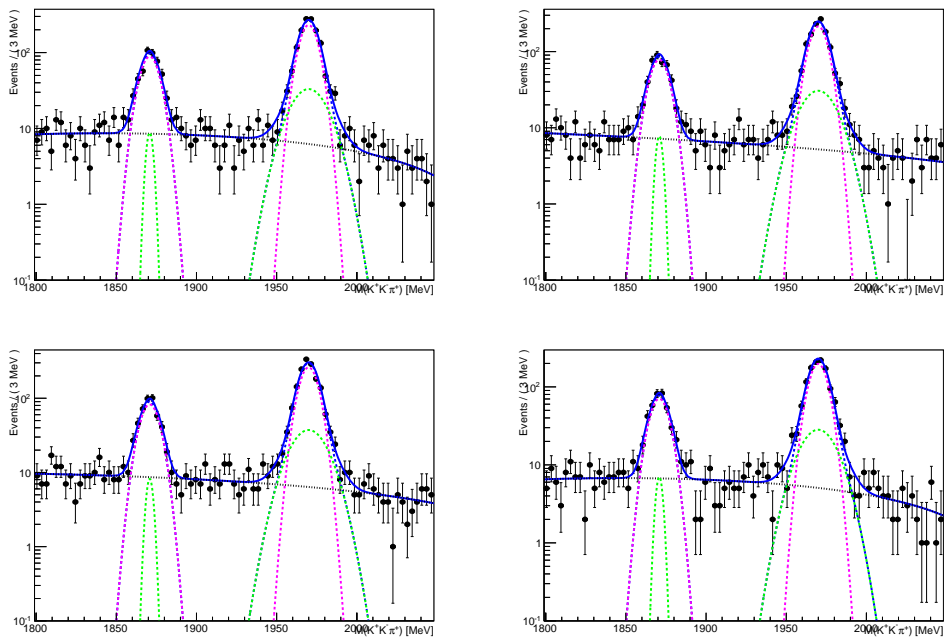


Figure 2.34: Signal data 1D fit results for magnet up, muon momentum bin 20 – 30 GeV, for  $D_s^+$ . The blue dotted line is DfB and the black dashed line is BKG. The bins in each plot are the bins of  $q \times \varphi$  vs  $p_T$  with respect to the muon. The upper left is bin 5, upper right is bin 6, bottom left is bin 7 and the bottom right is bin 8.

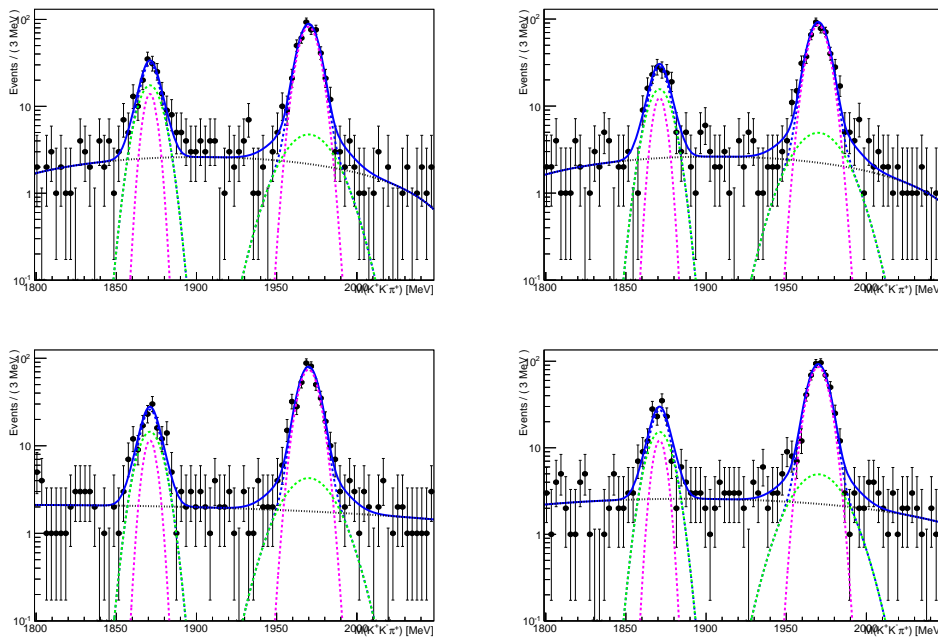


Figure 2.35: Signal data 1D fit results for magnet up, muon momentum bin 30 – 40 GeV, for  $D_s^+$ . The blue dotted line is DfB and the black dashed line is BKG. The bins in each plot are the bins of  $q \times \varphi$  vs  $p_T$  with respect to the muon. The upper left is bin 1, upper right is bin 2, bottom left is bin 3 and bottom right is bin 4.



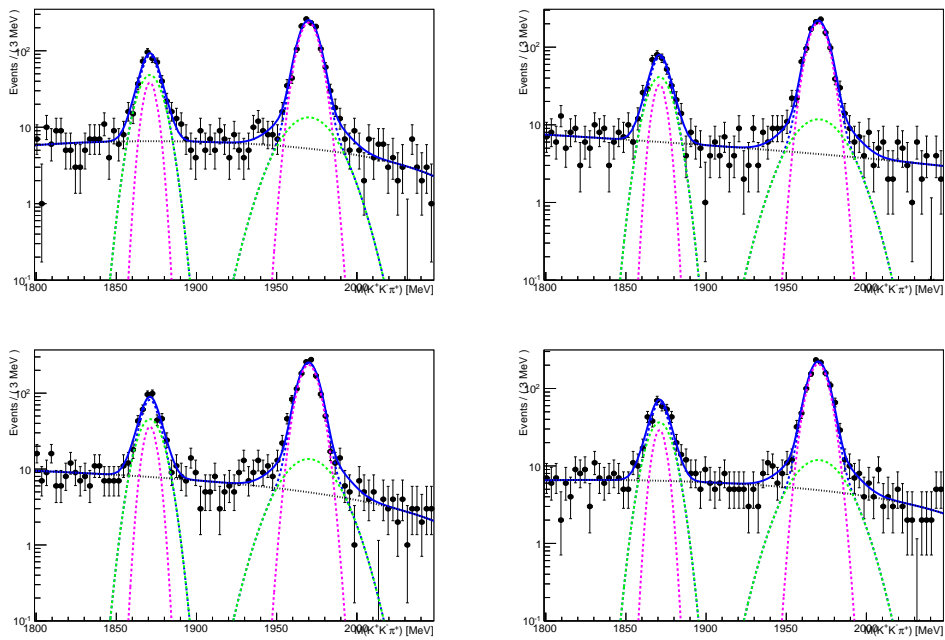


Figure 2.36: Signal data 1D fit results for magnet up, muon momentum bin 30 – 40 GeV, for  $D_s^+$ . The blue dotted line is DfB and the black dashed line is BKG. The bins in each plot are the bins of  $q \times \varphi$  vs  $p_T$  with respect to the muon. The upper left is bin 5, upper right is bin 6, bottom left is bin 7 and the bottom right is bin 8.

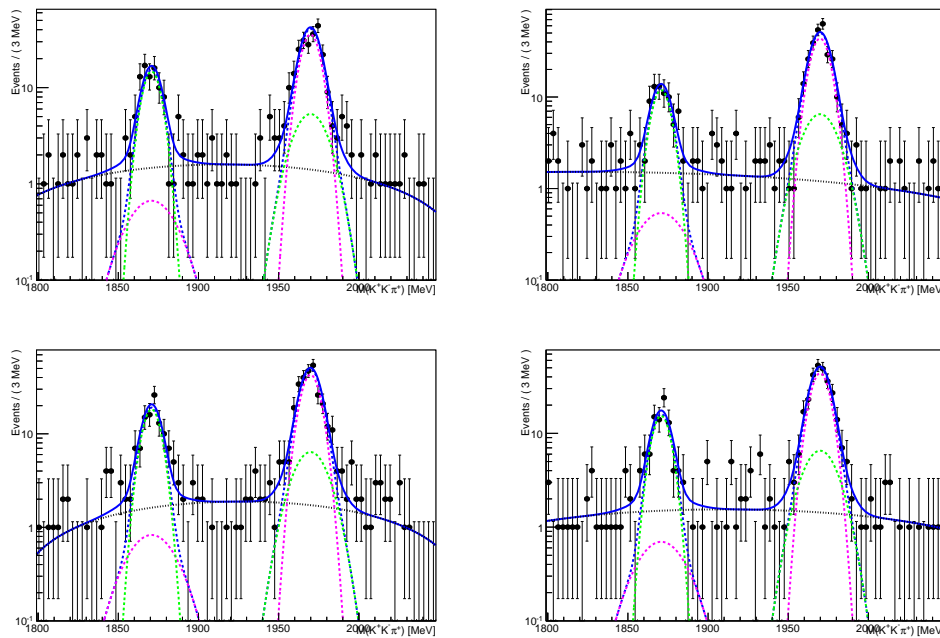


Figure 2.37: Signal data 1D fit results for magnet up, muon momentum bin 40 – 50 GeV, for  $D_s^+$ . The blue dotted line is DfB and the black dashed line is BKG. The bins in each plot are the bins of  $q \times \varphi$  vs  $p_T$  with respect to the muon. The upper left is bin 1, upper right is bin 2, bottom left is bin 3 and bottom right is bin 4.

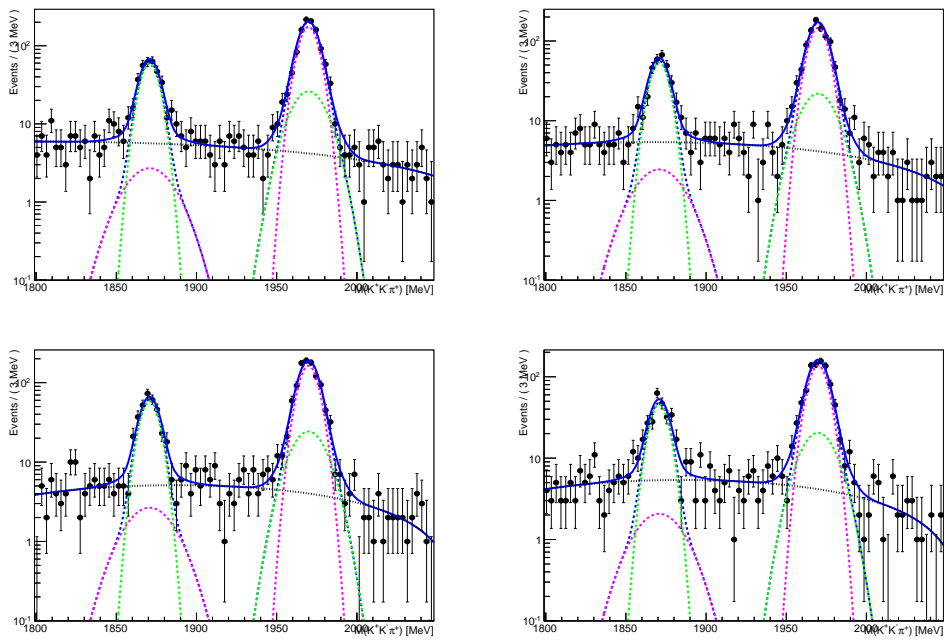


Figure 2.38: Signal data 1D fit results for magnet up, muon momentum bin 40 – 50 GeV, for  $D_s^+$ . The blue dotted line is DfB and the black dashed line is BKG. The bins in each plot are the bins of  $q \times \varphi$  vs  $p_T$  with respect to the muon. The upper left is bin 5, upper right is bin 6, bottom left is bin 7 and the bottom right is bin 8.

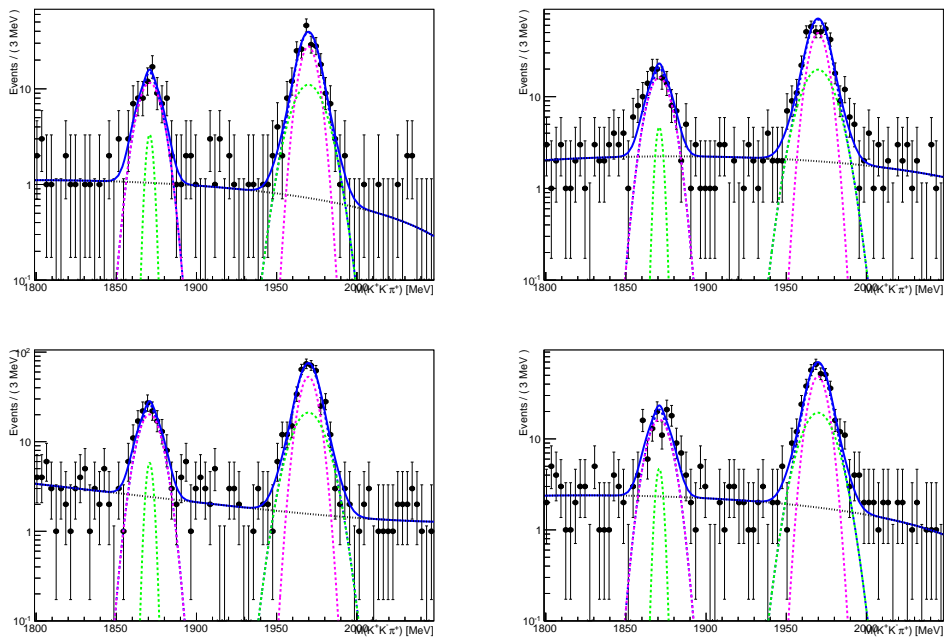


Figure 2.39: Signal data 1D fit results for magnet up, muon momentum bin 50 – 100 GeV, for  $D_s^+$ . The blue dotted line is DfB and the black dashed line is BKG. The bins in each plot are the bins of  $q \times \varphi$  vs  $p_T$  with respect to the muon. The upper left is bin 1, upper right is bin 2, bottom left is bin 3 and bottom right is bin 4.

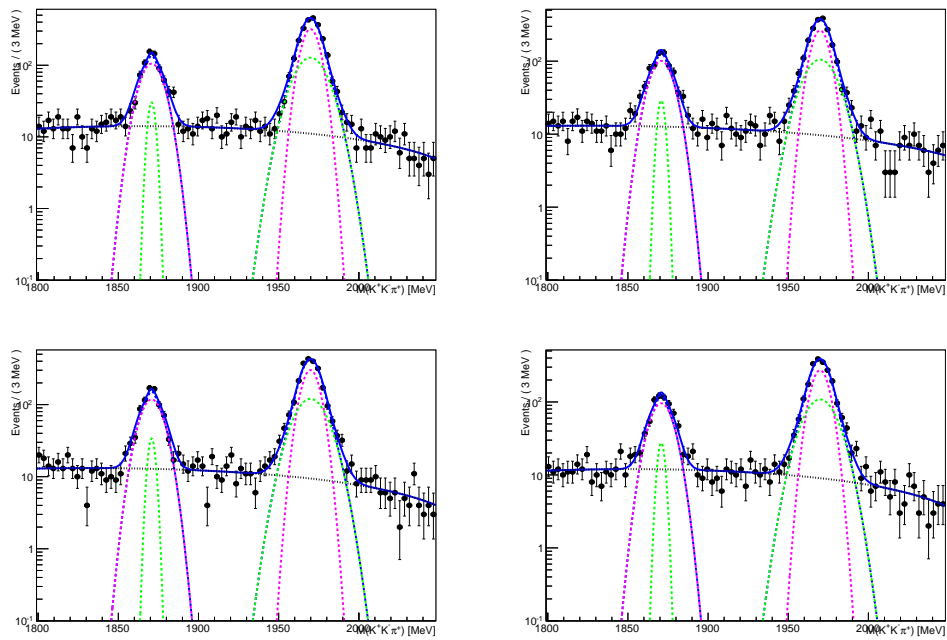


Figure 2.40: Signal data 1D fit results for magnet up, muon momentum bin 50 – 100 GeV, for  $D_s^+$ . The blue dotted line is DfB and the black dashed line is BKG. The bins in each plot are the bins of  $q \times \varphi$  vs  $p_T$  with respect to the muon. The upper left is bin 5, upper right is bin 6, bottom left is bin 7 and the bottom right is bin 8.

# Appendix 3

## 2D Binned Signal Fits

All figures in this section show the fit results for the magnet down polarity data for the two-dimensional fitting procedure. In each mass plot, the dashed blue line is the signal shape, the red solid line is the prompt background shape and the dotted black line is the combinatoric background shape. The overall P.D.F. is represented by the blue solid line.

In each lnIP plot, the dashed blue line is the signal shape, the red solid line is the prompt background shape and the dotted black line is the combinatoric background shape. The overall P.D.F. is represented by the green solid line.

### 3.1 Magnet Down

Figures 3.1 through 3.5 illustrate the fits magnet down polarity.

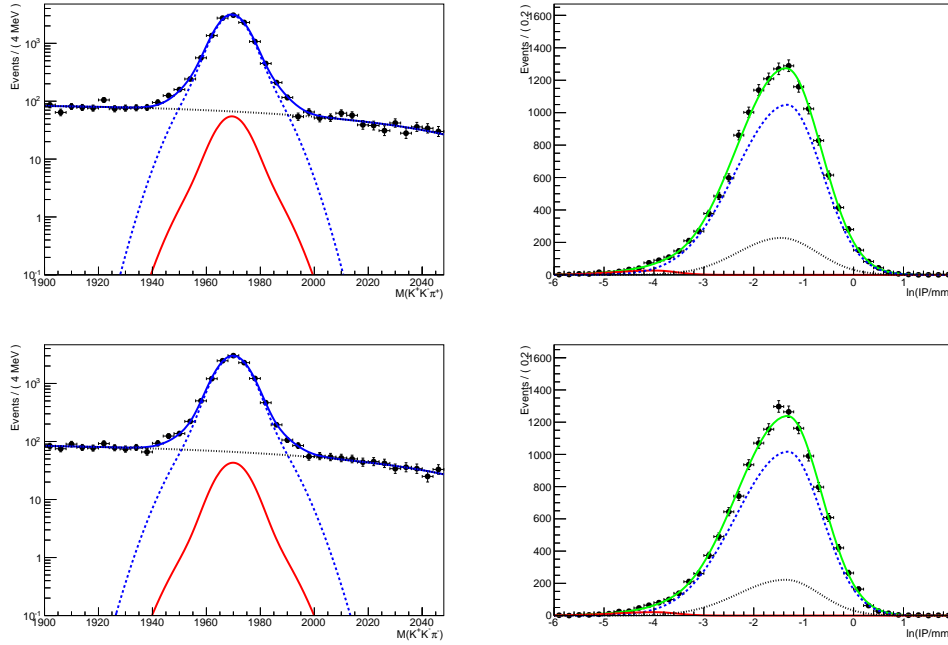


Figure 3.1: Two dimensional fits of magnet down data for muon momentum bin 6 – 20 GeV. Top plots are for  $D_s^+$  and bottom plots are for  $D_s^-$ .

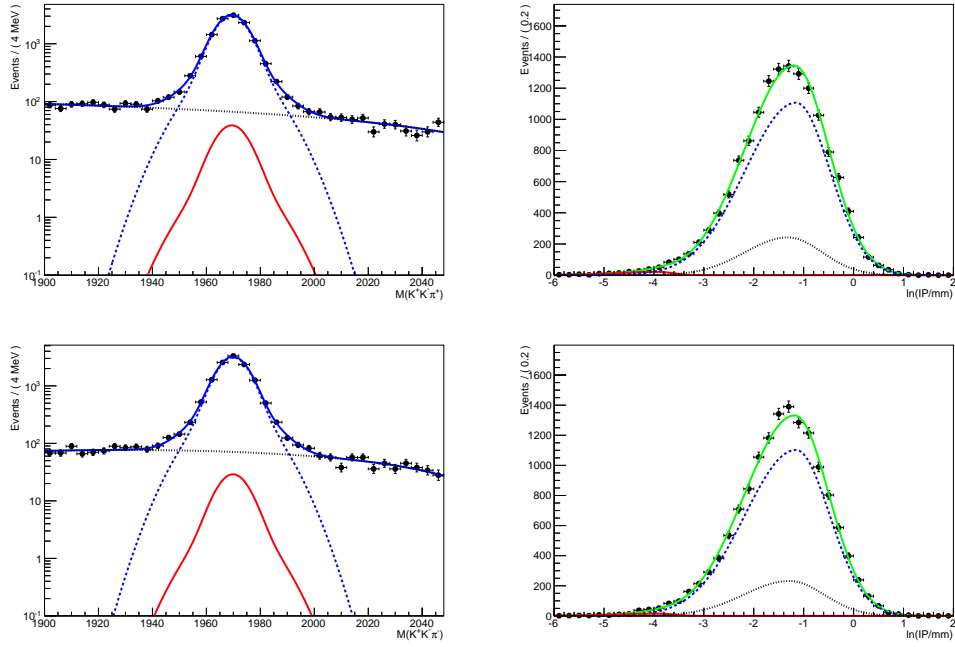


Figure 3.2: Two dimensional fits of magnet down data for muon momentum bin 20 – 30 GeV. Top plots are for  $D_s^+$  and bottom plots are for  $D_s^-$ .

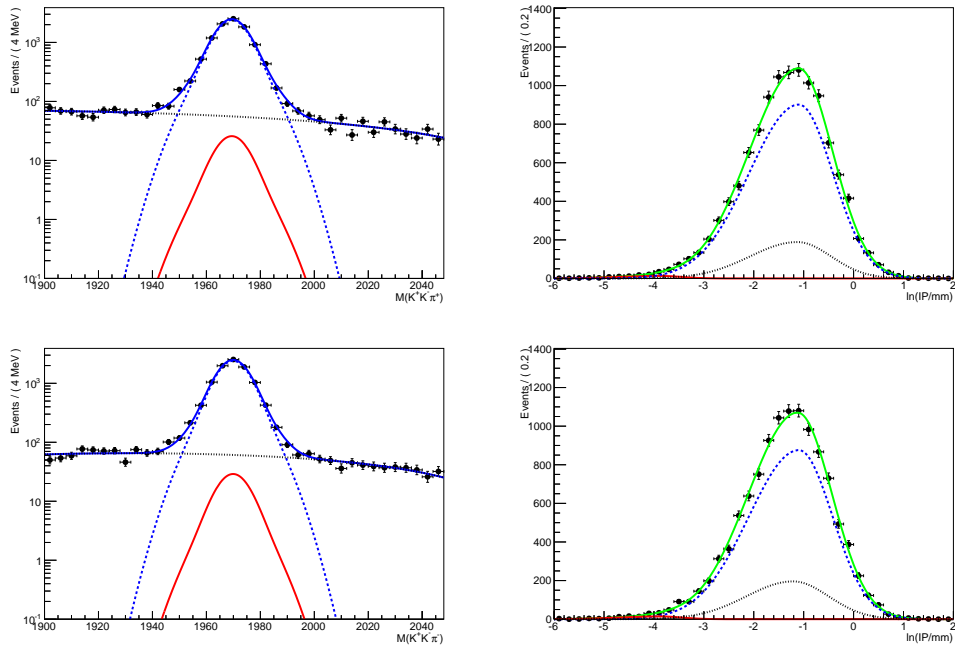


Figure 3.3: Two dimensional fits of magnet down data for muon momentum bin 30 – 40 GeV. Top plots are for  $D_s^+$  and bottom plots are for  $D_s^-$ .



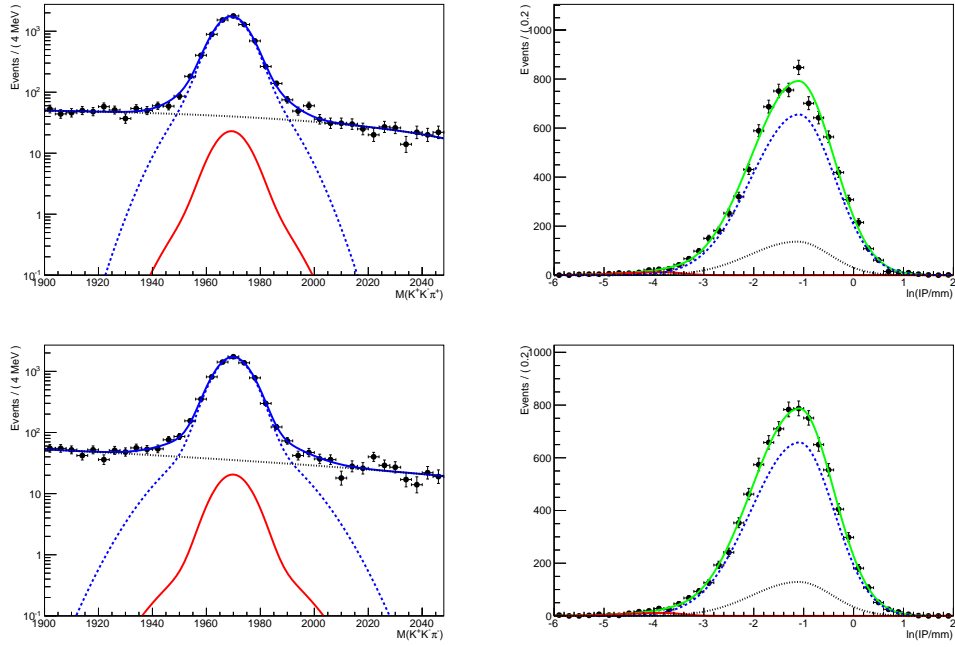


Figure 3.4: Two dimensional fits of magnet down data for muon momentum bin 40 – 50 GeV. Top plots are for  $D_s^+$  and bottom plots are for  $D_s^-$ .

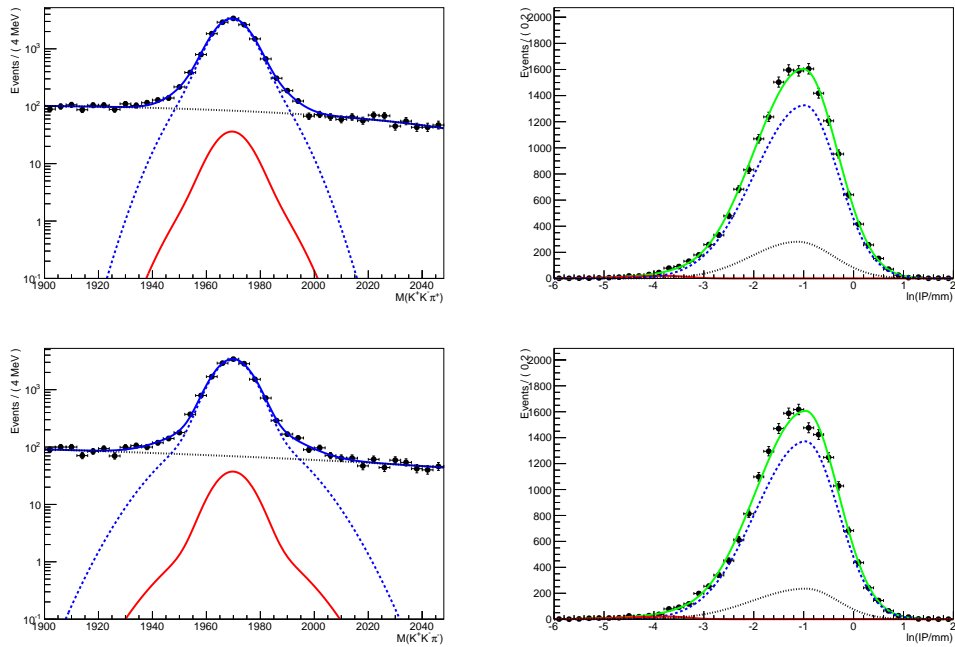


Figure 3.5: Two dimensional fits of magnet down data for muon momentum bin 50 – 100 GeV. Top plots are for  $D_s^+$  and bottom plots are for  $D_s^-$ .

## 3.2 Magnet Up

Figures 3.1 through 3.5 illustrate the fits magnet down polarity.

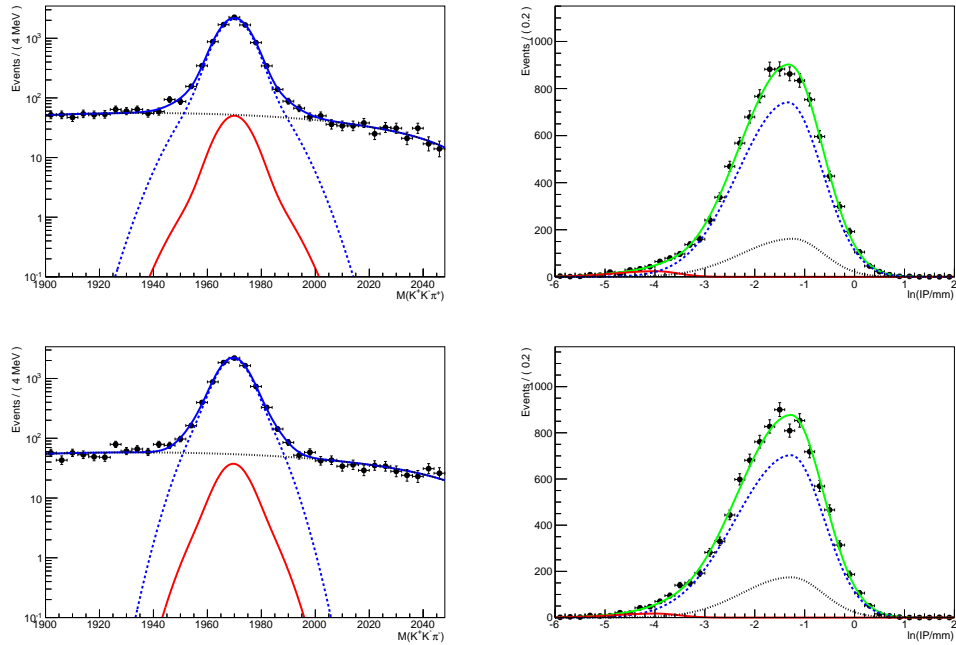


Figure 3.6: Two dimensional fits of magnet up data for muon momentum bin 6 – 20 GeV. Top plots are for  $D_s^+$  and bottom plots are for  $D_s^-$ .

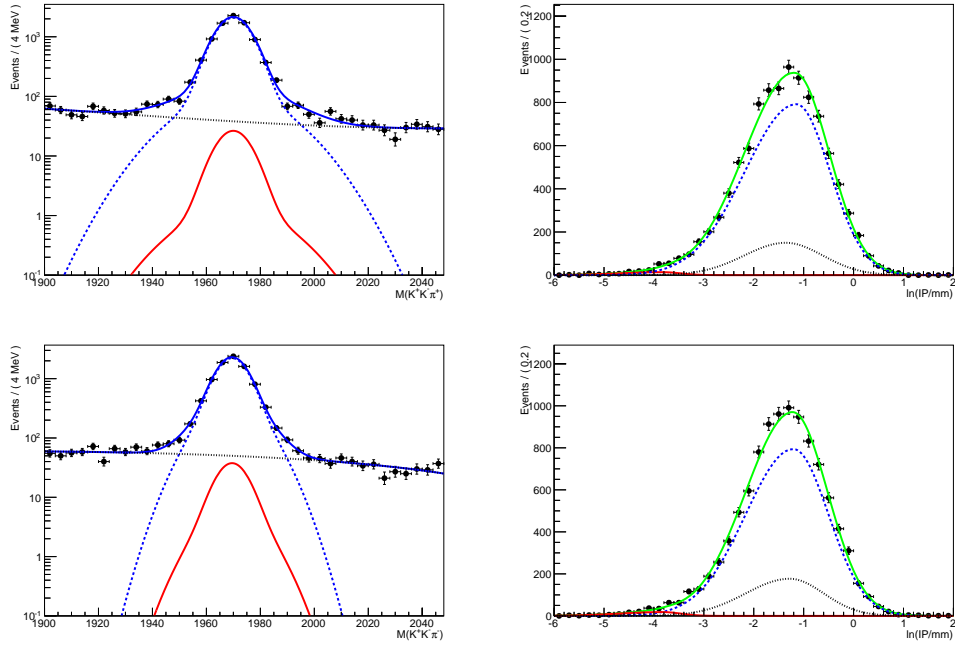


Figure 3.7: Two dimensional fits of magnet up data for muon momentum bin 20 – 30 GeV. Top plots are for  $D_s^+$  and bottom plots are for  $D_s^-$ .

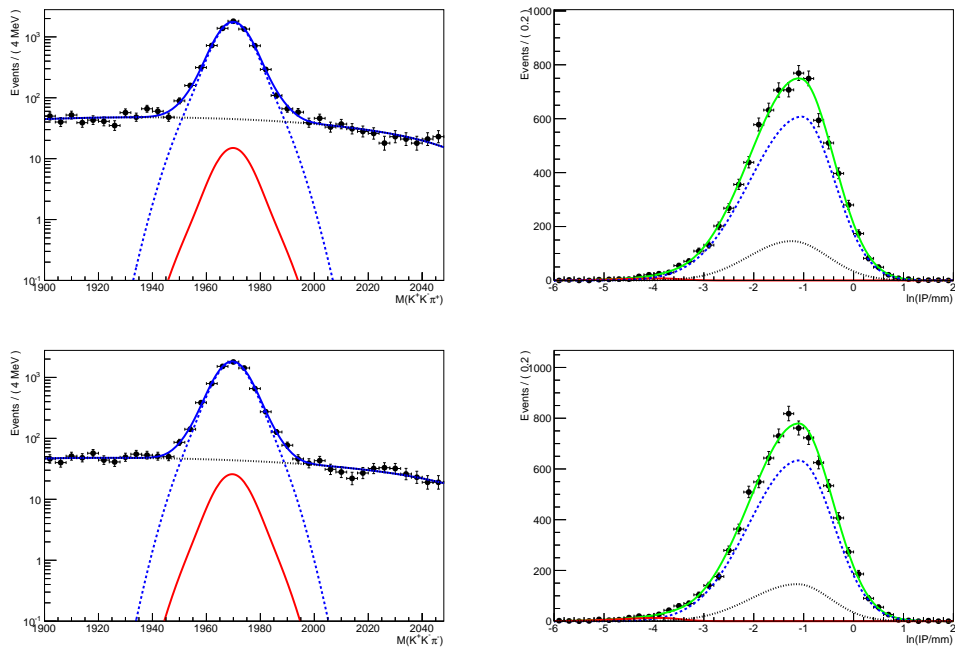


Figure 3.8: Two dimensional fits. Two dimensional fits of magnet up data for muon momentum bin 30 – 40 GeV. Top plots are for  $D_s^+$  and bottom plots are for  $D_s^-$ .

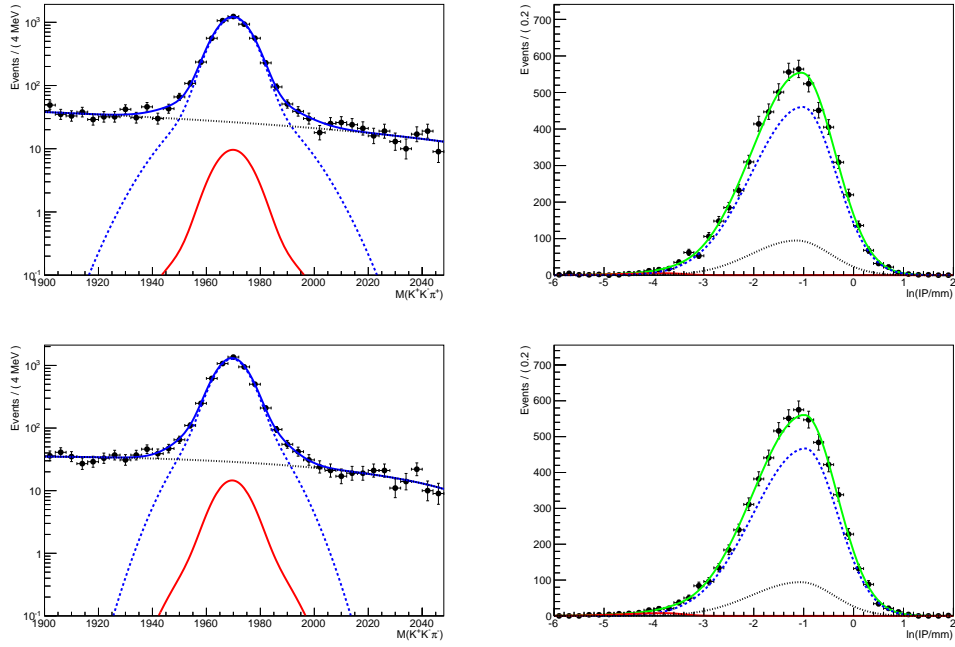


Figure 3.9: Two dimensional fits of magnet up data for muon momentum bin 40 – 50 GeV. Top plots are for  $D_s^+$  and bottom plots are for  $D_s^-$ .

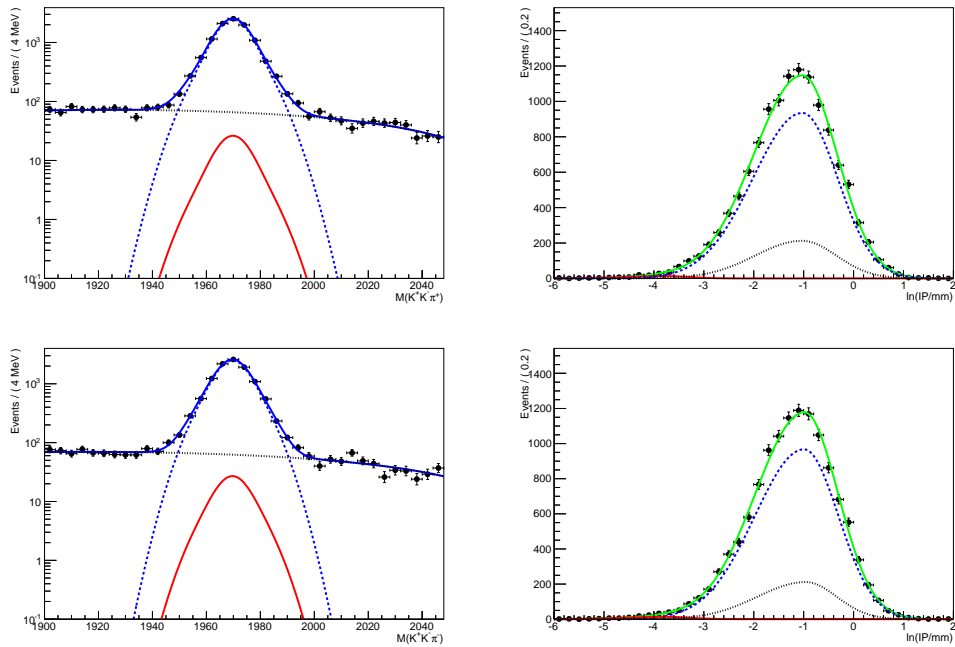


Figure 3.10: Two dimensional fits of magnet up data for muon momentum bin 50 – 100 GeV. Top plots are for  $D_s^+$  and bottom plots are for  $D_s^-$ .

# Appendix 4

## Muon Efficiency Studies

### 4.1 L0 Trigger Muon Studies

The Level-0 trigger is the first trigger in reducing the data to a usable data sample. L0 is a hardware trigger (discussed in section 2), which triggers on leptons and hadrons. Due to the physical nature of this trigger, there could be potential asymmetries not accounted for in the main analysis. The left and right sides of the detector, also called A and C respectively, are offset slightly. In fact, there has been a large asymmetry seen in the L0 Muon trigger occurring as a function of the muon  $p_T$ , which is due to this left-right offset. In order to reduce this asymmetry induced by the detector, a Look Up Table (LUT) is used. This LUT consists of corrected  $p_T$  values of muons when they hit the muon stations. The LUT does not contain all possible combinations due to a change in parameters in the system. Consequently, there is a 0.3 – 0.4% loss of event. This LUT fix is applied to the signal samples and the control samples ( $J/\psi$ ) alike, which are both used in computing the identification and trigger efficiencies. The application of this fix reduces the asymmetry due to the L0 Muon trigger to essentially zero<sup>1</sup>.

---

<sup>1</sup>Studies done by Z. Xing, A. Webber and M. Vesterinen.

## 4.2 HLT2 Muon (and Other Hadron) Studies

In order to assess the HLT2 effects on the samples used they must be investigated. This is done by using another sample, mainly  $B \rightarrow D\mu\nu$ , with  $D \rightarrow \phi\pi$  and  $\phi \rightarrow KK$ , which has the same topology as the signal channel. However with a factor of 16 higher statistics, analysis is a bit easier. All final state particles are required to pass the same cuts as the signal channel, including the muon passing the usual L0 TOS and HLT1 lines required of the signal channel. Instead of requiring that the entire  $B$  passes the trigger, it is broken down such that the trigger effects on each final state particle can be examined. For the muon, a ratio is defined:

$$\epsilon_{HLT2TopoMuNBody} = \frac{(B \text{ events passing HLT2TopoMu4BodyBBDT\_TOS})}{((D \rightarrow KK\pi) \text{ events passing HLT2Topo3BodyBBDT\_TOS})} \quad (4.1)$$

where the denominator trigger is the same as HLT2 trigger including the muon, but *without* the requirement that one of the particles passing the trigger be a muon. The TOS efficiency of the  $D$  hadron is used here rather than the TIS efficiency of the  $B$  hadron because the latter is significantly smaller than the former. Measuring the efficiencies in this method provides a statistical precision that is approximately three times larger than for the signal channel. Figure 4.1 illustrates the efficiency and efficiency ratios for the muon part of the HLT2 topological lines. The other hadron final state particle efficiencies are calculated in much the same way, allowing for the determination of the overall HLT2 bias. This bias is less than  $10^{-3}$  at the 68% C.L. A systematic error of  $5 \times 10^{-4}$  or 0.05% is assigned to possible HLT2 charge asymmetries.

## 4.3 Muon Efficiencies

For completeness, all muon efficiencies are listed in tables 4.1 to 4.5 for the kinematic binning  $q \times p_x$  vs  $p_y$ .

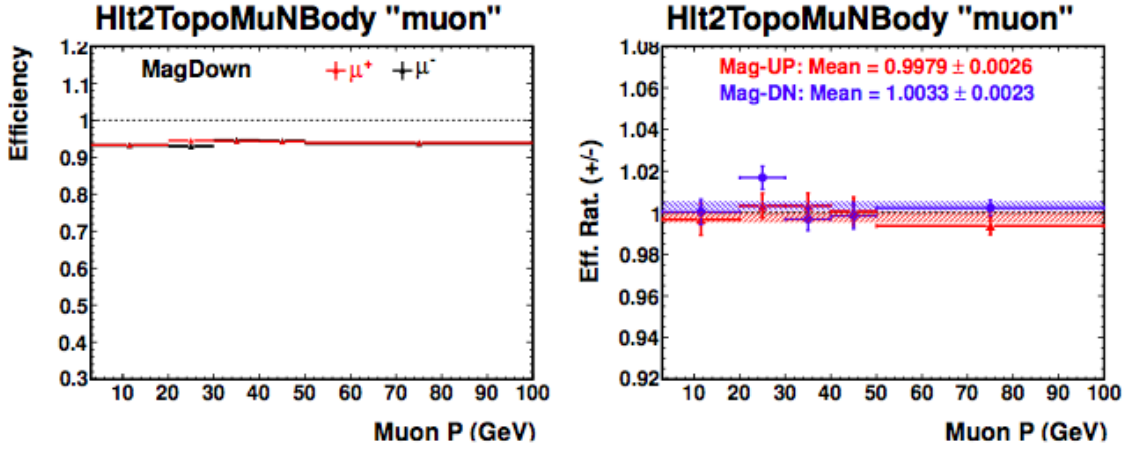


Figure 4.1: The left plot illustrates the efficiency for the muon portion of the HLT2 topological lines, for magnet down. The right plot illustrates the efficiency ratio of the  $\mu^+$  to  $\mu^-$  for the same HLT2 lines for both magnet up (red) and down (blue).

Table 4.1: Overall muon efficiency table using KS sample after the operation  $q \times p_x$  vs  $p_y$  for muon momentum bin 6 – 20 GeV.

	Mag Up		Mag Down	
$q \times p_x$ vs $p_y$ bin	$\epsilon(\mu^+)$	$\epsilon(\mu^-)$	$\epsilon(\mu^+)$	$\epsilon(\mu^-)$
1	$65.6 \pm 1.7$	$62.4 \pm 1.7$	$66.9 \pm 1.4$	$67.7 \pm 1.4$
2	$55.6 \pm 0.8$	$53.3 \pm 0.8$	$49.0 \pm 0.7$	$47.2 \pm 0.7$
3	$56.3 \pm 0.8$	$52.3 \pm 0.8$	$50.1 \pm 0.7$	$50.0 \pm 0.7$
4	$47.7 \pm 0.8$	$49.4 \pm 0.8$	$54.0 \pm 0.7$	$54.8 \pm 0.7$
5	$48.7 \pm 0.8$	$50.2 \pm 0.8$	$55.5 \pm 0.7$	$53.4 \pm 0.7$
6	$69.8 \pm 1.7$	$69.1 \pm 1.7$	$65.7 \pm 1.4$	$65.4 \pm 1.5$
7	$48.5 \pm 0.7$	$47.9 \pm 0.6$	$50.1 \pm 0.5$	$52.3 \pm 0.5$
8	$33.1 \pm 0.9$	$31.9 \pm 0.8$	$28.4 \pm 0.6$	$27.7 \pm 0.6$
9	$28.3 \pm 0.8$	$27.2 \pm 0.8$	$32.5 \pm 0.7$	$32.4 \pm 0.7$
10	$51.8 \pm 0.6$	$50.3 \pm 0.6$	$49.1 \pm 0.5$	$50.0 \pm 0.5$

Table 4.2: Overall muon efficiency table using KS sample after the operation  $q \times p_x$  vs  $p_y$  for muon momentum bin 20 – 30 GeV.

	Mag Up		Mag Down	
$q \times p_x$ vs $p_y$ bin	$\epsilon(\mu^+)$	$\epsilon(\mu^-)$	$\epsilon(\mu^+)$	$\epsilon(\mu^-)$
1	$76.9 \pm 0.9$	$75.7 \pm 0.9$	$75.0 \pm 0.8$	$77.1 \pm 0.7$
2	$66.6 \pm 0.8$	$64.2 \pm 0.8$	$61.7 \pm 0.7$	$61.2 \pm 0.7$
3	$64.7 \pm 0.8$	$64.0 \pm 0.8$	$61.1 \pm 0.7$	$60.0 \pm 0.7$
4	$59.0 \pm 0.8$	$60.4 \pm 0.8$	$65.5 \pm 0.7$	$66.2 \pm 0.7$
5	$59.4 \pm 0.8$	$63.1 \pm 0.8$	$66.6 \pm 0.6$	$64.9 \pm 0.6$
6	$77.4 \pm 0.9$	$76.2 \pm 0.9$	$74.6 \pm 0.8$	$76.0 \pm 0.8$
7	$59.6 \pm 0.8$	$57.9 \pm 0.8$	$58.8 \pm 0.6$	$62.1 \pm 0.6$
8	$36.9 \pm 1.2$	$35.6 \pm 1.1$	$35.4 \pm 1.0$	$34.9 \pm 1.0$
9	$35.4 \pm 1.2$	$34.7 \pm 1.2$	$37.4 \pm 1.0$	$36.1 \pm 1.0$
10	$60.8 \pm 0.7$	$59.1 \pm 0.7$	$59.1 \pm 0.6$	$56.9 \pm 0.6$

Table 4.3: Overall muon efficiency table using KS sample after the operation  $q \times p_x$  vs  $p_y$  for muon momentum bin 30 – 40 GeV.

	Mag Up		Mag Down	
$q \times p_x$ vs $p_y$ bin	$\epsilon(\mu^+)$	$\epsilon(\mu^-)$	$\epsilon(\mu^+)$	$\epsilon(\mu^-)$
1	$78.4 \pm 0.8$	$75.7 \pm 0.9$	$77.1 \pm 0.7$	$79.7 \pm 0.7$
2	$67.4 \pm 0.9$	$67.1 \pm 0.9$	$65.0 \pm 0.8$	$65.3 \pm 0.8$
3	$69.0 \pm 0.9$	$66.5 \pm 0.9$	$64.8 \pm 0.7$	$62.2 \pm 0.7$
4	$65.3 \pm 0.9$	$65.8 \pm 0.9$	$67.8 \pm 0.7$	$68.9 \pm 0.7$
5	$63.7 \pm 0.9$	$64.1 \pm 0.9$	$67.3 \pm 0.7$	$68.3 \pm 0.7$
6	$77.5 \pm 0.8$	$78.2 \pm 0.8$	$77.0 \pm 0.7$	$76.9 \pm 0.7$
7	$56.6 \pm 0.9$	$53.4 \pm 0.9$	$60.0 \pm 0.7$	$60.6 \pm 0.8$
8	$42.0 \pm 1.6$	$38.8 \pm 1.5$	$35.6 \pm 1.2$	$36.7 \pm 1.3$
9	$36.1 \pm 1.5$	$36.2 \pm 1.6$	$41.2 \pm 1.3$	$40.1 \pm 1.3$
10	$61.5 \pm 0.9$	$59.1 \pm 0.9$	$56.3 \pm 0.8$	$54.7 \pm 0.8$



Table 4.4: Overall muon efficiency table using KS sample after the operation  $q \times p_x$  vs  $p_y$  for muon momentum bin 40 – 50 GeV.

	Mag Up		Mag Down	
$q \times p_x$ vs $p_y$ bin	$\epsilon(\mu^+)$	$\epsilon(\mu^-)$	$\epsilon(\mu^+)$	$\epsilon(\mu^-)$
1	$75.4 \pm 0.9$	$77.6 \pm 0.9$	$79.0 \pm 0.7$	$79.3 \pm 0.7$
2	$69.1 \pm 1.0$	$69.0 \pm 1.0$	$66.3 \pm 0.9$	$66.2 \pm 0.9$
3	$70.5 \pm 1.0$	$67.8 \pm 1.0$	$66.0 \pm 0.9$	$66.5 \pm 0.9$
4	$64.8 \pm 1.0$	$65.8 \pm 1.1$	$68.5 \pm 0.9$	$69.5 \pm 0.9$
5	$63.9 \pm 1.0$	$62.9 \pm 1.0$	$68.9 \pm 0.9$	$68.8 \pm 0.8$
6	$80.2 \pm 0.8$	$78.9 \pm 0.8$	$76.5 \pm 0.7$	$76.3 \pm 0.7$
7	$57.8 \pm 1.1$	$60.2 \pm 1.1$	$55.4 \pm 0.9$	$57.8 \pm 0.9$
8	$36.3 \pm 2.0$	$39.7 \pm 2.0$	$31.6 \pm 1.5$	$36.4 \pm 1.6$
9	$38.0 \pm 2.0$	$39.3 \pm 2.0$	$41.8 \pm 1.7$	$36.0 \pm 1.7$
10	$55.6 \pm 1.1$	$55.2 \pm 1.1$	$59.7 \pm 1.0$	$57.0 \pm 1.0$

Table 4.5: Overall muon efficiency table using KS sample after the operation  $q \times p_x$  vs  $p_y$  for muon momentum bin 50 – 100 GeV.

	Mag Up		Mag Down	
$q \times p_x$ vs $p_y$ bin	$\epsilon(\mu^+)$	$\epsilon(\mu^-)$	$\epsilon(\mu^+)$	$\epsilon(\mu^-)$
1	$76.2 \pm 0.5$	$76.7 \pm 0.5$	$78.1 \pm 0.4$	$79.7 \pm 0.4$
2	$65.6 \pm 0.7$	$67.3 \pm 0.7$	$63.0 \pm 0.6$	$65.4 \pm 0.6$
3	$68.5 \pm 0.7$	$68.0 \pm 0.7$	$62.5 \pm 0.6$	$62.7 \pm 0.6$
4	$63.7 \pm 0.7$	$63.1 \pm 0.7$	$67.9 \pm 0.6$	$65.9 \pm 0.6$
5	$63.9 \pm 0.7$	$61.4 \pm 0.7$	$67.8 \pm 0.6$	$67.3 \pm 0.6$
6	$78.7 \pm 0.5$	$78.2 \pm 0.5$	$77.5 \pm 0.5$	$77.3 \pm 0.5$
7	$54.2 \pm 0.8$	$55.4 \pm 0.8$	$37.6 \pm 0.6$	$39.4 \pm 0.7$
8	$31.9 \pm 1.4$	$30.8 \pm 1.3$	$26.7 \pm 1.2$	$26.9 \pm 1.2$
9	$27.0 \pm 1.5$	$25.4 \pm 1.3$	$34.3 \pm 1.3$	$29.7 \pm 1.2$
10	$39.1 \pm 0.8$	$36.4 \pm 0.7$	$57.2 \pm 0.7$	$54.8 \pm 0.7$

# Appendix 5

## Pion Efficiency Studies

The pion efficiency studies have been discussed in the main body of the text, however there are some criteria and other items too long to discuss there. Firstly, the stripping cuts and offline cuts that are applied to the data sample used in these studies are listed in tables 5.1 and 5.2 respectively.

Additional cuts are applied on the significance of the kinematically fitted momentum and transverse momentum for the missing pion in the partial reconstruction. This is done to remove kinematic regions where the constraints are not strong enough to infer the momentum information of the missing particle. The cuts are  $p^{\text{Inferred}}/\sigma(p^{\text{Inferred}}) > 2$  and  $p_T^{\text{Inferred}}/\sigma(p_T^{\text{Inferred}}) > 2.5$ , where  $p^{\text{Inferred}}$  and  $p_T^{\text{Inferred}}$  are the inferred momentum and transverse momentum, and  $\sigma(p^{\text{Inferred}})$  and  $\sigma(p_T^{\text{Inferred}})$  are the estimated uncertainties. In addition to the stripping and offline cuts listed, fiducial cuts are applied to the data to remove kinematic areas of large ( $\sim 100\%$ ) raw asymmetry as seen in figure 5.1. These fiducial cuts are applied only to the additional pion in the fully reconstructed sample. These are included in the table 5.2 however it is important to understand these cuts. The first cut set<sup>1</sup> is made to

---

<sup>1</sup>This is located in the third row of table 5.2. Within the third row, the fiducial cuts are the last three listed.

Table 5.1: Stripping cuts on  $D^{*+} \rightarrow D^0(\rightarrow K^-\pi^+\pi^-\pi^+)\pi_s$ .

Particle	Requirement
$D^0(\rightarrow K^-\pi^+\pi^-)$ final state particles	$p > 2 \text{ GeV}$ $p_T > 400 \text{ MeV}$ IP $\chi^2 > 4$ Track $\chi^2/NDOF < 3$ K: $DLL_{K\pi} > 4$ $\pi$ : $DLL_{K\pi} < 10$ and $DLL_{\mu\pi} < 10$
Slow $\pi^\pm$ Selections	$p_T > 250 \text{ MeV}$ IP $\chi^2 < 4$ IP $< 0.3 \text{ mm}$ Track $\chi^2/NDOF < 3$ K: $DLL_{K\pi} < 10$
$D^0(\rightarrow K^-\pi^+\pi^-)$ Meson Selections	$p_T > 3 \text{ GeV}$ Vertex fit $\chi^2/NDOF < 6$ FD $\chi^2 > 120$ FD $> 4 \text{ mm}$ $DIRA(\cos\theta) > 0.9997$ IP $\chi^2 < 25$ $1.4 < m(K\pi\pi) < 1.7 \text{ GeV}$
$D^+$ Selections	Vertex fit $\chi^2/NDOF < 5$ FD $\chi^2 > 25$ IP $\chi^2 < 25$ $p_T > 3 \text{ GeV}$
Additional Selections	$ m(\pi^+\pi^-) - m_{PDG}(\rho)  < 200 \text{ MeV}$ $m(\pi_s K^-\pi^+\pi^-) - m(K^-\pi^+\pi^-) - m(\pi_s) < 40 \text{ MeV}$ HLT Global TOS on $(K^-\pi^+\pi^-, \pi_s^+)$

remove a region where the results do not overlap. The cut is defined as

$$|p_x| \leq \alpha(p_z - p_0), \quad (5.1)$$

$$\alpha = 0.317,$$

$$p_0 = 2400 \text{ MeV}.$$

Table 5.2: Offline selections on  $D^{*+} \rightarrow D^0(\rightarrow K^-\pi^+\pi^-\pi^+)\pi_s$ , for the additional  $\pi$ .

Particle	Requirement
Partially Reconstructed Sample	$p^{\text{Inferred}}/\sigma(p^{\text{Inferred}}) > 2$ $p_T^{\text{Inferred}}/\sigma(p_T^{\text{Inferred}}) > 2.5$
Fully Reconstructed Sample	$ m(K^-\pi^+\pi^-\pi^+) - m_{PDG}(D^0)  < 30 \text{ MeV}$ Vertex fit $\chi^2/NDOF < 6$
Additional $\pi$ Selections	$p > 2 \text{ GeV}$ $p_T > 300 \text{ MeV}$ Track $\chi^2/NDOF < 4$ CloneDist $\leq 0$ $ p_x  \leq \alpha(p_z - p_0), \alpha = 0.317, p_0 = 2400 \text{ MeV}$ $p_1 - \beta p_z <  p_x  < p_2 + \beta_2 p_z$ for events with $ p_y/p_x  < 0.02$ , $p_1 = 418 \text{ MeV}, p_2 = 497 \text{ MeV}, \beta_1 = 0.01397, \beta_2 = 0.01605$
Additional PID Selections	$DLL_{K\pi} < -2$

The second set is made to remove an acceptance hole when the pion's  $p_x$  value is  $\simeq 500 \text{ MeV}$ .

This is when the pion events have a value of  $|p_y/p_x| < 0.02$ . This cut is defined as

$$p_1 - \beta p_z < |p_x| < p_2 + \beta_2 p_z \quad (5.2)$$

$$p_1 = 418 \text{ MeV},$$

$$p_2 = 497 \text{ MeV},$$

$$\beta_1 = 0.01397,$$

$$\beta_2 = 0.01605.$$

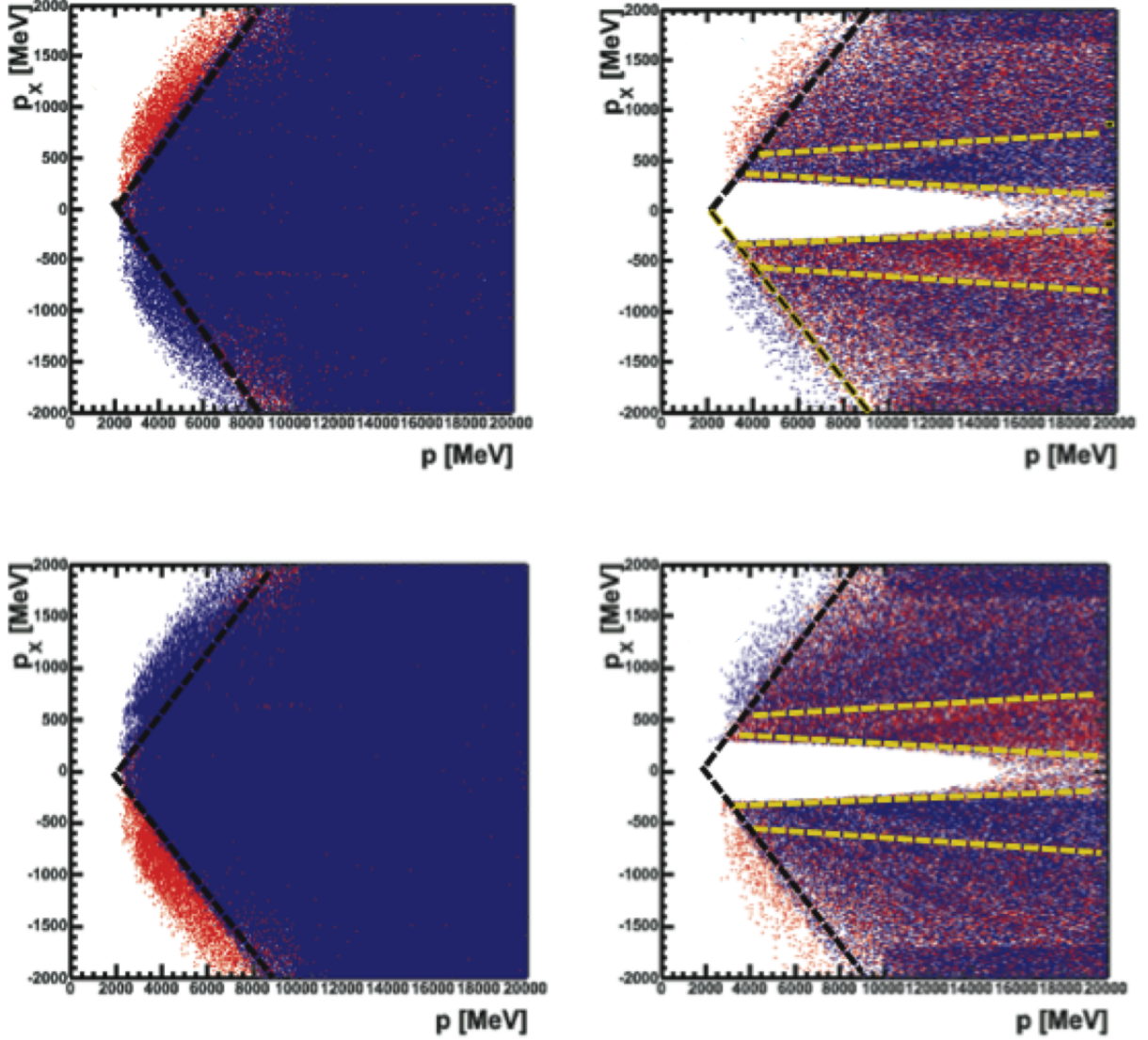


Figure 5.1: Four plots show the distribution of  $p$  versus  $p_x$  of the additional pion in the fully reconstructed sample prior to the application of the two sets of fiducial cuts. For data taken with magnet polarity up: (a) when  $|p_y/p_z| > 0.02$ , (b) when  $|p_y/p_z| < 0.02$  and for data taken with magnet polarity down: (c) when  $|p_y/p_z| > 0.02$ , (d) when  $|p_y/p_z| < 0.02$ . The red and blue points correspond to  $\pi^+$  and  $\pi^-$ , respectively.

# Bibliography

- [1] Particle Data Group, J. Beringer *et al.*, *Review of Particle Physics*, Phys. Rev. **D86** (2012) 010001.
- [2] D. H. Perkins, *Introduction to High Energy Physics*, Cambridge University Press, 2000.
- [3] F. Halzen and A. D. Martin, *Quarks & Leptons: An Introductory Course in Modern Particle Physics*, John Wiley & Sons, 1984.
- [4] C. S. Wu *et al.*, *Experimental Test of Parity Conservation in Beta Decay*, Phys. Rev. **105** (1957) 1413.
- [5] T. D. Lee and C. N. Yang, *Question of Parity Conservation in Weak Interactions*, Phys. Rev. **104** (1956) 254.
- [6] J. H. Christenson, J. W. Cronin, V. L. Fitch, and R. Turlay, *Evidence for the  $2\pi$  Decay of the  $K_2^0$  Meson*, Phys. Rev. Lett. **13** (1964) 138.
- [7] N. Cabibbo, *Unitary Symmetry and Leptonic Decays*, Phys. Rev. Lett. **10** (1963) 531.
- [8] M. Kobayashi and T. Maskawa, *CP-Violation in the Renormalizable Theory of Weak Interaction*, Progress of Theoretical Physics **49** (1973), no. 2 652.
- [9] L. Wolfenstein, *Parametrization of the Kobayashi-Maskawa Matrix*, Phys. Rev. Lett. **51** (1983) 1945.

- [10] M. Artuso, E. Barberio, and S. Stone, *B Meson Decays*, PMC Phys. **A3** (2009) 3, [arXiv:0902.3743](#).
- [11] Z. Ligeti, *Introduction to Heavy Meson Decays and CP Asymmetries*, eConf **C020805** (2002) L02, [arXiv:hep-ph/0302031](#).
- [12] N. Isgur and M. B. Wise, *Weak decays of heavy mesons in the static quark approximation*, Phys. Lett. **B232** (1989) 113.
- [13] V. G. Luth, *Semileptonic B Meson Decays*, Ann. Rev. Nucl. Part. Sci. **61** (2011) 119.
- [14] C. W. Bauer *et al.*, *Global analysis of inclusive B decays*, Phys. Rev. D **70** (2004) 094017.
- [15] K. Berkelman and S. L. Stone, *Decays of B Mesons*, Annual Review of Nuclear and Particle Science **41** (1991), no. 1 1.
- [16] U. Nierste, *Three Lectures on Meson Mixing and CKM phenomenology*, [arXiv:0904.1869](#).
- [17] A. J. Lenz, *Simple relation for  $B_s$  mixing*, Phys. Rev. **D84** (2011) 031501, [arXiv:1106.3200](#).
- [18] A. Lenz, *Theoretical update of B-Mixing and Lifetimes*, [arXiv:1205.1444](#).
- [19] D0 collaboration, V. M. Abazov *et al.*, *Measurement of the anomalous like-sign dimuon charge asymmetry with  $9\text{fb}^{-1}$  of  $p\bar{p}$  collisions*, Phys. Rev. **D84** (2011) 052007.
- [20] D0 collaboration, V. M. Abazov *et al.*, *Measurement of the semileptonic charge asymmetry using  $B_s^0 \rightarrow D_s\mu X$  decays*, Phys. Rev. Lett. **110** (2013) 011801.
- [21] D0 Collaboration, V. M. Abazov *et al.*, *Measurement of the semileptonic charge asymmetry in  $B^0$  meson mixing with the D0 detector*, Phys. Rev. **D86** (2012) 072009, [arXiv:1208.5813](#).

- [22] L. Evans and P. Bryant, *LHC Machine*, JINST **3** (2008) S08001.
- [23] G. Lutz, *Semiconductor Radiation Detectors: Device Physics (Accelerator Physics)*, Springer, 2007.
- [24] H. Spieler, *Semiconductor Detector Systems (Semiconductor Science and Technology)*, Oxford University Press, USA, 2005.
- [25] LHCb collaboration, A. A. Alves Jr. *et al.*, *The LHCb detector at the LHC*, JINST **3** (2008) S08005.
- [26] S. Amato *et al.*, *LHCb magnet: Technical Design Report*, Technical Design Report LHCb, CERN, Geneva, 2000.
- [27] M. Tobin, *Performance of the LHCb Silicon Tracker in pp collisions at the LHC*, in *Nuclear Science Symposium Conference Record (NSS/MIC), 2010 IEEE*, pp. 935–938, 2010.
- [28] Antunes-Nobrega *et al.*, *LHCb reoptimized detector design and performance: Technical Design Report*, Technical Design Report LHCb, CERN, Geneva, 2003.
- [29] W. R. Leo, *Techniques for Nuclear and Particle Physics Experiments: A How-to Approach*, Springer, Berlin, 2., überarb. a. ed., 1994.
- [30] A. Borgia *et al.*, *The Magnetic Distortion Calibration System of the LHCb RICH1 Detector*, Tech. Rep. LHCb-PUB-2011-018. CERN-LHCb-PUB-2011-018, CERN, Geneva, 2012.
- [31] M. Adinolfi *et al.*, *Performance of the LHCb RICH detector at the LHC*, arXiv:1211.6759.
- [32] R. Wigmans, *Calorimetry: Energy Measurement in Particle Physics*, Clarendon Press, Oxford, 2000.



- [33] T. Ferbel, *Experimental Techniques in High Energy Physics*, Frontiers in Physics, Addison-Wesley, Menlo Park, CA, 1st ed. ed., 1987.
- [34] A. Alves Jr *et al.*, *Performance of the LHCb muon system*, tech. rep., CERN, Geneva, 2012.
- [35] Barbosa-Marinho *et al.*, *LHCb muon system: second addendum to the Technical Design Report*, Technical Design Report LHCb, CERN, Geneva, 2005.
- [36] G. Bencivenni *et al.*, *Advances in triple-GEM detector operation for high-rate particle triggering*, Nuclear Instruments and Methods in Physics Research Section A: Accelerators, Spectrometers, Detectors and Associated Equipment **513** (2003), no. 12 264.
- [37] E. Aslanides *et al.*, *The Level-0 Muon Trigger for the LHCb Experiment*, Nuclear Instruments and Methods in Physics Research Section A: Accelerators, Spectrometers, Detectors and Associated Equipment **579** (2007), no. 3 989.
- [38] G. Lanfranchi *et al.*, *The Muon Identification Procedure of the LHCb Experiment for the First Data*, tech. rep., CERN, Geneva, 2009.
- [39] LHCb collaboration, R. Aaij *et al.*, *Measurement of  $b$  hadron production fractions in  $7\text{TeV}$   $pp$  collisions*, Phys. Rev. D **85** (2012) 032008.
- [40] M. Gandelman and E. Polcarpo, *The Performance of the LHCb Muon Identification Procedure*, Tech. Rep. LHCb-2007-145. CERN-LHCb-2007-145, CERN, 2008.
- [41] TMVA Core Developer Team, J. Therhaag, *TMVA: Toolkit for multivariate data analysis*, AIP Conf. Proc. **1504** (2009) 1013.
- [42] V. Gligorov *et al.*, *The HLT inclusive  $B$  triggers*, LHCb-PUB-2011-016.
- [43] LHCb collaboration, R. Aaij *et al.*, *Measurement of the  $D_s^+ - D_s^-$  Production Asymmetry in  $7\text{TeV}$   $pp$  collisions*, Phys. Lett. **713** (2012) 186, arXiv:1205.0897.

- [44] T. Skwarnicki, *A study of the radiative CASCADE transitions between the Upsilon-prime and Upsilon resonances*, PhD thesis, Institute of Nuclear Physics, Krakow, 1986, DESY-F31-86-02.
- [45] H. Gordon, R. W. Lambert, J. van Tilburg, and M. Vesterinen, *A Measurement of the  $K\pi$  Detection Asymmetry*, Tech. Rep. LHCb-INT-2012-027. CERN-LHCb-INT-2012-027, CERN, Geneva, Feb, 2013.
- [46] C. Hadjivasiliou, *Personal Correspondence*, 2012.
- [47] Z. Xing, *Measurement of the semileptonic CP violating asymmetry  $a_{sl}^s$  in  $\overline{B}_s^0$  decays and the  $D_s^+D_s^-$  production asymmetry in 7 TeV pp collisions*, PhD thesis, Syracuse University, Syracuse, NY, 2013.
- [48] HFAG, *Fall 2012 averages: Neutral B meson mixing: CP violation*, May, 2013. [http://www.slac.stanford.edu/xorg/hfag/osc/fall\\_2012/CPV](http://www.slac.stanford.edu/xorg/hfag/osc/fall_2012/CPV).

# VITA

AUTHOR'S NAME: Alessandra Borgia

PLACE OF BIRTH: Brooklyn, New York, U.S.A.

DATE OF BIRTH: October 24, 1984

DEGREES AWARDED:

Bachelor of Science, Physics, SUNY Binghamton, May 2007, *cum laude*

DISTINCTIONS:

*Young Scientist Lightning Round Competition Winner,*

USLUO Meeting, Syracuse University, 2012

*Women in Science and Engineering Future Professoriate Program Associate,*

Syracuse University, 2008-2010

*George E. Moore Award of Academic Achievements in Physics,*

Department of Physics, SUNY Binghamton, 2007

*Honors in Physics, Distinguished Independent Study,*

Department of Physics, SUNY Binghamton, 2007

*Sigma Pi Sigma, National Physics Honor Society,*

SUNY Binghamton, 2005

PROFESSIONAL EXPERIENCE:

*LHCb Semileptonic Working Group Monte Carlo Simulation Lead,*

Department of Physics, Syracuse University & LHCb, 2010–2012

*High Energy Physics Research Assistant,*

Department of Physics, Syracuse University, 2008–2013

*High Energy Physics Outreach Coordinator,*

Department of Physics, Syracuse University, 2008–2013

*Teaching Assistant,*

Department of Physics, Syracuse University, 2007–2008